Spectroscopic Investigations of Interactions and Dynamical Complexities in Electrolytes and Multicomponent Chemical Systems

Thesis Submitted for the Degree of

Doctor of Philosophy (Science)

of

Jadavpur University

By

Amrita Mondal

Department of Chemical and Biological Sciences
S. N. Bose National Centre for Basic Sciences
Block - JD, Sector - III, Salt Lake
Kolkata-700106, India

May 2025

S.N. Bose National Centre for Basic Sciences
Sector - III, Block - JD, Salt Lake, Kolkata - 700098

Dr. Ranjit Biswas *Phone: 033 2335 5706-08 (O)*

Senior Professor *Email: ranjit@bose.res.in*

Chemical and Biological Sciences *Fax: 033 2335 3477*

CERTIFICATE FROM THE SUPERVISOR

This is to certify that the thesis entitled **"Spectroscopic Investigations of Interactions and Dynamical Complexities in Electrolytes and Multicomponent Chemical Systems"** submitted by **Smt. Amrita Mondal** (Index No: **43|20|Chem.|27**), who got her name registered on 16/10/2020 for the award of Ph.D. (Science) degree of Jadavpur University is absolutely based upon her own work under the supervision of **Prof. Ranjit Biswas** and that neither her thesis nor any part of the thesis has been submitted for either any degree/diploma or any other academic award anywhere before.

Dr. Ranjit Biswas
Senior Professor,
Department of Chemical and Biological Sciences
S. N. Bose National Centre for Basic Sciences
Block - JD, Sector - III, Salt Lake, Kolkata-700106, West Bengal, India

Dedicated to

My Parents

Acknowledgement

As I reach the culmination of this thesis journey, my heart is filled with gratitude for all those who have walked alongside me, guiding, supporting, and inspiring me in countless ways. Without their presence and blessings, this thesis would not have been possible.

First and foremost, I would like to express my sincere thanks and deepest gratitude to my supervisor, *Prof. Ranjit Biswas*. His invaluable guidance, constant support, and thoughtful mentorship have molded every stage of my research journey. His encouragement toward independent thinking and scientific integrity has not only enriched my academic growth but also helped me to develop a strong sense of responsibility and confidence as a researcher. His novel ideas, ethical approach, patience, and unwavering commitment to academic excellence have been a constant source of motivation and inspiration. I consider myself truly fortunate to have worked under such a principled and knowledgeable mentor, and I remain deeply grateful for his kind-hearted support throughout this journey.

I express my sincere gratitude to *Prof. Priyadarsi De* (IISER Kolkata) for his highly reassuring collaboration. I am also thankful to *Prof. Mark Maroncelli* (Pennsylvania State University, USA) for authorizing access to his spectral analysis software. I would like to extend my sincere acknowledgement to all the members of my Thesis Committee, *Prof. Manik Pradhan* and *Dr. Suman Chakrabarty* (both from SNBNCBS), for their valuable time, vital feedback, and constructive criticism throughout my PhD journey. I am also grateful to the Department of Chemistry, Jadavpur University, for granting me the opportunity to register for the PhD program.

I would like to express my profound thanks to SNBNCBS for offering me the research fellowship and access to the necessary experimental facilities. My heartfelt thanks extend to all the faculty members, research scholars, and the administrative and technical personnel for their assistance and co-operation throughout my journey. I am also grateful to all the staffs of SNB Mess and Bhagirathi

Canteen for consistently serving delicious meals during my stay at SNBNCBS. Special thanks to *Piyali di*, my household maid, for her steady help and care in managing my room and daily needs.

My sincere thanks go to my present lab mates: *Dhrubajyoti da*, *Jayanta da*, *Narayan da*, *Sudipto*, *Rik*, *Aziz*, and *Jayeta di* from "Physical Chemistry Chemical Physics (PCCP) Lab" for fostering a healthy lab culture. I am also truly thankful to the former members of our research group, *Juriti di*, *Kajal di*, *Atanu da*, *Ejaj da*, *Soumita di*, *Arnab da*, *Shirshendu da*, *Tonima di*, and *Samir da*.

A special note of thanks goes to *Kajal di*. Her guidance significantly shaped my understanding of various experimental procedures and data interpretation during the early stages of my research. I deeply value the insightful scientific discussions we shared, which not only enriched my research perspective but were generously offered at any time, reflecting her tireless inspiration and dedication.

I am also especially grateful to *Jayeta di* and *Tonima di* for their kindness, guidance, and affectionate support. Their warm gestures, from academic assistance to sharing moments of relaxation over tea or brief outings after long, exhausting days, brought much-needed balance and comfort to my daily routine.

A very special note of thanks goes to *Juriti di*. What began as a lab-mate relationship soon blossomed into a bond that feels no less than that of an elder sister, one whose presence has become an inseparable part of my life. Her steadfast support and nurturing care, both academically and personally, have guided me through the most demanding phases of my life. From scientific discussions to everyday conversations, our shared moments have been countless and deeply meaningful. Her boundless emotional support, genuine care, heartfelt affection, and even her occasional scoldings are treasures I hold close to my heart, gifts I will always cherish with deep gratitude. No words can fully capture the appreciation I feel for everything she has been to me.

My heartfelt thanks to *Dr. Parijat Das (Biswas)* for her caring nature and, in particular, for her support during certain medical concerns. I will always cherish the sweet moments spent with little *Rwitoban (Rwik)* and *Arshaman (Sham)*.

I feel truly blessed and thankful to all my senior colleagues, specially, *Shubhrasish da*, *Pabi da*, *Rafiqul da*, *Debayan da*, *Shubhadip*, *Didhiti di*, *Shubhamita di*, *Priyanka di*, *Swarnali di*, *Anwesha di*, *Samrat da*, and *Anubhab da*. Special thanks to *Debayan da*, *Rafiqul da*, and *Shubhadip* for their genuine support and guidance, which have contributed to my growth both professionally and personally. I am sincerely grateful to have shared this path with you all.

I am equally thankful to all my junior colleagues, especially, *Riya*, *Gaurav*, *Shubhangkar*, *Dhritisundar*, *Dayal*, *Premananda*, *Anumita*, *Mohana*, *Tiyasha*, *Pragya*, *Sneha*, *Eveningstar*, and *Muskan*, for their enthusiastic support and cheerful companionship. A special thanks to my friends at SNBNCBS, in particular, *Ria*, *Nivedita*, *Manjari*, *Suranjana*, and *Shreya*, whose warmth and friendship added joy and comfort to every phase of my research journey. Together, their support created not just a productive environment, but a truly homely one, filled with laughter, learning, and lasting memories.

I heartily thank my best friend *Sayani*, whose friendship holds a significance beyond what words can convey. She is my unfailing source of solace and all-time entertainment partner, supporting me through both academic and non-academic aspects of life.

I am immensely grateful to a very special person, *Tanmoy Sarkar*, who provided me priceless assistance throughout my PhD journey, particularly during the challenging times of COVID − 19 pandemic. His loyalty and understanding were instrumental in helping me navigate a personal crisis and move forward in life. I will forever be grateful for his wholehearted friendship and encouragement when I needed it most.

I am deeply grateful to my parents (*Mr. Kalipada Mondal* and *Mrs. Ruma Mondal*) for their enduring love, patience, and belief in me throughout this journey. With all my heart, I express my deepest love for my little sister, *Sontai*, my partner-in-crime and constant source of joy. Her innocence and indispensable encouragement brought me strength during the toughest moments.

Finally, I wish to express my grateful acknowledgment to all those, both near and far, whose guidance and support, whether direct, or, subtle, have enriched my PhD journey at every step.

Amrita Mondal

Abstract

Understanding the molecular-level structure and dynamics of complex liquids and multi-component mixtures is essential for elucidating the fundamental interactions that govern their macroscopic behavior. At the microscopic scale, intermolecular forces, such as hydrogen bonding, van der Waals interactions, electrostatic forces, and ion - solvent co-ordination, collectively shape the spatial arrangement and temporal evolution of molecules within the liquid phase. These microscopic interactions directly influence key properties such as viscosity, ionic conductivity, diffusion coefficients, solvation dynamics, and phase stability. By probing liquid structure and dynamics, one could gain critical insight into how short-range and long-range correlations manifest in transport phenomena and thermodynamic responses. This understanding is pivotal for the rational design of functional materials and systems, particularly in applications involving electrolytes for energy storage, solvent systems in catalysis, biomolecular environments, and soft condensed matter. Ultimately, a microscopic perspective provides the foundation for predictive models and targeted optimization in a wide range of scientific and technological domains.

In the first part of this thesis, the molecular structure and dynamics of Glyme (G3)/LiTFSI electrolyte solutions have been systematically investigated using a combination of spectroscopic and transport measurement techniques. Raman spectroscopy has been employed to characterize the distribution of ion species, including solvent-shared ion pairs (SSIP), contact ion pairs (CIP), and aggregated ion pairs (AGGIP). The relationship between ionic conductivity and the microscopic structure and dynamics was examined through concentration- and temperature-dependent measurements of conductivity, viscosity, dielectric relaxation (DR), and ultrafast fluorescence dynamics. Conductivity exhibited a non-linear dependence on LiTFSI concentration, while both the glass transition temperature (T_g) and static dielectric constant (ε_s) showed linear trends. Furthermore, ultrafast fluorescence Stokes shift measurements have been performed using a Streak camera and time-correlated single photon counting (TCSPC) with two fluorescent probes, DMASBT and Coumarin 153 (C153), to explore complete solvation dynamics. Dynamic heterogeneity and its influence on ion transport phenomena in Li-ion battery electrolytes have been

demonstrated by analyzing decoupling between viscosity, dielectric relaxation (DR) dynamics, and time-resolved fluorescence (TRF) measurements. This decoupling underscores the presence of spatial and temporal variations in the local environment, revealing complex ion - solvent interactions that operate across multiple time and length scales.

Building on our findings from liquid electrolytes, our study was extended to gel polymer electrolytes (GPEs), which offer several advantages over conventional liquid systems, including reduced leakage, enhanced mechanical stability, improved solid electrolyte interphase (SEI) formation, and superior electrochemical performance. We have studied a model GPE system composed of propylene carbonate (PC), $LiClO_4$, and polypropylene glycol (PPG 425) to gain molecular-level insights into the interplay between ions, solvent molecules, and polymer chains, and how these interactions govern ion transport. Raman spectroscopy has been utilized to probe the modification of ion - solvent coordination environments in the presence of the PPG. The polymer segmental dynamics was probed via TRF measurements using environment-sensitive dyes, while DRS captured the intrinsic, probe-independent medium dynamics. Together, these complementary techniques reveal how the polymer matrix modulates both structural organization and dynamic pathways, thereby facilitating enhanced ion transport in the GPE relative to its liquid counterpart.

Phase transitions are a fundamental aspect of physical chemistry, offering deep insights into changes in material states and molecular organization. In the second part of this thesis, two distinct liquid - liquid phase transition (LLPT) systems have been explored through structural and dynamical analyses. The sol - gel transition in aqueous solutions of hydrophobically modified poly(acrylic acid)-based copolymers has been characterized using particle size distribution and other spectroscopic techniques, revealing the molecular underpinnings of supramolecular assembly. In a parallel study, bio-photonic approaches have been applied to investigate charge states and pH-responsive aggregation dynamics of Tryptophan in aqueous media, shedding light on molecular mechanisms relevant to protein misfolding and neurodegenerative diseases such as Alzheimer’s.

সারমর্ম

জটিল তরল ও বহু-উপাদানযুক্ত মিশ্রণের অণু-স্তরের গঠন ও গতিশীলতা বোঝা তাদের স্থূলমাত্রিক আচরণকে নিয়ন্ত্রণকারী মৌলিক পারস্পরিক ক্রিয়াগুলোর ব্যাখ্যার জন্য অপরিহার্য। সূক্ষ্মস্তরে, হাইড্রোজেন বন্ডিং, ভ্যান ডার ওয়ালস পারস্পরিক ক্রিয়া, তড়িৎ-আধানজনিত বল এবং আয়ন-দ্রাবক সমন্বয়ের মতো আন্তঃআণবিক বলসমূহ মিলিতভাবে তরল পর্যায়ে অণুগুলোর স্থানিক বিন্যাস এবং কালানুক্রমিক বিবর্তন নির্ধারণ করে। এই মাইক্রোস্কোপিক পারস্পরিক ক্রিয়াগুলো সান্দ্রতা, আয়নিক পরিবাহিতা, বিসরণের গুণাঙ্ক, দ্রবণগত গতিবিদ্যা এবং পর্যায়ের স্থিতিশীলতার মতো গুরুত্বপূর্ণ বৈশিষ্ট্যের ওপর সরাসরি প্রভাব ফেলে। তরলের সূক্ষ্মমাত্রিক গঠন ও গতিশীলতা পর্যবেক্ষণের মাধ্যমে, স্বল্প-পরিসরের ও দীর্ঘ-পরিসরের সহসম্পর্ক কীভাবে পরিবহন ঘটনা ও তাপগতীয় প্রতিক্রিয়ায় প্রকাশ পায়, তা সম্পর্কে বিশ্লেষণধর্মী উপলব্ধি অর্জন করা যায়। এই জ্ঞান কার্যকর উপকরণ ও ব্যবস্থার যুক্তিপূর্ণ নকশার জন্য অপরিহার্য, বিশেষ করে শক্তি সংরক্ষণে ব্যবহৃত ইলেকট্রোলাইট, অনুঘটন প্রক্রিয়ায় দ্রাবক ব্যবস্থা, জৈব-আণবিক পরিবেশ এবং নরম ঘনীভূত পদার্থের প্রয়োগক্ষেত্রে। এইভাবে, একটি মাইক্রোস্কোপিক দৃষ্টিভঙ্গি বৈজ্ঞানিক ও প্রযুক্তিগত বিভিন্ন ক্ষেত্রে পূর্বানুমানযোগ্য মডেল ও লক্ষ্যভিত্তিক সর্বোত্তমীকরণের ভিত্তি প্রদান করে।

এই গবেষণার প্রথম অংশে, Glyme (G3)/LiTFSI ইলেকট্রোলাইট দ্রবণের অণুগত গঠন ও গতিশীলতা পদ্ধতিগতভাবে অনুসন্ধান করা হয়েছে স্পেক্ট্রোস্কোপিক এবং পরিবহনমূলক পরিমাপ পদ্ধতির সমন্বয় ব্যবহার করে। Raman স্পেক্ট্রোস্কপিক প্রযুক্তি ব্যবহার করে আয়নসমূহের ভিন্ন ভিন্ন গঠনাবলী বিশ্লেষণ করা হয়েছে। এই ইলেকট্রোলাইট দ্রবণের আয়নিক পরিবাহিতা এবং সূক্ষ্মমাত্রিক গঠন ও গতিশীলতার মধ্যকার গভীর সম্পর্কটি বিশ্লেষণ করা হয়েছে উক্ত দ্রবনের ঘনত্ব, তাপমাত্রা-নির্ভর পরিবাহিতা, সান্দ্রতা, ডাই-ইলেকট্রিক রিলাক্সেশন (DR), এবং অতিদ্রুত ফ্লরোসেন্স গতিবিদ্যার পরিমাপের মাধ্যমে। পরিবাহিতা LiTFSI-এর ঘনত্বের সাথে একটি অরৈখিক নির্ভরতা প্রদর্শন করেছে, তবে গ্লাস স্থানান্তর তাপমাত্রা (T_g) এবং স্থির ডাইইলেকট্রিক ধ্রুবক (ε_s) উভয়ই রৈখিক প্রবণতা দেখিয়েছে। পরবর্তীতে, সম্পূর্ণ দ্রবণগত গতিবিদ্যা অন্বেষণের জন্য Streak ক্যামেরা এবং TCSPC প্রযুক্তি ব্যবহার করে দুটি ফ্লরোসেন্ট প্রোব, যথাক্রমে, DMASBT এবং C153 -এর মাধ্যমে অতিদ্রুত ফ্লরোসেন্স স্টোকস শিফট (Stokes-Shift) পরিমাপ সম্পাদিত হয়েছে। আয়ন পরিবহণ ঘটনায় গতি-অসমতা (Dynamic Heterogeneity) এবং তার প্রভাব প্রমাণিত হয়েছে সান্দ্রতা, ডাই-ইলেকট্রিক রিলাক্সেশন (DR) গতিবিদ্যা এবং ফ্লরোসেন্স গতিপ্রকিতির মধ্যে

পারস্পারিক বিচ্ছিন্নকরণ বিশ্লেষণের মাধ্যমে। এই বিচ্ছিন্নতা স্থানিক ও কালগত মাত্রায় স্থানীয় পরিবেশের অনুস্তরীয় বৈচিত্র্য নির্দেশ করে, যা বিভিন্ন সময় এবং দৈর্ঘ্যের স্তরে ক্রিয়াশীল জটিল আয়ন-দ্রাবক পারস্পরিক ক্রিয়ার অস্তিত্বকে উদঘাটিত করে।

তরল ইলেকট্রোলাইট সংক্রান্ত আমাদের পূর্ববর্তী গবেষণার ভিত্তিতে, এই গবেষণাকে সম্প্রসারিত করা হয়েছে জেল পলিমার ইলেকট্রোলাইটের (GPE) দিকে, যেগুলো প্রচলিত তরল ব্যবস্থার তুলনায় একাধিক সুবিধা প্রদান করে, যেমন, কম তরল নির্গমন, উন্নত যান্ত্রিক স্থিতিশীলতা, উন্নত সলিড ইলেকট্রোলাইট ইন্টারফেস (SEI) গঠন এবং উৎকৃষ্ট তড়িৎ-রাসায়নিক কর্মক্ষমতা। এখানে, আমরা একটি মডেল GPE সিস্টেম হিসেবে প্রোপিলিন কার্বোনেট (PC), লিথিয়াম পারক্লওরেট ($LiClO_4$), এবং পলিপ্রোপিলিন গ্লাইকোল (PPG 425) সমন্বিত একটি দ্রবণ বিশ্লেষণ করেছি, যার মধ্যে আণবিক পর্যায়ে আয়ন, দ্রাবক অণু এবং পলিমার শৃঙ্খলের পারস্পরিক ক্রিয়ার সূক্ষ্ম বিবরণ ব্যাখ্যা করা হয়েছে, এবং কিভাবে এই আন্তঃক্রিয়াগুলো আয়ন পরিবহণকে নিয়ন্ত্রণ তা পর্যালোচনা করা হয়েছে। এই গবেষণায় একইসঙ্গে পলিমার সেগমেন্টের গতিশীলতা বিশ্লেষণ করা হয়েছে পরিবেশ-সংবেদনশীল ফ্লুরোসেন্ট প্রোবের মাধ্যমে, এবং DRS ব্যবহার করে প্রোব-নিরপেক্ষ, স্বতঃস্ফূর্ত মাধ্যমগত গতিবিদ্যা অন্বেষণ করা হয়েছে। এই পরিপূরক বিশ্লেষণপ্রক্রিয়াগুলোর সমন্বয়ে উঠে এসেছে যে পলিমার ম্যাট্রিক্স গঠনগত সংগঠন ও গতিশীল পথকে এমনভাবে প্রভাবিত করে,যে তরল ইলেকট্রোলাইটের তুলনায় GPE -তে আয়ন পরিবহণ আরও দক্ষভাবে সম্পন্ন হয়।

এই থিসিসের দ্বিতীয় অংশে, দুটি ভিন্ন তরল-তরল পর্যায় পরিবর্তন (LLPT) প্রক্রিয়াকে গঠনগত ও গতিশীল বিশ্লেষণের মাধ্যমে অন্বেষণ করা হয়েছে। পর্যায় পরিবর্তন হলো ভৌত রসায়নের একটি মৌলিক দিক, যা পদার্থের অবস্থার পরিবর্তন ও আণবিক সংগঠনের অন্তর্নিহিত বৈশিষ্ট্যগুলোর বিষয়ে গভীর অন্তর্দৃষ্টি প্রদান করে। হাইড্রোফোবিকভাবে পরিবর্তিত পলি(অ্যাক্রিলিক অ্যাসিড)-ভিত্তিক পলিমারের জলীয় দ্রবণে সংঘটিত সল-জেল পরিবর্তন প্রক্রিয়াটি পলিমারের আকার বণ্টন এবং অন্যান্য স্পেকট্রোস্কোপিক পদ্ধতির মাধ্যমে বিশ্লেষণ করা হয়েছে, যার মাধ্যমে সুপ্রামলিকিউলার সমবিন্যাসের আণবিক ভিত্তি উন্মোচিত হয়েছে। একইসঙ্গে, আরেকটি সমান্তরাল গবেষণায়, বায়ো-ফোটোনিক পদ্ধতি ব্যবহার করে একটি অপরিহার্য অ্যামিনো অ্যাসিড ট্রিপটোফ্যানের চার্জ অবস্থা ও pH-নির্ভর অণুসংগঠন গতিবিদ্যার অনুসন্ধান চালানো হয়েছে, যা প্রোটিনের বিন্যাসজনিত ত্রুটি এবং আলঝেইমার রোগের মতো স্নায়বিক অবক্ষয়জনিত রোগের সঙ্গে সম্পর্কিত আণবিক প্রক্রিয়া সম্পর্কে আলোকপাত করে।

List of Publications

1. "Correlating Ionic Conductivity to Structure and Dynamics of Li-Ion Battery Electrolyte Systems: Raman Spectroscopy, Dielectric Relaxation Measurements, and Streak Camera Solvation Data Analysis"
Amrita Mondal, Kajal Kumbhakar, Ranjit Biswas*
J. Phys. Chem. B ***128*** (48), 11924 - 11937 (2024). DOI: 10.1021/acs.jpcb.4c05521

2. "Dynamical Signature of the Onset of Sol-Gel Phase Transition in Aqueous Solutions of Hydrophobically Modified Poly(acrylic acid)-Based Copolymers"
Amrita Mondal, Asmita Dey, Kajal Kumbhakar, Priyadarsi De, Ranjit Biswas*
J. Chem. Phys. ***162*** (16), 164903 (2025). DOI: 10.1063/5.0260194

3. "Dynamic Heterogeneity and Its Role in Ion Conductivity in Li-Ion Electrolytes: A Multi-Timescales Fluorescence Investigation Combining Streak Camera and TCSPC Techniques"
Amrita Mondal, Ranjit Biswas*
J. Phys. Chem. B (to be submitted)

4. "Investigation of Polymer Dynamics Influencing Ion Transport in Gel Polymer Electrolytes for Li-ion Cells"
Amrita Mondal, Ranjit Biswas*
J. Chem. Phys. (to be submitted)

5. "Understanding pH-Tuned Aggregation Dynamics of Tryptophan: Implications for Amyloid Fibrillation"
Amrita Mondal, Tonima Nandy, Ranjit Biswas*
J. Chem. Sc. (to be submitted)

6. **"Interactions and Dynamics in Aqueous Solutions of pH-Responsive Polymers: A Combined Fluorescence and Dielectric Relaxation Study"
Kajal Kumbhakar, Asmita Dey, ***Amrita Mondal***, Priyadarsi De*, Ranjit Biswas*
J. Phys. Chem. B ***125*** (22), 6023 - 6035 (2021). DOI: 10.1021/acs.jpcb.1c03435

7. **"Surface Interactions of Gold Nanoparticles in Water-in-Salt Electrolyte Medium"
Amrita Mondal, Jayeta Banerjee and Ranjit Biswas*
(Manuscript in preparation)

8. **"Dielectric Insights into Water Structure and Hydration Dynamics in PVA-Based Hydrogels"
Amrita Mondal, Ranjit Biswas*
(Manuscript in preparation)

**not included in this Thesis

Commonly Used Abbreviation

LIB	Lithium-ion battery
DRS	Dielectric relaxation spectroscopy
DH	Dynamic heterogeneity
TCSPC	Time-correlated single photon counting
TRF	Time-resolved fluorescence
MCP	Micro-channel plate
IRF	Instrument response function
FWHM	Full width half maxima
TRES	Time-resolved emission spectra
TDFSS	Time dependent fluorescence Stokes shift
SIL	Solvated ionic liquid
GPE	Gel polymer electrolyte
PAA	Polyacrylic acid
SED	Stokes-Einstein-Debye
DHO	Debye-Huckel-Onsager
DFE	Debye-Falkenhagen effect
G3	Triglyme
DSC	Differential scanning calorimetry
DLS	Dynamic light scattering
SSIP	Solvent shared ion pair
CIP	Contact ion pair
AGGIP	Aggregated ion pair
Trp	Tryptophan
Th − T	Thioflavin-T
FESEM	Field emission scanning electron microscope
PBS	Phosphate buffered Saline

Contents

Chapter 1

Introduction

Electrolytes, chemical compounds producing ions upon dissociation in solutions that conduct electricity, are essential materials for driving technological innovations involving batteries and fuel cells, as well as supporting vital biological processes, by facilitating ion transport critically regulating system performance and ensuring safety. The development of lithium-ion (Li^+) batteries, integral to portable electronics and electric vehicles, began in the 1970s with *Stanley Whittingham*'s discovery of lithium intercalation in titanium disulfide (TiS_2).[1] Next, *John Goodenough*'s development of high-voltage lithium cobalt oxide cathodes in the 1980s,[2] combined with *Akira Yoshino*'s introduction of a carbon-based anode in 1985,[3] led to the first commercial lithium-ion battery, released by Sony in 1991. In recognition to their seminal contributions, these three scientists were awarded the Nobel Prize in Chemistry in 2019.[4] In parallel, polymer chemistry has revolutionized electrolyte design through polymer electrolytes, pioneered by *Peter Wright*'s discovery[5] of ion-conducting poly(ethylene oxide) (PEO) in 1975 and advanced by *Michel Armand*[6]. The groundbreaking research studies by *Takuzo Aida* and *Samuel I. Stupp* have significantly propelled the development of supramolecular polymer gels, for functional and biomedical applications.[7–9] Additionally, the study of amyloid fibrillation, first identified in the 19^{th} century through *Rudolf Virchow*'s work on amyloid deposits and later linked to protein misfolding in diseases like Alzheimer's, has inspired polymer chemistry.[10] Insights from amyloid fibril self-assembly have guided the design of bioinspired supramolecular polymers with tailored nanostructures, linking electrolyte science and biomedicine.[11] This intertwined history underscores the dynamic evolution of electrolyte and polymer chemistry in advancing energy and health technologies. This chapter provides a brief introduction to various electrolyte materials for batteries, and biologically relevant solutions, summarizing their essential physical and chemical properties to support the dynamic analyses in later chapters.

1.1 Battery Electrolytes

1.1.1 Liquid Electrolytes (LE) for Li-Ion Battery (LIB)

Rechargeable lithium-ion batteries (LIBs) have long been regarded as the "holy grail" of energy storage technologies, emerging as the cornerstone for portable electronics, electric vehicles, and large-scale energy storage systems. A typical LIB is comprised of cathode (positive electrode), anode (negative electrode), electrolyte, separator, and the external casing or, battery shell. The operation of LIB relies on the reversible shuttling of Li^+ ions between the cathode and anode, along with de-intercalating from the cathode during charging and re-intercalating during discharge to release stored energy. A conventional LIB configuration has been shown in **Fig. 1.1 [a]** that uses graphite as the anode and lithium cobalt oxide ($LiCoO_2$) as the cathode, providing a clear illustration of the ion transport and electrochemical processes involved in.[12,13] The charging principle is as follows: Cathode reaction: $LiCoO_2 \rightarrow Li_{1-x}CoO_2 + xLi + xe^-$, anode reaction: $6C + xLi^+ + xe^- \rightarrow Li_xC_6$ and overall battery reactions: $LiCoO_2 + 6C \rightarrow Li_{1-x}CoO_2 + Li_xC_6$.

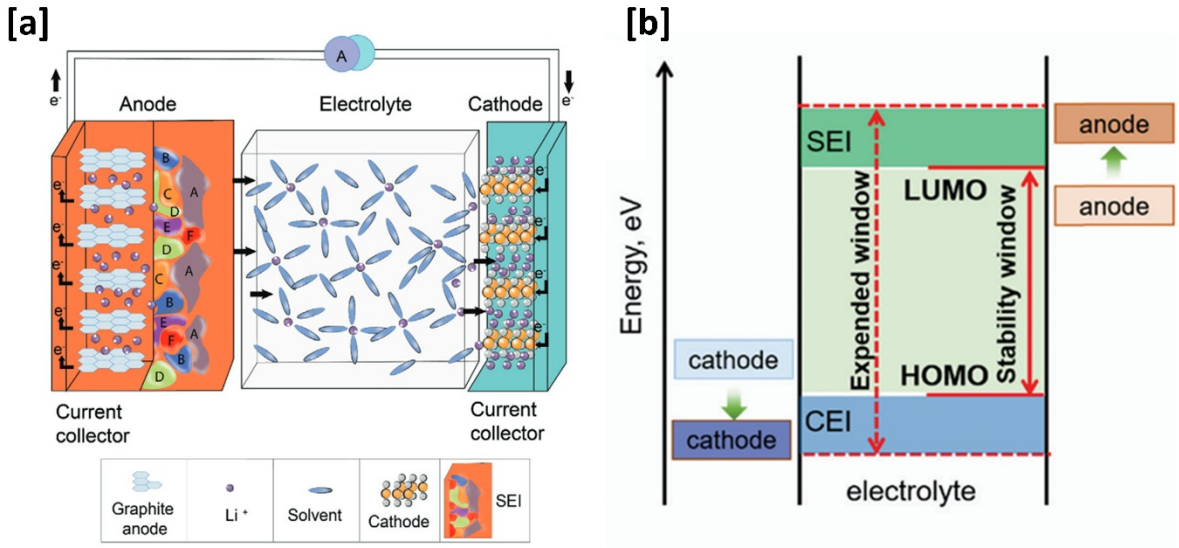

FIG. 1.1. [a] Schematic of a conventional LIB showing SEI layer formed on graphite anode.[14]

[b] Electrochemical stability window of the electrolyte: Alignment of HOMO and LUMO with anode and cathode energy levels, featuring protective SEI and CEI Layers.[15]

The electrolytes in LIBs not only facilitates lithium-ion transport but also governs the formation of solid electrolyte interphase (SEI) and cathode electrolyte interphase (CEI) layers, (as described in **Fig. 1.1 [b]**) which are critical to battery performance, stability, and longevity.[15,16] A major challenge lies in the chemical instability of electrolyte components, particularly solvents, under high-voltage or high-capacity conditions. At elevated cathode potentials, oxidative decomposition is primarily driven by solvent reactivity, while at the anode, especially with lithium metal or graphite, reductive decomposition forms the SEI.[17] These interphases must be ionically conductive yet electronically insulating to suppress parasitic reactions and ensure stable cycling. To widen the electrochemical stability window, two key strategies are employed: (i) Thermodynamic design, using solvents with higher oxidative /reductive stability than conventional EC-based systems,[18] and (ii) Kinetic stabilization, by engineering robust SEI/CEI layers that mitigate interfacial degradation.[19,20] Advancing electrolyte chemistry is thus essential for enabling high-voltage and lithium-metal battery technologies.

Glyme or, poly(ethylene glycol) dimethyl ethers [$CH_3O(CH_2CH_2O)_nCH_3$, n = 1 - 4], represent a class of saturated, polar aprotic ethers drawing increasing attention as promising electrolyte solvents for LIBs.[21] Their unique ability to coordinate with metal ions through oxygen lone pairs enables the formation of stable glyme - cation complexes, giving rise to a distinct category of electrolytes known as “solvate ionic liquids” (SILs).[22] These systems, comprising equimolar mixtures of glymes (e.g., triglyme or tetraglyme) and alkali metal salts, consist entirely of complex ions and their counterions in a molten or quasi-liquid state, offering enhanced thermal and electrochemical stability.[22,23]

Compared to conventional carbonate-based electrolytes (CBEs), glyme-based electrolytes (GBEs) exhibit several superior properties such as, high oxidative stability exceeding 4 V, wide thermal operating ranges (100 - 200 ºC), low volatility and flammability, and elevated ionic conductivities ($\sim 10^{-3}$ S cm^{-1}).[24,25] Glyme molecules intercalate into layered electrodes as lithium - glyme complexes, reducing ion transport barriers and boosting Li^+ mobility and charge-transfer kinetics through their unique solvation and interfacial properties.[26] Far from a peripheral concern, glyme-

based electrolytes represent a foundational element of LIB research, directly influencing battery safety, energy density, and lifespan. As the demand for high-performance energy storage continues to grow, research on electrolytes will remain a central pillar in the development of next-generation battery sciences.

1.1.2 Gel Polymer Electrolytes (GPE)

Gel polymer electrolytes (GPEs) are quasi-solid-state systems (as illustrated in **Fig. 1.2 [1]**) formed by a polymer matrix swollen with liquid electrolyte, uniting the mechanical robustness of solids with the superior ionic conductivity of liquids.[27] This structure prevents leakage and ensures stable, efficient ion transport, offering a safer alternative to traditional liquid electrolytes.[27,28] Traditional liquid electrolytes, while offering excellent ionic transport ($10^{-3} - 10^{-2}$ S cm^{-1}), suffer from drawbacks such as leakage, toxicity, flammability, low viscosity and poor interfacial stability, raising safety and durability concerns. Conversely, solid-state electrolytes, though safer and more stable, often exhibit limited ionic conductivity ($10^{-8} - 10^{-6}$ S cm^{-1}) and poor interfacial contact with electrodes.[28]

GPEs are among the most promising materials for next-generation energy storage, offering a balance of safety, flexibility, processability, and sufficient ionic conductivity. Ion transport in GPEs relies on the dissociation of salts into mobile ions, with solvents enhancing mobility and polymers providing mechanical integrity and viscosity.[29] Efficient conduction requires salts with low dissociation energy and solvents with high dielectric constants, low viscosity, and suitable thermal properties. The polymer matrix not only serves as a structural scaffold but also facilitates ion transport via segmental motion and polymer-salt interactions (see **Fig. 1.2 [2]**). Polymers such as PEO, PVA, PMMA, PAN, PVDF, and PVDF − HFP are widely studied for their electrochemical stability and mechanical performance, enabling GPEs to range from viscous gels to rigid films, ideal for safe, flexible, and high-performance energy devices.[29–31] GPEs are categorized into four main types: (1) lithium-ion GPEs, (2) proton-conducting GPEs, (3) alkaline GPEs, and (4) other ion gels. The ion conduction mechanism in GPEs varies depending on the system: lithium-ion conduction is primarily governed by ion hopping and solvent-assisted diffusion, whereas proton

conduction is highly temperature-dependent and predominantly follows a diffusion-based pathway, with a secondary contribution from the Grothaus's mechanism[32–34] (as described in **Fig. 1.2 [3]**). Advancements in GPE research lays the groundwork for developing next-generation batteries that are safe, high-performance, and flexible, offering environmentally friendly and adaptable energy storage solutions for applications ranging from portable electronics to grid storage and aerospace.

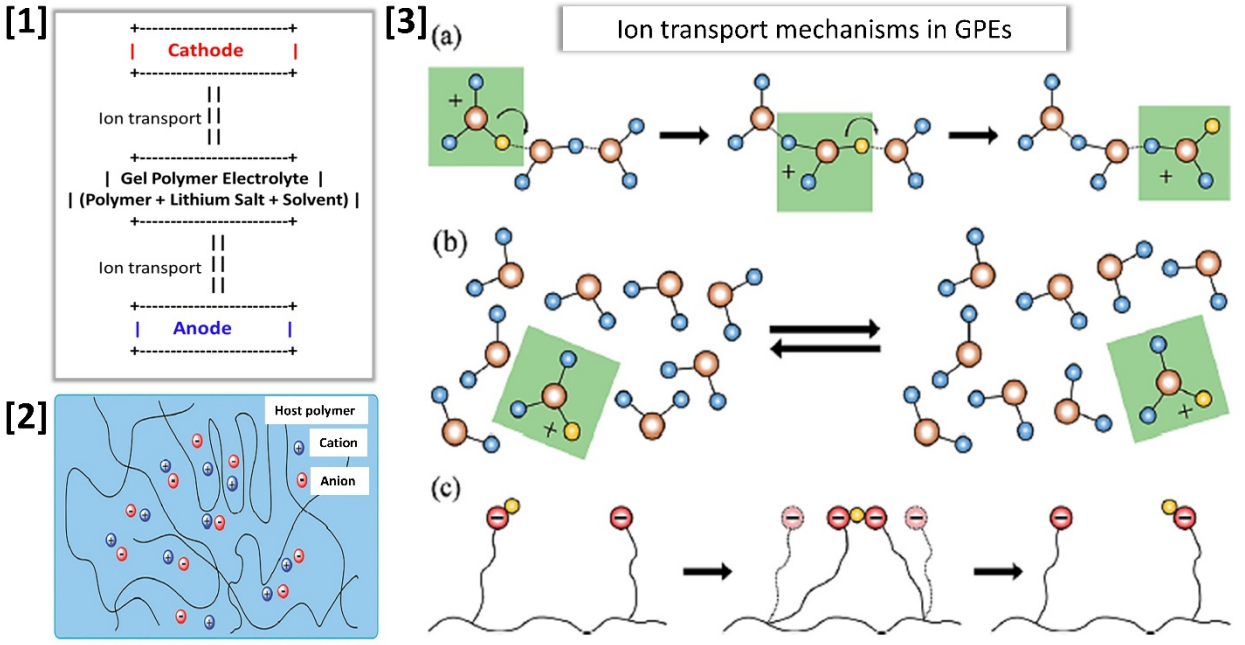

FIG. 1.2. [1] Schematic representation of ion transport across a GPE (polymer + lithium salt + solvent) between cathode and anode in a LIB system.

[2] Schematic of the structural arrangements in GPE.[35]

[3] Schematic illustration of proton transport mechanisms in GPE: (a) ion hopping (Grotthuss mechanism) in systems with strong H-bonding; (b) diffusion (vehicle mechanism) in systems with weak H-bonding; and (c) direct transport facilitated by polymer chain segmental motion.[36]

1.1.3 Supramolecular Polymeric Hydrogel

Supramolecular polymeric hydrogels are a class of soft materials formed by three-dimensional networks of polymer chains interconnected through non-covalent, reversible interactions (as shown in **Fig. 1.3**). These materials are capable of entrapping large amounts of water, typically driven by surface tension and capillary forces, which lends them unique physicochemical and functional properties. Unlike traditional covalently crosslinked hydrogels, supramolecular hydrogels leverage the principles of molecular recognition and self-assembly, providing dynamic responsiveness to environmental stimuli, such as pH, temperature, or, ionic strength.[37–40]

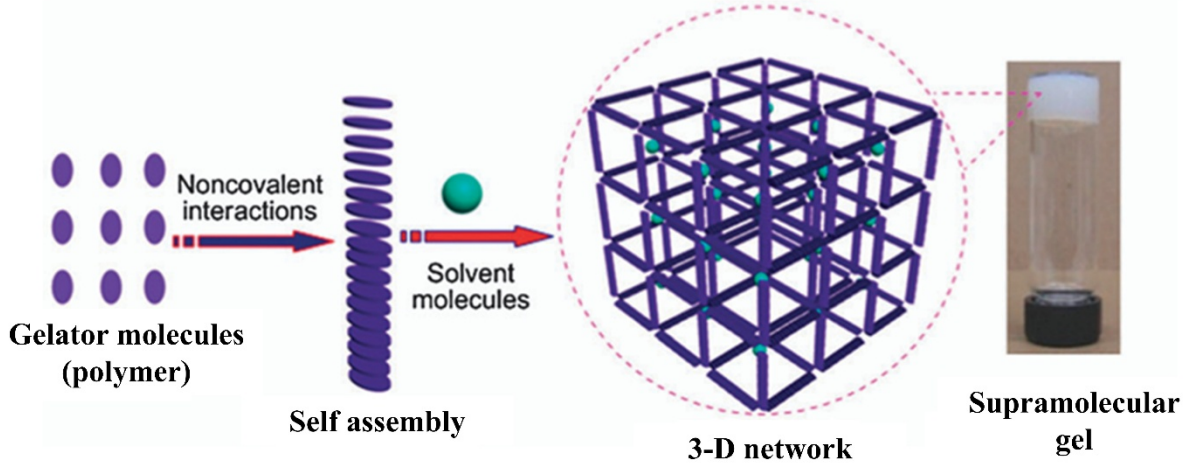

FIG. 1.3. Schematic presentation of formation of supramolecular gel by self-assembly of polymers.[37]

Polymeric hydrogels could broadly be classified based on the nature of their polymer chains (neutral and ionic) and the type of crosslinking (chemical and physical, as described in **Fig. 1.4 [1]**).[41] Chemically crosslinked hydrogels involve permanent covalent bonds between polymer chains, formed through various reactions such as Michael addition, Schiff base formation, photo-polymerization, enzyme-catalyzed processes, and click chemistry (e.g., azide-alkyne cycloaddition).[42–44] These hydrogels are robust, mechanically stable, and ideal for applications demanding high strength and durability.[45] However, they are typically brittle, opaque, and non-self-healing, limiting their use in dynamic environments.

Physically crosslinked hydrogels, on the other hand, rely on transient, reversible interactions such as hydrogen bonding, ionic interactions, π − π stacking, host - guest chemistry, and hydrophobic effects (see **Fig. 1.4 [2]**).[46–48] These gels form via molecular self-assembly in aqueous media, eliminating the need for additional crosslinking reagents and often proceeding without significant volume change. Although physically crosslinked gels are mechanically weaker and more prone to shear-induced breakdown, their reversible and adaptive nature enables desirable properties such as shear-thinning and self-healing, making them increasingly attractive for biomedical applications.[49]

Supramolecular polymeric hydrogels represent a subclass of physically crosslinked networks, wherein dynamic, non-covalent supramolecular interactions function as reversible crosslinking points. These interactions are highly tunable in terms of specificity and strength, enabling precise control over network architecture and behavior. By integrating the functional versatility of supramolecular chemistry with the structural adaptability of polymeric matrices, these hydrogels offer a unique platform for the development of stimuli-responsive, injectable, and biocompatible materials. Such systems are particularly well-suited for advanced biomedical applications, including targeted drug delivery, regenerative tissue engineering, and wound healing.[41,45]

Poly(acrylic acid) (PAA)-based copolymers exemplify supramolecular hydrogel systems capable of dynamic network formation through hydrogen bonding, ionic interactions, and metal coordination.[50,51] Importantly, their gelation behavior is highly pH-responsive: low pH favors hydrogen bonding via protonated carboxyl groups (−COOH), while higher pH promotes ionization, leading to either disruption or, ionic crosslinking depending on the ionic environment.[52] Moreover, PAA -based supramolecular hydrogels hold significant biomedical promise due to their pH-responsiveness, biocompatibility, and adaptive behavior.[53,54] Their ability to self-heal and flow under stress enables applications in injectable therapeutics and regenerative medicine.[51] Moreover, insights into their gelation dynamics (typical schematic illustrating the phase transition in a supramolecular hydrogel is presented in **Fig. 1.4 [3]** and **Fig. 1.4 [4]**)[55,56] and molecular interactions pave the way for designing next-generation smart biomaterials for precision clinical use.

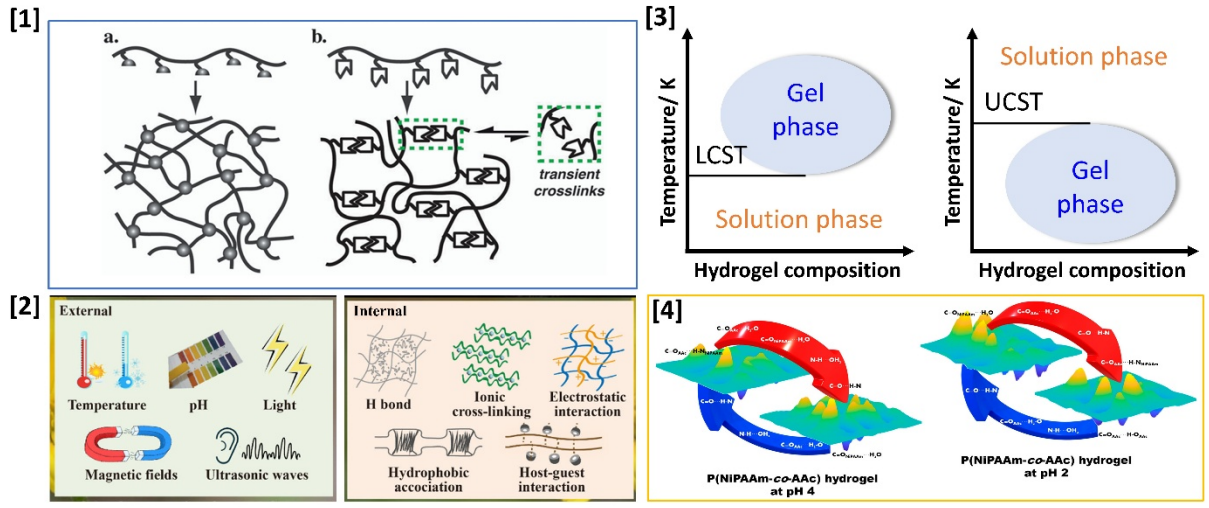

FIG. 1.4. [1] Schematic illustration of (a) covalent crosslinking of functional polymer precursors to form permanently crosslinked (static) hydrogels, and (b) supramolecular crosslinking of functional polymer precursors to create transiently crosslinked hydrogels.[41]

[2] Different internal and external factors influencing the formation of physical hydrogels.[57]

[3] Schematic presentation of temperature-induced phase transitions in hydrogels: (a) Lower Critical Solution Temperature (LCST), where hydrogels undergo phase transition and solidify upon heating, and (b) Upper Critical Solution Temperature (UCST), where hydrogels solidify upon cooling.

[4] Schematic of energy landscape governing phase transition mechanism in pH-responsive $P(NiPAAm-co-AAc)$ hydrogel.[56]

1.1.4 Tryptophan (Trp)

Tryptophan (Trp or, W) is an essential aromatic amino acid with the molecular formula $C_{11}H_{12}N_2O_2$. From a chemical perspective, the structure of Trp features a bulky indole ring, and a fusion of a benzene and pyrrole ring, connected to the amino acid backbone *via* a methylene $(-CH_2)$ group. This aromatic side chain contributes to hydrophobicity and allows Trp to participate in $\pi-\pi$ stacking and hydrogen bonding, making it a key stabilizer of protein tertiary

structures. In proteins, Trp is typically found in the L-conformation and is often located in regions critical for protein structure and function.[58]

Biologically, Trp plays dual role in human body. It is structurally essential for proper protein folding and functioning, and also it serves as a metabolic precursor to important neuroactive compounds. Its incorporation into proteins helps to maintain conformational stability, while misfolding or, abnormal aggregation of Trp -containing proteins can result in amyloid fibril formation, characteristic of neurodegenerative disorders (see **Fig. 1.5 [1]**) such as Alzheimer's, Parkinson's, and Huntington's diseases.[59] Metabolically, Trp gives rise to serotonin and melatonin, which are neurotransmitters, vital for regulating mood, sleep, and circadian rhythms. Additionally, most dietary Trp is catabolized through the kynurenine pathway (KP), which produces neuroactive metabolites.[60,61] An imbalance in KP pathway (as described in **Fig. 1.5 [2]**), often driven by inflammation, can lead to the accumulation of neurotoxic compounds such as quinolinic acid, contributing to oxidative stress, excitotoxicity, and neuronal damage.[60–63]

Beyond its metabolic and structural roles, Trp is a molecule of high interest due to its intrinsic fluorescence properties used for studying structure, dynamics, and interactions in protein.[64,65] It has a strong absorption maximum at ~ 280 nm and emits fluorescence typically near 350 nm, with a high quantum yield compared to other amino acids.[66] The fluorescence properties of Trp are highly sensitive to its local environment, including solvent polarity and the presence of nearby charged residues. Notably, the radiative decay rate of Trp fluorescence depends on the refractive index of the surrounding medium, whether the Trp residue is located on the protein surface or, enclosed within its hydrophobic core.[67] Thus, a change in protein shape, such as during ligand binding or, fibrillation, may alter the local refractive index and consequently influence both the lifetime and quantum yield of Trp fluorescence.[68] These environment-sensitive features enable Trp emission an effective probe to investigate protein aggregation, dynamics, and molecular interactions.[69,70] The unique combination of structural, metabolic, and optical properties of Trp makes it a biologically significant and versatile molecule. Its involvement in critical physiological

processes and disease pathways, along with its dual role as a structural stabilizer and a sensitive fluorescent reporter, continues to drive progress in molecular biology and biomedical research.

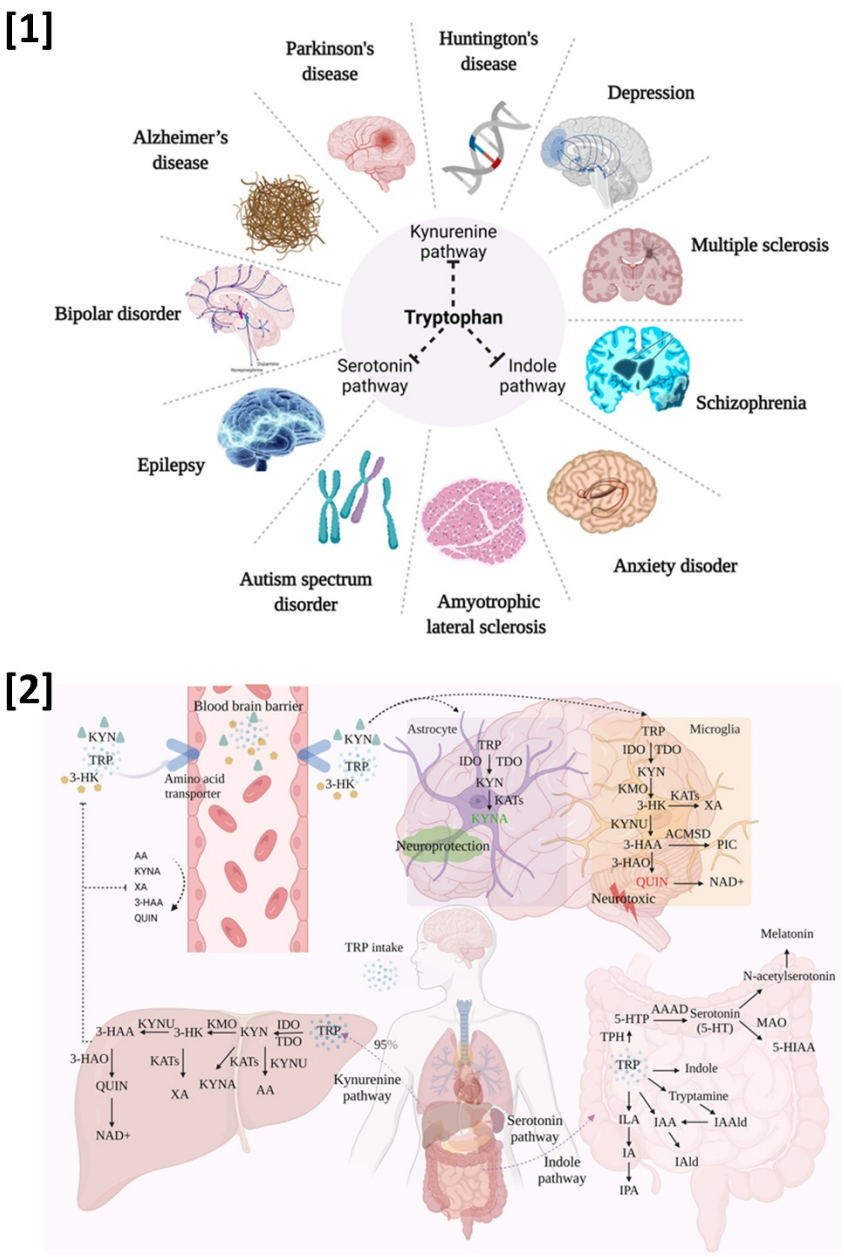

FIG. 1.5. **[1]** Schematic overview of Trp metabolism and its relevance to neurological and psychiatric disorders. **[2]** Schematic representation of the three metabolic pathways of Trp: The kynurenine pathway (KP), serotonin pathway (SP), and indole pathway (IP). Approximately 95% of Trp is metabolized via the KP in the liver, while a smaller portion is processed through the SP and IP in the gastrointestinal tract.[59]

1.2 Structure and Dynamics in Liquid

1.2.1 Spatial Heterogeneity

Steady-state fluorescence emission spectroscopy is a powerful tool for probing the interaction between fluorophores and their surrounding medium. In general, according to the Kasha rule,[71] fluorescence emission from a photo-excited fluorophore originates from the lowest vibrational level of the singlet state (S_1) after complete relaxation, regardless of the excitation wavelength (λ_{ex}). However, in more complex systems, it has been observed that the fluorescence emission of dissolved fluorophores shifts toward the red edge when the excitation wavelength (λ_{ex}) is changed to longer values.[72,73] This wavelength-dependent shift in fluorescence spectra occurs when fluorophores are surrounded by varying microscopic solvation environments (or, micro-domains), which exhibit spatial heterogeneity.[74] The spatial variation in these environments can be attributed to differences in local solvent properties, such as polarity and viscosity, as well as the molecular dynamics of the medium. The timescale for inter-conversion between solvation shells can exceed or, match the lifetime (τ_{life}) of fluorophore molecule, leading to spatially heterogeneous solvation environments. This spatial variation causes fluorescence emission spectra to vary, reflecting both temporal solvent dynamics and the local distribution of solvation micro-domains, thus adding complexity and offering deeper insight into the local structural and dynamic properties of the medium surrounding the fluorophore.[75–78]

1.2.2 Rotational Diffusion

Rotational diffusion of a fluorescent probe is a sensitive and informative approach to investigate the microscopic dynamics of the surrounding liquid medium. Upon photo-excitation, the fluorescence anisotropy of the fluorophore decays over time from an initial maximum (typically ~0.4) to zero, reflecting the randomization of the dipole orientation of fluorophore due to rotational motion.[79,80] This decay is characterized by the rotational correlation time ($\langle\tau_{rot}\rangle$), which provides direct insight into the frictional interactions between the fluorophore and its local environment. According to the Stokes-Einstein-Debye (SED) model,[81,82] in a homogenous medium, the rotational correlation time is linearly proportional to the temperature-reduced viscosity of the medium (η/T). This relationship serves as a benchmark for assessing solvent-probe coupling.

However, in complex or, heterogeneous environments, such as glasses, supercooled liquids, and polymeric systems, deviations from this linear dependence are often observed.[83] Specifically, a fractional power-law dependence of the form: $\langle \tau_{rot} \rangle = A(\eta/T)^p$ with $0<p<1$, indicates non-Stokesian behavior, suggesting the presence of dynamic heterogeneity within the medium.[84–86]

Such fractional dependence implies that the probe experiences spatially and temporally varying friction, revealing regions within the medium with differing local viscosities or relaxation times. Therefore, rotational diffusion not only serves as a measure of viscosity but also acts as a sensitive reporter of the probe-dependent microenvironment dynamics, allowing for the detection of sub-diffusive or, constrained motions typical of complex fluids.

1.2.3 Stokes Shift Dynamics

Stokes shift dynamics, the time-dependent shift in fluorescence emission spectra due to solvent reorganization around an excited fluorophore, is a critical tool for studying molecular interactions in electrolytes, polymer-aggregated solutions and related chemical systems. In electrolyte solutions, Stokes shift dynamics probes solvent relaxation and ion - solvent interactions, revealing how ions influence the local solvation environment and impact processes such as charge transfer and ionic conductivity in batteries.[87–89] By tracking the timescale of solvent reorganization (femtoseconds to nanoseconds), Stokes shift dynamics provides insights into solvation shell structure, and the coupling between ion transport and solvent relaxation dynamics, which are essential for optimizing electrolyte performance in energy storage and electrochemical systems.[90,91]

In polymer-aggregated solutions, such as those containing micelles or, polyelectrolyte complexes, Stokes shift dynamics elucidates the microenvironment within aggregates and the interplay between polymer, solvent, and solutes.[92] Stokes shift measurements could reveal restricted solvent mobility in polymer aggregates, influenced by hydrophobic and electrostatic interactions. This is important for understanding drug delivery systems, where the dynamics of encapsulated molecules

depend on the aggregate's solvation properties. By quantifying both the heterogeneity and the ultrafast and slow components of solvent relaxation within these aggregates, Stokes shift dynamics offers valuable insights for designing polymer-based materials with tailored functionalities. It connects molecular-level interactions to bulk properties such as viscosity, phase behavior, and dynamic response in the liquid phase.

1.2.4 Orientation Relaxation Dynamics

Orientation relaxation dynamics describes the time-dependent reorientation of molecular dipoles under an applied electric field, a process effectively probed by dielectric relaxation spectroscopy (DRS).[93] This phenomenon is fundamental for elucidating molecular and ionic interactions in such complex systems. DRS measures the dielectric response across an extensive frequency range, capturing dynamic processes from femtoseconds (intermolecular vibrations)[94] to hours (structural relaxation in viscous systems like glasses).[95] This broad temporal coverage establishes DRS as a powerful tool for investigating electrolyte and polymer solutions, where ion - ion, ion - solvent, and polymer - solvent interactions dictate physicochemical properties.

In electrolyte solutions, DRS provides a comprehensive view of molecular motions, spanning femtosecond vibrational modes to nanosecond solvation dynamics, thereby linking atomic-scale interactions to bulk dielectric behavior.[96] In case of polymer solutions, DRS probes solvent molecule reorientation near polymer chains, revealing the influence of polymer polarity, hydrophobicity, or, charge density on solvent dynamics. Additionally, the dielectric response reflects polymer segment relaxation, enabling DRS to distinguish between rapid local segmental motions and slower global chain dynamics, thus offering insights into polymer flexibility and conformation.[97,98] With its unmatched timescale range and sensitivity, DRS is an indispensable tool for unraveling the intricate dynamics of these systems, seamlessly connecting microscopic interactions to macroscopic properties.[99]

1.2.5 Vibrational Modes as Molecular Fingerprints

Raman spectroscopy is a powerful, non-destructive analytical technique that enables the chemical and structural characterization of solids, liquids, and gases at high spatial resolution. Among its key advantages is the ability to analyze samples as small as ~ 1 μm, making it particularly suitable for studying localized features in heterogeneous systems such as electrolytes, microdroplets, or biological assemblies.[100–102] Unlike other techniques such as infrared spectroscopy (IR) or, micro-thermometry, Raman spectroscopy provides rich vibrational information without the need for labels or, extensive sample preparation.

Vibrational modes of solvent molecules (e.g., water, glymes) are sensitive to the presence of dissolved salts (e.g., $LiClO_4$, LiTFSI), exhibiting characteristic shifts in frequency, band broadening, and intensity changes. These spectral modifications provide insight into ion coordination, solvation shell structure, and ion pairing, which are critical for understanding ion transport and conductivity in electrolyte systems.[103]

In systems undergoing liquid - liquid phase transition (LLPT), such as amyloid fibrillation or, polymer coil - globule transitions, micro-Raman spectroscopy could capture molecular-level changes in hydrogen bonding networks and conformational rearrangements.[104] Key vibrational markers, including amide I (~ 1650 cm^{-1}: ∝- helix, ~ 1630 cm^{-1}: β-sheet, ~ 1680 cm^{-1}: unordered structure), amide III (~ 1200 – 1350 cm^{-1}), and aromatic side-chain bands, reflect alterations in protein secondary structure and molecular packing.[105,106] In macromolecular solutions, monitoring the O–H stretching band provides critical insight into changes in water structure.[107] For example, a red-shift in O–H band typically indicates strengthened hydrogen bonding, while peak splitting and the emergence of new bands may signal the formation of ion pairs or, supramolecular assemblies. Thus, this technique not only identifies molecular species but also deciphers the strength, geometry, and dynamics of interactions that govern solution structure and dynamics. By tracking such vibrational fingerprints in situ and in real time, Raman spectroscopy provides essential insights into the structure - dynamics - function relationships governing complex chemical and biological systems.

1.3 Motivation of the Thesis

Solution chemistry, despite being one of the oldest branches of physical chemistry, continues to pose fundamental challenges and remains a dynamic area of research. The central goal of solution chemistry is to achieve a molecular-level understanding of solvent effects on chemical equilibria and reaction mechanisms, an insight essential to advancing catalysis, materials science, and biochemistry.[108] Although rooted in classical physical chemistry, the field continues to reveal unresolved questions when revisited with modern experimental and theoretical approaches, transforming it into a vibrant frontier of contemporary research.

Most chemical processes, including reactions, separations, and extractions in both laboratory and industrial settings, take place in liquid phase. However, liquids exhibit a unique complexity from chemistry point of view. They possess strong intermolecular interactions like solids, yet lack the fixed lattice structure of crystalline phases, making their theoretical description and experimental characterization particularly challenging. Understanding solute-solvent interactions, molecular structure, and dynamic behavior in liquid systems is essential for decoding the physicochemical basis of reaction media. This thesis is driven by the need to unravel these structural and dynamical complexities and contribute to the broader understanding of molecular processes in solution, ultimately aiding the rational design of functional materials and efficient chemical systems.

In the first part of this thesis, we focus on unraveling the microscopic structure and dynamical behavior of electrolyte solutions, with particular relevance to the development of next-generation Li-ion batteries. This investigation is grounded in electrochemical significance, where ion transport, solvation dynamics, and interfacial processes critically influence conductivity, electrochemical stability, and reaction kinetics. As a model system, we study a binary mixture comprising of lithium bis(trifluoromethanesulfonyl)imide (LiTFSI) and triethylene glycol dimethyl ether (Triglyme or, G3), a promising class of electrolytes known for their relevance in high-performance battery electrolytes.[109]

Despite decades of research, the complex coupling of solvent reorganization, ion-ion correlations, and non-covalent interactions in electrolyte media remains incompletely understood. Most electrolyte systems, including neat solvents, binary solvent mixtures, and salt-solvent combinations, exhibit a high degree of micro-heterogeneity.[110] Even neat solvents are known to form dimers, trimers, and transient clusters, contributing to spatially inhomogeneous liquid structures. This structural heterogeneity arises from a range of molecular interactions including electrostatic forces, van der Waals interactions, hydrogen bonding, halogen bonding, and in some systems, $\pi - \pi$ stacking.[111] Notably, such structural organization is not static and its dynamic evolution with time gives rise to dynamic heterogeneity, a phenomenon well-documented in supercooled and glassy liquids.[75,84]

However, these heterogeneities are not exclusive to glassy phases. Hydrogen-bonded liquids, ionic liquids, deep eutectic solvents, and concentrated electrolyte solutions all exhibit spatial and temporal fluctuations in molecular coordination and mobility.[112,113] These lead to coexisting domains with varying dynamic properties, further complicating the mechanistic understanding of such systems. While molecular dynamics (MD) simulations have offered important theoretical insights by quantifying properties like radial distribution function (RDF), mean square displacement (MSD), and hydrogen-bond fluctuation dynamics, they often fall short in fully capturing the experimental reality.[114–116] Conversely, experimental approaches can access macroscopic transport properties (e.g., viscosity, conductivity) and microscopic relaxation timescales, but linking the two is far from trivial.

Understanding the macro-micro relationship in electrolyte solutions, specifically, how slow ion translational motion (diffusion) couples with fast solvent reorientation (dipolar relaxation), is both scientifically fascinating and technologically crucial. Bridging this knowledge gap is essential for the rational design of advanced energy storage materials, and positions electrolyte research as a vibrant, evolving frontier in physical chemistry. Advances in experimental and computational techniques could unravel these complex interactions, paving the way for optimized electrolytes in next-generation batteries and supercapacitors.

In the next part of this thesis, we would like to investigate the structural and dynamical signatures associated with the onset of sol-gel phase transition in hydrophobically modified poly(acrylic acid) copolymer solutions. Capturing the subtle evolution of intermolecular interactions and polymer aggregation dynamics during this transition poses significant challenges, particularly because conventional external fluorescent probes often fail to sensitively track localized interfacial changes.

To overcome this limitation, we introduce a novel strategy by covalently attaching the fluorescent dye Coumarin 343 (C343) directly to the polymer backbone. This fixed incorporation ensures that the probe remains localized within the polymer matrix, enabling more accurate reporting of dynamical changes at the polymer-water interface during phase transition. In this work, we address key questions related to probe-environment coupling, medium-induced relaxation dynamics, and the degree to which probe anchoring perturbs or, reveals the true nature of sol-gel phase transition processes in responsive polymer systems

Lastly, we turn our attention to another biologically significant chemical process. Amyloid fibrillation, a critical biochemical process linked to neurodegenerative diseases, involves protein misfolding and aggregation driven by hydrogen bonding, hydrophobic forces, and other non-covalent interactions. These aggregates form insoluble fibrils that accumulate in tissues and disrupt normal cellular function. Among various physicochemical factors, pH plays a pivotal role in modulating protein aggregation by influencing surface charge distribution, structural collapse, and intermolecular interactions. While most research focuses on peptides or full proteins, the contribution of individual amino acids, such as Tryptophan (Trp), to early-stage fibrillation remains poorly understood. Trp, with its aromatic structure and pH-sensitive charge states, offers a minimal yet powerful model for exploring the fundamental mechanisms of amyloid formation. This work aims to illuminate molecular-level insights into pH-dependent Trp aggregation by linking morphological transitions to accompanying water dynamics, and also, addressing substantial gaps in our understanding of how single amino acids contribute to amyloidogenesis, with broader implications for the development of targeted diagnostics and therapeutics.

1.4 Organization of the Thesis

Chapter 1 introduces an overview of the field of battery electrolyte materials, covering systems such as organic electrolytes, polymer electrolytes, and water-in-salt electrolytes, as well as smart copolymers. It introduces their fundamental physicochemical properties, including density, viscosity, and kinetic parameters along with an emphasis on the dynamic behavior of these systems. A key focus is placed on ion transport mechanisms, particularly how the translational diffusion of ions is coupled to both macroscopic properties (such as viscosity and fluidity) and microscopic solvent dynamics. The chapter also explores the importance of understanding sol - gel phase transitions in smart copolymer systems, especially those that occur without external stimuli. Additionally, it discusses the fibrillation of amino acid residues, linking it to amyloid formation and aggregation pathways. Finally, the chapter introduces the concept of spatio-temporal heterogeneity in complex chemical systems, with relevance to electrolyte transport pathways, sol - gel transitions, and amino acid fibrillation dynamics. These insights set the stage for deeper exploration of structure-property relationships in advanced electrolyte and soft matter systems.

Chapter 2 provides a detailed account of the experimental methodologies and techniques employed throughout the study. This includes a comprehensive description of time-resolved fluorescence spectroscopy using a time-correlated single-photon counting (TCSPC) setup, and ultrafast fluorescence measurements using a Streak Camera detection system to probe solvent dynamics on femtosecond to picosecond timescales. The chapter also covers Raman spectroscopy to investigate solute - solvent interactions and structural features in solution. Additionally, this chapter presents an in-depth overview of dielectric relaxation spectroscopy (DRS) in the MHz – GHz frequency range to study the collective dipolar relaxation dynamics of the medium. For each technique, the underlying theoretical principles, experimental setups, measurement protocols, and data analysis procedures are systematically presented.

In **Chapter 3**, we investigate the correlation between ionic conductivity and the structural and dynamic properties of G3/LiTFSI electrolytes. Using Raman spectroscopy, dielectric relaxation (MHz – GHz), and ultrafast solvation dynamics *via* streak camera-based fluorescence measurements (using DMASBT probe), the study reveals an inverse power-law dependence between experimental ion conductivity and both dielectric and solvation timescales. The

decoupling of ion transport from bulk viscosity is critically examined, highlighting the influence of medium dynamics in governing conductivity in electrolyte solutions.

In **Chapter 4**, we explore the role of dynamic heterogeneity in governing ion transport mechanisms in G3/LiTFSI electrolytes by integrating TCSPC and streak camera techniques. A strong correlation has been presented between medium heterogeneity and Li^+ mobility, with coupled rotational - solvation dynamics revealing underlying structural complexity. We have analyzed both the spatial and dynamic heterogeneity aspects, emphasizing a pronounced decoupling between ion conductivity and medium viscosity. Furthermore, the impact of long-time components in rotation and solvation dynamics has been critically assessed, demonstrating how these factors contribute to establish optimal dynamic conditions for enhanced ionic conductivity.

Chapter 5 presents a comprehensive investigation into the structural and dynamic underpinnings of ion transport in PC/$LiClO_4$/PPG gel polymer electrolytes (GPEs). Despite the increase in medium viscosity upon polymer incorporation, we demonstrate that PPG modulates Li^+ speciation and electrolyte structure by suppressing ion pairing and altering solvation environments. Concurrently, PPG introduces cooperative segmental motions within the polymer matrix, which dominate the overall relaxation behavior and contribute to a reduction in ionic conductivity. Furthermore, Onsager conductivity analysis reveals that at elevated PPG loadings, mechanism of ion transport transitions from being viscosity-governed to being constrained by long-timescale segmental relaxation of the polymer matrix. These findings underscore that structural confinement and dynamic heterogeneity are not merely secondary effects but play a pivotal role in defining ion transport behavior in GPE systems.

In **Chapter 6**, we probe the sol - gel transition mediated medium dynamics in aqueous solutions of rationally engineered poly(acrylic acid)-based copolymers with incorporating hydrophobic modifications. This transition was systematically monitored over a 30-days of incubation period under ambient conditions, in the absence of any external stimuli. The study uncovers how spontaneous polymer aggregation and network formation progressively evolve, as evidenced by a gradual increase in hydrodynamic diameter and a continuous slowdown of medium dynamics captured via both rotational fluorescence anisotropy and DR spectroscopy. Notably, this dynamic deceleration is found to be predominantly governed by the emergence and intensification of the slowest relaxation mode, indicative of growing structural confinement within the polymer

solutions. Interestingly, the onset time of the sol - gel phase transition remains unaffected by the chemical binding of the fluorescent probe, indicating a robust, probe-independent aggregation-driven mechanism underlying the gelation process.

In **Chapter 7**, we investigate the pH-dependent fibrillation behavior of Tryptophan (Trp) using steady-state and time-resolved fluorescence (TRF) spectroscopy, complemented by morphological and vibrational analyses. The study demonstrates that the charge state of Trp, modulated by pH of the medium, plays an essential role in governing its fibrillation dynamics through various kind of non-covalent intermolecular interactions. We provide an extensive molecular-level understanding of water dynamics associated with Trp– Trp aggregation in buffer medium, derived from analyses of intrinsic fluorescence behavior of Trp and ultrafast relaxation dynamics probed by using the amyloid-specific dye Thioflavin-T (Th-T).

Chapter 8 concludes the thesis by summarizing the key findings, acknowledging its limitations, and proposing directions for future research to resolve these open questions. Additionally, several relevant and thought-provoking problems are briefly discussed, offering promising avenues for further investigation.

References

[1] M.S. Whittingham, *Science* **192**(4244), 1126–1127 (1976).

[2] P.K. Singh, S. Mallick, G.A. Kaur, S. Balayan, and A. Tiwari, *Nano Energy* **128**, 109792 (2024).

[3] A. Yoshino, *Lithium-Ion Batteries*, (Elsevier, 2014), pp. 1–20.

[4] A. Ramanan, *Reson* **24**(12), 1381–1395 (2019).

[5] P.V. Wright, *Brit. Poly. J.* **7**(5), 319–327 (1975).

[6] M. Armand, *Solid State Ionics* **69**(3–4), 309–319 (1994).

[7] T. Aida, E.W. Meijer, and S.I. Stupp, *Science* **335**(6070), 813–817 (2012).

[8] S.I. Stupp, V. LeBonheur, K. Walker, L.S. Li, K.E. Huggins, M. Keser, and A. Amstutz, *Science* **276**(5311), 384–389 (1997).

[9] K. Sato, M.P. Hendricks, L.C. Palmer, and S.I. Stupp, *Chem. Soc. Rev.* **47**(20), 7539–7551 (2018).

[10] R.A. Kyle, *Amyloid* **18**(sup1), 6–7 (2011).

[11] B.W. Walker, R. Portillo Lara, E. Mogadam, C. Hsiang Yu, W. Kimball, and N. Annabi, *Progress in Polymer Science* **92**, 135–157 (2019).

[12] M. Xu, W. Li, and B.L. Lucht, *Journal of Power Sources* **193**(2), 804–809 (2009).

[13] J.B. Goodenough, and K.-S. Park, *J. Am. Chem. Soc.* **135**(4), 1167–1176 (2013).

[14] H. Adenusi, G.A. Chass, S. Passerini, K.V. Tian, and G. Chen, *Adv. Energy Mat.* **13**(10), 2203307 (2023).

[15] J.B. Goodenough, and Y. Kim, *Chem. Mater.* **22**(3), 587–603 (2010).

[16] Sungjemmenla, V. S. K., C.B. Soni, V. Kumar, and Z.W. Seh, *Energy Tech* **10**(9), 2200421 (2022).

[17] Q. Liu, A. Cresce, M. Schroeder, K. Xu, D. Mu, B. Wu, L. Shi, and F. Wu, *Energy Storage Materials* **17**, 366–373 (2019).

[18] O. Borodin, W. Behl, and T.R. Jow, *J. Phys. Chem. C* **117**(17), 8661–8682 (2013).

[19] C. Yan, R. Xu, Y. Xiao, J. Ding, L. Xu, B. Li, and J. Huang, *Adv. Funct. Mat.* **30**(23), 1909887 (2020).

[20] M.D. Bouguern, A.K. M R, and K. Zaghib, *Journal of Power Sources* **623**, 235457 (2024).

[21] D. Di Lecce, V. Marangon, H.-G. Jung, Y. Tominaga, S. Greenbaum, and J. Hassoun, *Green Chem.* **24**(3), 1021–1048 (2022).

[22] K. Ueno, R. Tatara, S. Tsuzuki, S. Saito, H. Doi, K. Yoshida, T. Mandai, M. Matsugami, Y. Umebayashi, K. Dokko, and M. Watanabe, *Phys. Chem. Chem. Phys.* **17**(12), 8248–8257 (2015).

[23] K. Ueno, K. Yoshida, M. Tsuchiya, N. Tachikawa, K. Dokko, and M. Watanabe, *J. Phys. Chem. B* **116**(36), 11323–11331 (2012).

[24] S. Seko, H. Nara, M. Jeong, T. Yokoshima, T. Momma, and T. Osaka, *Electrochimica Acta* **243**, 65–71 (2017).

[25] J. Liu, S. Ihuaenyi, R. Kuphal, J. Salinas, L. Xie, L. Yang, U. Janakiraman, M.E. Fortier, and C. Fang, *J. Electrochem. Soc.* **170**(1), 010535 (2023).

[26] B. Jache, J.O. Binder, T. Abe, and P. Adelhelm, *Phys. Chem. Chem. Phys.* **18**(21), 14299–14316 (2016).

[27] A. Manuel Stephan, *European Polymer Journal* **42**(1), 21–42 (2006).

[28] X. Cheng, J. Pan, Y. Zhao, M. Liao, and H. Peng, *Adv. Energy Mat.* **8**(7), 1702184 (2018).

[29] Md.S. Ahmed, M. Islam, B. Raut, S. Yun, H.Y. Kim, and K.-W. Nam, *Gels* **10**(9), 563 (2024).

[30] K. Aruchamy, S. Ramasundaram, S. Divya, M. Chandran, K. Yun, and T.H. Oh, *Gels* **9**(7), 585 (2023).

[31] C. Tang, L. Yu, Q. Jiang, R. Gu, Y. Zhang, Z. Liu, W. Cai, H. Wu, Y. Zhang, and M. Yao, *Renewables* **2**(5), 297–340 (2024).

[32] N. Agmon, *Chem. Phys. Lett.* **244**(5–6), 456–462 (1995).

[33] S. Cukierman, *Biochimica et Biophysica Acta (BBA) - Bioenergetics* **1757**(8), 876–885 (2006).

[34] I. Rubinstein, M. Bixon, and E. Gileadi, *J. Phys. Chem.* **84**(7), 715–721 (1980).

[35] C. Zhong, Y. Deng, W. Hu, J. Qiao, L. Zhang, and J. Zhang, *Chem. Soc. Rev.* **44**(21), 7484–7539 (2015).

[36] H. Gao, and K. Lian, *RSC Adv.* **4**(62), 33091–33113 (2014).

[37] G. Yu, X. Yan, C. Han, and F. Huang, *Chem. Soc. Rev.* **42**(16), 6697 (2013).

[38] T. Rossow, and S. Seiffert, *Polym. Chem.* **5**(8), 3018–3029 (2014).

[39] A. Noro, M. Hayashi, and Y. Matsushita, *Soft Matter* **8**(24), 6416 (2012).

[40] X. Yan, D. Xu, X. Chi, J. Chen, S. Dong, X. Ding, Y. Yu, and F. Huang, *Adv. Mat.* **24**(3), 362–369 (2012).

[41] E.A. Appel, J. Del Barrio, X.J. Loh, and O.A. Scherman, *Chem. Soc. Rev.* **41**(18), 6195 (2012).

[42] C.N. Munyiri, E.S. Madivoli, J. Kisato, J. Gichuki, and P.G. Kareru, *Int. J. Polymeric Materials and Polymeric Biomaterials* **74**(7), 625–640 (2025).

[43] P. Nezhad-Mokhtari, M. Ghorbani, L. Roshangar, and J. Soleimani Rad, *Int. J. Bio. Macromolecules* **139**, 760–772 (2019).

[44] W. Hu, Z. Wang, Y. Xiao, S. Zhang, and J. Wang, *Biomater. Sci.* **7**(3), 843–855 (2019).

[45] W.A. Laftah, S. Hashim, and A.N. Ibrahim, *Polymer-Plastics Technology and Engineering* **50**(14), 1475–1486 (2011).

[46] M. Guo, L.M. Pitet, H.M. Wyss, M. Vos, P.Y.W. Dankers, and E.W. Meijer, *J. Am. Chem. Soc.* **136**(19), 6969–6977 (2014).

[47] Z. Zhang, T. Chao, and S. Jiang, *J. Phys. Chem. B* **112**(17), 5327–5332 (2008).

[48] S. Zhang, D. Ren, Q. Zhao, M. Peng, X. Wang, Z. Zhang, W. Liu, and F. Huang, *Nat. Commun.* **16**(1), 2371 (2025).

[49] S. Uman, A. Dhand, and J.A. Burdick, *J. App. Poly. Sci.* **137**(25), 48668 (2020).

[50] E. Jabbari, and S. Nozari, *European Polymer Journal* **36**(12), 2685–2692 (2000).

[51] U. Gulyuz, and O. Okay, *Soft Matter* **9**(43), 10287 (2013).

[52] J.E. Elliott, M. Macdonald, J. Nie, and C.N. Bowman, *Polymer* **45**(5), 1503–1510 (2004).

[53] S.S. Halacheva, D.J. Adlam, E.K. Hendow, T.J. Freemont, J. Hoyland, and B.R. Saunders, *Biomacromolecules* **15**(5), 1814–1827 (2014).

[54] X. Gao, C. He, C. Xiao, X. Zhuang, and X. Chen, *Polymer* **54**(7), 1786–1793 (2013).

[55] S. Ashraf, H.-K. Park, H. Park, and S.-H. Lee, *Macromol. Res.* **24**(4), 297–304 (2016).

[56] Y. Park, M. Kim, H. Chung, A. Woo, I. Noda, and Y. Jung, *Polymers* **13**(9), 1447 (2021).

[57] J. Yang, Y. Chen, L. Zhao, J. Zhang, and H. Luo, *Polymer Reviews* **63**(3), 574–612 (2023).

[58] A.V. Efimov, *Progress in Biophysics and Molecular Biology* **60**(3), 201–239 (1993).

[59] D. Li, S. Yu, Y. Long, A. Shi, J. Deng, Y. Ma, J. Wen, X. Li, S. Liu, Y. Zhang, J. Wan, N. Li, and R. Ao, *Front. Immunol.* **13**, 985378 (2022).

[60] A. Tutakhail, L. Boulet, S. Khabil, Q.A. Nazari, H. Hamid, and F. Coudoré, *Curr Pharmacol Rep* **6**(1), 8–23 (2020).

[61] X. Gong, R. Chang, J. Zou, S. Tan, and Z. Huang, *Reviews in Neurosciences* **34**(3), 313–324 (2023).

[62] M.D. Lovelace, B. Varney, G. Sundaram, M.J. Lennon, C.K. Lim, K. Jacobs, G.J. Guillemin, and B.J. Brew, *Neuropharmacology* **112**, 373–388 (2017).

[63] M.D. Lovelace, B. Varney, G. Sundaram, N.F. Franco, M.L. Ng, S. Pai, C.K. Lim, G.J. Guillemin, and B.J. Brew, *Front. Immunol.* **7**, (2016).

[64] Y. Chen, and M.D. Barkley, *Biochemistry* **37**(28), 9976–9982 (1998).

[65] J.T. Vivian, and P.R. Callis, *Biophysical Journal* **80**(5), 2093–2109 (2001).

[66] D. Creed, *Photochem & Photobiology* **39**(4), 537–562 (1984).

[67] D. Toptygin, R.S. Savtchenko, N.D. Meadow, S. Roseman, and L. Brand, *J. Phys. Chem. B* **106**(14), 3724–3734 (2002).

[68] M. Jia, H. Yi, M. Chang, X. Cao, L. Li, Z. Zhou, H. Pan, Y. Chen, S. Zhang, and J. Xu, *J. Photochem. Photobio. B: Bio.* **149**, 243–248 (2015).

[69] B. Christiaens, S. Symoens, S. Vanderheyden, Y. Engelborghs, A. Joliot, A. Prochiantz, J. Vandekerckhove, M. Rosseneu, and B. Vanloo, *European Journal of Biochemistry* **269**(12), 2918–2926 (2002).

[70] Y. Engelborghs, *Spectrochimica Acta Part A: Molecular and Biomolecular Spectroscopy* **57**(11), 2255–2270 (2001).

[71] J. Marniemi, and M.G. Parkki, *Biochem Pharmacol* **24**(17), 1569–1572 (1975).

[72] M. Kasha, and S.P. McGlynn, *Annu. Rev. Phys. Chem.* **7**(1), 403–424 (1956).

[73] A.P. Demchenko, V.I. Tomin, and P.-T. Chou, *Chem. Rev.* **117**(21), 13353–13381 (2017).

[74] P.G. Kusalik, and I.M. Svishchev, *Science* **265**(5176), 1219–1221 (1994).

[75] Y.-L. Wang, B. Li, S. Sarman, F. Mocci, Z.-Y. Lu, J. Yuan, A. Laaksonen, and M.D. Fayer, *Chem. Rev.* **120**(13), 5798–5877 (2020).

[76] Y.-R. Duan, T. Li, W.-K. Wu, J. Li, X.-Y. Zhou, S.-D. Liu, and H. Li, *Chinese Phys. B* **26**(3), 036401 (2017).

[77] M.D. Ediger, *Annu. Rev. Phys. Chem.* **51**(1), 99–128 (2000).

[78] M. Sasai, *Physica A: Statistical Mechanics and Its Applications* **285**(3–4), 315–324 (2000).

[79] J.R. Lakowicz, *Principles of Fluorescence Spectroscopy*, (Springer US, Boston, MA, 1999), pp. 291–319.

[80] R.F. Steiner, *Fluorescence Spectroscopy*, edited by J.R. Lakowicz, (Kluwer Academic Publishers, Boston, 2002), pp. 1–52.

[81] T.A.A. Broadbent, *Math. Gaz.* **41**(337), 231–231 (1957).

[82] J.H. Calderwood, and W.T. Coffey, *Proc. R. Soc. Lond. A* **356**(1685), 269–286 (1977).

[83] R. Kind, O. Liechti, N. Korner, J. Hulliger, J. Dolinsek, and R. Blinc, *Phys. Rev. B* **45**(14), 7697–7703 (1992).

[84] H. Tanaka, *J. Phys. Chem. B* **129**(3), 789–813 (2025).

[85] S.C. Glotzer, J. *Non Cryst Solids* **274**(1–3), 342–355 (2000).

[86] R. Yamamoto, and A. Onuki, *Phys. Rev. E* **58**(3), 3515–3529 (1998).

[87] B. Bagchi, and B. Jana, *Chem. Soc. Rev.* **39**(6), 1936 (2010).

[88] M. Andreev, J.J. De Pablo, A. Chremos, and J.F. Douglas, *J. Phys. Chem.* B **122**(14), 4029–4034 (2018).

[89] G. Van Der Zwan, and J.T. Hynes, *Chem. Phys.* **152**(1–2), 169–183 (1991).

[90] K.-K. Lee, K. Park, H. Lee, Y. Noh, D. Kossowska, K. Kwak, and M. Cho, *Nat. Commun.* **8**(1), 14658 (2017).

[91] N.J. Shah, C. Fang, N.C. Osti, E. Mamontov, X. Yu, J. Lee, H. Watanabe, R. Wang, and N.P. Balsara, *Nat. Mater.* **23**(5), 664–669 (2024).

[92] K. Bhattacharyya, *Acc. Chem. Res.* **36**(2), 95–101 (2003).

[93] G. Smith, A.P. Duffy, J. Shen, and C.J. Olliff, *J. Pharm. Sci.* **84**(9), 1029–1044 (1995).

[94] I. Popov, P.B. Ishai, A. Khamzin, and Y. Feldman, *Phys. Chem. Chem. Phys.* **18**(20), 13941–13953 (2016).

[95] M. Tomozawa, and R.H. Doremus, *J. Non Cryst Solids* **14**(1), 54–64 (1974).

[96] R. Buchner, and J. Barthel, *Annu. Rep. Prog. Chem.*, Sect. C **97**(1), 349–382.

[97] P. Pissis, D. Fragiadakis, A. Kanapitsas, and K. Delides, *Macromolecular Symposia* **265**(1), 12–20 (2008).

[98] R. Pethrick, *Progress in Polymer Science* **27**(9), 1983–2017 (2002).

[99] R. Buchner, *Pure and Applied Chemistry* **80**(6), 1239–1252 (2008).

[100] Y. Maeda, N. Tsukida, H. Kitano, T. Terada, and J. Yamanaka, *J. Phys. Chem.* **97**(51), 13903–13906 (1993).

[101] C.D. Syme, C. Martino, R. Yusvana, N.M.S. Sirimuthu, and J.M. Cooper, *Anal. Chem.* **84**(3), 1491–1495 (2012).

[102] E. Cazzanelli, G. Mariotto, G.B. Appetecchi, F. Croce, and B. Scrosati, *Electrochimica Acta* **40**(13–14), 2379–2382 (1995).

[103] L. Wang, A. Morita, N.M. North, S.M. Baumler, E.W. Springfield, and H.C. Allen, *J. Phys. Chem. B* **127**(7), 1618–1627 (2023).

[104] N. Kuhar, S. Sil, and S. Umapathy, *Spectrochimica Acta Part A: Molecular and Biomolecular Spectroscopy* **258**, 119712 (2021).

[105] D. Kurouski, T. Postiglione, T. Deckert-Gaudig, V. Deckert, and I.K. Lednev, *Analyst* **138**(6), 1665 (2013).

[106] R.W. Williams, *Methods in Enzymology*, (Elsevier, 1986), pp. 311–331.

[107] Q. Sun, *Vib. Spec.* **51**(2), 213–217 (2009).

[108] G.R. Fleming, and P.G. Wolynes, *Physics Today* **43**(5), 36–43 (1990).

[109] M. Nakamura, Y. Kazue, S. Seki, K. Dokko, and M. Watanabe, *Meet. Abstr.* MA2008-02(10), 742–742 (2008).

[110] M. Požar, and A. Perera, *J. Mol. Liq.* **227**, 210–217 (2017).

[111] A.S. Mahadevi, and G.N. Sastry, *Chem. Rev.* **116**(5), 2775–2825 (2016).

[112] R. Ghosh, T. Samanta, S. Banaerjee, R. Biswas, and B. Bagchi, *Faraday Discuss.* **177**, 313–328 (2015).

[113] R. Ghosh, and B. Bagchi, *J. Phys. Chem. B* **120**(49), 12568–12583 (2016).

[114] S. Spittle, D. Poe, B. Doherty, C. Kolodziej, L. Heroux, M.A. Haque, H. Squire, T. Cosby, Y. Zhang, C. Fraenza, S. Bhattacharyya, M. Tyagi, J. Peng, R.A. Elgammal, T. Zawodzinski, M. Tuckerman, S. Greenbaum, B. Gurkan, C. Burda, M. Dadmun, E.J. Maginn, and J. Sangoro, *Nat. Commun.* **13**(1), 1081 (2022).

[115] M. Pagliai, G. Cardini, R. Righini, and V. Schettino, *J. Chem. Phys.* **119**(13), 6655–6662 (2003).

[116] M. Tarek, and D.J. Tobias, *Phys. Rev. Lett.* **88**(13), 138101 (2002).

Chapter 2

Experimental Techniques

This chapter presents a concise overview of the experimental techniques utilized in this thesis. It primarily offers brief descriptions of the methodologies employed and the corresponding data analysis protocols.

2.1 Steady-State UV-Vis Absorption Spectroscopy

2.1.1 Principle

UV-Vis spectroscopy probes the electronic transitions of organic molecules, where electrons are excited from the highest occupied molecular orbital (HOMO) to the lowest unoccupied molecular orbital (LUMO). Absorption occurs when the photon energy matches the HOMO-LUMO energy gap (ΔE) (see **Fig. 2.1**). In conjugated π-systems, the reduced energy gap compared to isolated double bonds leads to absorption at longer wavelengths, with larger conjugated systems shifting absorption further into longer wavelengths.

The fundamental principle of UV -Vis absorption spectroscopy is governed by the Beer-Lambert Law, which states that the absorbance (A) of a sample is directly proportional to its path length (l /cm) and concentration (c) /mol L^{-1}. Mathematically, it can be expressed as: $A = \log_{10} I_0/I = \varepsilon cl$. Here, ε is the molar extinction coefficient (also known as molar absorptivity). Here, I_0 and I represent the intensities of the incident and transmitted light, respectively. In this thesis, all UV -Vis absorption measurements were performed using a path length of $l = 1$ cm and a sample concentration of $C \leq 10^{-5}$M.

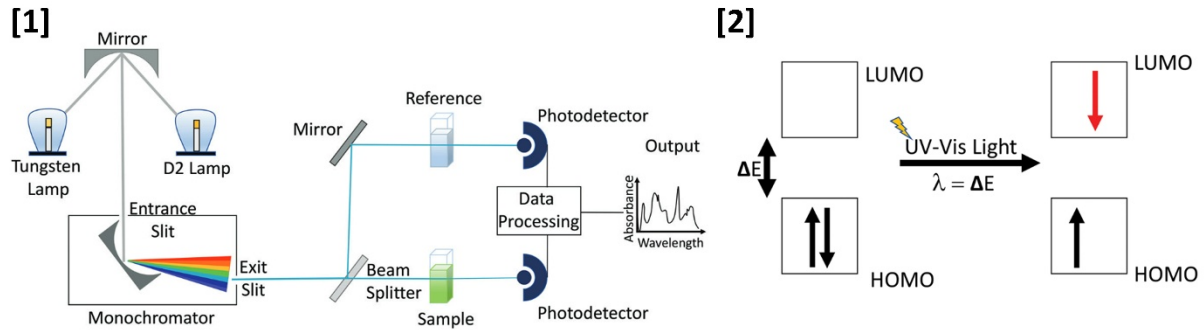

2.2 Steady-State Fluorescence Spectroscopy

Steady-state fluorescence emission measurements presented in this thesis were performed using a fluorimeter (Fluorolog, Jobin-Yvon, Horiba). A continuous xenon (Xe) lamp served as the excitation source, with its light passed through an excitation monochromator to select the desired wavelength and eliminate stray light. The monochromatic light excites the sample, and the emitted fluorescence is collected at a right angle by an emission monochromator. The signal is then detected by a photomultiplier tube (PMT), amplified, electronically processed, and displayed on a computer.[2]

2.3 Time-Resolved Fluorescence Spectroscopy

2.3.1 TCSPC Set-up

Time-correlated single photon counting (TCSPC) measurements (see **Fig. 2.2**) were performed using a LifeSpec-ps system (Edinburgh Instruments, U. K.). A pulsed diode laser excites the fluorophores in a quartz cuvette, generating an emission photon detected by a constant fraction

discriminator (CFD). In reverse mode TCSPC, the first detected photon triggers the start signal for the time-to-amplitude converter (TAC), while a subsequent laser pulse provides the stop signal. The resulting voltage ramp, proportional to the time delay between start and stop signals, is digitized via an ADC and analyzed using a multichannel analyzer (MCA). Repeated cycles generate a decay histogram representing photon counts versus time.[2] The instrument response function (IRF) was determined by measuring the magic angle (54.7°) intensity decay at 409 nm in a scattering medium (water) following excitation with a 409 nm laser, yielding a full width at half maximum (FWHM) of ~ 85 ps.

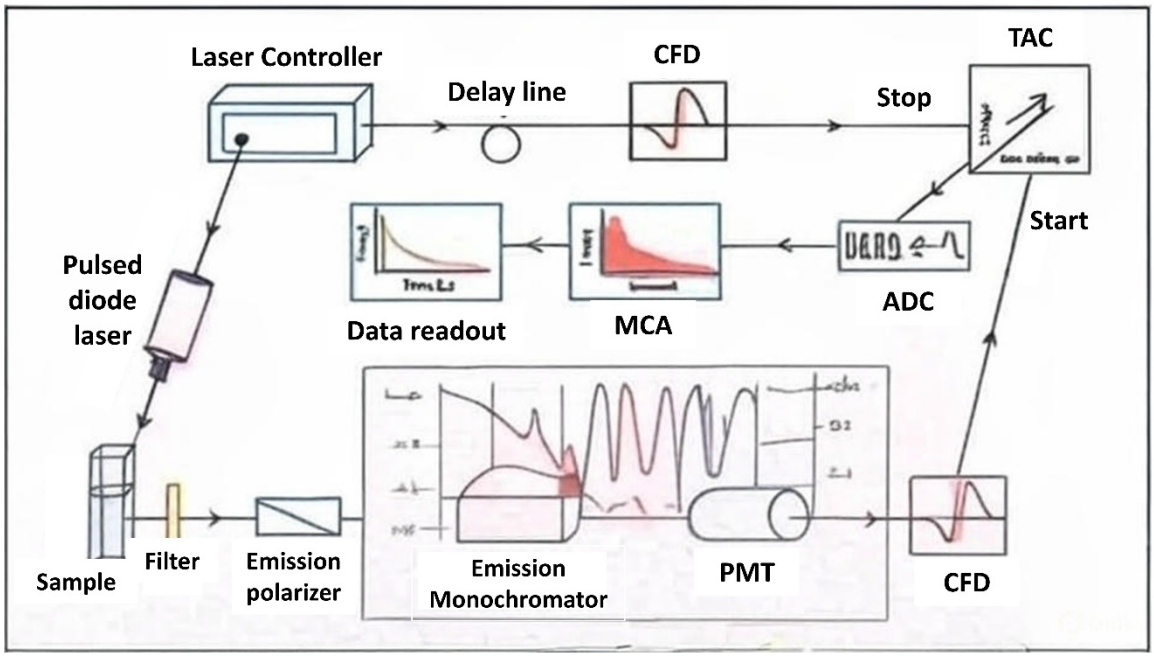

2.3.2 Streak Camera Detection Technique

The streak camera enables detection of ultrafast events with temporal resolution down to the picosecond range, surpassing the capabilities of TCSPC. Time-resolved fluorescence spectra (TRFS) were captured using a Streak Camera[3,4] (Optoscope SC − 10) coupled with a spectrograph (HRS − 300SS, Princeton Instruments; 300 mm path, 300 grooves/mm grating), as illustrated in **Fig. 2.3**. The central wavelength was tuned to the fluorescence emission peak of the sample.

Excitation was achieved using a Ti:Sapphire laser (Mai Tai HP-1040S, 100 fs pulses, 80 MHz), frequency-doubled to 440 nm via a BBO crystal. The 440 nm light, filtered and focused onto the sample in a 1 cm quartz cuvette, excited the fluorophore. Emission was collected at 90°, passed through a 471 nm bandpass filter, and directed via lenses to a monochromator slit (10 µm × 4 mm). Measurements used the magic angle (54.7°) polarization to suppress rotational effects. Instrument response function (IRF), determined from scattering in water, showed an FWHM of ~ 2 ps. Data acquisition included 1000 sweeps with a 15 ps/mm sweep speed, 33.5% delay, and MCP gain set at 750 V.

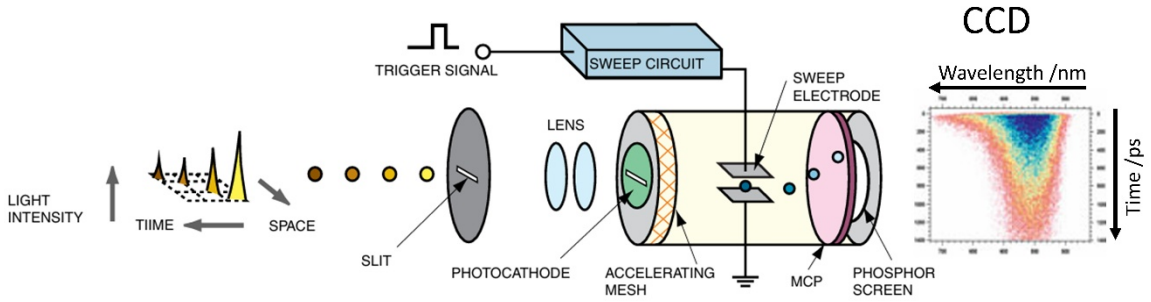

FIG. 2.3. A simplified representation of Streak Camera set-up.

2.3.3 Solvation Dynamics Analysis

For solvation dynamics (also known as, Stokes shift dynamics, as illustrated in **Fig. 2.4**) studies, 14 - 16 fluorescence decays were recorded at the magic angle (54.7°) across evenly spaced wavelengths spanning the steady-state emission spectrum of the fluorophore in the sample. A decay at the blue edge and a rise followed by decay behavior at the red edge relative to the emission peak are characteristic features of dynamic Stokes shift.[5] The measured fluorescence decay, $N(t)$ is a convolution of the IRF, $R(t)$, and the sample response, $I(t)$. The sample response was retrieved using an iterative reconvolution method via nonlinear least-squares fitting. The recovered $I(t)$ was fitted to a sum of exponential terms: $I(t) = \sum_{i=1}^{N} \alpha_i \exp(-t/\tau_i)$, where α_i and τ_i are the pre-exponential factors and lifetimes, respectively.

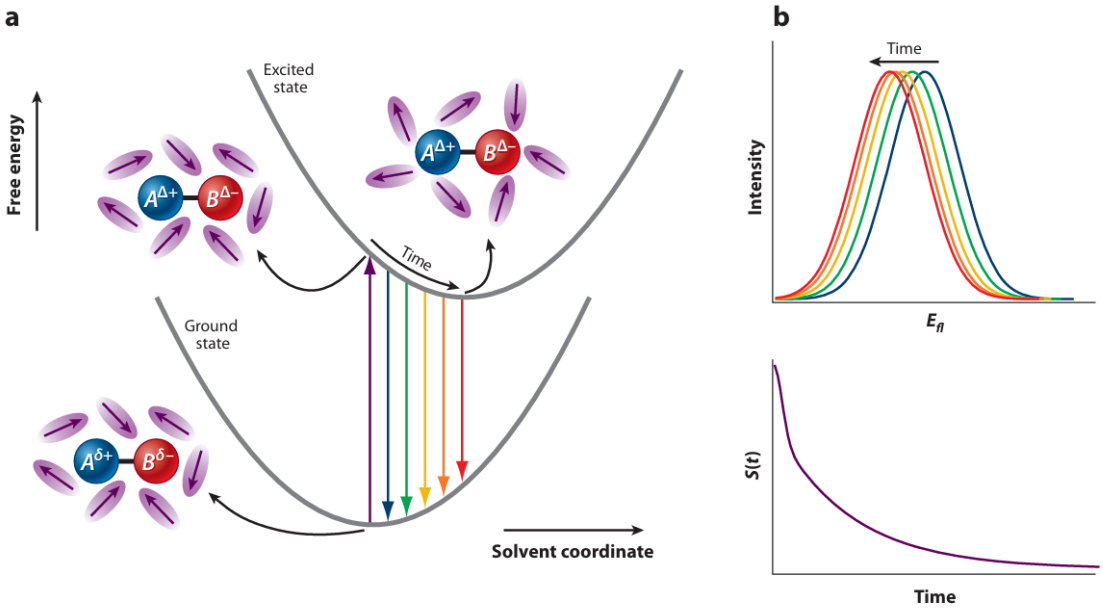

FIG. 2.4. Schematic representation of the time-dependent fluorescence process. **(a)** Free energy diagram illustrating the solvent relaxation following photoexcitation of a donor-acceptor dye molecule ($A-B$) undergoing charge transfer. Upon excitation, the solute dipole moment changes (e.g., from $A^{+}-B^{-}$ to $A^{\delta+}-B^{\delta-}$), prompting dynamic reorientation of surrounding solvent dipoles (purple arrows). The system relaxes along the solvent coordinate in the excited state, leading to a time-dependent red shift in emission. **(b)** Top: Fluorescence emission spectra at successive delay times after excitation, showing a progressive red shift due to solvent relaxation. Bottom panel: Corresponding normalized dynamic Stokes shift function, $S(t)$, depicting the decay of solvation energy with time as the medium approaches equilibrium around the excited-state fluorophore.[7]

Time-resolved emission spectra (TRES) were reconstructed from the wavelength-resolved intensity decays following standard protocols.[5,6] As discussed above, the fluorescence decays collected at various wavelengths (λ_j) were fitted with multi-exponential function, $I(\lambda_j, t) = \sum_{i=1}^{N} \alpha_i(\lambda_j)\exp(-t/\tau_i(\lambda_j))$, where $\alpha_i(\lambda_j)$ denotes the pre-exponential factor, with $\sum_i \alpha_i(\lambda_j) = 1$. Each decay was first normalized so that its time-integrated intensity matched the steady-state emission intensity at that wavelength, $F(\lambda_j)$, using the normalization factor:

$H(\lambda_j) = \frac{F(\lambda_j)}{\int_0^\infty I(\lambda_j,t)dt} = \frac{F(\lambda_j)}{\sum_i \alpha_i(\lambda_j)\tau_i(\lambda_j)}$. The normalization factor, $H(\lambda_j)$ was multiplied with $I(\lambda_j, t)$ to obtain the normalized function: $I'(\lambda_j, t) = H(\lambda_j)I(\lambda_j, t) = \sum_{i=1}^{N} \alpha_i(\lambda_j)\exp(-t/\tau_i(\lambda_j))$, where $\alpha_i(\lambda_j) = H(\lambda_j)\alpha_i(\lambda_j)$. TRES at any wavelength and time could be calculated from $I'(\lambda_j, t)$.

The TRES data were then converted to frequency-domain representations by appropriately weighting the intensity by frequency. Each TRES was fitted with a log-normal function to obtain a continuous spectral profile, and the peak frequencies at different times were used to construct the solvation response function, $S(t)$, as: $S(t) = \frac{\nu(t)-\nu(\infty)}{\nu(0)-\nu(\infty)}$. Here, $\nu(0)$, $\nu(t)$, and $\nu(\infty)$ denote the emission peak frequencies at time zero, at given time t, and after complete solvent relaxation, respectively. $S(t)$ thus captures the normalized temporal evolution of solvent relaxation following photoexcitation. Typically, $\nu(\infty)$ matches the steady-state emission peak. However, discrepancies often a slight blue shift in steady-state spectra, may arise due to emission from solute molecules surrounded by only partially relaxed solvent environments. The average solvation time $\langle\tau_s\rangle$ was obtained by integrating the solvation response function: $\langle\tau_s\rangle = \int_0^\infty dtS(t) = \int_0^\infty dt \sum_{i=1}^{n} a_i \exp[-t/\tau_i] = \sum_{i=1}^{n} a_i\tau_i$, with $\sum_{i=1}^{n} a_i = 1$ and a_i, τ_i are the amplitudes and time constants of the multi-exponential fit to $S(t)$.

2.3.4 Rotation Anisotropy Decay

TCSPC technique is not only a powerful tool for measuring fluorescence lifetimes, but it is also widely employed to investigate the re-orientational dynamics of fluorophores and the time-dependent frictional characteristics of the surrounding medium. The fundamental principle underlying the measurement of re-orientational dynamics lies in photo-selective excitation: only those fluorophores whose absorption transition dipole moments are aligned parallel to the electric vector of the polarized excitation light are excited. Upon excitation, the time evolution of the emission polarization provides insight into how the fluorophore reorients within the medium. Fluorescence emission is collected in two orthogonal polarization geometries with respect to the polarized excitation light, parallel $[I_{\parallel}(t)]$ and perpendicular $[I_{\perp}(t)]$ components. As the excited fluorophores undergo rotational diffusion, the initially high polarization of the emission decreases,

leading to a decay in the difference between $I_{\parallel}(t)$ and $I_{\perp}(t)$ over time. This loss of polarization, referred to as anisotropy decay, reflects the rate and extent of molecular reorientation.[8]

To ensure meaningful analysis, the fluorescence lifetime of the fluorophore should be comparable to or, longer than its rotational correlation time, so that sufficient anisotropy decay is captured during the excited-state lifetime. In practice, fluorescence anisotropy measurements are performed at the peak wavelength of the steady-state emission spectrum. The dynamic fluorescence anisotropy, $r(t)$, is calculated using the following relation: $r(t) = \frac{I_{\parallel}(t) - I_{\perp}(t)}{I_{\parallel}(t) + 2I_{\perp}(t)}$

The polarization response of the optical detection setup significantly influences the accuracy of measured fluorescence anisotropy. Due to inherent instrumental biases favoring one polarization direction over another, a correction is necessary to ensure reliable anisotropy measurements. This correction is accounted for using the geometric factor, commonly denoted as G, which quantifies the relative transmission efficiency of vertically vs. horizontally polarized emission. Specifically, G is defined as the ratio of the detection sensitivity for vertically polarized light to that for horizontally polarized light. To determine G, the emission intensity decays collected in parallel $[I_{\parallel}(t)]$ and perpendicular $[I_{\perp}(t)]$ polarization geometries are matched in their tail regions, where anisotropy has fully decayed and the emission becomes depolarized. With the corrected data, the time-resolved fluorescence anisotropy, $r(t)$, is calculated as: $r(t) = \frac{I_{\parallel}(t) - GI_{\perp}(t)}{I_{\parallel}(t) + 2GI_{\perp}(t)}$;

The resulting anisotropy decay, $r(t)$, is then analyzed by fitting to a single or, multi-exponential model: $r(t) = r(0) \sum_i \alpha_i \exp(-t/\tau_i)$, with $\sum_i \alpha_i = 1$. In this expression, $r(0)$ is the initial anisotropy, α_i and τ_i are the amplitude of the i^{th} component and corresponding rotation correlation time. In this thesis, the value of $r(0)$ was fixed during fitting based on known photophysical properties of the fluorophores used: 0.376[9] for C153, 0.35[10] for C343, 0.35[10] for C102 and 0.38[11] for trans-DMASBT. To obtain a representative timescale for molecular rotation, the average rotational correlation time, $\langle \tau_{rot} \rangle$, was calculated as: $\langle \tau_{rot} \rangle = \int_0^{\infty} dt[r(t)/r(0)] = \sum_i \alpha_i \tau_i$ with

$\sum_i \alpha_i = 1$. This average value reflects the weighted contribution of each rotational component and provides a concise measure of the re-orientational dynamics of the fluorophore in the given medium. This time-resolved anisotropy function, $r(t)$, provides direct access to the rotational dynamics of the fluorophore and, indirectly, to the viscosity and microenvironmental friction within the medium.

2.4 Dielectric Relaxation Spectroscopy

2.4.1 Theoretical Background

Dielectric relaxation spectroscopy (DRS) investigates the response of a material's polarization to an external alternating electric field over a range of frequencies. When an electric field is applied, dipoles and charges in the material attempt to align with the field. Due to molecular inertia and interactions, this alignment is not instantaneous, leading to a frequency-dependent dielectric response. DRS measures the complex permittivity, $\varepsilon^*(\omega) = \varepsilon'(\omega) - i\varepsilon''(\omega)$, where ε' represents stored energy (real part) and ε'' represents energy dissipation (imaginary part).[12] Analysis of the relaxation processes provides insights into molecular dynamics, conductivity, and polarization mechanisms.

2.4.2 Instrumentation

Dielectric relaxation measurements were carried out using a Keysight $PNA-L$ vector network analyzer (model $N5235B$) equipped with an open-ended coaxial probe kit (model $N1501A$) over the frequency range of $0.2 \leq \nu/\mathrm{GHz} \leq 50$, which is suitable for characterizing the complex permittivity of the sample. Prior to each measurement session, the system was calibrated using the standard three-point calibration method, employing air, a shorting block, and deionized water as the open, short, and load references, respectively. This ensured accurate impedance matching and minimized systematic errors. The sample was brought into contact with the probe tip under controlled conditions to ensure consistent contact quality and minimize measurement artifacts. The complex dielectric spectra were recorded directly by the analyzer software and further processed for analysis.

2.4.3 Mathematical Modeling and Spectral Data Analysis

2.4.3.1 Debye Model

The Debye model is the simplest and most popular approach to describe the complex frequency dependent dielectric response $\varepsilon^*(\omega)$ of dipolar solvents and solutions containing dipolar molecules. In the diffusive limit, it assumes a single relaxation process characterized by a distinct relaxation time. The Debye model[13] is mathematically expressed as: $\varepsilon^*(\omega) = \varepsilon_\infty + \Delta\varepsilon/[1 + i\omega\tau_D]$, where $\Delta\varepsilon = \varepsilon_s - \varepsilon_\infty$, is the dielectric strength, defined as the difference between the static dielectric constant, ε_s and the high-frequency limiting dielectric constant, ε_∞. The angular frequency (ω) is related to the linear frequency (f) by $\omega = 2\pi f$, and τ_D is the characteristic Debye relaxation time, representing the average time required for dipoles to reorient in response to an external electric field.

2.4.3.2 Non-Debye Model

While the Debye model assumes a single relaxation time and ideal dipolar behavior characterized by a single diffusive relaxation, many real systems exhibit deviations and show multimodal relaxations due to diverse interactions, disorder, or a distribution of microscopic environments. These features often result in symmetric or, asymmetric broadening of the dielectric response, which are better represented by model descriptions such as the Cole - Cole, Cole - Davidson, and Havriliak - Negami functions.

The Cole - Cole (CC) model accounts for symmetric broadening of the dielectric relaxation spectrum.[14] It introduces a parameter α to describe the distribution of relaxation times, and is given by: $\varepsilon^*(\omega) = \varepsilon_\infty + \Delta\varepsilon/[1 + (i\omega\tau_{cc})^{1-\alpha}]$. Here, $0 \leq \alpha < 1$ is the broadening parameter and τ_{cc} is the characteristic Cole - Cole relaxation time. The model reduces to Debye form when $\alpha = 0$.

The Cole - Davidson (CD) model captures asymmetric broadening of the dielectric spectrum.[15,16] It is expressed as: $\varepsilon^*(\omega) = \varepsilon_\infty + \Delta\varepsilon/\left[1 + (i\omega\tau_{CD})^{\beta}\right]$, where $0 < \beta \leq 1$ is the asymmetric

broadening parameter and τ_{CD} is the characteristic Cole - Davidson relaxation time. When $\beta = 1$, the model again reduces to the Debye form.

The Havriliak - Negami (HN) model is a more general empirical function that simultaneously accounts for both symmetric and asymmetric broadening.[17] It is expressed as: $\varepsilon^*(\omega) = \varepsilon_\infty + \Delta\varepsilon/\left[1 + (i\omega\tau_{HN})^{(1-\alpha)}\right]^\beta$. In this expression, $0 \leq \alpha < 1$ and $0 < \beta \leq 1$ control the symmetric and asymmetric broadening of the relaxation peak, respectively, while τ_{HN} represents the characteristic relaxation time. For complex systems exhibiting multiple relaxation mechanisms, the overall dielectric response can be described by a superposition of multiple Havriliak–Negami functions, each with its own set of parameters: $\varepsilon^*(\omega) = \varepsilon_\infty + \sum_j \Delta\varepsilon_j/[1 + (i\omega\tau_j)^{1-\alpha_j}]^{\beta_j}$. This approach provides a flexible framework for modeling the broadband dielectric behavior of disordered and heterogeneous systems.

2.4.4 Data Processing

To extract physically meaningful parameters from the complex dielectric response, the selection of an appropriate mathematical model is essential. Accurate modeling allows for the interpretation of relaxation processes and molecular dynamics within the system. The quality of the model fitting was assessed using both the goodness-of-fit parameter and analysis of the residuals between the experimental and calculated values.

The goodness-of-fit parameter, χ^2, is defined as: $\chi^2 = \frac{1}{2m-l}\sum_{i=1}^{m}\left[\left(\frac{\delta\varepsilon_i'}{\sigma(\varepsilon_i')}\right)^2 + \left(\frac{\delta\varepsilon_i''}{\sigma(\varepsilon_i'')}\right)^2\right]$, Where m is the number of data triples $(\nu, \varepsilon', \varepsilon'')$, l denotes the number of adjustable parameters, $\delta\varepsilon_i$ and $\sigma\varepsilon_i$ are the residuals and standard deviations of the individual data points, respectively.[18]

2.4.5 Conductivity Correction in Dielectric Response

In conducting samples, the DC conductivity of the medium contributes significantly to the imaginary part of the complex dielectric permittivity. To account for this effect, a conductivity

correction is applied to the dielectric response. The corrected complex dielectric function is expressed as: $\varepsilon^*(\nu) = \varepsilon'(\nu) - [i\varepsilon''(\nu) + i\kappa/2\pi\varepsilon_p\nu]$, where κ is the DC conductivity of the sample and ε_p is the permittivity of the free space.[19,20] This conductivity correction has been consistently applied to all dielectric data fittings presented throughout this Thesis to ensure accurate modeling of the intrinsic dielectric relaxation processes.

2.5 Raman Spectroscopy

2.5.1 Basic Principle

Raman spectroscopy is based on the inelastic scattering of light due to molecular vibrations.[21] When light interacts with a molecule, it induces a dipole moment proportional to the applied electric field via the molecule's polarizability (α). As the molecule vibrates, its polarizability changes, modulating the induced dipole and giving rise to Raman-scattered light at shifted frequencies. These frequency shifts provide a molecular fingerprint that reflects the vibrational modes of the molecule, enabling structural and compositional analysis.

For vibrating molecules, α varies with nuclear motion, leading to scattering at frequencies different from the incident light, known as Raman scattering. Therefore, the time-dependent induced dipole moment μ results in:

$$\mu = \alpha_0 E_0 \cos\omega_0 t + \frac{1}{2}\left(\frac{\delta\alpha}{\delta q}\right)\Big|_{q=0} . q_0 E_0 \cos(\omega_0 - \omega_R)t + \frac{1}{2}\left(\frac{\delta\alpha}{\delta q}\right)\Big|_{q=0} . q_0 E_0 \cos(\omega_0 + \omega_R)t$$

Here, the polarizability α is expanded around the equilibrium position $q = 0$ using a Taylor series. As a result, the induced dipole moment, μ oscillates at three frequencies: the excitation frequency ω_0 (Rayleigh scattering), $\omega_0 - \omega_R$ (red-shifted Stokes scattering), and $\omega_0 + \omega_R$ (blue-shifted anti-Stokes scattering), as depicted in **Fig. 2.5**. The classical model of Raman scattering cannot explain the differing intensities of Stokes and anti-Stokes lines or account for rotational and electronic Raman effects. A quantum mechanical approach is therefore required, where Raman scattering is viewed as an inelastic two-photon process involving a virtual energy state. It is

complementary to IR spectroscopy, with Raman spectra typically plotted as a wavenumber shift from the excitation frequency.

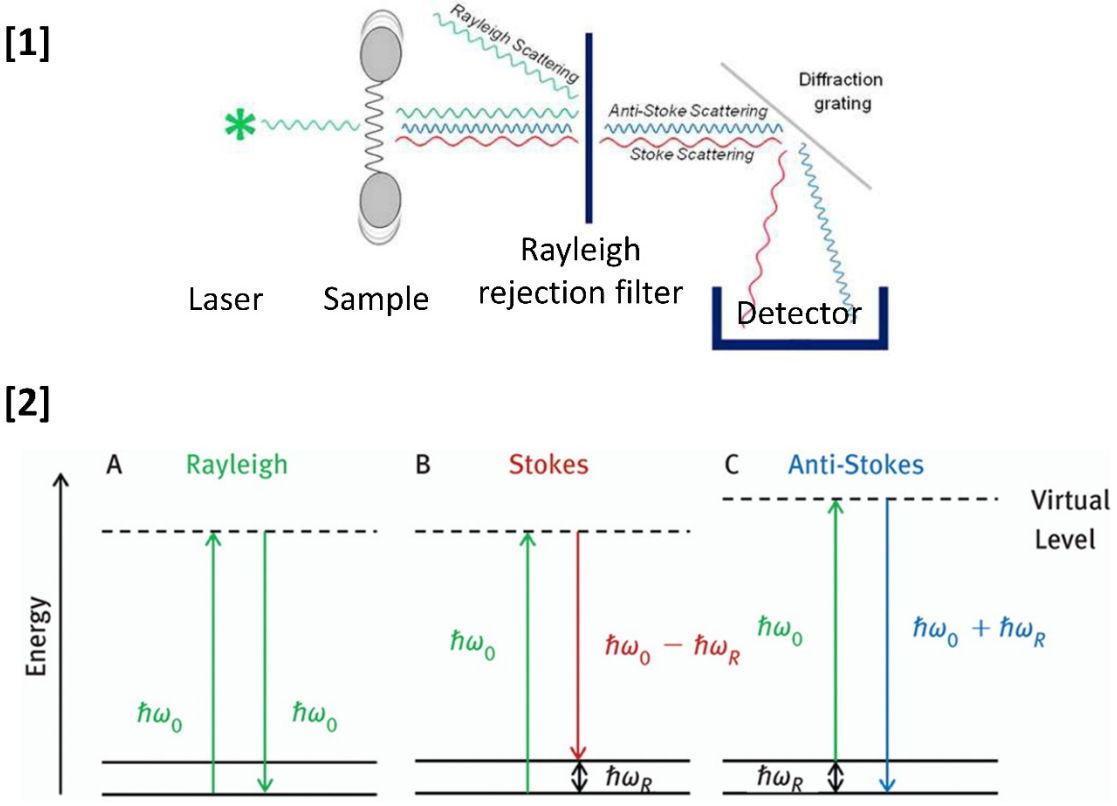

FIG. 2.5. [1] Schematic diagram of a micro-Raman spectrometer.[22]

[2] Schematic energy diagrams of Rayleigh, Stokes, and anti-Stokes Raman scattering.[21]

2.5.2 Instrumentation

Raman spectra of the samples were recorded using a micro-Raman spectrometer (LabRAM HR Evolution, Horiba France SAS) with a 532 nm laser excitation source at an output power of 11.5 mW. Each spectrum was acquired over 20 seconds, and 20 accumulations were collected using an 1800 lines /mm grating. Resolvable peaks in the raw spectra were fitted using Voigt, Lorentzian, or Gaussian functions, depending on the specific characteristics of each sample.

References

[1] F.S. Rocha, A.J. Gomes, C.N. Lunardi, S. Kaliaguine, and G.S. Patience, *Can J Chem Eng* **96**(12), 2512–2517 (2018).

[2] J.R. Lakowicz, editor , *Principles of Fluorescence Spectroscopy*, (Springer US, Boston, MA, 2006), pp. 27–61.

[3] T.M. Nordlund, *Topics in Fluorescence Spectroscopy*, edited by J.R. Lakowicz, (Kluwer Academic Publishers, Boston, 2002), pp. 183–260.

[4] G. Fleming, J. Morris, and H. Robinson, *Aust. J. Chem.* **30**(11), 2337 (1977).

[5] J.R. Lakowicz, *Principles of Fluorescence Spectroscopy*, (Springer US, Boston, MA, 1983), pp. 217–255.

[6] M.L. Horng, J.A. Gardecki, A. Papazyan, and M. Maroncelli, *J. Phys. Chem.* **99**(48), 17311–17337 (1995).

[7] W.H. Thompson, *Annu. Rev. Phys. Chem.* **62**, 599–619 (2011).

[8] J.R. Lakowicz, *Principles of Fluorescence Spectroscopy*, (Springer US, Boston, MA, 1999), pp. 291–319.

[9] M.-L. Horng, J.A. Gardecki, and M. Maroncelli, *J. Phys. Chem. A* **101**(6), 1030–1047 (1997).

[10] S. Koley, H. Kaur, and S. Ghosh, *Phys. Chem. Chem. Phys.* **16**(40), 22352–22363 (2014).

[11] S.K. Saha, P. Purkayastha, A.B. Das, and S. Dhara, *J. Photochem. and Photobio. A: Chemistry* **199**(2–3), 179–187 (2008).

[12] D. Kivelson, and P. Madden, *Mol. Phys.* **30**(6), 1749–1780 (1975).

[13] P.J.W. Debye, *The Collected Papers of Peter* (Interscience Pub., New York, 1954).

[14] K.S. Cole, and R.H. Cole, *J. Chem. Phys.* **9**(4), 341–351 (1941).

[15] D.W. Davidson, and R.H. Cole, *J. Chem. Phys.* **18**(10), 1417–1417 (1950).

[16] D.W. Davidson, and R.H. Cole, *J. Chem. Phys.* **19**(12), 1484–1490 (1951).

[17] S. Havriliak, and S. Negami, *Polymer* **8**, 161–210 (1967).

[18] P.R. Bevington, and D.K. Robinson, *Data Reduction and Error Analysis* (McGrawâ€“Hill, New York, 2003).

[19] R. Buchner, and J. Barthel, *Annu. Rep. Prog. Chem.*, Sect. C **97**(1), 349–382.

[20] A. Schönhals, and F. Kremer, *Broadband Dielectric Spectroscopy*, (Springer Berlin Heidelberg, Berlin, Heidelberg, 2003), pp. 59–98.

[21] D. Cialla-May, M. Schmitt, and J. Popp, *Physical Sciences Reviews* **4**(6), (2019).

[22] M.L. Frezzotti, F. Tecce, and A. Casagli, *Journal of Geochemical Exploration* **112**, 1–20 (2012).

Chapter 3

An Integrated Spectroscopic Approach to Structure-Dynamics-Conductivity Insights in Li-Ion Electrolytes

3.1 Introduction

Knowledge of electrolyte conductivity and speciation is pivotal in optimizing charging-discharging processes and identifying decomposition mechanisms in lithium-ion batteries (LIB). This is because chemical reactions in batteries generate undesired side products that reduce electrolyte stability and device performance.[1,2] Study of dispersion and transport mechanism of ions reveals the fundamental thermodynamics and microscopic interactions in electrolyte solutions.[3–6] It is known that both ion atmosphere relaxation and electrophoretic effects influence the net ionic conductivity.[7] The celebrated Debye-Huckel-Onsager (DHO) relation describing the concentration effects on ion conductivity was derived by considering macroscopic hydrodynamics and irreversible thermodynamics.[7] This theory studied the effects of the ion atmosphere relaxation and the electrophoretic effects on zero frequency macroscopic ion conductivities in solutions of strong electrolytes of symmetrically charged ions at very low concentrations ($<10^{-3}$ M) in highly polar solvents. Subsequent theoretical study, via employing the time correlation function formalism of transport quantities, not only pushed the upper bound of electrolyte concentration limit set by the DHO relation but provided also a microscopic framework for understanding conductivities of electrolytes containing asymmetrically charged ions.[8,9]

Interestingly, the DHO relation and its subsequent expansion assumed weak (and thus linear) coupling of the ions to the voltage applied across the electrodes. However, the ion conductivity

was found to increase with the frequency of the applied voltage because of finite timescales associated with the ion atmosphere relaxation and the host solvent dynamics (electrophoretic effects). This dependence of ionic conductivity on the frequency of the applied electric field is known as the Debye-Falkenhagen (DF) effect.[7,9,10] Molecular theories developed later predicted that the DF effect is operative in the low frequency regime only and further increase of the field frequency leads to a decrease of electrolyte conductivity.[10,11] Interestingly, when the electric potential gradient is very high (>20000 V/cm), the coupling between the ions and the voltage becomes too strong to be influenced by the ion atmosphere relaxation and the electrophoretic effects. This increases the electrolyte conductance at very high voltage and is known as the Wien effect.[7] All these studies, although provided a feedback loop between the experimental conductivity data and the predictive abilities of different theories, did not address the impact of solvation process and solvated state of the ions on electrolyte conductivity. The role of the solution structure on ion transport was also not addressed.

The above aspects assume even more importance in LIB where electrolytes are often used in relatively larger concentrations (~1 M) in moderately polar solvents (static dielectric constant, ε_s ~ 10).[12,13] At such large concentrations, particularly in moderately polar solvents, complex ionic species such as ion-pairs, triple ions etc. are expected to populate the solution structure. The presence of ion-pairs can influence the polar solvation response as the latter is dominated by molecular rotations.[14,15] In addition, solvent molecules pinned down by ions through strong Coulomb interaction may generate a slow component in the frequency dependent dielectric response[16–18] of the medium, providing a way to select between "solvent-carriage" and "hopping" modes[19] of ion transport in these solutions. Studies on effects of solvent dynamics on limiting ionic conductivity at infinite dilution already indicated that the ultrafast component of the solvation response can reduce the dielectric part of the total friction, while the hydrodynamic "solvent-berg" description could be realized in the dielectric friction model for ions with high charge-by-radius ratios.[20–23] However, similar study on battery electrolytes at different concentrations in moderately polar solvents has not been carried out yet and as a result, the inter-relationship between the experimental conductivity and solvent response has remained totally unexplored. In addition, the physical chemistry aspect of choosing a specific concentration of electrolyte for battery application

has not been investigated yet. We present here such a study by considering lithium bis(trifluoromethane)sulfonimide (LiTFSI) and triglyme (G3) as representative electrolyte and solvent respectively where temperature and electrolyte concentration dependent measurements have been performed to investigate solution structure and dynamics.

The above choices of the solvent and electrolyte are based on several factors. For example, LiX electrolytes in glyme solvents, that is, organic ethers with molecular formula $CH_3O[CH_2CH_2O]_nCH_3$ differing by ethereal chain length, exhibit an excellent alternative electrolyte-medium for next generation Li-metal cell, $Li-S$, $Li-O_2$ cells, superconductors and other energy storage devices.[24–27] Glyme-based electrolytes are preferred over carbonate-based electrolytes in industrial applications because of their reduced toxicity, improved environmental compatibility, a wider electrochemical window and cost effectiveness.[27,28] In addition, non-flammable cosolvents[29] and flame-retardant additives such as phosphorus containing compounds[30–32] and fluorinated species, which are commonly added to conventional organic solvents[31,33] for safety purposes, are not required when glyme solvents are employed. Moreover, highly concentrated glyme-based electrolytes are increasingly being chosen because of several promising features, such as, high ionic conductivity, high flash point, lower volatility and excellent solubility, all of which contribute to maximizing the efficient transport of active ions.[24,34] They have been described as either solvent-in-salt solutions or solvated ionic liquids (SILs),[35–37] presenting a fascinating dilemma that continues to be explored and understood. The electrolyte, LiTFSI, is chosen considering the fact that a much weaker electrostatic interaction between $[Li]^+$ and $[TFSI]^-$ (due to shape asymmetry and extended charge distribution over a relatively larger anion) may help higher dissociation of LiTFSI in the moderately polar solvent, triglyme, employed in the present study. This brings the microscopic solution structure in focus, which has been investigated by probing the interactions of $[Li]^+$ and $[TFSI]^-$ with triglyme molecules via Raman spectroscopic measurements. Notice here that the dipolar nature of the anion,[38] $[TFSI]^-$, can modify not only the dielectric properties of the electrolyte solution but also the total solvation response, influencing thereby the mobility of $[Li]^+$ through the solution. The interconnection between the solution's dielectric response and solvation dynamics has been investigated in order to examine the solvent-carriage mode of $[Li]^+$ transport in LiTFSI solutions of triglyme. Our

dielectric relaxation (DR) measurements in the frequency window, $0.2 \leq \nu/\mathrm{GHz} \leq 50$, can successfully probe the slow re-orientational relaxation of complex species involving $[TFSI]^-$along with the sluggish orientations of $[Li]^+$-pinned triglyme molecules. Analysis of measured DR parameters at different temperatures and electrolyte concentrations[13,39–41] then assists in exploring solution structure and understanding the coupling between the experimental relaxation rates and the medium viscosity. Moreover, the dependence of the conductivity on the solvent dynamics can be examined via electrolyte concentration dependent measurements of both DR and time-dependent fluorescence Stokes shift (TDFSS) experiments. Our streak camera-based measurement setup, providing an effective temporal resolution of ~500 fs, can capture sub-picosecond solvation response[22,42,43] and compliment the present DR measurements through accessing the solvent dynamics generated by the collective solvent intermolecular modes. Detection of the full solvent dynamics of these electrolyte solutions via broad-band DR experiments and TDFSS measurements, is necessary to understand why the maximum efficiency of lithium electrolyte batteries is connected to a particular $[Li]^+$ concentration. This is because the dynamical solvent response of electrolyte solutions often covers a broad timescale, ranging from sub-picosecond to a few nanoseconds,[44–46] and can influence both reactions that are associated with either no barrier (for example, electron transfer reaction) or moderate barriers (for example, cis-trans isomerization reactions). [47–50] This places the complete measurements of solvation response of the present system, triglyme/LiTFSI, in the proper perspective and underlines its importance for understanding the proper functioning of the electrolyte batteries.

3.2 Experimental Methods

3.2.1 Materials

Triethylene glycol dimethyl ether (triglyme, $CH_3O[CH_2CH_2O]_3CH_3$, 99%), bis(trifluoromethane)sulfonimide lithium salt (LiTFSI, ≥99%) and trans-2-[4-[(dimethylamino)styryl]benzothiazole (trans- DMASBT) were purchased from Sigma-Aldrich and used without further purification. LiTFSI was vacuum dried prior to experiment. The chemical structures of these materials are shown in **Scheme 3.1**.

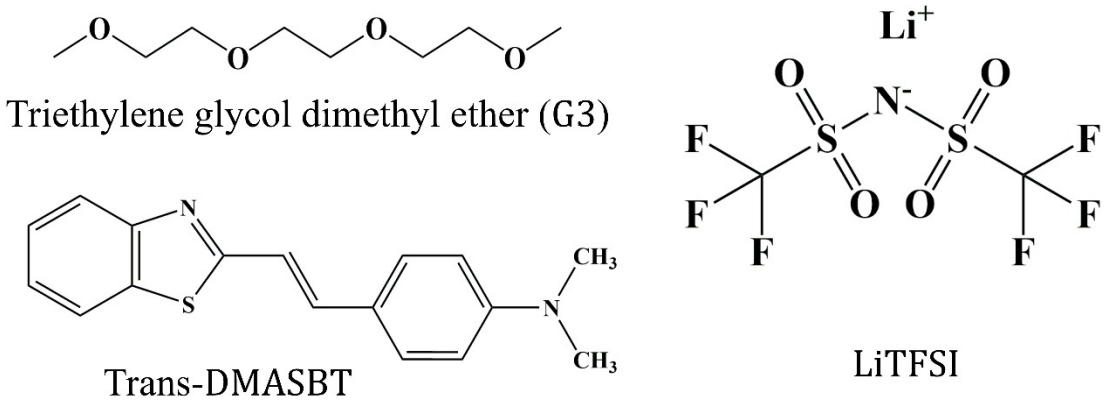

Scheme 3.1. Chemical structures of triethylene glycol dimethyl ether (triglyme or, G3), LiTFSI and trans-DMASBT.

3.2.2. Sample Preparation

Requisite amounts of LiTFSI were dissolved in triglyme (G3) to make the electrolyte solutions of varying G3/LiTFSI mole ratios and heated at ~ 323 K under continuous stirring condition. The transparent G3/LiTFSI solutions thus prepared were allowed to cool down gradually to room temperature before any experimental studies. UV-Vis absorption and fluorescence emission spectroscopic measurements were performed using ~ 2-3 mL electrolyte solution in a quartz cuvette preloaded with DMASBT ($\leq 10^{-5}$M). All temperature-dependent measurements included a 15 minutes equilibration period. Sample preparation, preservation and subsequent experiments were performed in a tightly humidity-controlled environment to prevent moisture contamination.

3.2.3 Refractive Index, Density and Viscosity Coefficients Measurements

Temperature dependent refractive indices (n), densities (ρ) and viscosity coefficients (η) were recorded respectively by using an automated temperature-controlled refractometer (RUDOLPH, J357), an automated temperature-controlled density-sound velocity analyzer (Anton Paar, model DSA 5000) and an automated micro-viscometer (AMVn, Anton Paar), respectively.

Measured ρ and η values are provided in **Table 3.B.1** (Appendix 3.B), while refractive indices (n values) are summarized in **Table 3.1**.

3.2.4 Conductivity Measurements

Conductivity of the electrolyte solutions were measured by a bench-top multi-parameter electrochemical meter (SESHIN BIOTECH, Model: ECM − 610). Experimentally measured conductivity values are provided in **Table 3.B.2** (Appendix 3.B).

3.2.5 Differential Scanning Calorimetry (DSC) Experiments

Differential scanning calorimetric measurements (TA Instruments Q2000) were performed to estimate the respective glass transition temperatures of the samples studied. DSC thermograms were recorded in the temperature range 113-353 K with heat flow rate at 5 K/min under a nitrogen atmosphere. In order to minimize evaporation during the measurements, the solutions were hermetically sealed in an aluminum pan (40 µl, TA Tzero). The DSC thermograms and the values of T_g of all electrolyte solutions under study are shown in **Fig. 3.A.1** and **Table 3.B.2** (Appendix 3.A and Appendix 3.B), respectively.

3.2.6 Raman, DR and TDFSS Experiments

The data collection and analysis protocols for Raman spectroscopy, dielectric relaxation (DR) dynamics, steady-state spectroscopy, and time-dependent fluorescence Stokes shift (TDFSS) measurements are detailed in Chapter 2. We now proceed directly to the presentation and discussion of the results.

3.3 Results and Discussion

3.3.1 Conductivity, Viscosity and Glass Transition Temperature: Electrolyte Concentration and Temperature Dependences

The temperature and electrolyte concentration dependent conductivities (σ) and viscosities (η) of G3/LiTFSI solutions are shown in the upper and middle panels of **Fig. 3.1**, whereas LiTFSI concentration dependence of the measured glass transition temperature (T_g) is presented in the lower panel. Notice that σ increases with temperature (because of higher dissociation) at all the concentrations studied, although a nonmonotonic LiTFSI concentration dependence of σ with a peak value at 1 M has been observed. Viscosities (η), in contrast, decrease with temperature and increase with concentration with no irregular concentration dependence. A closer examination of the concentration dependent σ and η values, however, reveal that the solution conductivity decreases by a factor of ~ 4 – 6 upon increasing LiTFSI concentration from ~0.5 M to 3.2 M in the temperature range 298 – 328 K, while the solution viscosity increases by a factor of ~10 – 30! Interestingly, the effects of temperature on conductivity and viscosity at a given electrolyte concentration is very similar and is limited to a factor of ~2 only. The later observation clearly suggest that the electrolyte concentration induced breakdown of the inverse relationship between the solution conductivity and viscosity is probably arising from the difference in solution structure at different LiTFSI concentrations because of formation of complex ionic species, such as, solvent-assisted and solvent-separated ion pairs, triple ions and other higher order ionic species. This means that the hydrodynamic description of diffusion-viscosity relationship originating from the consideration of a large spherical body moving in a solvent continuum is invalid because of the inhomogeneous solution structure. The impact of inhomogeneity may be addressed within the hydrodynamic framework, as was done previously for solute rotation[51] by incorporating the LiTFSI concentration dependent solvent packing around the moving ion. In another approach, this partial decoupling between conductivity and viscosity may be thought of arising from non-Brownian movements, such as, ion jumps.[52–54] The issue of ion jumps in solutions of battery electrolytes has been discussed at length previously by several authors[55,56] and therefore, these results may also be explained in terms of non-Gaussian large length scale jump displacements of one or both of the ions.

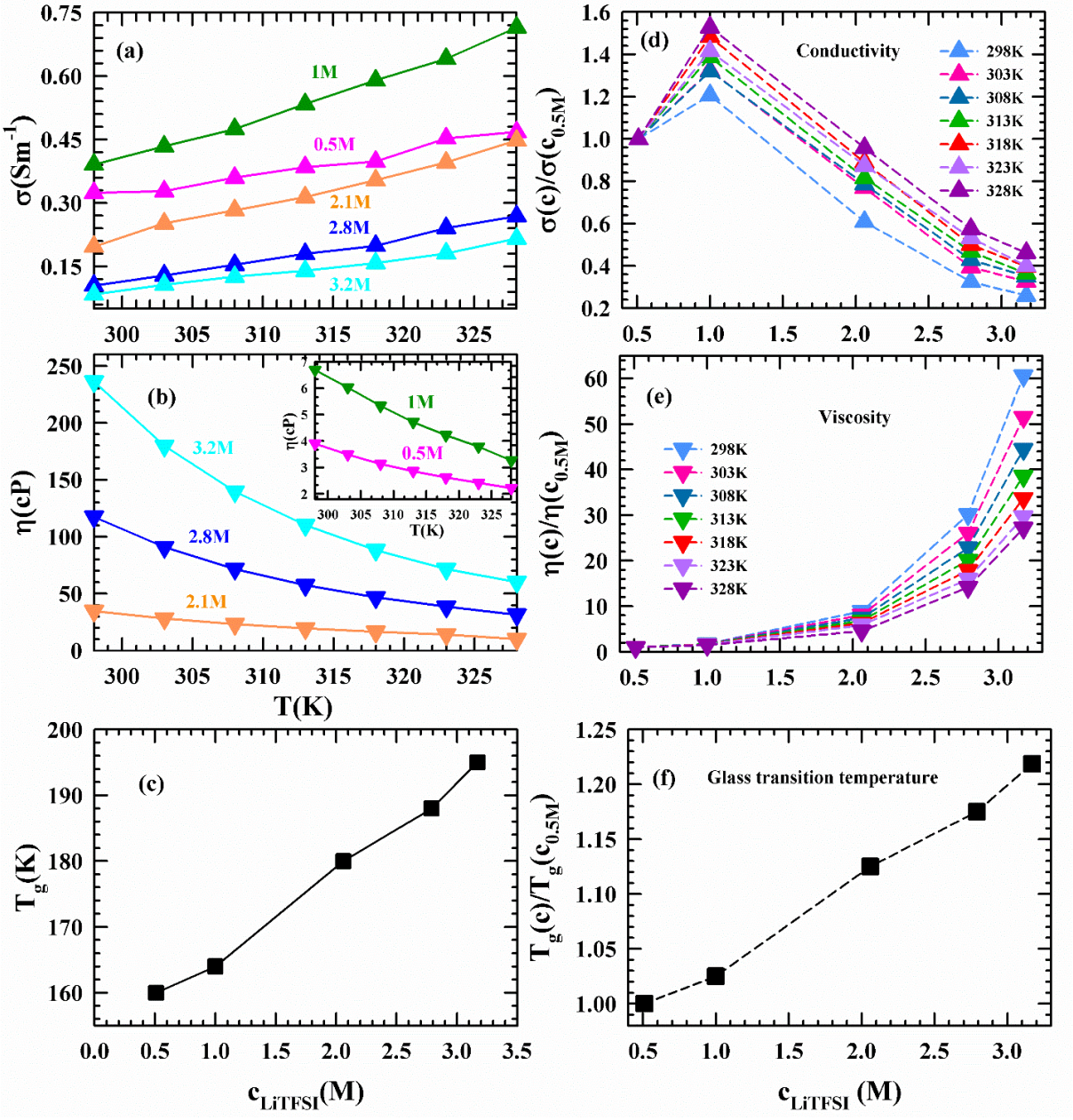

FIG. 3.1. Experimental temperature dependent ionic conductivities,σ, (a), viscosities (η) with lower concentration data in the inset (b), and the concentration dependent glass transition temperatures (T_g) for G3/LiTFSI electrolyte solutions are presented. The scaled conductivity, viscosity and glass transition temperatures with respect to the corresponding values at the lowest concentration of LiTFSI (0.5 M) are shown as a function of LiTFSI concentration respectively in the right panels, (d), (e) and (f). Solid and dashed lines are used for eye-guidance.

3.3.2 Raman Spectroscopic Analysis

The change in the collective polarizability is what critically dictates the Raman spectroscopic signal and makes Raman spectroscopy useful in qualitatively understanding solution structure.[57] We have focused on the LiTFSI breathing mode (700-800 cm^{-1}) which corresponds to the coordination state of LiTFSI anions[58] and performed the Raman measurements accordingly. Subsequently, the baseline-corrected spectra were fitted to Voigt function and deconvoluted in order to examine the possible presence of multiple species in the solution.[58–62]

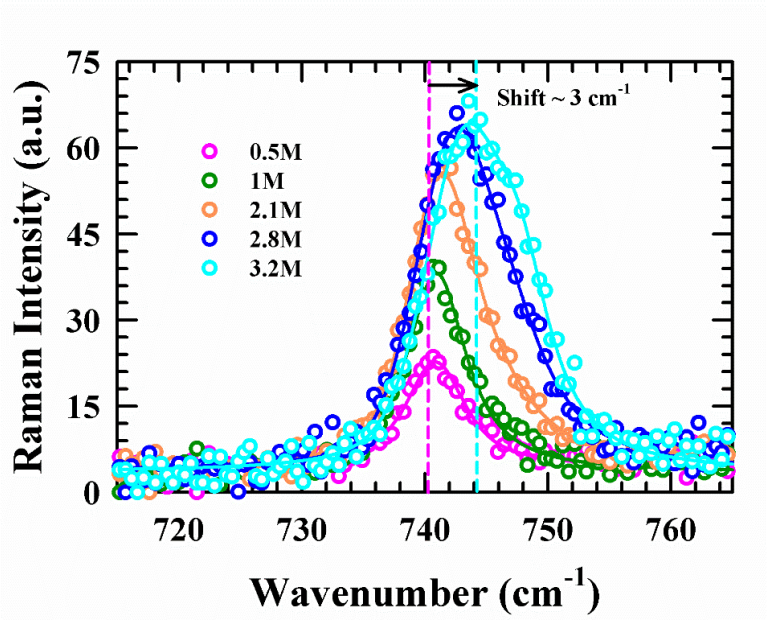

FIG. 3.2. LiTFSI concentration dependence of the Raman spectral features (shift and broadening) in G3/LiTFSI solutions at 298 K. Solid lines through the color-coded spectral data points represent the fits, obtained by using the Voigt function.

Fig. 3.2 displays the LiTFSI concentration dependent Raman spectra (700 - 800 cm^{-1}), which demonstrates not only changes in the relative intensity but also shift in the spectral peak position. These spectra were then subjected to deconvolution and the deconvoluted spectra are shown in **Fig. 3.3**. Notice here that the deconvoluted spectra at concentrations lower than 1 M are not shown here because the measured spectra at those two lower concentrations could not be resolved into

two separate bands. **Table 3.B.3** (Appendix 3.B) summarizes the spectral peak positions, band areas and the relative contributions of the deconvoluted spectral bands. The blue shift in the spectral peak positions (small but not negligible), and the increase in intensity upon addition of LiTFSI clearly indicates successive changes in the local environment around TFSI anions. Note that the single band located at ~740 cm^{-1} at lower concentrations, 0.5 M and 1 M, develops into a doublet at higher concentrations with band peaks appearing at 740-743 cm^{-1} and 746 -748 cm^{-1}.

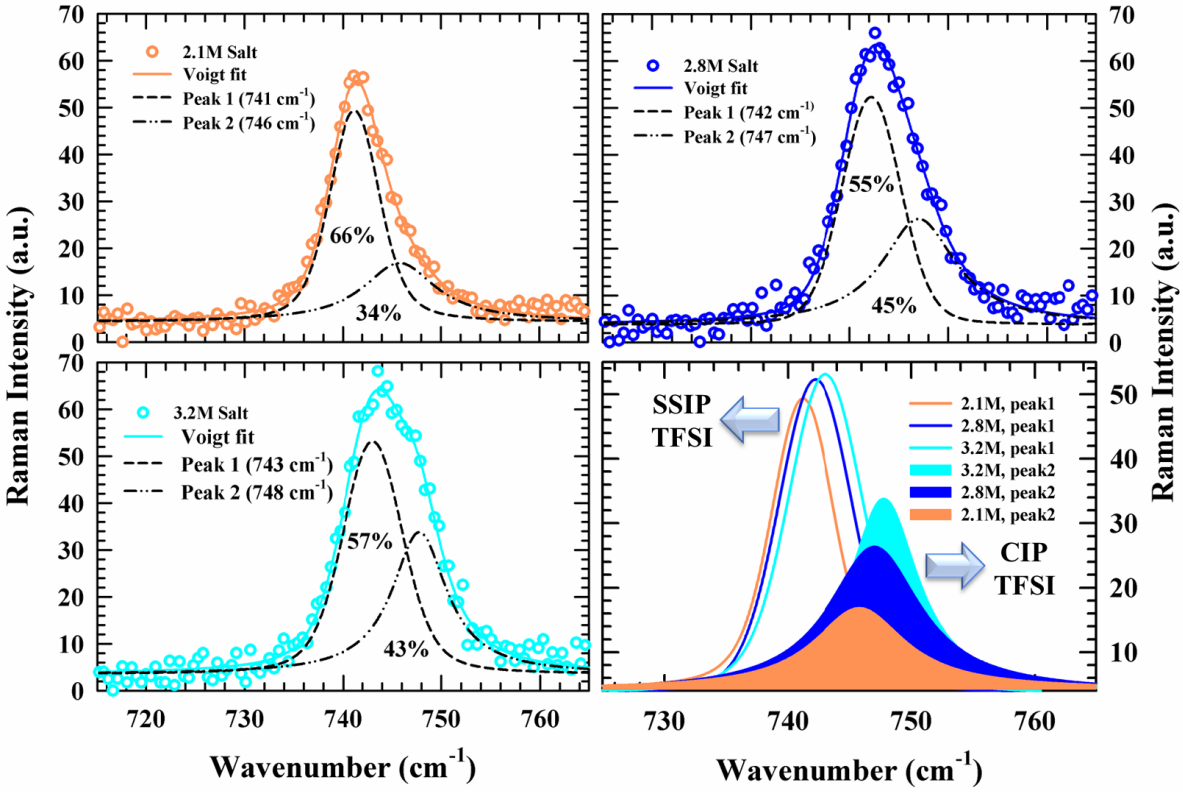

FIG. 3.3. Fitted curves (by using Voigt function) through Raman spectral data points and their deconvolutions at three different LiTFSI concentrations: 2.1 M (upper left), 2.8 M (upper right), 3.2 M (lower left) and the relative population of each deconvoluted spectrum (lower right). Solid lines are cumulative fits, whereas the dashed and the dash-dot-dot lines represent the deconvoluted bands of each spectrum. All the presentations are color-coded.

Interestingly, the resolved two bands appearing at ~2.1 M undergoes modification upon further addition of LiTFSI. Specifically, the band with peak at ~746 cm^{-1} grows up at the expense of the other, suggesting concentration-induced alteration of the ionic species populations (for example, contact ion pairs and solvent separated ion pairs etc.) in the solution. This is more clearly shown in right-lower panel of **Fig. 3.3**. It is already reported[63,64] that the band with peak at 739-741 cm^{-1} corresponds to solvent separated ion pair (SSIP, $Li^+ - G3 - TFSI^-$) and the band with peak at 744-747 cm^{-1} to the contact ion pair (CIP, $Li^+ - TFSI^-$). Moreover, another band with peak at 747-750 cm^{-1} was assigned to aggregated ion pair (AGGIP, $(Li^+)_n (TFSI^-)_m$).[63,64] Therefore, it is likely that our deconvoluted Raman band with peak at 740-743 cm^{-1} derives contributions from both SSIP and CIP, and the band with peak at 746 - 748 cm^{-1} corresponds to the presence of both CIP and AGGIP. The changes in areas under these two bands with concentration therefore simply indicate the alteration of the relative populations of these complex ionic species. The fact that the Raman spectra collected at 0.5 M and 1 M did not suggest any presence of AGGIP is probably because of high solvent-to-electrolyte ratio; that is, 10:1 at 0.5 M and 5:1 at 1 M. The presence of sufficient number of G3 molecules per LiTFSI molecule at these two concentrations might have inhibited the formation of AGGIP. At higher concentrations, for example, at 2.8 M and 3.2 M, these ratios are 1:0.8 and 1:1, respectively, which readily support the formation of AGGIP at these concentrations. As these complex ionic species (CIP, SSIP and AGGIP) are expected to influence the overall polarity and dynamics of electrolyte solutions, dielectric relaxation measurements, described next, may provide indirect evidence regarding their presence in these media.

3.3.3 Dielectric Relaxation Measurements

3.3.3.1 LiTFSI Concentration and Temperature Dependence

Fig. 3.4 (a) presents real (ε') and imaginary (ε'') components of the complex dielectric spectra of G3/LiTFSI solutions at a few representative LiTFSI concentrations and those for the neat G3 at 298 K. Notice that the DR spectra for electrolyte solutions shown here are not conductivity corrected spectra. The corresponding conductivity-corrected spectra along with multi-Debye fits through them are shown in **Fig. 3.A.3** (Appendix 3.A), while the temperature dependent DR spectra at each of the LiTFSI concentrations considered are presented in **Fig. 3.A.4** and **Fig. 3.A.5**

(Appendix 3.A). Parameters obtained from multi-Debye fits to the conductivity corrected spectra are summarized in **Table 3.1**. DR spectra shown in these figures (**Fig. 3.4** and **Fig. 3.A.3**, Appendix 3.A), and fit parameters in **Table 3.1** suggest that DR relaxation not only becomes slower upon addition of LiTFSI in neat G3 but also increases the static dielectric constant of the solution over that of the neat solvent. In our measurements, the static dielectric constant of G3 is found to be ~9, which is consistent to those reported earlier for monoglyme (ε_s ~6.4) and diglyme (ε_s ~7.8).[65] Note here that the biphasic DR relaxation with nearly equal amplitudes for neat G3 measured here is characterized by time constants, ~25 ps and ~6 ps. If the slower of these two time constants is employed in the Stokes-Einstein-Debye (SED) formula,[66] $V_{eff} = k_B T \tau_r / 3\eta$, we predict ~2.6 Å as radius for G3 molecule at T = 300 K where solvent viscosity, η = 2 cP.[67] However, this value of molecular radius is ~1.6 times smaller than that estimated from molar mass and density of neat G3 at the same temperature. This suggests that the effective volume involved in DR is not that of an entire G3 molecule but a part of it. Interestingly, earlier DR measurements of crown-ethers assigned the slower time constant to the cooperative segmental motion of ether group (-C-O-C-) and the faster one to the 'crankshaft motion' of free -C-O-C- group.[68]

We may therefore attribute the slower of the biphasic DR response measured for neat G3 to the cooperative segmental motion of the ether group and the faster component to the crankshaft motion. Addition of electrolyte is expected to significantly slow down this segmental motion mainly through the interaction between the small-sized cation, Li^+, and the oxygen atom of the ether group. The emergence of a new and much slower component with a timescale in the range of ~150 – 350 ps in the measured DR probably reflects such an ion-solvent interactions.

LiTFSI concentration dependent time constants and amplitudes obtained from the measured DR relaxations at 298 K are shown in **Fig. 3.5 (a)**. A quick and general observation is that both the DR time constants (τ_1 and τ_2) increase with LiTFSI concentration, although the associated amplitudes (a_1 and a_2) show a mutually opposite electrolyte concentration dependence. The value of the fastest time constant (τ_3) remains between 6-7 ps at all the electrolyte concentrations studied over the temperature range of 298–328 K. This insensitivity of τ_3 to LiTFSI concentration and

temperature highlights the inability of the present measurement set-up to detect medium polarization fluctuations at frequencies beyond 50 GHz.

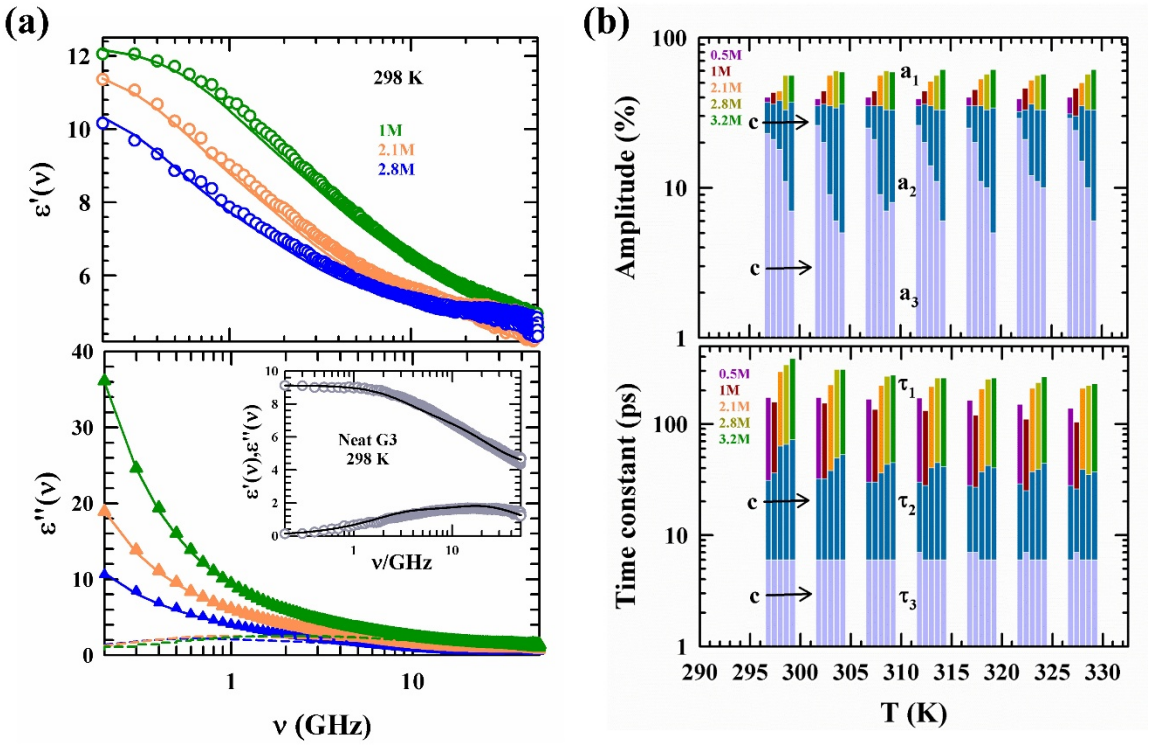

FIG. 3.4. (a) Frequency dependent real (ε') and imaginary (ε'') components of the complex dielectric spectra recorded for G3/LiTFSI electrolyte solutions at 298 K for a few representative concentrations. Experimental data points are shown as symbols and solid lines passing through them denote 3-Debye fits. Note that the dashed lines in the lower panel represent the conductivity-corrected fits through the experimental data points. All representations are color-coded.

(b) Change in amplitudes (a_1, a_2, a_3) and DR individual timescales (τ_1, τ_2, τ_3) of G3/LiTFSI electrolyte at different temperatures ranging from 298-328 K. From left to right, electrolyte concentration is increasing at each temperature as indicated by arrows. Individual concentrations are color-coded at the top of each bar.

Table 3.1. Multi-Debye fit parameters for experimental DR spectra for neat G3 and G3/LiTFSI electrolyte solutions. The values in parenthesis denote the corresponding amplitudes in percentage.

T/K	ε_s	$\Delta\varepsilon_1$	τ_1 /ps	$\Delta\varepsilon_2$	τ_2 /ps	$\Delta\varepsilon_3$	τ_3 /ps	ε_∞	n^2	$\varepsilon_\infty - n^2$	$<\tau_{DR}>$ /ps
Neat G3											
298	8.7	-	-	2.2 (46)	29	2.6 (54)	6	4	2.025	2	16
303	8.2	-	-	2.0 (44)	26	2.6 (56)	6	3.6	2.023	1.6	15
308	8.6	-	-	1.9 (43)	26	2.5 (57)	6	4.2	2.017	2.2	15
313	8.1	-	-	1.6 (36)	25	2.8 (64)	6	3.8	2.013	1.8	13
318	8.3	-	-	1.4 (33)	27	2.9 (67)	6	4	2.011	2	13
323	8.3	-	-	1.4 (33)	24	2.8 (67)	6	4	2.007	2	12
328	8.1	-	-	1.4 (33)	24	2.8 (67)	6	3.9	2.001	1.9	12
0.5 M G3/LiTFSI											
298	12.5	3.1 (40)	173	2.9 (37)	31	1.8 (23)	6	4.9	2.026	2.9	82
303	12.2	3.0 (39)	172	2.8 (35)	32	2.0 (26)	6	4.4	2.024	2.4	80
308	12.3	3.2 (40)	166	2.8 (35)	30	2.0 (25)	6	4.4	2.021	2.4	78
313	12.3	3.2 (39)	170	2.9 (35)	30	2.1 (26)	7	4.2	2.016	2.2	79
318	12.3	3.2 (40)	162	2.9 (35)	28	2.0 (25)	7	4.2	2.013	2.2	76
323	12.2	3.2 (39)	149	2.6 (32)	29	2.3 (29)	6	4.3	2.010	2.3	70
328	12.2	3.1 (40)	137	2.4 (31)	28	2.2 (29)	6	4.4	2.006	2.4	66
1 M G3/LiTFSI											
298	12.3	3.4 (43)	156	2.8 (36)	36	1.6 (21)	6	4.5	2.028	2.5	81
303	12.5	3.6 (44)	153	2.9 (36)	32	1.7 (20)	6	4.4	2.024	2.4	79
308	12.3	3.5 (44)	135	2.8 (35)	30	1.7 (21)	6	4.3	2.023	2.3	71
313	12.6	3.6 (44)	132	2.9 (36)	28	1.7 (20)	6	4.4	2.019	2.4	69
318	12.6	3.7 (45)	119	2.9 (35)	27	1.7 (20)	7	4.4	2.014	2.4	64
323	12.6	3.7 (46)	110	2.7 (33)	25	1.7 (21)	7	4.6	2.011	2.6	60
328	12.8	3.7 (46)	103	2.5 (30)	26	1.9 (24)	7	4.8	2.008	2.8	57
2.1 M G3/LiTFSI											
298	11.8	3.4 (44)	292	2.9 (38)	63	1.4 (18)	6	4.2	1.997	2.2	154
303	13.5	4.6 (56)	224	2.9 (35)	38	0.7 (9)	6	5.2	1.994	3.2	140
308	13.7	4.8 (56)	221	3.0 (35)	36	0.8 (9)	6	5	1.992	3	136
313	13.2	4.4 (51)	216	3.0 (35)	40	1.2 (14)	6	4.6	1.990	2.6	125
318	13.8	4.7 (53)	205	3.1 (35)	37	1.0 (11)	6	5	1.987	3	123
323	14.2	4.8 (52)	209	3.3 (36)	37	1.1 (12)	6	5	1.984	3	123
328	14.1	4.7 (50)	208	3.3 (35)	39	1.4 (15)	6	4.7	1.980	2.7	119
2.8 M G3/LiTFSI											
298	10.9	3.5 (56)	338	2.1 (33)	65	0.7 (11)	6	4.6	1.976	2.6	210
303	12.2	4.2 (60)	307	2.4 (34)	49	0.4 (6)	6	5.2	1.973	3.2	201
308	12.2	4.3 (60)	268	2.4 (33)	43	0.5 (7)	6	5	1.971	3	175
313	12.1	4.2 (56)	259	2.5 (33)	45	0.8 (11)	6	4.6	1.969	2.6	161
318	12.3	4.4 (57)	251	2.6 (33)	42	0.7 (10)	6	4.6	1.968	2.6	158
323	12.8	4.6 (56)	234	2.7 (33)	39	0.9 (11)	6	4.6	1.966	2.6	145
328	13.1	4.9 (57)	222	2.8 (33)	35	0.9 (10)	6	4.5	1.965	2.5	139
3.2 M G3/LiTFSI											
298	10.3	3.0 (56)	384	1.9 (37)	72	0.4 (7)	6	5	1.963	3	244
303	11.0	3.4 (59)	310	2.1 (36)	53	0.3 (5)	6	5.2	1.962	3.2	201
308	10.8	3.6 (59)	272	2.0 (33)	45	0.5 (8)	6	4.6	1.960	2.6	176
313	11.3	3.9 (61)	258	2.1 (33)	41	0.4 (6)	6	4.9	1.957	2.9	171
318	11.7	4.1 (61)	259	2.2 (34)	40	0.4 (5)	6	5.1	1.955	3.1	172
323	11.7	4.0 (57)	265	2.3 (33)	44	0.7 (10)	6	4.6	1.954	2.6	166
328	12.4	4.4 (61)	229	2.4 (33)	37	0.4 (6)	6	5.2	1.952	3.2	153

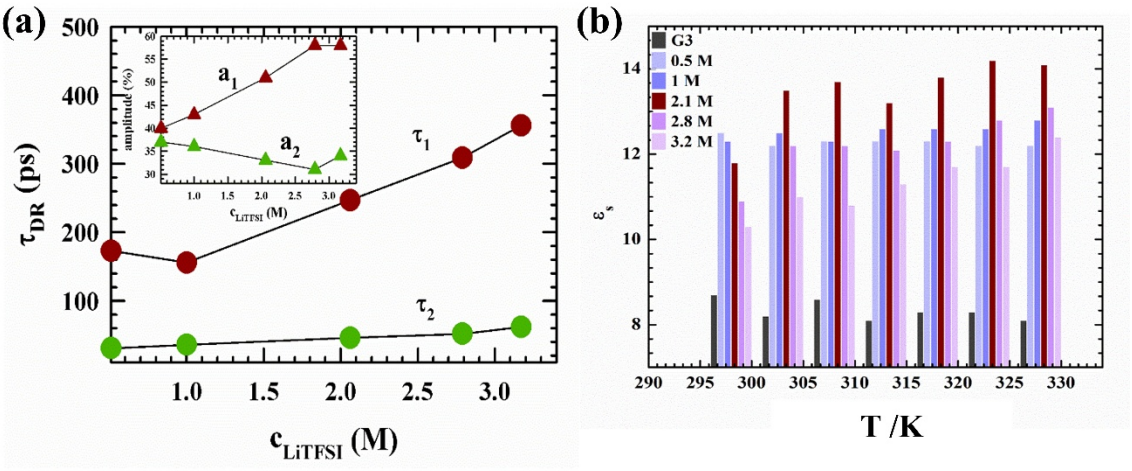

FIG. 3.5. (a) LiTFSI concentration dependence of τ_1^{DR} and τ_2^{DR} at 298 K. The corresponding amplitudes are shown in the inset. Different colors are used to denote different DR time constants and amplitudes.

(b) Temperature dependent static dielectric constant (ε_s) in G3/LiTFSI electrolyte solutions at various concentrations of LiTFSI along with neat solvent. All presentations are color-coded.

The decrease of a_2, is, however, overcompensated by the increase of τ_2 and therefore the amplitude weighted contribution to the average DR time constant increases with increasing electrolyte concentration. The increase of DR time constants may, at a first glance, appear as a viscosity effect, although a closer inspection of the viscosity data (**Table 3.B.1**, Appendix 3.B) and the subsequent comparison between the DR time constants and viscosities at the lowest and the highest LiTFSI concentrations suggest substantial viscosity decoupling of DR. This was also found earlier during the analysis of viscosity-conductivity relationship for these solutions. The concentration-induced increase of a_1 accompanies concomitant decrease of the other two amplitudes, a_2 and a_3. This may suggest that the slowest component grows at the cost of the other two, although the total increase of a_1 is ~45% for increasing the LiTFSI concentration from 0.5 M to 3.2 M, while the reduction of a_2 and a_3, on the other hand, is ~20% and ~70%, respectively. Interestingly, the DR amplitudes and time constants show a weak temperature dependence in the range considered (298-328 K), indicating a good thermal stability of the complex electrolyte-solvent species formed in these

solutions. Another interesting aspect to notice is that the slowest time constant (τ_1) for 1 M solution is the shortest among all the LiTFSI concentrations studied throughout the temperature range (298-328 K), although the corresponding amplitude follows a regular concentration dependence. This is shown in **Fig. 3.4 (b)**. This has an important consequence as it induces a non-linear concentration dependence to the DR dynamics of these electrolyte solutions, which in turn may influence the concentration dependence of the solution conductivity.

We now conjecture on the origin of the slowest DR timescale measured in our experiments. The slowest of the three timescales (~ 150 - 380 ps) is probably arising from the re-orientational relaxations of the SSIP and CIP formed in these solutions. The collective segmental motion of the free (not complexed with Li^+) ether group in more viscous media (because of the presence of electrolyte) may have generated the other relatively faster DR timescale (~30 - 70 ps). The contribution from AGGIP is probably hidden in the amplitude and the slowest time constant of the measured DR. This is because the increase of amplitude and timescale of this slowest component with LiTFSI concentration across the temperature studied accompanies a simultaneous decrease of the amplitudes of the other two components. Another interesting point to note in these DR data is that the value of static dielectric constant (ε_s) increases over that of neat G3 upon addition of LiTFSI. This is shown in **Fig. 3.5 (b)** which indicates a ~50-80% increase of the solution dielectric constant across the temperature range studied. Such a dielectric behavior of electrolyte solutions of low polar solvents has also been reported earlier.[69]

3.3.3.2 Correlation to Ion Conductivity with DR Dynamics

Next, the coupling of the medium viscosity to the measured average DR time and solution conductivity is explored in order to gain further information on LiTFSI concentration induced changes in solution structure and dynamics. **Fig. 3.6** demonstrates this where temperature-dependent average DR times ($\langle\tau_{DR}\rangle$) and conductivity (σ) at different electrolyte concentrations are shown as a function of temperature-reduced solution viscosity, (η/T), in a double logarithmic fashion. The different slopes of $\langle\tau_{DR}\rangle$ and σ with η/T have provided different values of the fraction power after fitting the data to the following equation, $A \propto (\eta/T)^{-p}$ where $A = \langle\tau_{DR}\rangle^{-1}$ or σ,

suggesting difference in viscosity coupling arising from different solution structure at each of the electrolyte concentrations studied. This is also reflected in the activation energies estimated via Arrhenius-type temperature dependence of the measured solution conductivity, viscosity and average DR time at different concentrations, shown in **Fig. 3.A.6** and in **Table 3.B.4** (Appendix 3.A and Appendix 3.B). Both $\langle\tau_{DR}\rangle$ and σ clearly depict a strong fractional viscosity dependence. Interestingly, however, the fraction power (p) shows a non-monotonic LiTFSI concentration dependence with the highest value for solution at ~1 M. Considering that σ and the $\langle\tau_{DR}\rangle$ at ~1 M are respectively the largest and the shortest, it is clear that σ in these solutions are regulated by the solvent dynamics and not by the macroscopic solution viscosity.

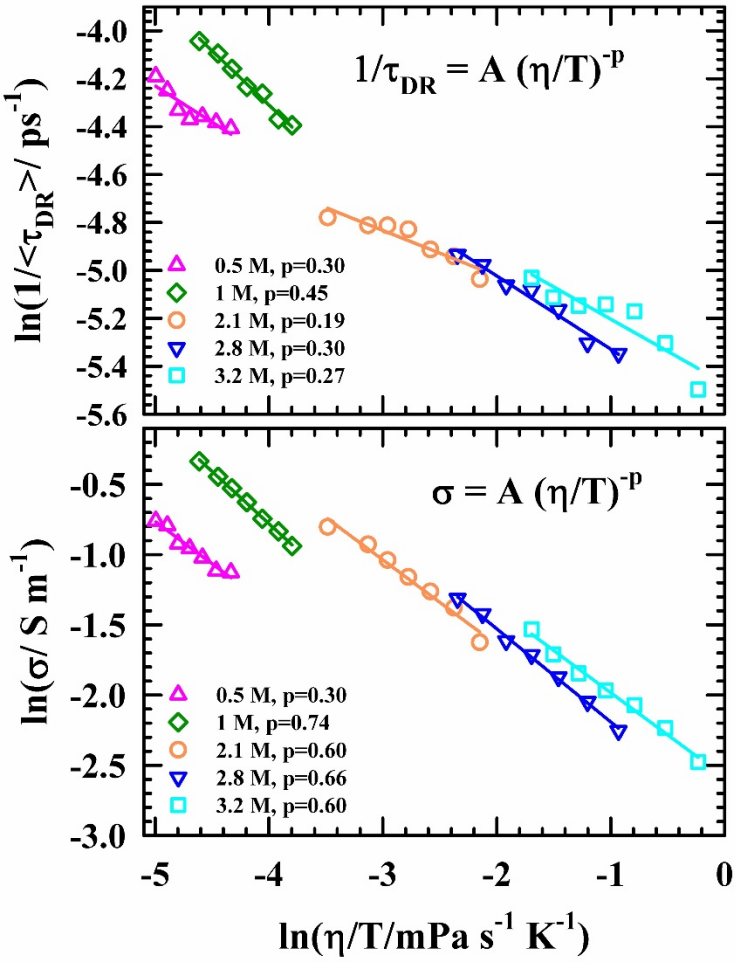

FIG. 3.6. Viscosity (η/T) dependence of the DR rate, $(1/\langle\tau_{DR}\rangle)$ and σ in G3/LiTFSI electrolyte solutions at different electrolyte concentrations are shown in log-log fashion. Solid lines through the measured data denote linear fits.

Next, we explore how the measured temperature dependent conductivities (σ) are correlated to the static dielectric constants (ε_s) and DR time constants of these electrolyte solutions. This is because the measured conductivities showed a clear non-linear electrolyte concentration dependence, while the DR measurements indicated LiTFSI concentration dependent changes in both solution ε_s and DR time constants. **Fig. 3.7** presents correlations of temperature dependent σ at different electrolyte concentrations to the corresponding several measured DR parameters, such as, ε_s, the average DR time constant ($\langle\tau_{DR}\rangle$), and the slower two (τ_1 and τ_2) of three time-constants. Notice in the left upper panel of this figure that the conductivities for solutions at 0.5 M and 1 M constitute a separate linear correlation with ε_s from that by the conductivities at other three higher concentrations. This is understandable if we consider that Raman spectral analysis did not suggest presence of AGGIP at these two relatively lower LiTFSI concentrations, while the same analysis for solutions at the other three concentrations indicated presence of, in addition to CIP and SSIP, AGGIP. This is a signature of ion mobilities being governed by different solution environments at these two different sets of electrolyte concentrations. Moreover, the conductivities at these two concentrations (0.5 M and 1 M) sharper changes with solution ε_s than at the other three higher concentrations. The plot of σ versus $\langle\tau_{DR}\rangle$, shown in upper right panel, suggests the following dependence, $\sigma \propto (\langle\tau_{DR}\rangle)^{-m}$. This dependence or correlation may be understood by recalling that average DR time or solvation time provides a measure of microscopic friction[70–72] and the inverse relationship between center-of-mass diffusion and microscopic friction (Stokes relation). Such a consideration motivates one to explore the dependencies of σ on the individual DR time constants (τ_1 and τ_2), and they are presented in lower panels of this figure. Notice in these correlations between conductivity and DR times that the value of the exponent (m) is the largest for the dependence of σ on the shorter of these three times, τ_2. This probably suggests that electrolyte conductivity is strongly influenced by the faster relaxation processes of the electrolyte solutions. Interestingly, this was also predicted earlier for limiting ionic conductivities in neat dipolar solvents.[15,21,23]

A relatively stronger dependence of σ on the faster of the two DR time constants, shown above, suggest a strong interconnection between the measured electrolyte conductivity and the solvation energy relaxation timescales in these electrolyte solutions. As the present DR measurements missed

a significant portion of the faster DR response because of the limited frequency window employed and this is reflected in $\varepsilon_\infty - n^2$ values summarized in **Table 3.1**, measurements of solvation energy relaxation via an ultrafast detection technique may be carried out to further examine this relationship. Because the initial fast part of the total polar solvation response is dictated by the fast nuclear and electronic parts of the medium polarization contained in the $\varepsilon_\infty - n^2$, the influence of this missing component in DR can be investigated through ultrafast measurements of solvation response. This aspect has been investigated in the next section where we have measured the ultrafast polar solvation response via streak camera detection of time dependent fluorescence spectral shifts of an external solute probe, DMASBT, dissolved in these electrolyte solutions.

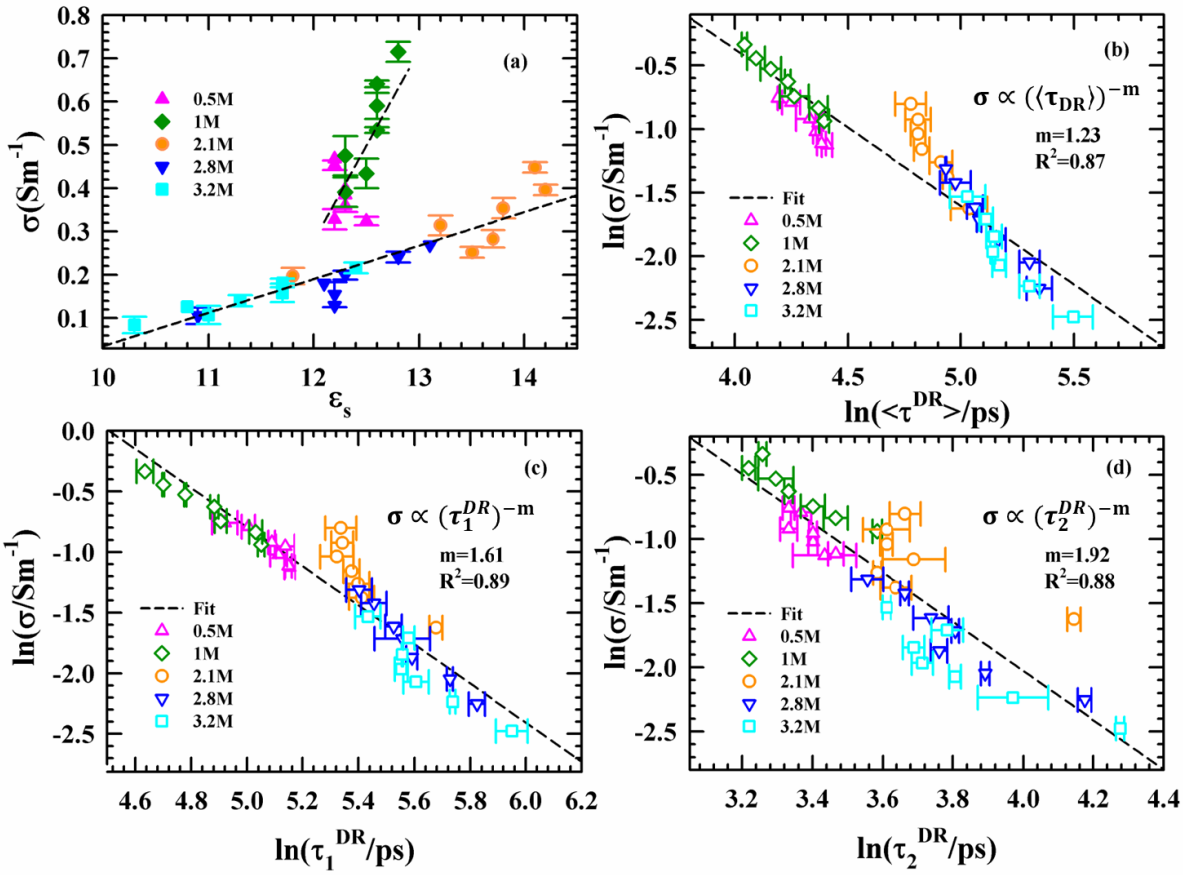

FIG. 3.7. Correlation between ionic conductivity (σ/S m^{-1}) and static dielectric constant (ε_s) (a), between ionic conductivity and average DR timescales (b), individual DR time-components, τ_1 (c), and τ_2 (d). Experimental data were collected in the temperature range, 298-328 K. Different concentrations of G3/LiTFSI electrolytes are color-coded.

3.3.4 Streak Camera Detection of Ultrafast Solution Dynamics: Correlation to Experimental Ion Conductivity

Fig. 3.A.8 (Appendix 3.A) shows two dimensional representations of streak camera images detected simultaneously in three dimensions (wavelength, time and intensity) for DMASBT in neat G3, and in G3/LiTFSI solutions at five different electrolyte concentrations. Notice here the horizontal axis of each of these images represents time, while the vertical axis denotes fluorescence emission wavelength. Therefore, the vertical slices correspond to wavelength dependent fluorescence intensity emission at a fixed time, while the horizontal slices represent time dependent fluorescence intensity at a fixed emission wavelength. This is shown in **Fig. 3.A.9**, (Appendix 3.A). These spectral movements are occurring in sub-100 ps timescale and well captured by the dissolved probe because the measured average lifetimes of DMASBT in these solutions were found in ~30-100 ps range (see **Table 3.B.6** and **Fig. 3.A.10**). A separate examination of horizontal slices at the blue and the red ends to the emission peak wavelengths reveals only decay at the blue wavelengths, and rise followed by decay at the red wavelengths (see **Fig. 3.A.10**, Appendix 3.A), respectively. This is a customary signature of the presence of dynamic Stokes shift in these systems.

Next, we present in **Fig. 3.8** the time resolved emission spectra (TRES) at two representatives LiTFSI concentrations (1 M and 3.2 M) with the corresponding steady state emission spectra of DMASBT. Note that the steady state emission spectra at these representative electrolyte concentrations are redshifted with respect to the time-resolved emission spectra at the longest time (that is, emission spectra at $t = \infty$). This indicates that the faster component of the total polar solvation energy relaxation has been predominantly captured by the present measurements, while the remaining slow solvation component, arising from slow diffusive rotations and translations of the medium particles, has remained inaccessible because of the relatively shorter lifetime of the probe employed. However, this slow part of the solvent dynamics has already been captured and characterized by our DR experiments and therefore was not in our focus. Subsequently, normalized solvation response functions, $S(t)$, obtained from this time dependent progress of the emission spectral shifts, are shown in **Fig. 3.A.10 (c)** (Appendix 3.A) and fitted to bi-exponential functions of time (fit parameters summarized in **Table 3.B.7**, Appendix 3.B).

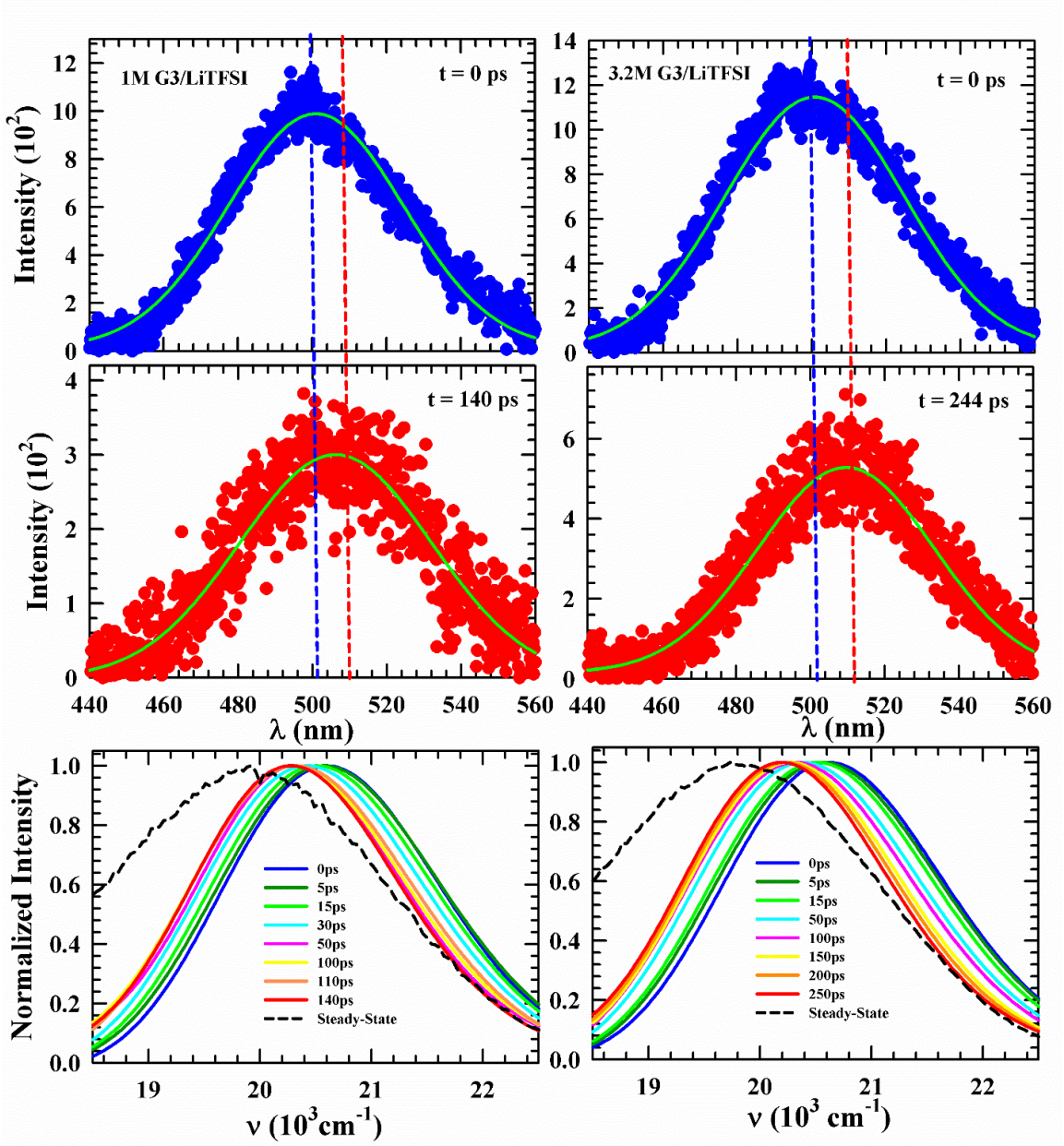

FIG. 3.8. Representative streak camera recorded time-resolved emission spectra (TRES) of DMASBT dissolved in G3/ LiTFSI electrolyte solutions at different time-intervals at ~298 K. Black dashed lines in each panel represent the corresponding steady-state emission spectra of DMASBT. Left and right panels show data at two representative electrolyte concentrations.

The average solvation time, $\langle\tau_s\rangle$, was then obtained from time integrating the measured S(t). **Fig. 3.A.10 (d)** (Appendix 3.A) compares the correlations between the measured $\langle\tau_s\rangle$ and $\langle\tau_{DR}\rangle$ obtained for these electrolyte solutions and those for neat solvents and reflects the validity of the interrelationship between solvation dynamics and DR, originally observed for neat solvents,[14] for these electrolyte solutions also.

Fig. 3.9 presents the dependence of the measured conductivity on the average solvation time for the electrolyte solutions studied here. Clearly, both these measured quantities are correlated to each other, and the interdependence can be described by the following relation, $\sigma \propto (\langle\tau_s\rangle)^{-m}$, with m ~1.5. This provides further support to the view that the conductivity, which is originating from the translational motion of the ions, is indeed influenced by the fast rotational motion of the dipolar species present in the system. This correlation between ion translation and solvent rotation is an interesting observation for electrolyte solutions at finite concentrations. In addition, this correlation explains why LiTFSI concentration should be ~1 M when used as battery electrolyte because of the largest conductivity and not-so-long average solvation time among the concentrations studied.

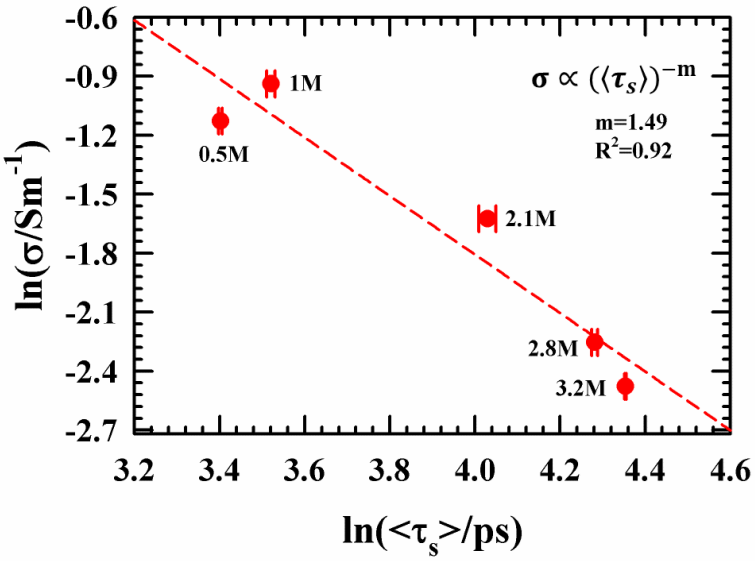

FIG. 3.9. Correlation between the measured average solvation time and the measured ionic conductivity of G3/LiTFSI electrolyte solutions at 298 K. Dashed lines represent fit through experimental data.

3.4 Summary

The correlation between experimental ion conductivity with solution polarization relaxation dynamics has been presented in G3/LiTFSI electrolyte medium by measuring DR and solvation response. Raman spectroscopic analysis reveals that solvent-shared and contact or aggregated ion pairs characterize the solutions at different LiTFSI concentrations considered. A strong correlation between the measured conductivities and relaxation timescales (associated with both DR and solvation response) has been found, which has subsequently been explained in terms of the intimate relationship of friction with both conductivity and relaxation timescales. In addition, fractional viscosity dependence has been registered for both solution viscosities and average DR times with the electrolyte solution at 1 M exhibiting the largest conductivity and shortest longtime component. Differential scanning calorimetry measurements indicated increase of glass transition temperature with LiTFSI concentration and suggested more fragility and larger participation of cooperativity in solution dynamics. An understanding of the intricate relationship that solution conductivity maintains with solution structures and dynamics is therefore required in designing new electrolytes possessing higher ionic conductivities but with modified capabilities of minimizing electrode and medium poisoning. Further experimental and simulation studies with a variety of electrolyte-solvent systems may be carried out for this purpose.

Appendix 3.A

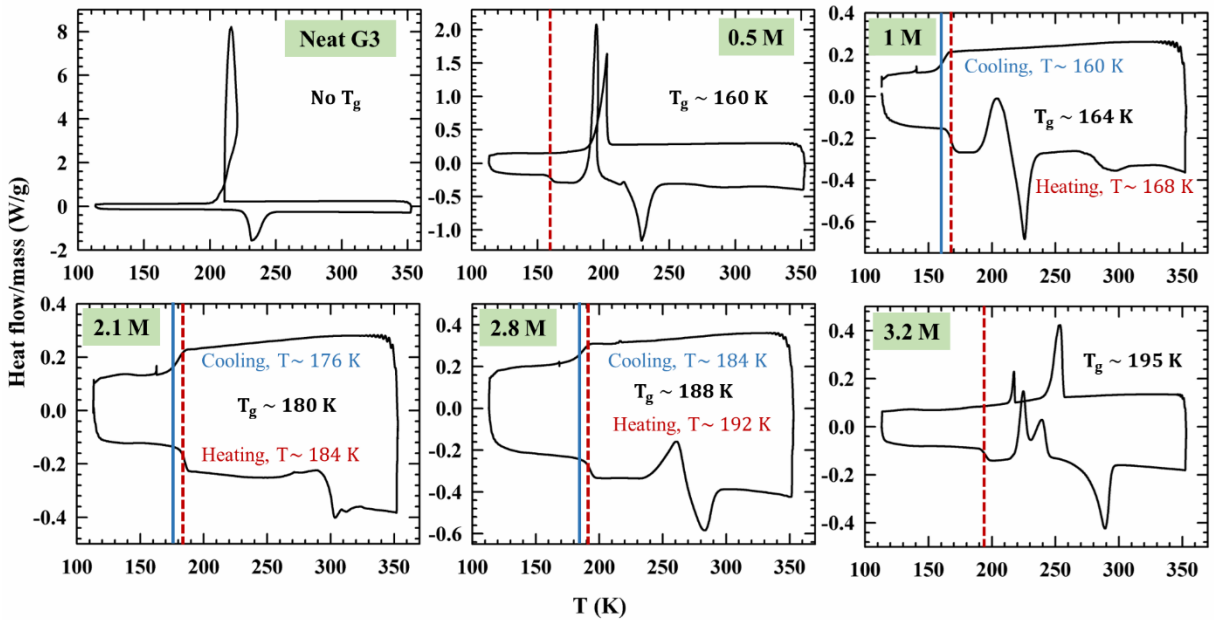

FIG. 3.A.1. Differential scanning calorimetric (DSC) scans of G3/ LiTFSI electrolyte solutions with different LiTFSI concentrations along with neat G3. Analyzed glass transition temperature (T_g) is presented in each plot.

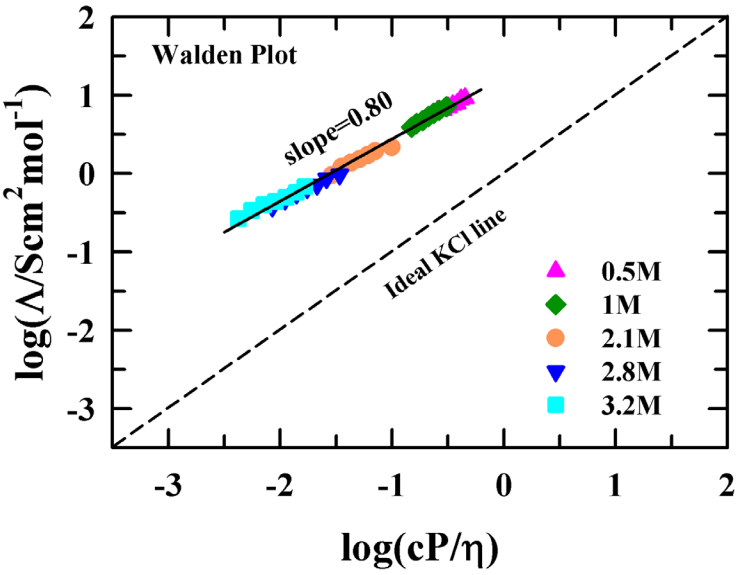

FIG. 3.A.2. Walden plot representing correlation between viscosity (η/ cP) and molar conductivity (Λ/S cm^2 mol^{-1}) in G3/ LiTFSI electrolyte solutions.

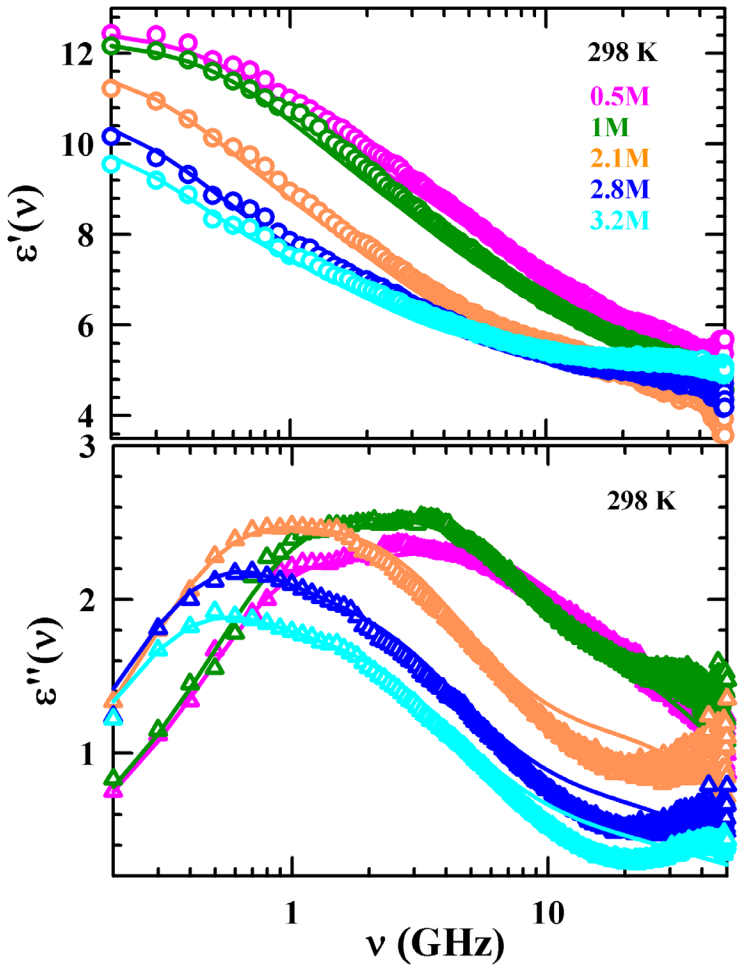

FIG. 3.A.3. Real ($\varepsilon'(\nu)$) and imaginary ($\varepsilon''(\nu)$) components of the complex dielectric spectra recorded for G3/ LiTFSI electrolyte solutions at 298 K. Experimental data points are shown as symbols and solid lines passing through them represent 3-Debye fits after conductivity correction.[73] All representations are color-coded. Note that fits to $\varepsilon''(\nu)$ at higher concentrations (2.1 M, 2.8 M and 3.2 M) of electrolytes are not able to properly describe the experimental data in the high frequency region. This may be due to conductivity dispersion.[10,11]

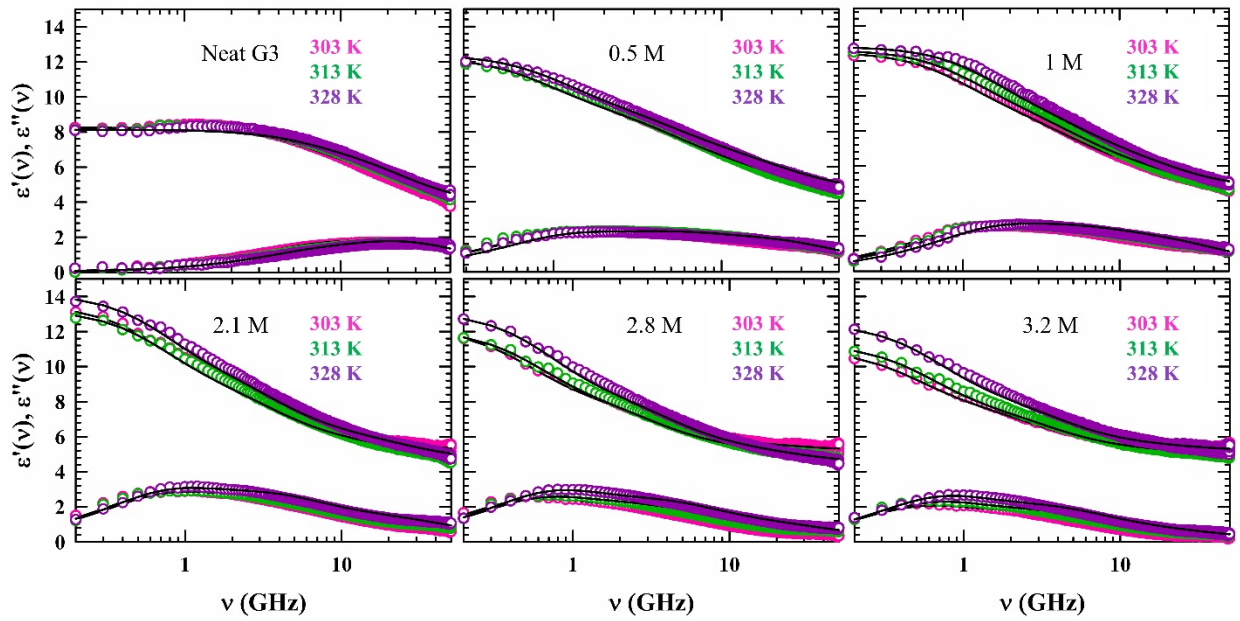

FIG. 3.A.4. Temperature-dependence of real ($\varepsilon'(\nu)$) and imaginary ($\varepsilon''(\nu)$) components of the complex dielectric spectra are shown at six different concentrations of G3/ LiTFSI electrolyte solutions. Experimental data points are shown as symbols and solid lines passing through them represent multi-Debye fits. Temperatures (303 K, 313 K, 328 K) are color-indicated.

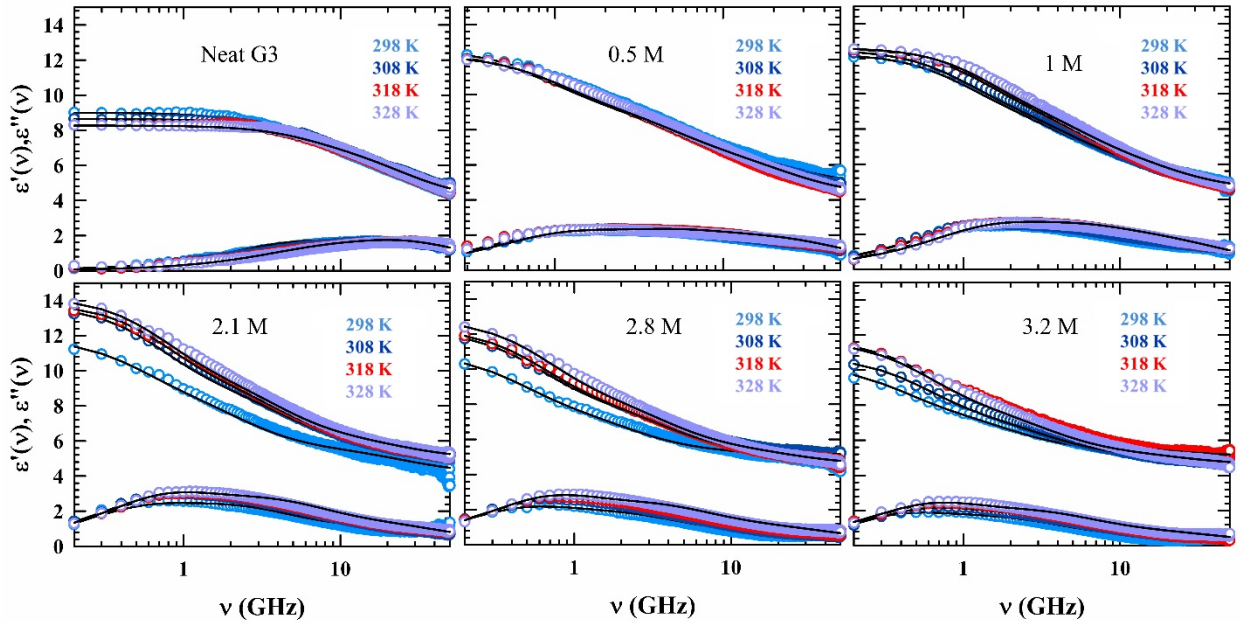

FIG. 3.A.5. Temperature-dependent real ($\varepsilon'(\nu)$) and imaginary ($\varepsilon''(\nu)$) components of the complex dielectric spectra are shown for six compositions of G3/ LiTFSI electrolyte solutions. Experimental data points are shown as symbols and solid lines passing through them represent multi-Debye fits. Four different temperatures (298 K, 308 K, 318 K and 328 K) are color indicated.

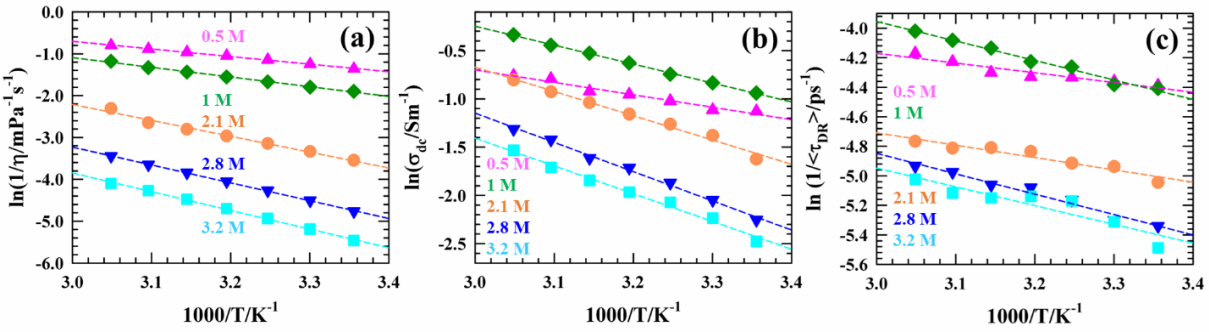

FIG. 3.A.6. Arrhenius-type temperature dependence of medium viscosity (a), dc conductivity (b) and average DR times (c) for G3/LiTFSI electrolyte solutions at various concentrations. Dashed lines passing through the data points represent linear fits. Different colors are utilized for different compositions.

Steady State UV-Visible Absorption & Fluorescence Emission Studies

Steady-state UV-Vis absorption and fluorescence emission spectra of DMASBT in G3/LiTFSI electrolyte solutions are presented in **Fig. 3.A.7** and the corresponding average peak frequencies and spectral widths (FWHM) are provided in **Table 3.B.5**. With successive increase of LiTFSI concentration, the absorption spectra are getting red-shifted of about ~300 cm^{-1} whereas emission spectra are practically unchanged. In comparison with neat solvent G3 it can be said that a stronger ion-dipole interaction plays an important role to be the absorption spectra red-shifted in presence of electrolyte whereas only dipole-dipole interaction is solely responsible for steady-state spectral features of DMASBT in G3. Note that the width of both absorption and fluorescence emission spectra does not undergo monotonous changes with increasing moles of LiTFSI in G3 implying that aggregation of ions and electrostatic interactions between ions and solvent molecules induced the probe molecules to feel the local environment of the system differently.

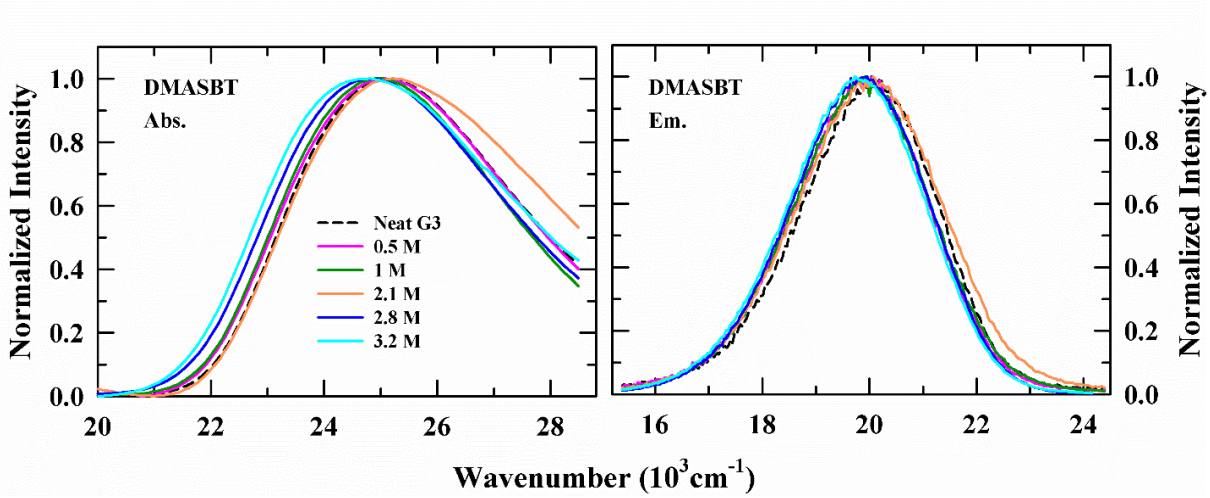

FIG. 3.A.7. Normalized absorption (left panel) and emission (right panel) spectra of DMASBT in G3/LiTFSI electrolyte solutions at different compositions at ~298 K. All concentrations of electrolyte solutions are color-coded.

Fluorescence Lifetime Measurements *via* Streak Camera

In our streak camera setup, the excitation source is a femtosecond laser pulse with a wavelength of 440 nm. Fluorescence is captured at a right angle to the excitation path, with the signal passing through a polarizer set at the magic angle (54.7°). This configuration allows for the recording of fluorescence lifetime decay. All the measurements on streak camera have been carried out by taking streak images through the spectrograph with fix central wavelength at 500 nm and 495 nm for neat G3 and electrolyte added G3, respectively. This central wavelength is the steady-state emission wavelength obtained from steady-state spectral analysis of DMASBT in each solution. It is important to note that the lifetime fluorescence decay of DMASBT in each sample studied here is completely seized by streak camera within the available detection time window of ~280 ps. **Fig. 3.A.8** presents two-dimensional representations of streak camera images, capturing data simultaneously across three dimensions: wavelength, time, and intensity. Analysis protocol of these streak images and collected fluorescence decay profile of all the compositions are presented in **Fig. 3.A.9** and **Fig. 3.A.10**. Details about streak camera technique can be found in earlier report.[74]

The fluorescence decay of DMASBT captured by streak camera is fitted with bi-exponential function for 2.8 M and 3.2 M of LiTFSI concentrations whereas at lower concentrations (0.5 M, 1 M and 2.1 M) decay are fitted with only single exponential function (see Table S5). DMASBT is popular as a short-lifetime fluorophore subsisting $< \tau_{life} >$ ~ 10-100 ps in low to medium viscous aprotic and polar solvents in common.[75] Note LiTFSI electrolyte induced viscosity impact on fluorescence dynamics of DMASBT in G3/LiTFSI solutions are clearly displayed here. With increasing concentration up to 1M, the majority of solvent molecules are preoccupied with completely solvating the ions posing maximum ionic conductivity. Consequently, ion-solvent interactions intensify, leading to an increase in the non-radiative decay of DMASBT. Simultaneously, the enhanced viscosity strives to extend the fluorescence lifetime. These two opposing effects reduces the fluorescence lifetime down to approximately 135 fs, or, practically no impact gains. The turning point occurs upon the addition of 2.1 M salt in G3. At this juncture, the initiation of CIP, AGGIP formation becomes apparent.

This process leads to a partial reduction in ion - solvent interactions, meaning that the lithium ions become less tightly coordinated with the surrounding solvent molecules. As a result, the local environment around the fluorescent species becomes less perturbed by dynamic solvent relaxation effects. This reduced solvent reorganization contributes to an increase in the radiative decay rate of the excited state, ultimately manifesting as an extended fluorescence lifetime, observed to be ~80 picoseconds. The increase in fluorescence lifetime aligns well with the structural characteristics of the electrolyte solutions, as revealed by Raman spectroscopy. Specifically, Raman analysis indicates distinct coordination environments and varying degrees of ion pairing or aggregation, which support the notion of weaker or altered ion - solvent interactions. The consistency between the spectroscopic data and the fluorescence lifetime measurements reinforces the interpretation that structural rearrangements at the molecular level significantly influence the excited-state dynamics of the system.

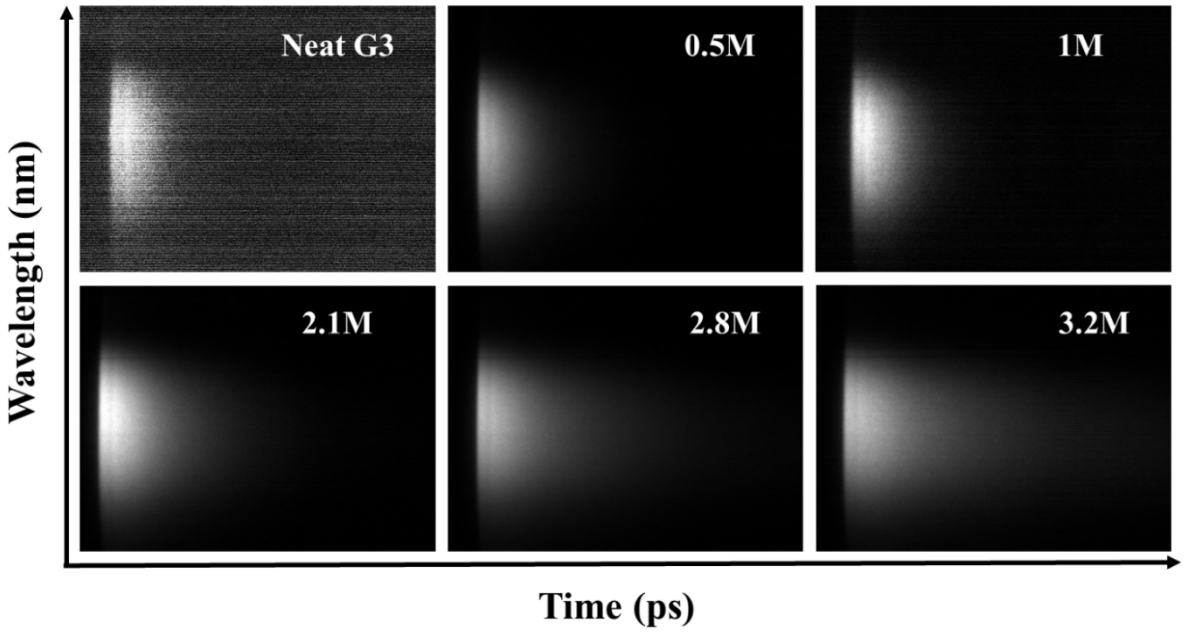

FIG. 3.A.8. Two-dimensional streak camera images of DMASBT in G3/LiTFSI electrolyte at 298 K. X-axis represents the time evolution of the fluorescence intensity, while Y-axis denotes spatial variation (wavelength) of the fluorescence emission at a given time.

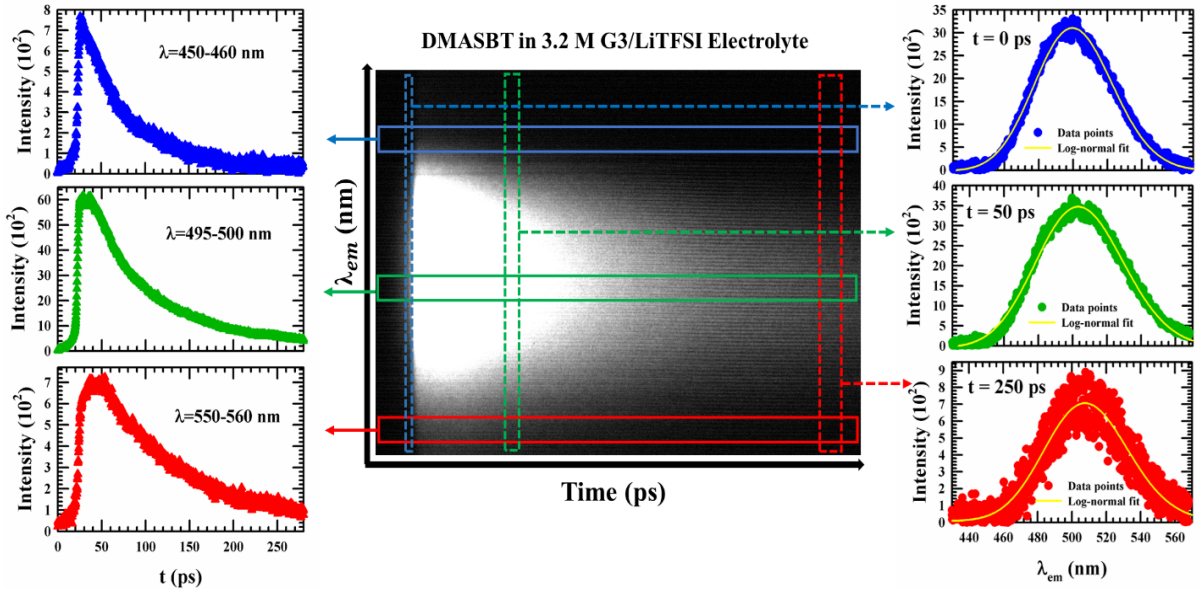

FIG. 3.A.9. 2D-streak image of DMASBT in G3/LiTFSI electrolyte. Horizontal line and vertical line represent time axis and wavelength axis, respectively. The colored stripes represent the blue end, emission peak wavelength and the red end emission region in the 2D-streak camera image, respectively. t_0 represents the initial time or zero time from where the emission decay starts and the time value increases along the positive x- axis.

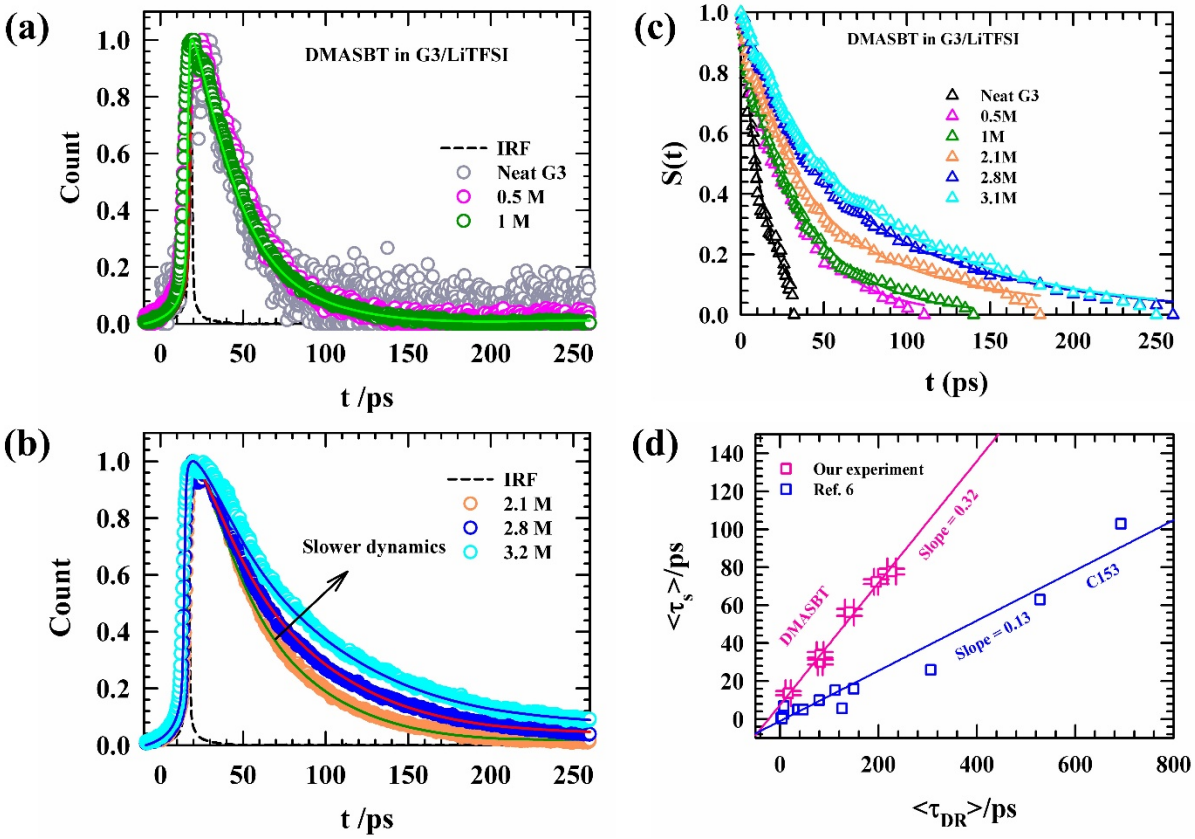

FIG. 3.A.10. (a) Fluorescence emission decay profiles of DMASBT in G3/LiTFSI electrolyte solutions along with neat solvent recorded *via* streak camera. **(b)** Fluorescence emission decay profiles of DMASBT in G3/LiTFSI electrolyte solutions at high concentration of LiTFSI. **(c)** Solvation response function S(t) decays of DMASBT in various electrolyte concentrations in G3/LiTFSI electrolyte together with neat solvent G3 at ~298K. All compositions are color-coded. **(d)** Correlation between $< \tau_s >$/ ps and $< \tau_{DR} >$/ ps obtained from experiments at all the compositions in G3/LiTFSI electrolyte solutions at 298 K. Solid lines through the data points are linear fits. Blue color-coded data representing solvation times of C153 and DR times in neat solvents are taken from earlier works of M. Maroncelli and coworkers.[76]

Appendix 3.B

Table 3.B.1. Temperature dependent measured densities (ρ) and viscosities (η) in G3/LiTFSI electrolyte solutions with varying LiTFSI concentrations from 0.5 M to 3.2 M.

Density (ρ/ gcm^{-3})					
T/K	0.5 M	1 M	2.1 M	2.8 M	3.2 M
298	1.065	1.134	1.286	1.380	1.429
303	1.060	1.129	1.281	1.375	1.424
308	1.055	1.124	1.276	1.370	1.419
313	1.050	1.120	1.271	1.365	1.414
318	1.046	1.115	1.266	1.360	1.410
323	1.041	1.110	1.260	1.356	1.405
328	1.036	1.104	1.256	1.350	1.401
Viscosity (η/ cP)					
T/K	0. 5 M	1 M	2.1 M	2.8 M	3.2 M
298	3.90	6.69	34.73	117.50	236.20
303	3.49	6.03	28.18	90.90	179.80
308	3.14	5.33	23.26	71.65	139.60
313	2.86	4.72	19.48	57.47	110.20
318	2.62	4.22	16.50	46.76	88.25
323	2.42	3.79	14.12	38.57	71.72
328	2.22	3.26	10.06	31.46	60.27

Table 3.B.2. Measured conductivity ($\sigma/\mu S\ cm^{-1}$) and glass transition temperature (T_g/ K) in G3/LiTFSI electrolyte.

Conc (M)	T/ K	Conductivity ($\mu S\ cm^{-1}$)	Molar Conductivity ($S\ cm^2 mol^{-1}$)	Glass transition temperature (T_g/ K)
0.5	298	3240	6.3529	160
	303	3280	6.4314	
	308	3600	7.0588	
	313	3850	7.5490	
	318	3980	7.8093	
	323	4530	8.8824	
	328	4680	9.1765	
1	298	3910	3.9100	164
	303	4340	4.3400	
	308	4750	4.7500	
	313	5340	5.3400	
	318	5900	5.9000	
	323	6410	6.4100	
	328	7150	7.1500	
2.1	298	1970	0.9563	180
	303	2520	1.2233	
	308	2830	1.3738	
	313	3140	1.5243	
	318	3540	1.7184	
	323	3960	1.9223	
	328	4480	2.1748	
2.8	298	1050	0.3763	188
	303	1290	0.4624	
	308	1540	0.5520	
	313	1800	0.6452	
	318	1990	0.7134	
	323	2410	0.8638	
	328	2690	0.9642	
3.2	298	840	0.2650	195
	303	1070	0.3375	
	308	1260	0.3975	
	313	1400	0.4416	
	318	1580	0.4984	
	323	1810	0.5710	
	328	2160	0.6814	

Table 3.B.3. Raman spectral characteristics of deconvoluted peaks for various LiTFSI concentrations in G3/LiTFSI electrolytes.

LiTFSI (M)			Deconvolution of peak			
	Peak position (cm^{-1})	Area of peak	Peak 1 (cm^{-1})	Relative area of peak 1 (%)	Peak 2 (cm^{-1})	Relative area of peak 2 (%)
0.5	741	155	741	100	-	-
1	741	312	741	100	-	-
2.1	742	519	741	66	746	34
2.8	743	693	742	55	747	45
3.2	744	710	743	57	748	43

Table 3.B.4 Estimated activation energies calculated from viscosity, ionic conductivity and DR rate for G3/LiTFSI electrolyte solutions.

C_{LiTFSI}/M	E_a^{η} /kJ mol^{-1}	$E_a^{\sigma_{dc}}$ /kJ mol^{-1}	$E_a^{\frac{1}{\tau_{DR}}}$ /kJ mol^{-1}
0.5	15.11	10.71	5.48
1	19.25	16.30	10.96
2.1	31.55	20.91	6.95
2.8	35.42	25.17	11.47
3.2	37.17	23.90	10.56

Table 3.B.5. UV-Vis absorption and emission frequencies[a] ($\tilde{\nu}_{abs/em}$) and FWHM[b] ($\Gamma_{abs/em}$) of DMASBT in G3/LiTFSI electrolyte solutions at ~298K.

LiTFSI (M)	$\tilde{\nu}_{abs}$ (10^3 cm^{-1})	$\tilde{\nu}_{em}$(10^3 cm^{-1})	Γ_{abs} (10^3 cm^{-1})	Γ_{em} (10^3 cm^{-1})
0	25.37	19.99	4.85	3.00
0.5	25.31	19.86	4.91	2.95
1	25.18	19.85	4.70	2.89
2.1	25.24	19.94	4.51	2.98
2.8	25.09	20.01	4.95	3.05
3.2	25.08	19.96	4.97	3.04

[a]Uncertainty in spectral frequencies: ± 100 cm^{-1}

[b]FWHM represents full width at half maximum of the spectra.

Table 3.B.6. Exponential fitting parameters of average lifetimes of DMASBT at various electrolyte compositions in G3/LiTFSI at ~298 K obtained from Streak Camera set-up.

LiTFSI /M	a_1	τ_1/ ps	a_2	τ_2/ ps	$< \tau_{life} >$/ ps
0	1	29.49	-	-	29.49
0.5	1	29.18	-	-	29.18
1	1	28.14	-	-	28.14
2.1	1	42.31	-	-	42.31
2.8	0.94	52.13	0.06	175.27	59.52
3.2	0.86	59.47	0.14	200.20	79.17

Table 3.B.7. Fit parameters for the S(t) decays and observed ($\Delta\tilde{\nu}_{obs}^{t}$) dynamic Stokes for DMASBT in G3/LiTFSI electrolyte solutions at ~298 K.

LiTFSI (M)	a_1	τ_1/ps	a_2	τ_2/ps	$<\tau_S>$/ps	$\tilde{\nu}(0)*10^3$ /cm^{-1}	$\tilde{\nu}(\infty)*10^3$ /cm^{-1}	$\Delta\tilde{\nu}_{obs}^{t}$ /cm^{-1}
0	0.05	5.25	0.95	14.08	13.64	20.222	19.999	223
0.5	0.10	3.26	0.90	33.00	30.03	20.347	20.004	343
1	0.12	2.89	0.88	38.02	33.80	20.599	20.306	293
2.1	0.65	30.40	0.35	104.17	56.22	20.511	20.130	381
2.8	0.40	32.36	0.60	99.01	72.35	20.532	20.125	407
3.2	0.22	28.09	0.78	91.74	77.74	20.629	20.230	399

References

[1] M.R. Palacín, *Chem Soc Rev* **47**(13), 4924–4933 (2018).

[2] B. Balagopal, and M.-Y. Chow, *Batteries* **6**(4), 53 (2020).

[3] S. Kournopoulos, M.S. Santos, S. Ravipati, A.J. Haslam, G. Jackson, I.G. Economou, and A. Galindo, *J Phys Chem B* **126**(47), 9821–9839 (2022).

[4] Z. Li, and J. Wu, *Phys Rev E* **70**(3), 031109 (2004).

[5] J.-F. Dufrêche, O. Bernard, P. Turq, A. Mukherjee, and B. Bagchi, *Phys Rev Lett* **88**(9), 095902 (2002).

[6] M. Andreev, J.J. de Pablo, A. Chremos, and J.F. Douglas, *J Phys Chem B* **122**(14), 4029–4034 (2018).

[7] S. Glasstone, *An Introduction to Electrochemistry* (1942).

[8] A. Chandra, R. Biswas, and B. Bagchi, *J Am Chem Soc* **121**(16), 4082–4083 (1999).

[9] A. Chandra, and B. Bagchi, *J Chem Phys* **110**(20), 10024–10034 (1999).

[10] A. Chandra, and B. Bagchi, *J Chem Phys* **112**(4), 1876–1886 (2000).

[11] A. Chandra, D. Wei, and G.N. Patey, *J Chem Phys* **99**(3), 2083–2094 (1993).

[12] J.M. Mollerup, and M.P. Breil, *AIChE Journal* **61**(9), 2854–2860 (2015).

[13] J. Barthel, and R. Buchner, *Chem Soc Rev* **21**(4), 263 (1992).

[14] B. Bagchi, *Annu Rev Phys Chem* **40**(1), 115–141 (1989).

[15] B. Bagchi, and R. Biswas, (1999), pp. 207–433.

[16] S. Das, R. Biswas, and B. Mukherjee, *J Chem Phys* **145**(8), (2016).

[17] J. Mondal, D. Maji, and R. Biswas, *J Chem Phys* **160**(8), (2024).

[18] D. Maji, and R. Biswas, *J Chem Phys* **158**(17), (2023).

[19] Y.-Q. Wang, H. Xu, B. Cao, J. Ma, and Z.-W. Yu, *J Phys Chem Lett* **15**(19), 5047–5055 (2024).

[20] R. Biswas, and B. Bagchi, *J Am Chem Soc* **119**(25), 5946–5953 (1997).

[21] R. Biswas, and B. Bagchi, *J Chem Phys* **106**(13), 5587–5598 (1997).

[22] B. Bagchi, and R. Biswas, *Acc Chem Res* **31**(4), 181–187 (1998).

[23] R. Biswas, S. Roy, and B. Bagchi, *Phys Rev Lett* **75**(6), 1098–1101 (1995).

[24] D. Di Lecce, V. Marangon, H.-G. Jung, Y. Tominaga, S. Greenbaum, and J. Hassoun, *Green Chemistry* **24**(3), 1021–1048 (2022).

[25] S. Tobishima, H. Morimoto, M. Aoki, Y. Saito, T. Inose, T. Fukumoto, and T. Kuryu, *Electrochim Acta* **49**(6), 979–987 (2004).

[26] M. Agostini, S. Xiong, A. Matic, and J. Hassoun, *Chemistry of Materials* **27**(13), 4604–4611 (2015).

[27] S. Wei, Z. Li, K. Kimura, S. Inoue, L. Pandini, D. Di Lecce, Y. Tominaga, and J. Hassoun, *Electrochim Acta* **306**, 85–95 (2019).

[28] A. Orita, K. Kamijima, M. Yoshida, K. Dokko, and M. Watanabe, *J Power Sources* **196**(8), 3874–3880 (2011).

[29] K. Xu, S. Zhang, J.L. Allen, and T.R. Jow, *J Electrochem Soc* **149**(8), A1079 (2002).

[30] P. Jaumaux, J. Wu, D. Shanmukaraj, Y. Wang, D. Zhou, B. Sun, F. Kang, B. Li, M. Armand, and G. Wang, *Adv Funct Mater* **31**(10), (2021).

[31] Y. Wang, Z. Li, Y. Hou, Z. Hao, Q. Zhang, Y. Ni, Y. Lu, Z. Yan, K. Zhang, Q. Zhao, F. Li, and J. Chen, *Chem Soc Rev* **52**(8), 2713–2763 (2023).

[32] R. Gond, W. van Ekeren, R. Mogensen, A.J. Naylor, and R. Younesi, *Mater Horiz* **8**(11), 2913–2928 (2021).

[33] X. Fan, X. Ji, L. Chen, J. Chen, T. Deng, F. Han, J. Yue, N. Piao, R. Wang, X. Zhou, X. Xiao, L. Chen, and C. Wang, *Nat Energy* **4**(10), 882–890 (2019).

[34] K. Shigenobu, K. Dokko, M. Watanabe, and K. Ueno, *Phys Chem Chem Phys* **22**(27), 15214–15221 (2020).

[35] K. Ueno, J. Murai, H. Moon, K. Dokko, and M. Watanabe, *J Electrochem Soc* **164**(1), A6088–A6094 (2017).

[36] T. Mandai, K. Dokko, and M. Watanabe, *The Chemical Record* **19**(4), 708–722 (2019).

[37] H.-M. Kwon, M.L. Thomas, R. Tatara, Y. Oda, Y. Kobayashi, A. Nakanishi, K. Ueno, K. Dokko, and M. Watanabe, *ACS Appl Mater Interfaces* **9**(7), 6014–6021 (2017).

[38] H. Jin, B. O'Hare, J. Dong, S. Arzhantsev, G.A. Baker, J.F. Wishart, A.J. Benesi, and M. Maroncelli, *J Phys Chem B* **112**(1), 81–92 (2008).

[39] Kremer F, and Schönhals A, *Broadband Dielectric Spectroscopy* (Springer Berlin Heidelberg, Berlin, Heidelberg, 2003).

[40] Myron, W Evans, and Vladimir I Gaiduk, *Dielectric Relaxation And Dynamics Of Polar Molecules* (1999).

[41] W.T. Coffey, *J Mol Liq* **114**(1–3), 5–25 (2004).

[42] K.-K. Lee, K. Park, H. Lee, Y. Noh, D. Kossowska, K. Kwak, and M. Cho, *Nat Commun* **8**(1), 14658 (2017).

[43] S.K. Saha, P. Purkayastha, A.B. Das, and S. Dhara, *J Photochem Photobio A Chem* **199**(2–3), 179–187 (2008).

[44] C.F. Chapman, and M. Maroncelli, *J Phys Chem* **95**(23), 9095–9114 (1991).

[45] A. Biswas, and B.S. Mallik, *J Phys Chem B* **124**(44), 9898–9912 (2020).

[46] T. Pradhan, and R. Biswas, *J Phys Chem A* **111**(45), 11514–11523 (2007).

[47] A. Chandra, and G.N. Patey, *J Chem Phys* **100**(11), 8385–8391 (1994).

[48] K. Ibuki, and M. Nakahara, *J Chem Phys* **92**(12), 7323–7329 (1990).

[49] J.T. Hynes, *Annu Rev Phys Chem* **36**(1), 573–597 (1985).

[50] B. Bagchi, and N. Gayathri, (1999), pp. 1–80.

[51] J. Gardecki, M.L. Horng, A. Papazyan, and M. Maroncelli, (1995), pp. 49–57.

[52] S. Banerjee, P.Kr. Ghorai, D. Maji, and R. Biswas, *J Phys Chem B* **126**(48), 10146–10155 (2022).

[53] S. Das, B. Mukherjee, and R. Biswas, *J Chem Phys* **148**(19), (2018).

[54] S. Das, R. Biswas, and B. Mukherjee, *J Phys Chem B* **119**(34), 11157–11168 (2015).

[55] S. Mukherji, N.V.S. Avula, R. Kumar, and S. Balasubramanian, *J Phys Chem Lett* **11**(22), 9613–9620 (2020).

[56] X. Huang, R. Li, C. Sun, H. Zhang, S. Zhang, L. Lv, Y. Huang, L. Fan, L. Chen, M. Noked, and X. Fan, *ACS Energy Lett* **7**(11), 3947–3957 (2022).

[57] T. Fukasawa, T. Sato, J. Watanabe, Y. Hama, W. Kunz, and R. Buchner, *Phys Rev Lett* **95**(19), 197802 (2005).

[58] T.J. Seguin, N.T. Hahn, K.R. Zavadil, and K.A. Persson, *Front Chem* **7**, (2019).

[59] M. Koch, C. Suhr, B. Roth, and M. Meinhardt-Wollweber, *Journal of Raman Spectroscopy* **48**(2), 336–342 (2017).

[60] H. Hu, J. Bai, G. Xia, W. Zhang, and Y. Ma, *Photonic Sensors* **8**(4), 332–340 (2018).

[61] S. He, W. Zhang, L. Liu, Y. Huang, J. He, W. Xie, P. Wu, and C. Du, *Anal. Methods* **6**(12), 4402–4407 (2014).

[62] T.J. Vickers, R.E. Wambles, and C.K. Mann, *Appl Spectrosc* **55**(4), 389–393 (2001).

[63] Y. Umebayashi, T. Mitsugi, S. Fukuda, T. Fujimori, K. Fujii, R. Kanzaki, M. Takeuchi, and S.-I. Ishiguro, *J Phys Chem B* **111**(45), 13028–13032 (2007).

[64] D. Brouillette, D.E. Irish, N.J. Taylor, G. Perron, M. Odziemkowski, and J.E. Desnoyers, *Phys Chem Chem Phys* **4**(24), 6063–6071 (2002).

[65] J.B. Shinde, K.S. Kanse, D.N. Rander, Y.S. Joshi, and A.C. Kumbharkhane, (2018).

[66] P. Banerjee, and B. Bagchi, *J Chem Phys* **148**(22), (2018).

[67] A. Pal, and H. Kumar, *J Chem Eng Data* **44**(6), 1330–1334 (1999).

[68] M. Olschewski, S. Knop, J. Seehusen, J. Lindner, and P. Vöhringer, *J Phys Chem A* **115**(7), 1210–1221 (2011).

[69] D. Huppert, V. Ittah, and E.M. Kosower, *Chem Phys Lett* **159**(2–3), 267–275 (1989).

[70] R. Biswas, A.R. Das, T. Pradhan, D. Touraud, W. Kunz, and S. Mahiuddin, *J Phys Chem B* **112**(21), 6620–6628 (2008).

[71] M.-L. Horng, J.A. Gardecki, and M. Maroncelli, *J Phys Chem A* **101**(6), 1030–1047 (1997).

[72] M. Maroncelli, *J Chem Phys* **106**(4), 1545–1557 (1997).

[73] R. Buchner, and J. Barthel, *Annual Reports Section "C" (Physical Chemistry)* **91**, 71 (1994).

[74] J. Mondal, N.C. Maity, and R. Biswas, *J Chem Sci* **135**(3), 84 (2023).

[75] M. Kondo, X. Li, and M. Maroncelli, *J Phys Chem B* **117**(40), 12224–12233 (2013).

[76] M.L. Horng, J.A. Gardecki, A. Papazyan, and M. Maroncelli, *J Phys Chem* **99**(48), 17311–17337 (1995).

1

Chapter 4

Linking Ion Mobility to Multi-Timescales Fluorescence Dynamics: Role of Dynamic Heterogeneity

4.1 Introduction

In recent years, rechargeable batteries, particularly lithium-ion batteries (LIBs), have revolutionized modern science and technology, driving transformative economic and societal advancements.[1,2] Their widespread adoption in portable electronics and electric vehicles has redefined energy storage, enabling the development of more sustainable and efficient systems. The solution chemistry of the electrolytes in LIBs plays an important role for efficient Li^+ transport, because it dictates electrolyte dissociation, ion mobility, and the system stability by influencing the electrode-electrolyte interfacial behavior.[3,4] It is known that solvent specifications and electrolyte concentration govern electrolyte dissociation, solution viscosity and ion mobilities. These key physical chemistry aspects directly impact battery performance, energy efficiency, and cell life.[5–7] Recent activities on improvement of battery performance have focused on optimizing electrolyte compositions by considering materials aspects and physical chemistry of the entire system comprising electrolyte, electrode and medium. Here, we have selected a model electrolyte system composed of triglyme (G3) and LiTFSI salt. The non-aqueous electrolytes, particularly those using fluorine-based salts like LiTFSI, are preferred due to their superior stability, higher ionic conductivity, and resistance to decomposition under high voltage conditions.[8,9] A relatively lower viscosity ($\eta_{G3} \sim 2$ cP)[10] and moderate polarity ($\varepsilon_s \sim 8$)[11,12] is believed to facilitate Li^+ transport and efficient charging-discharging process.

According to established understanding in the field of battery electrolyte solutions, high conductivity and low viscosity are key factors in achieving effective Li^+ conduction. In the majority of non-aqueous Li^+ transporting medium, the highest ion conductivity is typically observed at ~ 1 M salt concentration.[13] The conventional concentration of ~ 1 M in LIBs has been used since the early development of commercial rechargeable batteries, dating back to the late 1980s and early 1990s.[14,15] Particularly, the solution of 1 M $LiPF_6$ in organic solvents (such as ethylene carbonate and dimethyl carbonate) became popular and established as a "standard electrolyte formulation".[16–19] The influence of salt concentration on electrolyte properties is a major interesting area of investigation. Changes in the concentration of Li-salt significantly influences the solvation-shell structure of Li^+ ions, which may alter electrolyte system properties. These alterations include formation and stabilization of interphases such as the solid electrolyte interphase (SEI) and cathode electrolyte interphase (CEI), as well as the electrolyte decomposition or undesirable side reactions during cycling. The integrity of these interphases is essential for the stability, longevity on-call performance of LIBs.

Another important aspect related to ion conductivity of electrolyte solutions is spatio-temporal heterogeneity which has not been explored yet. Ion conductivity parameters depend upon number of charge carriers and mobility of these charge carriers. The mobility of the charge carriers, in turn, depends on, apart from solution viscosity, the structure electrolyte solution. In our previous study on G3/LiTFSI electrolyte system, we provided an analysis of the impact of electrolyte concentration on ion conductivity, viscosity, glass transition temperature, and solution structure.[11] Using Raman spectroscopy, we presented in this study the evidence of formation of solvent-shared ion pairs (SSIPs), contact ion pairs (CIPs), and aggregated ion pairs (AGGIPs). Furthermore, the correlation between experimental ion conductivity and solution polarization relaxation has been established, providing a qualitative support for the solvent-carriage mechanism of Li^+ transport and formation of ion-solvent composite species at various concentrations in G3/LiTFSI electrolyte solutions studied.[11] The presence of different kinds of ion-pairs and ion-solvent composite species renders spatio-temporal heterogeneity to these solutions and therefore a connection between the heterogeneous solution dynamics and ion transport needs to be explored and understood.

The presence of spatial and temporal inhomogeneity and their length-scales and timescales respectively has been explored while understanding the experimentally observed stretched exponential relaxation, diffusion-viscosity decoupling and the coupling between rotational and translational motion within the medium.[20–25] The heterogeneity timescales associated with glassy dynamics has already been demonstrated through both numerical and theoretical research, generally from a qualitative perspective.[26–30] However, the connection between the spatio-temporal heterogeneity or simply "dynamic heterogeneity" (DH) and ion transport in solutions relevant to battery applications has not been investigated yet and thus warrants a thorough and systematic study. For this purpose, both steady state and time-dependent fluorescence studies employing different probes might offer valuable information regarding the heterogeneity in both the solution structure and dynamics. Because the temporal profile of the underlying friction dictates the ion mobility in a condensed phase, a connection between the heterogeneous medium relaxation dynamics and ion mobility is natural.

In the present study, steady-state UV-Vis absorption, fluorescence emission and, time-resolved fluorescence spectroscopic (TRES) studies have been conducted by using a popular fluorescent probe, coumarin 153 (C153)[31] in order to investigate the heterogeneity in structure and dynamics of G3/LiTFSI electrolyte solutions with concentrations of LiTFSI from 0.5 - 3.2 M at a temperature range, T = 298 - 328 K. The time-resolved fluorescence measurements provided information about the solution dynamics, specifically the rate at which the solvent molecules surround and interact with the fluorophore.[31–34] The fluorescence lifetime of coumarin 102 (C102) has been measured and compared with that of C153 in order to understand the intricate aspects of solute-solvent interactions. The structural difference between C102 and C153 lies only in the functional groups attached to their aromatic rings: CF_3 (a strong electron-withdrawing group) for C153 and CH_3 (an electron-donating group via inductive effect) for C102. Consequently, the observed changes in the measured fluorescence lifetimes of both the probes are expected to reflect subtle variations in the interactions that they experience in these electrolyte solutions. Another fluorescent probe, trans-2-[4-(dimethylamino)styryl]benzothiazole (trans-DMASBT), with a relatively much shorter lifetime ($\tau_{life}^{DMASBT} \leq 100$ ps), has been utilized to investigate spatial heterogeneity arising from "short-lived" environmental fluctuations in G3/LiTFSI electrolyte solutions. For this, the excitation

wavelength (λ_{exc})-dependence of the steady-state fluorescence emission of these probes were examined and compared.[35,36] The chemical structures of G3, LiTFSI, C153, C102 and trans-DMASBT are shown in **Scheme 4.1**.

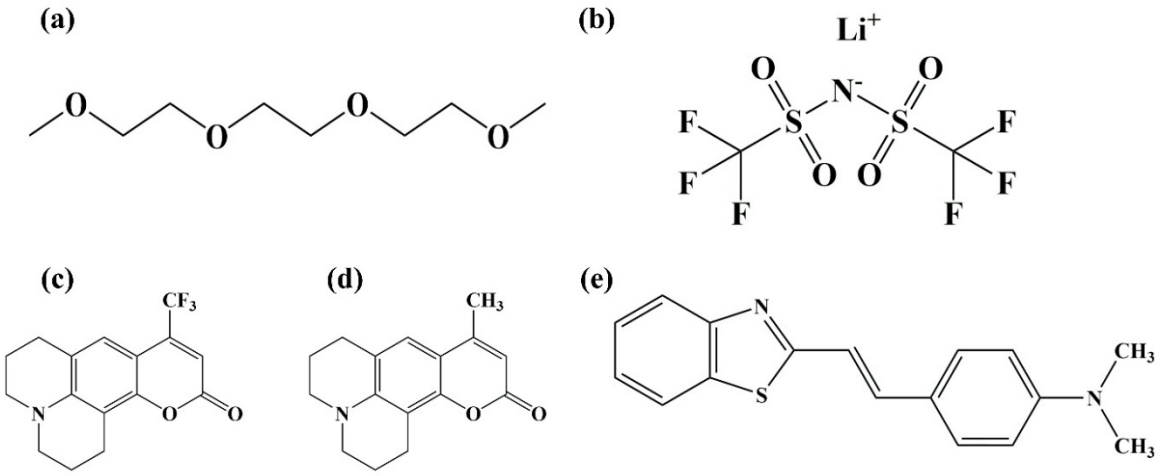

Scheme 4.1. Chemical structures of (a) G3, (b) LiTFSI, (c) C153, (d) C102 and (e) trans-DMASBT.

4.2 Experimental Details

4.2.1 Materials and Sample Preparation

Triethylene glycol dimethyl ether (also known as triglyme (G3), $CH_3O(CH_2CH_2O)_3CH_3$), bis(trifluoromethane)sulfonimide lithium salt (LiTFSI, ≥99%), Coumarin 153, Coumarin 102 and trans-2-[4-(dimethylamino)styryl]benzothiazole (trans-DMASBT) were purchased from Sigma-Aldrich and used without further purification. LiTFSI was vacuum dried for 72 hours prior to experiment. The requisite amount of LiTFSI was dissolved in G3 to make the concentrations 0.5 - 3.2 M and heated at ~ 323 K in stirring condition to prepare a transparent and colorless G3/LiTFSI electrolyte solution. Special care was taken to dissolve the salt and the dye in G3 solvent without absorption of moisture. For absorption and emission spectroscopic measurements, 2-3 mL sample solution was taken in a quartz cuvette preloaded with respective dye where the concentration of the fluorophore was maintained at $\leq 10^{-5}$ M. For temperature dependent measurements, sufficient time (20-30 min) was allowed for each solution to reach a proper thermal equilibrium before doing experiments. The samples were prepared, preserved, and subjected to subsequent experiments in a strictly controlled humidity environment to prevent moisture contamination.

4.2.2 Density and Viscosity Coefficients Measurements

Temperature dependent densities (ρ) and viscosity coefficients (η) of all the electrolyte samples were recorded in automated temperature-controlled density-sound velocity analyzer (Anton Paar, model DSA 5000) and automated micro-viscometer (AMVn, Anton Paar), respectively. Measured ρ and η values of G3/LiTFSI electrolyte solutions have been summarized in Chapter 3.

4.2.3 Steady-State Measurements and Spectral Analysis

UV-Vis spectrophotometer (UV − 2600, Shimadzu) and a fluorimeter (Fluorolog, Jobin-Yvon, Horiba) were used to record steady state absorption and fluorescence emission spectra, respectively. Peltier temperature controller was used to perform temperature-controlled measurements (accuracy ±1 K). The details of measurements techniques have been discussed in

Chapter 3 and corresponding standard spectral analysis protocol has been followed to determine spectral frequencies.[11,31,38,39] The typical error bar for the determined spectral frequencies was ±100 cm^{-1}. Steady-state spectra and corresponding peak positions of C153 in neat G3 and G3/LiTFSI electrolyte solutions are provided in **Fig. 4.1** and **Table 4.B.1** (Appendix 4.B), respectively.

4.2.4 TRF Measurements

4.2.4.1 TCSPC Set-up and Spectral Analysis

Time-resolved fluorescence (TRF) measurements were performed with a picosecond-resolved time-correlated single-photon counting (ps-TCSPC) system (LifeSpec-ps) from Edinburgh Instruments (Livingston, U. K.). A laser emitting at 409 nm with a 2 nm excitation slit served as the excitation source for both probes, C153 and C102, dissolved in electrolyte solutions. Magic angle (54.7°) intensity decay at 409 nm of a scattering medium (water) produced an instrument response function (IRF) ~ 85 ps. Lifetime emission decays (that is, the magic angle intensity decays) were recorded at the wavelength corresponding to the peak of steady state emission spectra (λ_{max}^{em}) of respective dissolved fluorescent probe. Temperature was controlled by employing Julabo temperature controller (accuracy ±1 K). Further details of data collection and analysis of fluorescence lifetime have been described in Chapter 2 and elsewhere.[31,40,41]

4.2.4.2 Streak Camera Technique and Related Spectral Analysis

The ultrafast solvent response was monitored by capturing time-resolved fluorescence spectra using a streak camera (Optoscope $SC-10$) integrated with a spectrograph ($HRS-300SS$, Princeton Instruments). The characterization details of the excitation light and the generated spectrograph have been covered in Chapter 2. Emitted fluorescence was collected orthogonally to the excitation beam path and focused onto the entrance slit of a monochromator (10 μm width, 4 mm height) using a pair of lenses. Calibration was performed by determining the instrument response function (IRF) of the streak camera with scattering particles in water. The recorded IRF had a full width at half maximum (FWHM) value of ~ 2.0 ps. During the data collection process,

1000 acquisitions were made along with maintaining Micro Channel Plate (MCP) gain at 750 V, and a delay of 33% involving a sweep speed of 15 ps/mm. To minimize scattering effects, a bandpass filter at 471 nm was applied to collect fluorescence and the magic angle (54.7°) polarized intensity decays at the peak wavelength of the steady state emission from the solute in the solutions have been captured to determine the lifetime of the probe dissolved in these electrolyte solutions. Further details on 3-dimensional streak image used for analyzing time-resolved emission spectra (TRES) and the solvent response function, S(t), are available in our previous sources.[11,37]

4.3 Results and Discussion

4.3.1 Ion-Induced Heterogeneity: Insights from Steady State Analysis

The steady-state UV-vis absorption and emission spectra of C153 in neat G3 and G3/LiTFSI electrolyte solutions are presented in **Fig. 4.1**, with the corresponding peak frequencies and spectral widths summarized in **Table 4.B.1** (Appendix 4.B). Previous studies on the polarity-dependent emission spectra of C153 in various ethylene glycol dimethyl ethers provide a foundation for interpreting our data.[42] Notably, the addition of LiTFSI to G3 induces a ~1000 cm^{-1} red shift in both absorption and emission spectra. This electrolyte-induced red shift is consistent with similar observations in other neat solvents and binary solvent mixtures.[40,43–45] The shift is attributed to enhanced stabilization of ion-dipole interactions between the fluorescent probe and the added LiTFSI.[45,46]

Steady-state studies as a function of LiTFSI concentration reveal a red shift in absorption spectra accompanied by spectral broadening (~ 250 cm^{-1}), while emission spectra exhibit concomitant narrowing, ~ 250 cm^{-1} (see **Table 4.B.1**, Appendix 4.B). In contrast, temperature-dependent absorption and emission measurements over the range 298 - 323 K, shown in **Fig. 4.A.1** (Appendix 4.A), demonstrate no significant peak shift with temperature. This indicates that the interaction between the probe solute and its surrounding environment is insensitive to changes in solution temperature. Similar behavior has been reported in other electrolyte solutions and deep eutectic solvents, further supporting these findings.[35,36]

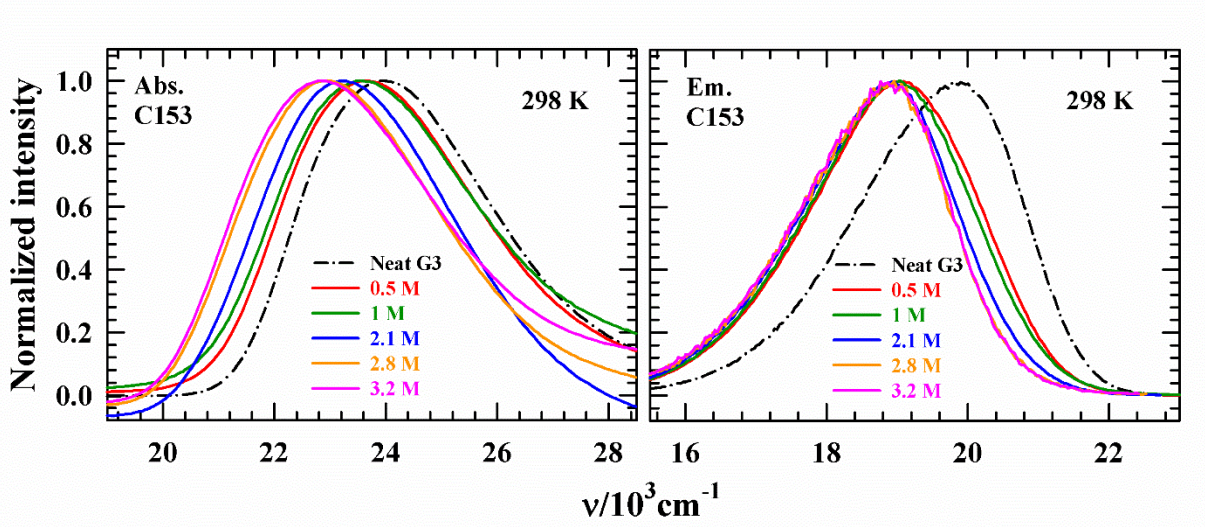

FIG. 4.1. UV-vis absorption (left panel) and emission (right panel) spectra of C153 in G3/LiTFSI electrolyte solutions at different LiTFSI concentrations at 298 K. Corresponding spectra of C153 in neat G3 is shown in black dash-dot line in each panel. All spectra are color-coded.

In our previous study, Raman spectroscopy was used to investigate LiTFSI-induced solution structures, revealing the existence of solvent-shared ion pairs (SSIPs), contact ion pairs (CIPs), and aggregated ion-pair (AGGIP) complexes.[11] To further validate the presence of ion-induced micro-heterogeneity in the current electrolyte medium, the excitation wavelength dependence of the emission spectrum of C153 was analyzed. representative λ_{exc} induced emission peak frequencies and spectral widths are shown in **Fig. 4.2**. A non-monotonic shift in the emission frequency, coupled with spectral narrowing, is observed with increasing LiTFSI concentration. Specifically, a weak dependence of dependence of λ_{em} on λ_{exc} is evident, showing a red shift of ~ 300 cm^{-1} accompanied by spectral narrowing of ~150–200 cm^{-1}. These results suggest the presence of weakly spatially heterogeneous micro-domains within the electrolyte system.

induced red shift in the emission frequency, accompanied by spectral narrowing, as the LiTFSI concentration increases. Specifically, a strong λ_{exc} dependence on λ_{em} is observed, with a red shift of ~500 - 900 cm^{-1} and spectral narrowing of ~160 - 600 cm^{-1}. These findings indicate the presence of spatially heterogeneous micro-domains within the electrolyte medium.

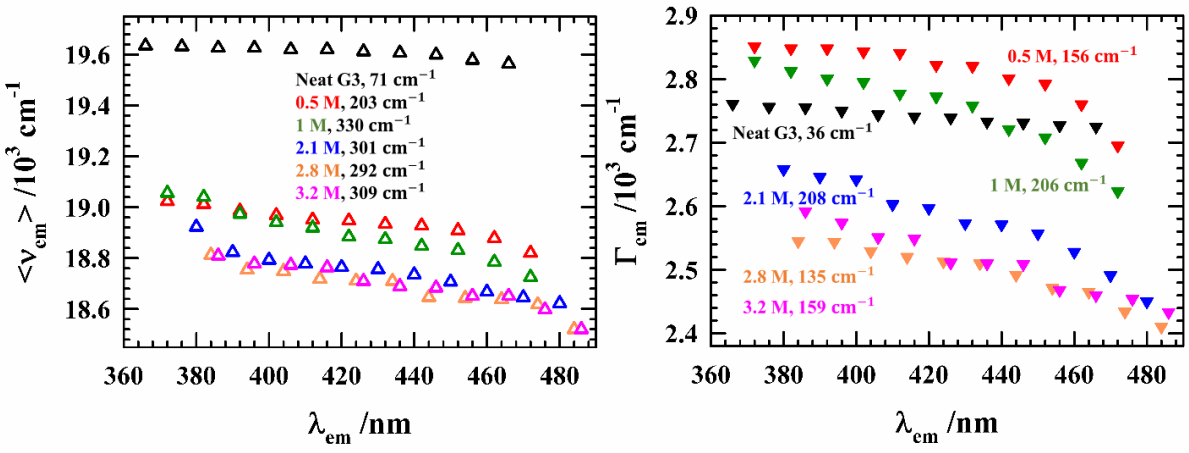

FIG. 4.2. LiTFSI concentration induced λ_{exc} dependent steady state emission frequencies (left panel) and spectral widths (right panel) of C153 in G3/LiTFSI electrolyte solutions. The value of total shift is shown in inset of each plot.

If a fluorescent probe exhibits 'solvatochromic averaging,' the rate of interconversion between different solvation states exceeds the probe's fluorescence lifetime. Consequently, the observed emission spectrum corresponds to a dynamically averaged, fully relaxed solvation state, masking the distinct emission characteristics of individual solvation environments.[47–49] However, in the present study, the fluorescence lifetime of DMASBT in the G3/LiTFSI electrolyte medium (~ 60 - 200 ps) is significantly longer than its lifetime in common solvents studied previously.[50] This extended lifetime allows the probe to capture excitation-wavelength-dependent emission features, reflecting the distinct solvation environments in the electrolyte solution. These results suggest that the heterogeneous solvation environments, or 'micro-domains,' surrounding DMASBT in the G3/LiTFSI electrolyte persist on a sub-nanosecond timescale, thereby enabling the observation of distinct emission characteristics.

4.3.2 Ion-Driven Heterogeneity: Evidence from Time-Resolved Spectroscopy

4.3.2.1 Fluorescence Lifetime Measurements

The composition- and temperature-dependent (see **Fig. 4.3(a)**) excited-state fluorescence lifetimes of C153 in G3/LiTFSI electrolyte solutions have been studied, with the numerical results summarized in **Table 4.1** and **Table 4.B.3** (Appendix 4.B), respectively. Notably, the fluorescence lifetimes of C153 in typical dipolar solvents are generally in the range of ~3–5 ns.[31,51] However, in G3, the τ_{life} of C153 is significantly lower (~1.6 ± 0.2 ns). This reduction in lifetime can be attributed to the relatively low dielectric constant ($\varepsilon_s \sim 9$)[11,52] and dipole moment ($\mu \sim 2.2$ D)[53] of G3, combined with its lower viscosity (~ 2 cP)[54] compared to highly dipolar solvents such as acetonitrile ($\mu \sim 3.4$ D)[55] or DMSO ($\mu \sim 4$ D).[56] These factors likely result in less efficient stabilization of the excited state, thereby facilitating non-radiative decay processes and reducing the fluorescence lifetime.

Table 4.1. Excited state fluorescence lifetimes $<\tau_{life}>$/ns of C153 in G3/LiTFSI electrolyte solutions at 298 K[a]

C_{LiTFSI}/M	a_1	τ_1/ns	a_2	τ_2/ns	a_3	τ_3/ns	$<\tau_{life}>$/ns
0	0.70	0.019	0.03	0.414	0.27	5.777	1.59
0.5	0.45	0.133	0.30	1.289	0.25	4.810	1.65
1	0.39	0.160	0.33	1.943	0.28	4.709	2.02
2.1	0.54	0.188	0.23	1.388	0.22	3.996	1.30
2.8	0.53	0.210	0.28	1.106	0.19	4.525	1.28
3.2	0.39	0.200	0.33	1.006	0.28	4.869	1.77

[a]Average lifetime $<\tau_{life}>$/ns can be reproduced within ±5% of the reported values.

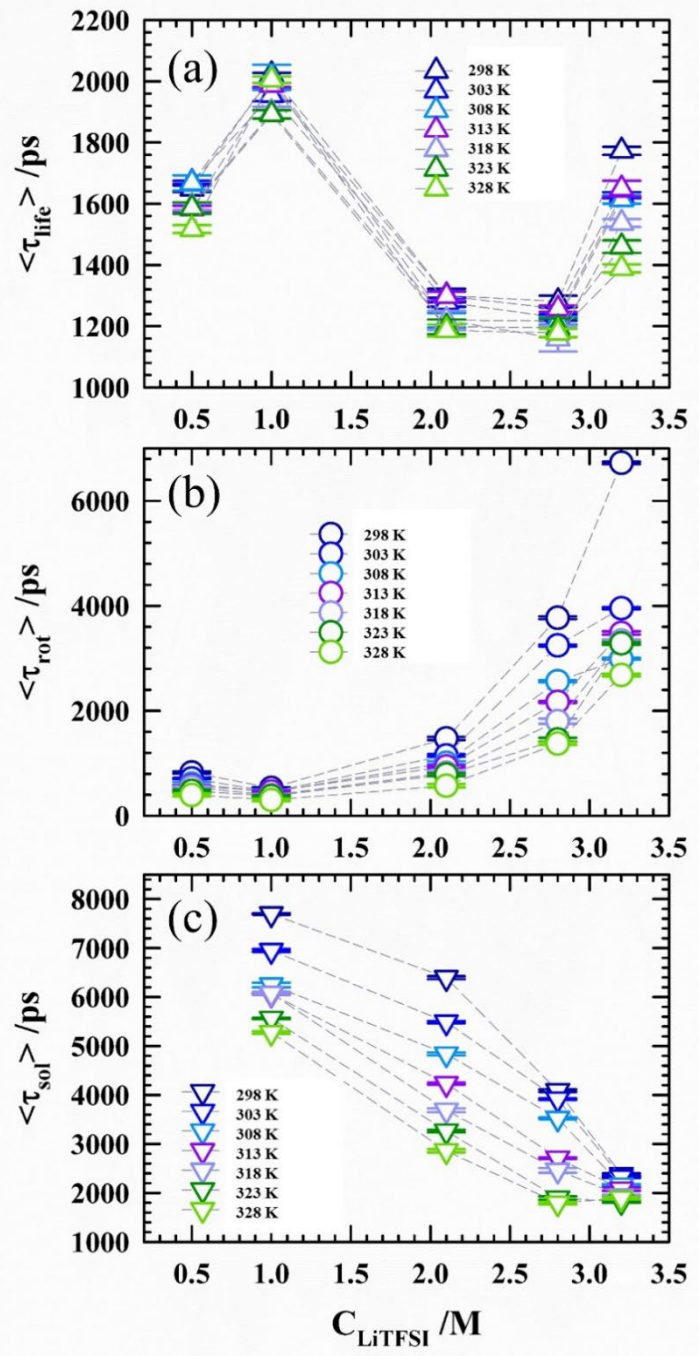

FIG. 4.3. Temperature dependent average (a) fluorescence lifetimes, (b) rotation times and (c) solvation times of C153 in G3/LiTFSI electrolyte solutions as a function of concentration of LiTFSI. Different colors have been used to denote different temperatures and dashed lines are for eye-guidance.

Another contributing factor is the weak hydrogen bonding capability of C153 in dipolar aprotic solvent, G3. The strong electron-withdrawing effect of the CF_3 group reduces the electron density on the carbonyl (C=O) group, making it less favorable for hydrogen bond formation with G3. This decreased hydrogen bonding interaction enhances the non-radiative decay pathways, further shortening the fluorescence lifetime.[57] This hypothesis is supported by the fluorescence lifetime data for C102 in G3 (see **Table 4.B.4**, Appendix 4.B). Unlike C153, C102 contains a CH_3 group instead of a CF_3 group. Due to inductive effect of CH_3 group C102 exhibits stronger hydrogen bonding interactions with G3 molecules. As a result, the fluorescence lifetime of C102 in G3 is significantly longer (~ 4 ns), consistent with its increased stabilization in the excited state.

Interesting point is that if LiTFSI electrolyte is added, they compete with solvent molecules for any weak interactions with the carbonyl group of C153. However, since the hydrogen bonding between C153 and G3 is already minimal, the addition of the electrolyte does not significantly alter the excited-state stabilization and lifetime of C153 (see **Table 4.1**). On the other hand, upon the addition of the electrolyte, Li^+ ions can strongly coordinate with the carbonyl group of C102, disrupting the existing hydrogen bonding network between C102 and G3. This disruption opens additional non-radiative decay pathways, leading to a significant reduction in the fluorescence lifetime of C102.

4.3.2.2 Dynamic Fluorescence Anisotropy Studies

Fig. 4.A.3 (Appendix 4.A) shows the fluorescence anisotropy, r(t) for C153 in neat G3 and G3/LiTFSI electrolyte solutions along with residuals (see **Fig. 4.A.4**, Appendix 4.A) and the fitting parameters are summarized in **Table 4.B.5** (Appendix 4.B). A bi- and tri-exponential function was used to fit the decay of C153 in G3/LiTFSI electrolyte solutions where as single exponential function is enough for fitting the rotational anisotropy decay coming from C153 in neat G3 solvent. The average rotational times become faster (see **Fig. 4.3 (b)**) in 1 M G3/LiTFSI electrolyte, where the ionic conductivity reaches its peak, indicating the most efficient Li^+ ion transport in the medium. Further increase of concentration of LiTFSI enhances the rotation time constant monotonically and slowest time-component is the guiding factor of average rotation times of

C153. These bi- and tri-phasic anisotropy decay of C153 reflects dynamic heterogeneity of the present electrolyte media. In contrast, the rotational anisotropy decays of C102 exhibit single-exponential behavior in neat G3 and bi-exponential in G3/LiTFSI electrolyte solutions. The r(t) decay profiles for C102, along with their corresponding exponential fitting parameters, are depicted in **Figure 4.A.3** (Appendix 4.A) and summarized in **Table 4.B.6**, (Appendix 4.B) respectively. The local environment around C102 is less sterically hindered, facilitating faster rotational dynamics compared to C153. This observation is corroborated by the fluorescence excited-state lifetimes of the two probes, discussed in previous section. The different behavior of these two probes suggests distinct microenvironments: for C102, the probe forms strong hydrogen bonds with G3 solvent molecules. Increasing LiTFSI concentration in G3 leads to an ~84% reduction in the fluorescence lifetime of C102, while its rotational correlation time increases by ~90%. In contrast, C153 displays a nearly invariant fluorescence lifetime as LiTFSI added to G3. However, its rotational correlation time increases significantly from ~1 ns to ~7 ns, indicative of a more restricted environment. This behavior suggests that C153 resides in close proximity to Li^+-solvent complexes, where the local solvent dynamics are significantly slowed due to the formation of ion-solvent complexes and higher-order ionic aggregates. These findings align with our earlier Raman spectroscopic investigations, which revealed structural changes in the solvent network driven by the formation of distinct ionic species as a function of LiTFSI concentration.[11] Such studies have highlighted the profound impact of ion pairing and solvent restructuring on the physicochemical properties of these electrolyte systems. The observed changes in rotational dynamics and fluorescence lifetimes thus provide complementary insights into the intricate interplay of Li^+ transport and ionic interactions in G3/LiTFSI electrolyte solutions.

4.3.2.3 Stokes-Shift Dynamics via TCSPC Set-up: Slow Temporal Evolution

Fig. 4.A.5 (a) (Appendix 4.A) displays representative fluorescence intensity decays at the blue (490 nm) and red (640 nm) ends of the emission spectrum for C153 dissolved in ~ 3.2 M G3/LiTFSI electrolyte solution at 298 K. A rapid decay is observed at the blue-end wavelength, while the red-end exhibits a characteristic rise followed by decay, an established hallmark of the dynamic Stokes shift phenomenon.[58] This shift reflects the time-dependent stabilization of the excited-state dipole as the surrounding solvent molecules reorganize. The initial non-equilibrium

solvation leads to a higher-energy emission (blue), which relaxes over time to a lower-energy state (red) as the solvation shell reorients. These dynamics provide direct insight into the local polarity, viscosity, and heterogeneity of the electrolyte environment surrounding the probe. **Fig. 4.4** presents the time-resolved emission spectra (TRES) of C153 in G3/LiTFSI solutions with varying LiTFSI concentrations at 298 K. Each panel also includes the corresponding steady-state emission spectra, shown as black dashed lines. Notably, these steady-state spectra are blue-shifted relative to the emission spectra recorded at $t = \infty$, indicating that the steady-state emissions originated from excited solute dye molecules in incompletely solvent-relaxed configurations.

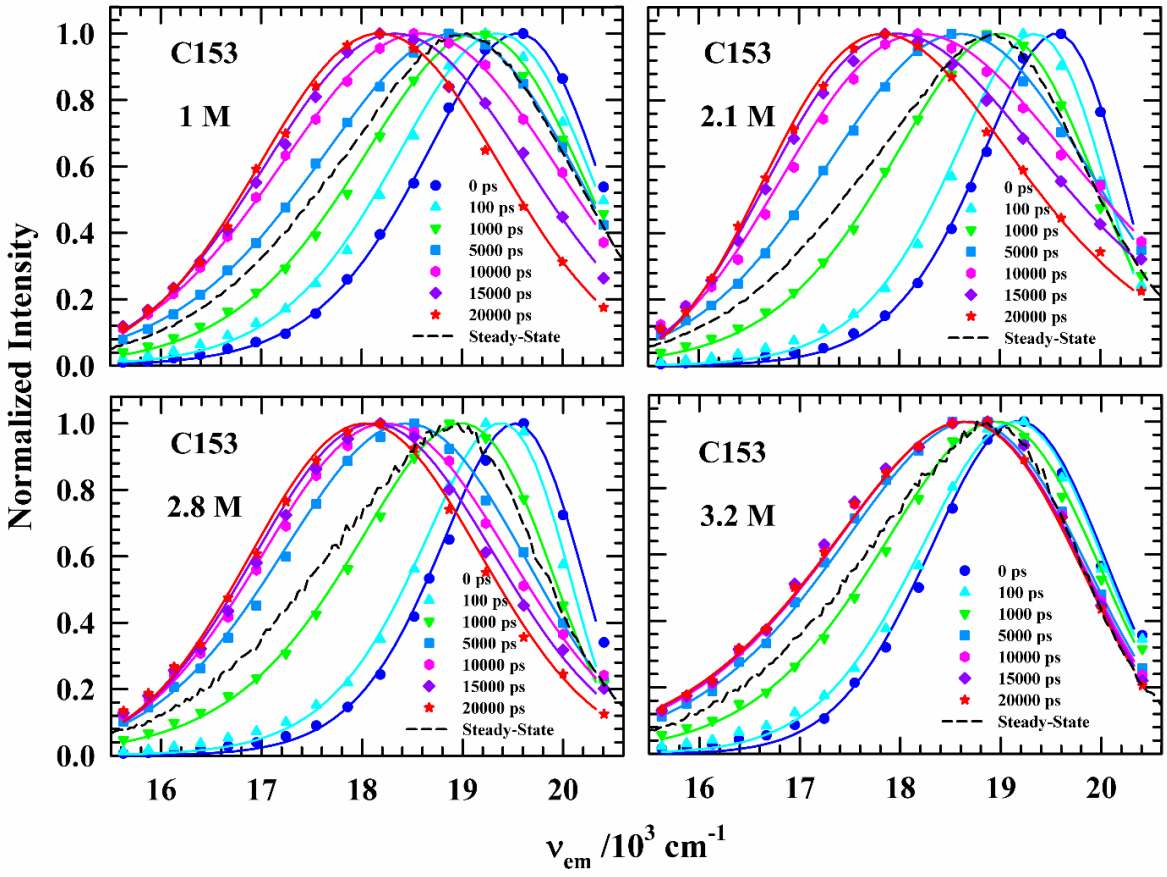

FIG. 4.4. Representative constructed time-resolved emission spectra (TRES) of C153 in G3/LiTFSI electrolyte solutions at various LiTFSI concentrations for different time intervals at 298 K. The steady state emission spectrum of C153 in electrolyte solutions are shown by black dashed lines. All representations are color-coded.

LiTFSI concentration dependent solvent response functions, S(t), determined from average peak frequencies of time-dependent emission spectrum of C153 in G3/LiTFSI electrolyte solutions at 298 K are presented in **Fig. 4.A.5 (b)** (Appendix 4.A) and their corresponding temperature dependent S(t) decays are shown in **Fig. 4.5**. The associated exponential fit parameters are summarized in **Table 4.B.8** (Appendix 4.B). The S(t) decays exhibit bi-exponential behavior, characterized by a fast component of ~ 80 - 300 ps with amplitudes of ~ 10 - 25 % and a dominant slower time-component of ~ 2 - 9 ns which governs the overall solvation dynamics. A consistent observation across all electrolyte compositions is that increasing temperature leads to a reduction in average solvation times while the amplitude contributions remain largely unaffected (see **Fig. 4.3 (c)**). This originates from temperature induced viscosity effect. Interestingly, with increasing LiTFSI concentrations, the fast timescale (τ_1^{sol}) progressively lengthens, whereas the slow timescale (τ_2^{sol}) decreases, resulting in an overall reduction of the average solvent relaxation times. The fast timescale (τ_1^{sol}) is attributed to the relaxation dynamics of G3-coordinated Li^+ ions. As the LiTFSI concentration increases, the formation of complex ionic species reduces the availability of free solvent molecules, restricting solvent mobility. This constraint slows the relaxation process, leading to an elongation of τ_1^{sol}.

Conversely, the slow component (τ_2^{sol}) reaches its maximum at ~ 1 M LiTFSI concentration, after which it decreases monotonically with further addition of LiTFSI. This trend likely reflects changes in the local medium dynamics, where increased ionic interactions and reduced solvent mobility leads to faster long-timescale relaxation. Such nanosecond-scale slow components are commonly observed in ionic liquids[58,59] and other electrolyte systems,[36] providing valuable insights into the structural relaxation and dynamic heterogeneity of the medium. The solvent response function measured using the ps-TCSPC setup does not fully capture the complete dynamic Stokes shift in these complex electrolyte systems. Note that **Table 4.B.9** (Appendix 4.B) summarizes the total Stokes shift dynamics of C153 in G3/LiTFSI solutions detected ($\Delta\nu_{obs}^{t}$) from TCSPC measurements and the corresponding estimated total shift ($\Delta\nu_{est}^{t}$) calculated using the Fee-Maroncelli method.[60] Due to the limited temporal resolution of the TCSPC setup (~ 85 ps), approximately 10 - 50% of the total dynamic Stokes shift is not detected, primarily missing the ultrafast components of solvent relaxation. To probe these missing ultrafast solvent dynamics, we

have employed a femtosecond-resolved streak camera detection technique with a significantly improved temporal resolution of ~ 500 fs. This approach enables the exploration of the sub-picosecond polar solvent response, providing a more comprehensive understanding of the complete solvation dynamics in G3/LiTFSI electrolyte solutions.

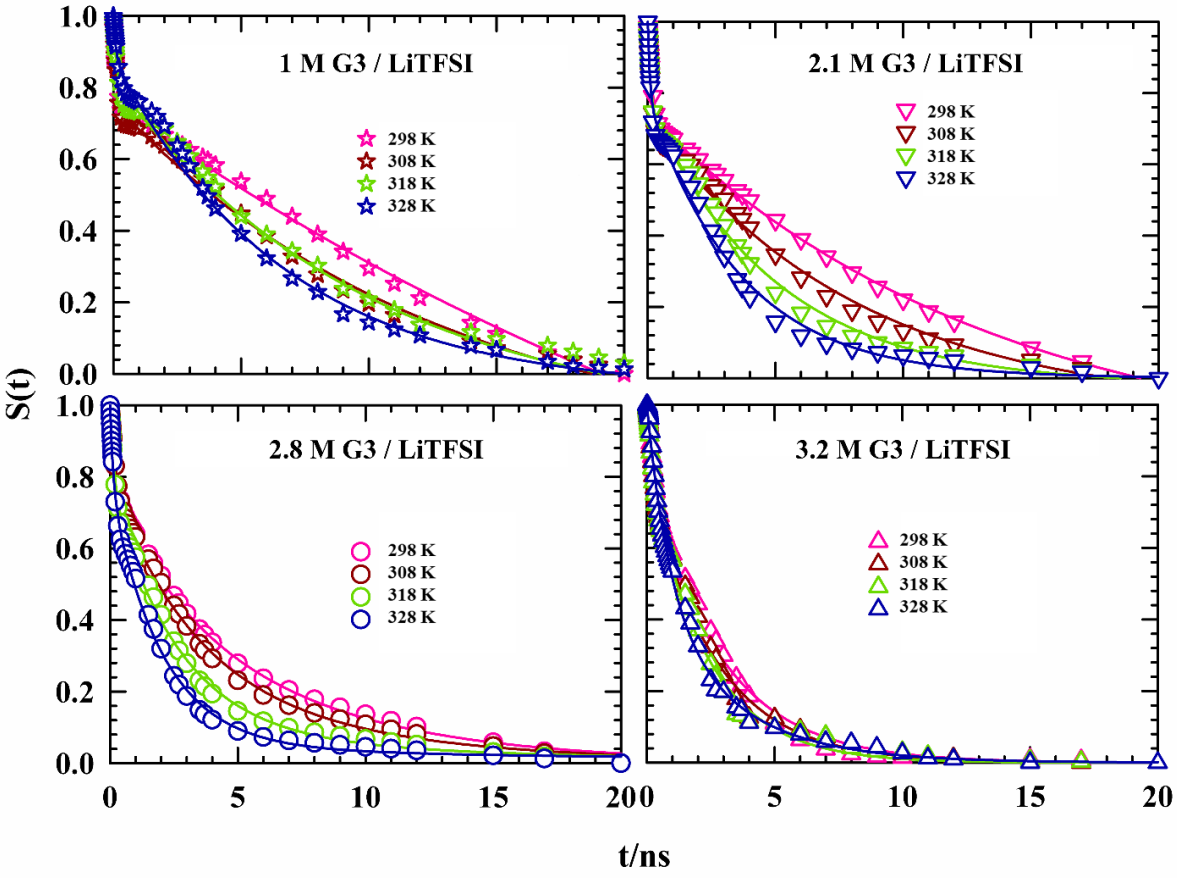

FIG. 4.5. Temperature dependent solvation response function, (S(t)) decay for C153 in G3/LiTFSI electrolyte solutions with different LiTFSI concentrations. All presentations are color coded.

4.3.2.4 Ultrafast Solvation Dynamics Probed via Streak Camera Set-up

To achieve comprehensive measurements of solvation dynamics through time-dependent Stokes shift analysis, we integrated femtosecond-resolved streak camera (fs-SC) data with picosecond-resolved TCSPC (ps- TCSPC) measurements. Representative three-dimensional streak images of C153 in G3/LiTFSI electrolyte solutions are presented in **Fig. 4.A.6** (Appendix 4.A). The

methodology for analyzing TRES and calculating the spectral response function, S(t), from streak images is described in detail elsewhere.[11]

TRES were extracted from streak camera images and combined with TCSPC data for C153 in G3/LiTFSI electrolyte solutions at concentrations ranging from 1 to 3.2 M. For the 0.5 M concentration, TRES data were obtained exclusively from the streak camera due to experimental constraints. The observed total fluorescence spectral shifts, or dynamic Stokes shifts, $\Delta\nu_{obs} = \nu_{t=0} - \nu_{t=\infty}$, are summarized in **Table 4.2**. A comparison of **Table 4.B.9** (Appendix 4.A) with **Table 4.2** reveals a noticeable reduction in the percentage of the missing dynamic Stokes shift when TCSPC data are integrated with streak camera measurements. This improvement highlights the ability of the streak camera technique to capture ultrafast polar solvent relaxation dynamics, thereby providing a more complete characterization of solvation processes when used in conjunction with TCSPC.

Table 4.2. Magnitudes of estimated ($\Delta\nu_{est}^{t}$) and observed ($\Delta\nu_{obs}^{Total}$) total dynamic Stokes shift, and the corresponding missing percentages for C153 in G3/LiTFSI electrolyte solutions at 298 K. % missed was calculated considering total spectral shift ($\Delta\nu_{obs}^{Total}$). $\Delta\nu_{obs}^{SC}$: Dynamic Stokes shift detected by streak camera set-up. $\Delta\nu_{obs}^{TCSPC}$: Dynamic Stokes shift detected by TCSPC technique.

C_{LiTFSI}/M	$\Delta\nu_{est}^{t}/10^3$ cm^{-1}	$\Delta\nu_{obs}^{SC}/10^3$ cm^{-1}	$\Delta\nu_{obs}^{TCSPC}/10^3$ cm^{-1}	$\Delta\nu_{obs}^{Total}/10^3$ cm^{-1}	% missed (total)
0.5*	0.151	0.122	-	0.122	19
1	1.717	0.148	1.376	1.524	11
2.1	2.426	0.183	1.730	1.913	21
2.8	1.986	0.194	1.494	1.688	15
3.2	0.889	0.199	0.544	0.743	16

*Measured only by using Streak Camera detector-based set-up.

Table 4.3 presents the multiexponential fit parameters of the solvent response function, S(t), characterizing ultrafast solvent relaxation dynamics obtained from streak camera measurements alone, as well as from combined fittings of streak camera and TCSPC data. The corresponding combined S(t) decays are shown in **Fig. 4.6**. The ultrafast dynamics exhibit two distinct

timescales: a fast component in the range of ~ 5 - 15 ps and a slower component between ~ 100 - 250 ps. Notably, at 1 M LiTFSI concentration, the average solvation time (<τ_s>) reaches its maximum (~ 190 ps), beyond which further increases in electrolyte concentration do not significantly alter the solvation timescales. This observation suggests that the ultrafast relaxation components remain largely unaffected by the addition of LiTFSI in G3.

Table 4.3. Multi-exponential fit parameters of solvation response function $S(t)$, for C153 in G3/LiTFSI electrolyte solutions at 298 K using streak camera technique only and also combining streak camera set-up with TCSPC.

Streak Camera set-up							
C_{LiTFSI}/M	a_1	τ_1/ps	a_2	τ_2/ps	a_3	τ_3/ps	$< \tau_{Sol} >$ /ps
0.5	0.71	17.39	0.29	119.05	-	-	46.87
1	0.23	7.278	0.77	243.90	-	-	189.48
2.1	0.37	16.58	0.63	158.73	-	-	106.13
2.8	0.30	16.37	0.70	147.06	-	-	107.85
3.2	0.27	15.31	0.73	136.99	-	-	104.14
Streak Camera + TCSPC set-up							
C_{LiTFSI}/M	a_1	τ_1/ps	a_2	τ_2/ps	a_3	τ_3/ps	$< \tau_{Sol} >$ /ps
1	0.35	523	0.65	9311	-	-	6235
2.1	0.36	586	0.64	8666	-	-	5757
2.8	0.46	678	0.54	6386	-	-	3760
3.2	0.29	437	0.62	2835	0.09	16	1886

When the ultrafast streak camera data are combined with the relatively slower dynamics captured by the TCSPC measurements, the overall solvation dynamics are predominantly influenced by the TCSPC data due to its sensitivity to longer timescales. Consistent with previous observations, solvation timescales decrease with increasing LiTFSI concentration. Importantly, the incorporation of streak camera data does not alter this trend; rather, it reinforces the observation of progressively

faster solvation dynamics with increasing LiTFSI concentration, providing a more comprehensive picture of the medium relaxation behavior across different timescales.

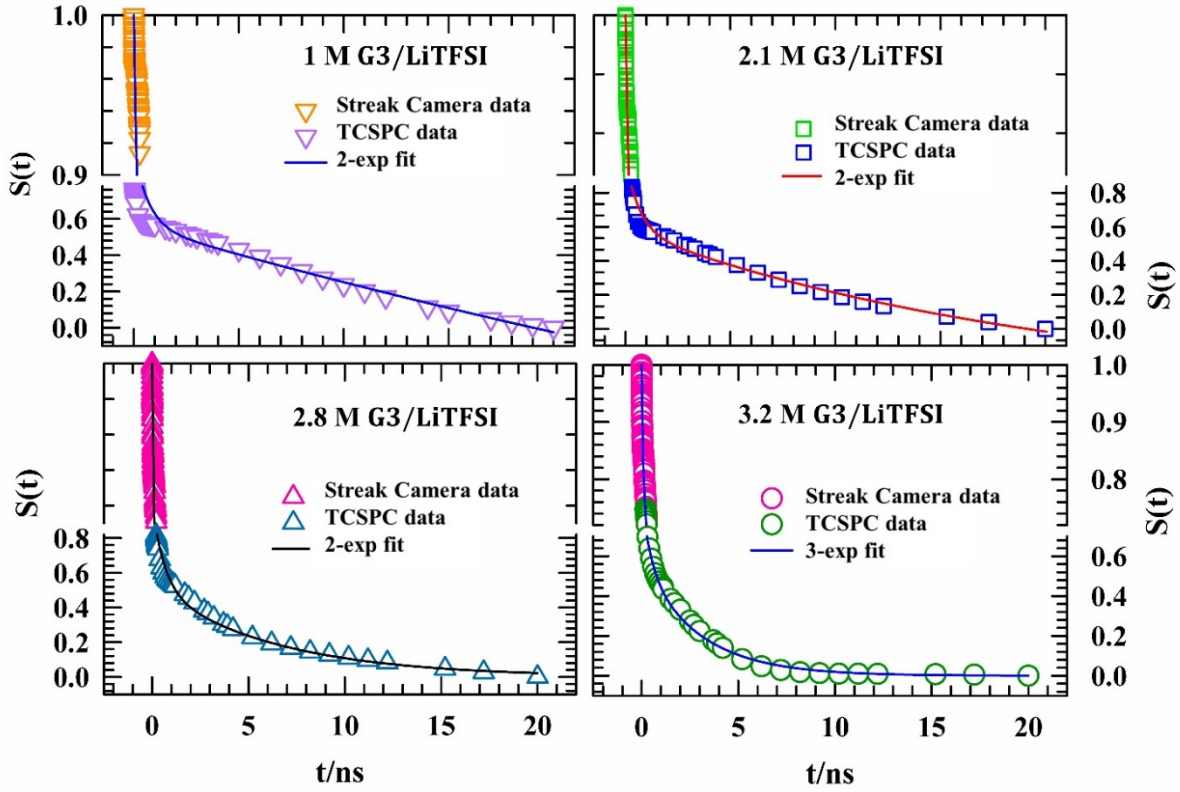

FIG. 4.6. Solvation response function, (S(t)) decay for C153 in G3/LiTFSI electrolytes with different LiTFSI concentrations at 298 K. Data collected from streak camera and TCSPC are symbolized and color-coded. Solid lines represent the combined fit for each composition.

4.3.3 Electrolyte Induced Decoupling of Viscosity-Temperature Scaling in Fluorescence Dynamics and Ionic Conductivity

Ion-solvent interactions and microscopic reorganization of the solvation shell influence ion conductivity in electrolytes. This could be understood in terms of electrolyte-induced decoupling of medium viscosity from fluorescence dynamics. **Fig. 4.7** illustrates the temperature dependence of experimental ion conductivity (σ), excited-state lifetimes ($<\tau_{life}>$), rotation times ($<\tau_{rot}>$) and solvation times ($<\tau_{sol}>$) of C153 at varying LiTFSI concentrations plotted as a function of temperature - reduced medium viscosity, (η/T) in a double logarithmic function. The dynamic heterogeneity parameter, represented by the varying slopes (p-values) of the measured quantities withη/T, yields different fractional power values when fitting the data to $A \propto (\eta/T)^p$, where A = $< \sigma >, < \tau_{life} >, < \tau_{rot} >, < \tau_{sol} >$. This suggests differences in viscosity coupling due to distinct solution structures at each electrolyte concentration.

In case of the fluorescence lifetimes (see **Fig. 4.7 (b)**) of C153 in G3/LiTFSI electrolytes exhibit a pronounced fractional decoupling (p ~ 0.1) from viscosity, indicating that the fluorescence dynamics of C153 are minimally influenced by the medium viscosity. Next, **Fig. 4.7 (c)** describes the interplay between solute rotational dynamics and medium friction in G3/LiTFSI electrolyte solutions, as we have plotted $< \tau_{rot} >$/ps of C153 against the temperature-scaled viscosity ((η/T)) in a log-log format. At low LiTFSI concentration (~ 0.5 M), the rotational diffusion of C153 follows a near stick boundary condition, as indicated by the p-value of ~ 1.02. However, with increasing LiTFSI concentration, the system transitions to a sub-slip regime, characterized by a fractional viscosity dependence of rotational dynamics, with p-values ranging from ~ 0.4 to 0.8. This fractional scaling behavior reflects pronounced temporal heterogeneity in the rotational relaxation dynamics of C153, consistent with observations in other complex systems such as concentrated electrolyte solutions, deep eutectic solvents and water–alcohol binary mixtures.[35,41,61–64]

The coupling of solute rotation to hydrodynamic friction under stick and slip boundary conditions was evaluated using the Stokes-Einstein-Debye (SED) relationship,[65–67] $\tau_{rot} = \eta V f C / k_B T$, where

the volume (V_{C153}) of C153 is 246 Å^3, the shape factor (f_{C153}) is 1.71, and the stick ($C_{stick}^{solute} = 1$) and slip ($C_{slip}^{C153} = 0.24$) coefficients are used.[68] This is shown in **Fig. 4.7 (c)** and the calculated numerical values are summarized in **Table 4.B.7** (Appendix 4.B), confirm a clear deviation from hydrodynamic predictions, underscoring partial decoupling of solute rotation from medium viscosity. Such decoupling likely arises from non-hydrodynamic contributions, such as angular orientation jumps and inertia-driven motions, reflecting the complex dynamics in these electrolyte solutions.[69–72]

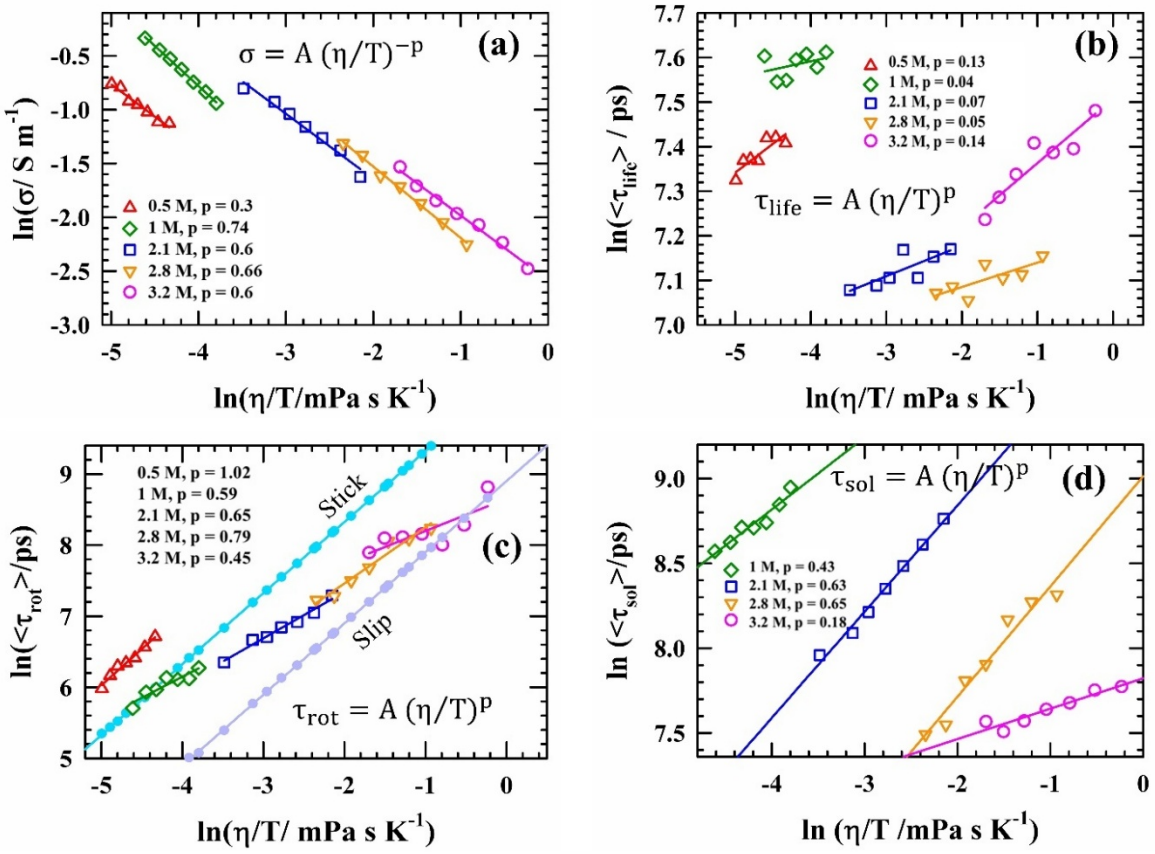

FIG. 4.7. (η/T) dependence of (a) ionic conductivity, σ/s m^{-1}, (b) average fluorescence lifetime, <τ_{life}>/ps, (c) average rotation time, <τ_{rot}>/ps and (d) average solvation time, <τ_{sol}>/ps for C153 in G3/LiTFSI electrolyte systems. Solid lines passing through data points represent the fits. All presentations are color-coded.

Fig. 4.7 (d) illustrates the extent of decoupling between the solvent relaxation times of C153 and viscosity in G3/LiTFSI electrolyte solutions, as reflected by p-values ranging from ~ 0.2 - 0.7. This partial viscosity decoupling behavior again indicates significant temporal heterogeneity in the solvent relaxation dynamics within these electrolytic environments.

Notably, at 1 M LiTFSI concentration, the dynamic heterogeneity parameter (p-value) exhibits distinct values depending on the measured property: it reaches a maximum (p ~ 0.74) when derived from ionic conductivity, suggesting a weak decoupling of ion transport from bulk viscosity. In contrast, the p-value is minimal (p ~ 0.04) when calculated from fluorescence lifetimes, indicating negligible viscosity dependence. For rotational diffusion and solvation dynamics, p-values are ~ 0.5, signifying moderate dynamic heterogeneity. This variation can be attributed to the differential sensitivity of these processes to local microstructural dynamics. Ionic conductivity (σ) is strongly influenced by ion-solvent interactions and local structural fluctuations, leading to a higher p-value. In contrast, $<\tau_{life}>$ is largely governed by electronic transitions, which are less affected by viscosity changes. Rotational and solvation dynamics fall in between, reflecting a balance between local microenvironment effects and bulk properties.

Furthermore, the activation energies (E_a) associated with σ, solute (C153) rotation dynamics, solvation and medium viscosity were analyzed and presented in **Fig. 4.8** with the corresponding values summarized in **Table 4.4**. If solute rotation and solvation dynamics were governed solely by viscosity-induced microscopic friction, the values of E_a^{η} and E_a^{rot}/ E_a^{sol} would be expected to be comparable. However, in G3/LiTFSI solutions, the E_a^{η} ranges from 15 - 40 kJ/mol, which is approximately twice that of C153 rotational dynamics (E_a^{rot} ~ 12 – 40 kJ/mol), indicating a partial decoupling of rotational motion from bulk viscosity.

Interestingly, the activation energy associated with solvation dynamics ($E_a^{\tau_{sol}}$) exhibits a distinct trend. For the 1 M LiTFSI electrolyte solution, $E_a^{\tau_{sol}}$ is nearly half that of both E_a^{η} and E_a^{σ}. This suggests that solvation dynamics are influenced not only by bulk viscosity but also by local

structural fluctuations and ion-solvent interactions, which facilitate faster solvent reorganization. The observed connection between ionic conductivity, viscosity, rotation, and solvation dynamics implies that while ion transport remains strongly coupled to viscosity through frictional resistance, rotational and solvation processes are partially decoupled. This decoupling arises from heterogeneous microenvironments within the electrolytes, where localized dynamics, ion pairing, and solvent-ion coordination significantly modulate the energy barriers for rotational and solvation processes compared to bulk viscous flow.

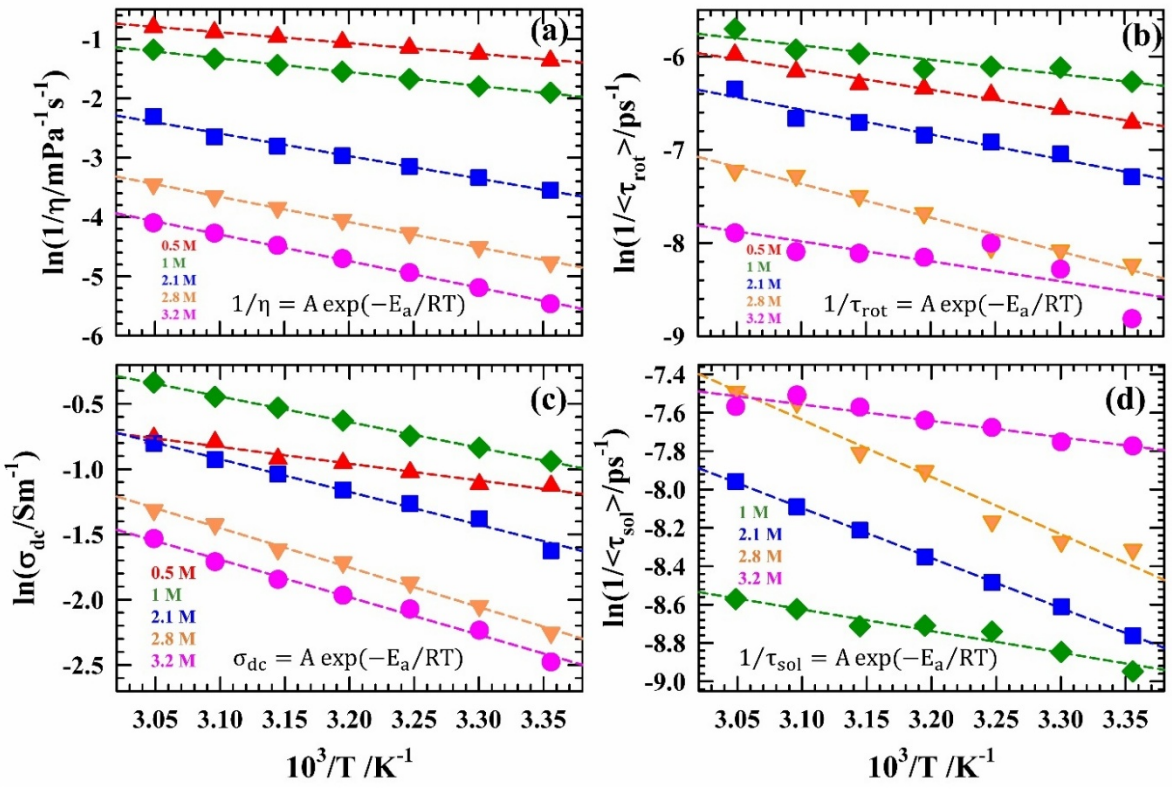

FIG. 4.8. Arrhenius-type temperature dependence of (a) medium viscosity, (b) average rotation time ($<\tau_{rot}>$/ps), (c) ionic conductivity (σ_{dc}/S m^{-1}), and (d) average solvation time, $<\tau_{sol}>$/ps for G3/LiTFSI electrolyte solutions at various LiTFSI concentrations. Dashed lines passing through the data points represent linear fits. Different colors have been used for different compositions.

Table 4.4. Estimated activation energies (E_a) calculated from medium viscosity (η)[#], ion conductivity (σ)[#], rotation (τ_{rot}) and solvation (τ_{sol}) dynamics for G3/LiTFSI electrolyte solutions at various temperatures.

C_{LiTFSI}/M	E_a^{η}/ kJ mol^{-1}	E_a^{σ}/ kJ mol^{-1}	$E_a^{\tau rot}$/ kJ mol^{-1}	$E_a^{\tau sol}$/ kJ mol^{-1}
0.5	15.11	10.71	18.12	-
1	19.25	16.30	11.39	9.36
2.1	31.55	20.91	22.12	21.63
2.8	35.42	25.17	30.13	24.80
3.2	37.17	23.90	17.79	7.08

#Data collected from Ref. 11.

4.3.4 Correlating Experimental Ion conductivity and Solution Dynamics

Fig. 4.9 illustrates the relationship between measured ionic conductivity (σ) and both the rotational and solvation times of C153 in the studied electrolyte solutions. These parameters exhibit a clear correlation, described by the relation, $\sigma \propto (\tau^{rot})^{-m}$ where m ~ 0.6 (see **Fig. 4.9 (a)**) for rotational dynamics across all the compositions. Additionally, the long-time component of rotational dynamics (τ_2^{rot}), which reflects the overall medium dynamics, displays a similar dependence on σ with the value of m ~ 0.5 (see **Fig. 4.9 (b)**), as expected. This observed coupling between Li^+ ion transport and solute (C153) rotational dynamics highlights the interconnected relationship between translational and rotational motions in electrolyte solutions at these concentrations, suggesting that both processes are influenced by common microstructural and dynamic factors within the medium.

Fig. 4.9 (c) and **Fig. 4.9 (d)** reveal a distinct correlation pattern between solvation dynamics and experimental ionic conductivity, differing significantly from the trends observed for rotational dynamics. Unlike rotational relaxation, where a consistent dependency across compositions is evident, solvation timescales exhibit composition-specific behavior. The relationship follows $\sigma \propto (\tau^{sol})^{-m}$, where the dependency is strongest at 1 M LiTFSI concentration, as indicated by the highest m-value (~ 3), coinciding with the highest σ at that composition. This suggests that, at this

concentration, ion transport is highly sensitive to changes in solvation dynamics. However, with further increases in LiTFSI concentration, the m-value decreases, indicating a reduced influence of solvation timescales on ionic conductivity. A similar trend is observed for the long-time component of solvation dynamics, which predominantly governs the overall solvent relaxation behavior.

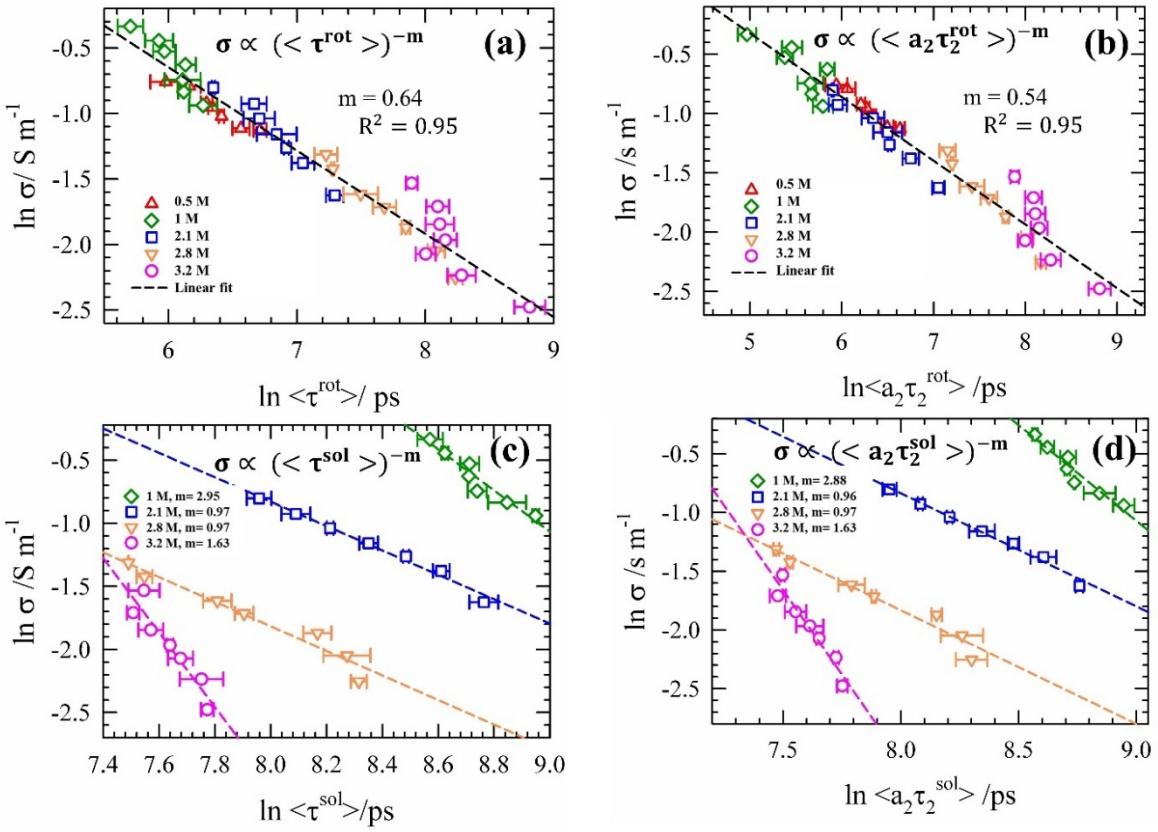

FIG. 4.9. Correlation between measured ionic conductivity and (a) average rotation times, (b) the long-time component of rotation times, (c) average solvation times, and (d) long-time component of solvation timescales, obtained from TCSPC set-up. Dashed lines represent the linear fits and slopes (m) are shown in insets. All the compositions are color-coded.

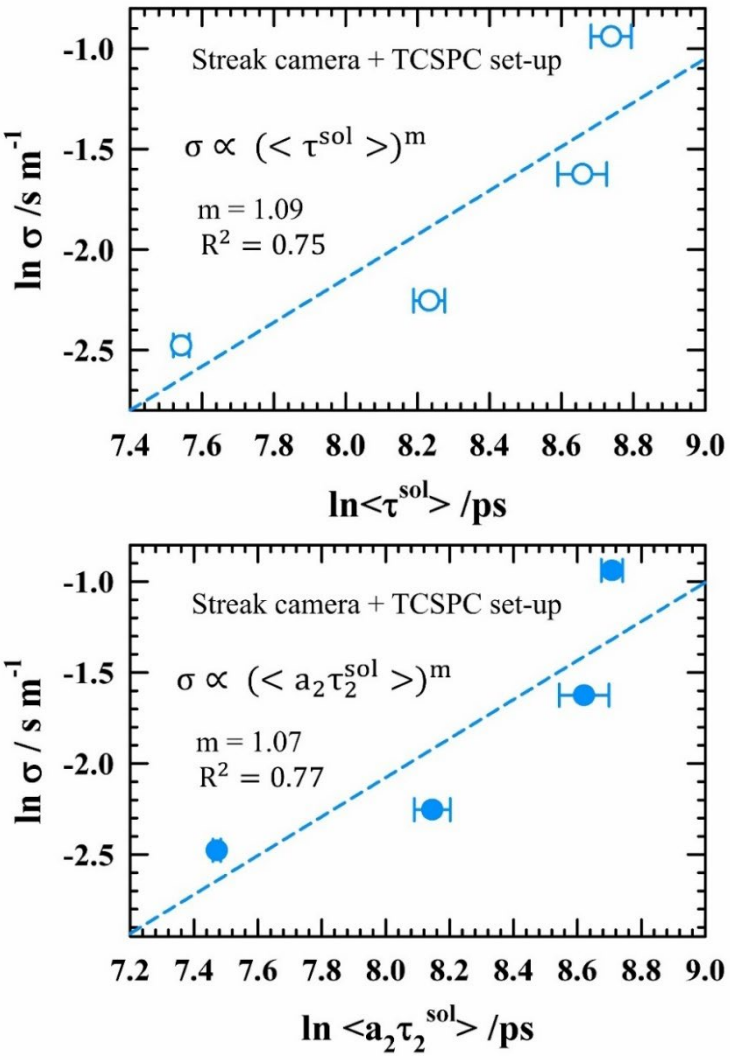

FIG. 4.10. Correlation between measured ionic conductivity and average solvation times (upper panel, open circles) as well as the long-time component of solvation times (lower panel, filled circles), obtained from the combined fitting of streak camera and TCSPC data in G3/LiTFSI electrolyte solutions at 298 K. Dashed lines represent the linear fits and slopes (m) and quality of fitting (R^2) are shown in insets.

At moderate electrolyte concentration (~ 1 M), efficient ion transport is strongly linked to solvation dynamics, where rapid solvent reorganization and optimal ion - solvent interactions facilitate the highest ionic conductivity. In contrast, at higher concentrations, the formation of complex ion aggregates or, stronger ion pairing reduces the role of solvation dynamics, leading to a weaker

correlation with σ. This highlights the shifting balance between solvation-mediated ion transport and ion-ion interactions as the electrolyte concentration varies.

The correlation between σ and combined solvation dynamics data, obtained from streak camera and TCSPC measurements, are presented in **Fig. 4.10**. Due to experimental constraints, temperature-dependent measurements could not be performed with the streak camera, limiting our solvation dynamics data to concentration-dependent studies. The correlation between σ and the combined solvation timescales follows the relation, $\sigma \propto (\tau^{sol})^{m}$ with a positive m-value of ~ 1.1. This indicates a distinct mechanistic relationship between ion transport and solvation dynamics compared to rotational relaxation, with solvation reorganization actively facilitating ion mobility. The comprehensive influence of complete solvation dynamics, including both fast and slow components, plays a crucial role in enabling efficient ion transport, ultimately contributing to the effective ionic conductivity observed in these electrolyte systems.

4.4 Summary

This study provides a comprehensive analysis of the dynamic heterogeneity in fluorescence dynamics and its impact on Li^{+} transport in G3/LiTFSI electrolytes. The correlation between ion conductivity and the coupled rotation-solvation dynamics has been systematically established using time-resolved fluorescence spectroscopy *via* TCSPC and streak camera techniques. Steady-state UV-vis absorption and fluorescence spectroscopy with C153 reveal the presence of ion-induced moderate spatial heterogeneity (~ 300 cm^{-1}) in these electrolyte systems, highlighting the structural complexity at the molecular level.

The bi-/tri-phasic anisotropy decay and bimodal solvation dynamics reveal a pronounced temporal heterogeneity in Li-ion battery electrolytes. Notably, the long-time component, which governs the overall medium dynamics, exhibits a clear dependence on ion conductivity. The fractional viscosity dependence observed in solution viscosities, rotation times and solvation times further underscore the intricate interplay between medium dynamics and ionic transport mechanisms. The

1 M LiTFSI electrolyte composition exhibits distinct transport and dynamic properties, characterized by the highest ion conductivity, the longest fluorescence lifetime, and the shortest rotational times addressed by suing C153. Additionally, solvation dynamics are notably extended, with ultrafast components (sub-10 ps) captured by the streak camera and slower nanosecond-scale dynamics revealed through the combined analysis of TCSPC and streak camera measurements.

These findings emphasize the crucial role of complete solvation dynamics (including both fast and slow timescales) in facilitating efficient ion transport and underscore the importance of understanding local medium dynamics and ion-solvent interactions in Li-ion battery electrolytes. Insights from this study provide valuable guidance for designing next-generation electrolytes with optimized conductivity and minimal side reactions. Future work, including extensive molecular dynamics simulations, is essential to gain deeper mechanistic insights and further refine electrolyte formulations for advanced energy storage applications.

Appendix 4.A

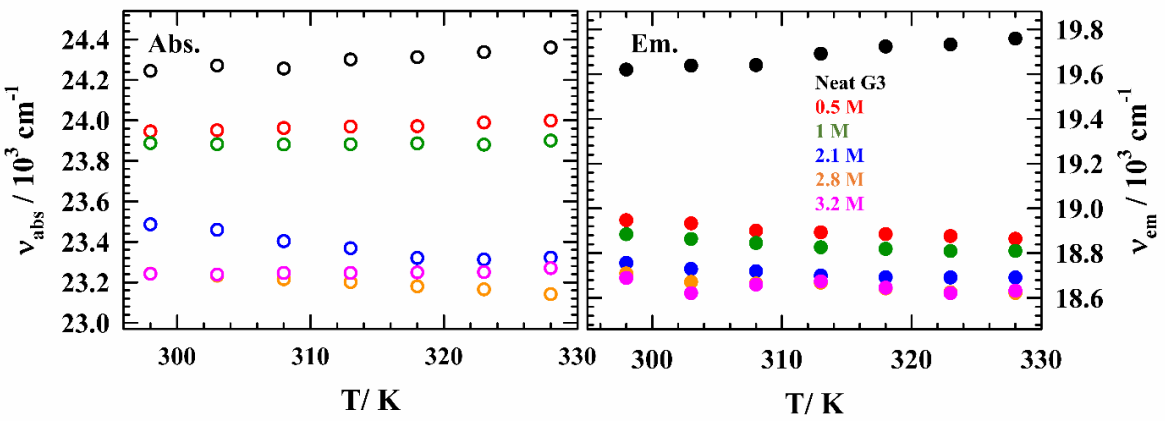

FIG. 4.A.1. Temperature dependent steady-state absorption and emission frequencies of C153 in G3/LiTFSI electrolyte at different LiTFSI concentrations. All compositions are color-coded.

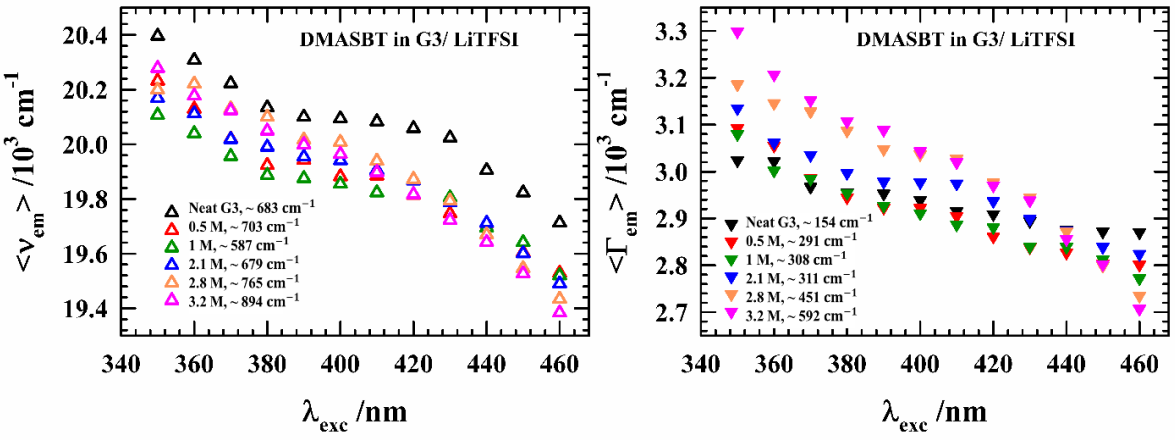

FIG. 4.A.2. LiTFSI concentration induced λ_{exc} dependent steady state emission frequencies (left panel) and spectral widths (right panel) of DMASBT in G3/LiTFSI electrolyte solutions. The value of total shift is shown in inset of each plot.

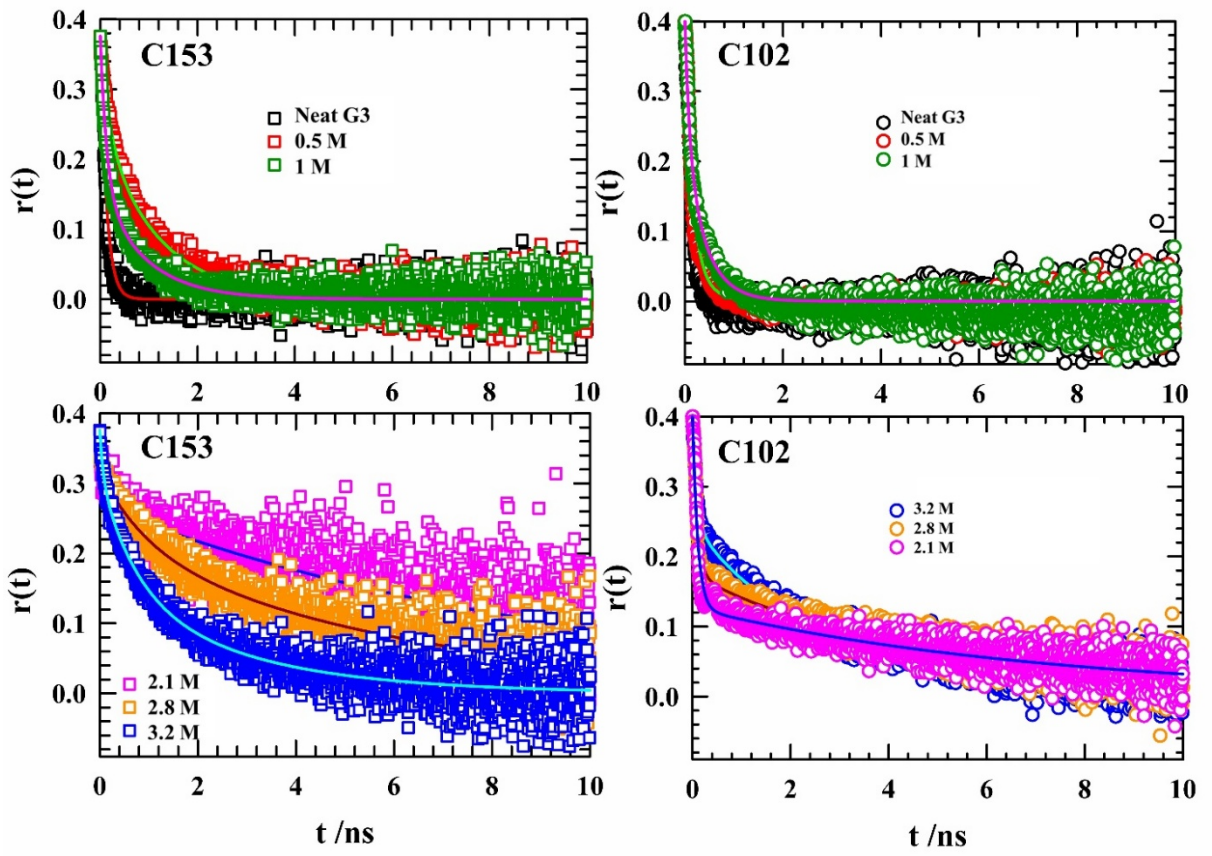

FIG. 4.A.3. The r(t) decays of C153 (left panel) and C102 (right panel) in G3/LiTFSI electrolyte solutions at different LiTFSI concentrations. Solid lines going through the data points represent multi-exponential fits. Presentations are color-coded.

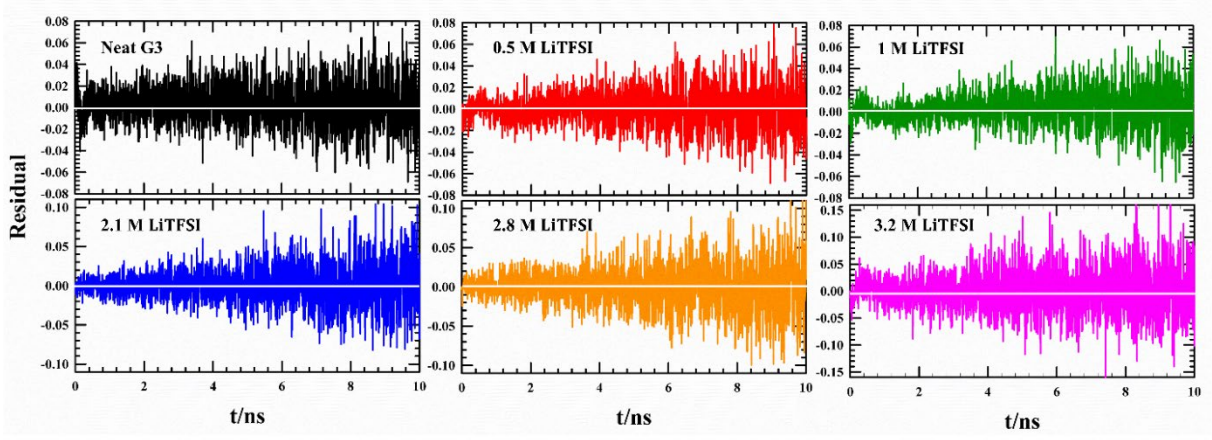

FIG. 4.A.4. Residuals for r(t) decay fits of C153 in G3/LiTFSI electrolyte solutions at 298 K. All compositions are color-coded.

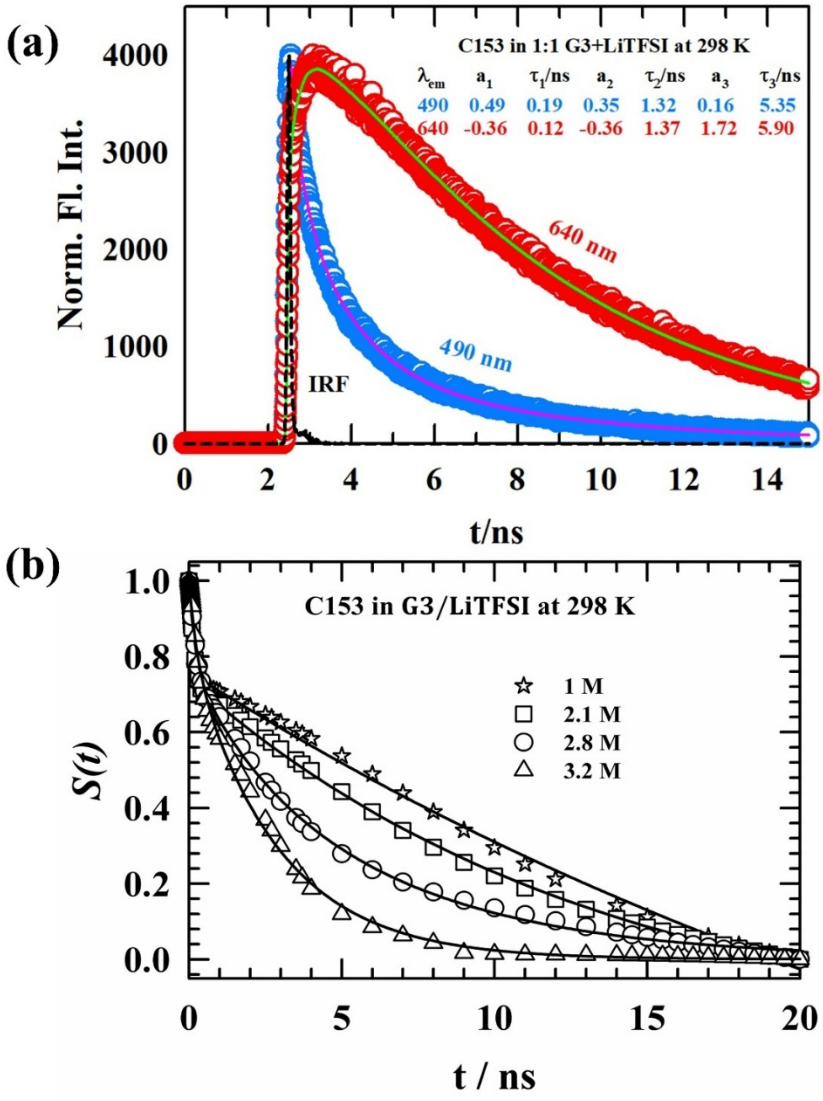

FIG. 4.A.5. (a) Representative time-dependent fluorescence intensity decays of C153 in G3/LiTFSI electrolyte solutions, collected at blue (490 nm) and red end (640 nm) wavelengths with respect to the peak wavelength of steady-state emission spectrum at 298 K. Black dashed line depicts instrument response function (IRF) and the exponential fit parameters are shown in the inset. All presentations are color-coded. (b) Solvation response function, (S(t)) decay for C153 in G3/LiTFSI electrolytes with different LiTFSI concentrations at 298 K. All compositions are symbolized and solid lines through the data points present the fit.

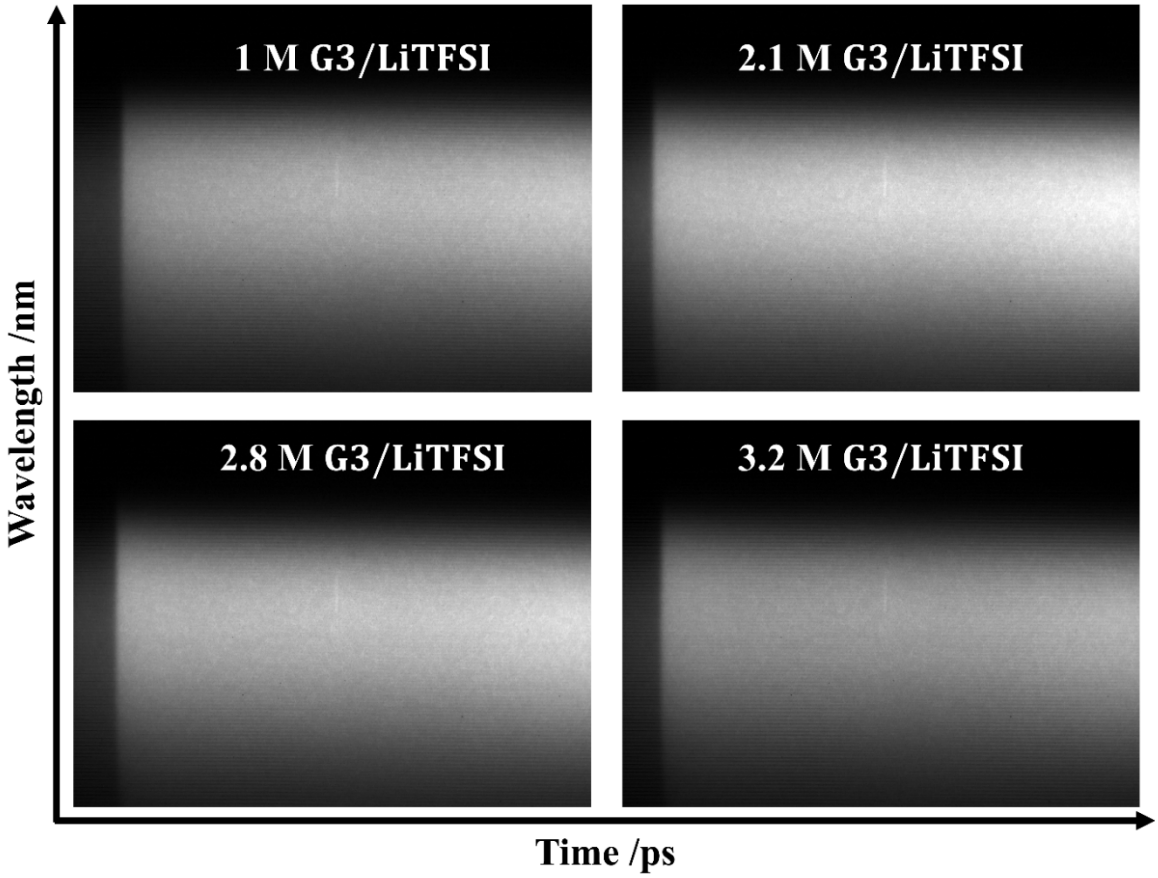

FIG. 4.A.6. Representative three-dimensional streak camera images of fluorescence decay of C153 in G3/LiTFSI electrolyte solutions with different compositions indicated in each image.

Appendix 4.B

Table 4.B.1. Steady-state absorption, emission frequencies[a] ($\nu_{abs/em}$) and spectral widths (FWHM)[b] ($\Gamma_{abs/em}$) of C153 in G3/LiTFSI electrolyte solutions at 298 K.

LiTFSI / M	ν_{abs} (10^3 cm^{-1})	ν_{em} (10^3 cm^{-1})	Γ_{abs} (10^3 cm^{-1})	Γ_{em} (10^3 cm^{-1})
0	24.24	19.62	4.01	2.76
0.5	23.95	18.95	4.13	2.82
1	23.89	18.88	4.30	2.77
2.1	23.49	18.76	3.88	2.57
2.8	23.24	18.71	4.07	2.53
3.2	23.24	18.69	4.23	2.51

[a]Uncertainty in average spectral frequencies is ± 100 cm^{-1}.

[b]FWHM represents full width half maxima of the spectra and uncertainty in spectral widths is ± 100 cm^{-1}.

Table 4.B.2. Exponential fitting parameters of average lifetimes of DMASBT at various compositions in G3/LiTFSI electrolyte solutions measured at ~ 298 K.

C_{LiTFSI}/ M	a_1	τ_1/ns	a_2	τ_2/ns	$<\tau_{life}>$/ps
0	-	-	-	-	61
0.5	-	-	-	-	68
1	-	-	-	-	74
2.1	0.99	0.1	0.01	1.28	112
2.8	0.98	0.15	0.02	0.59	159
3.2	0.96	0.16	0.04	0.65	180

Table 4.B.3. Exponential fitting parameters of average lifetimes ($< \tau_{life} >$/ps) of C153 at various compositions in G3/LiTFSI electrolyte solutions measured at different temperatures (298-328 K).

T/K	a_1	τ_1/ps	a_2	τ_2/ps	a_3	τ_3/ps	$<\tau_{life}>$/ps
Neat G3							
298	0.70	19	0.03	414	0.27	5777	1586
303	0.67	190	0.04	423	0.29	5779	1820
308	0.64	201	0.03	412	0.33	5769	2045
313	0.55	260	0.04	436	0.41	5747	2517
318	0.41	350	0.05	400	0.54	5721	3253
323	0.33	440	0.04	551	0.63	5715	3768
328	0.20	550	0.05	479	0.75	5676	4391
0.5 M G3/LiTFSI							
298	0.45	133	0.30	1289	0.25	4810	1649
303	0.44	130	0.30	1252	0.26	4760	1670
308	0.43	138	0.33	1319	0.24	4890	1668
313	0.44	118	0.32	1226	0.24	4749	1584
318	0.42	130	0.35	1247	0.23	4781	1591
323	0.42	132	0.36	1257	0.22	4898	1586
328	0.43	135	0.37	1267	0.20	4951	1517
1 M G3/LiTFSI							
298	0.39	160	0.33	1943	0.28	4709	2022
303	0.38	155	0.37	1836	0.25	4869	1955
308	0.32	134	0.40	1623	0.28	4719	2013
313	0.29	135	0.44	1502	0.27	4770	1988
318	0.29	130	0.48	1462	0.23	5038	1898
323	0.27	121	0.49	1348	0.24	4997	1892
328	0.21	142	0.53	1253	0.26	5043	2005
2.1 M G3/LiTFSI							
298	0.54	188	0.23	1388	0.22	3996	1300
303	0.54	166	0.28	1451	0.18	4343	1278
308	0.54	154	0.28	1365	0.18	4187	1219
313	0.51	148	0.32	1360	0.17	4630	1298
318	0.51	131	0.34	1264	0.15	4815	1219
323	0.50	130	0.36	1200	0.14	5011	1198
328	0.48	118	0.38	1094	0.14	5099	1186
2.8 M G3/LiTFSI							
298	0.53	210	0.28	1106	0.19	4525	1281
303	0.55	211	0.28	1151	0.17	4647	1228
308	0.55	193	0.28	1085	0.17	4751	1218
313	0.56	192	0.27	1105	0.17	5006	1257
318	0.58	176	0.27	1067	0.15	5128	1159
323	0.57	164	0.27	982	0.16	5228	1195
328	0.57	154	0.27	927	0.16	5252	1178
3.2 M G3/LiTFSI							
298	0.39	200	0.33	1006	0.28	4869	1773
303	0.47	212	0.31	1145	0.22	5332	1628
308	0.48	202	0.30	1102	0.22	5395	1614
313	0.49	200	0.28	1074	0.23	5437	1649
318	0.50	178	0.28	962	0.22	5358	1537
323	0.51	158	0.28	890	0.21	5383	1460
328	0.54	150	0.26	869	0.20	5411	1389

Table 4.B.4. Fluorescence lifetimes ($<\tau_{life}>$/ns) of C102 in G3/LiTFSI electrolytes at 298 K[c]

C_{LiTFSI}/M	a_1	τ_1/ns	a_2	τ_2/ns	a_3	τ_3/ns	$<\tau_{life}>$/ns
0	-	-	0.02	1.345	0.98	3.714	3.67
0.51	0.64	0.064	0.27	1.178	0.09	4.236	0.74
1.00	0.65	0.061	0.25	1.164	0.10	4.183	0.75
2.06	0.73	0.052	0.14	0.669	0.13	4.245	0.68
2.79	0.83	0.031	0.11	0.544	0.06	4.162	0.34
3.17	0.94	0.018	0.04	0.565	0.02	3.930	0.12

[c]Uncertainty ± 5%

Table 4.B.5. Exponential fitting parameters of average rotation times, $< \tau_{rot} >$/ps of C153 at various compositions of G3/LiTFSI electrolyte solutions at different temperatures (298 - 328 K).

Neat G3							
T/K	a_1	τ_1/ps	a_2	τ_2/ps	a_3	τ_3/ps	$< \tau_{rot} >$/ps
298	1	129	-	-	-	-	129
303	1	109	-	-	-	-	109
308	1	111	-	-	-	-	111
313	1	99	-	-	-	-	99
318	1	97	-	-	-	-	97
323	1	83	-	-	-	-	83
328	1	83	-	-	-	-	83
0.5 M G3/LiTFSI							
298	0.34	178	0.66	1155	-	-	823
303	0.33	139	0.67	990	-	-	709
308	0.32	108	0.68	846	-	-	610
313	0.32	124	0.68	778	-	-	569
318	0.31	147	0.69	721	-	-	543
323	0.33	140	0.67	639	-	-	474
328	0.22	66	0.78	488	-	-	395
1 M G3/LiTFSI							
298	0.43	90	0.54	609	0.03	5379	529
303	0.41	66	0.55	530	0.02	6803	455
308	0.46	114	0.51	563	0.03	3693	450
313	0.44	104	0.55	627	0.01	7076	461
318	0.58	156	0.40	543	0.02	4156	391
323	0.52	95	0.42	559	0.06	1509	375
328	0.58	140	0.36	400	0.06	1244	300

2.1 M G3/LiTFSI							
298	0.17	71	0.41	2816	0.42	726	1472
303	0.24	47	0.31	2760	0.45	628	1149
308	0.29	124	0.29	2344	0.42	700	1010
313	0.17	57	0.34	1957	0.49	535	937
318	0.17	80	0.35	1620	0.48	495	818
323	0.29	211	0.22	1758	0.49	687	785
328	0.26	111	0.31	1180	0.43	413	572
2.8 M G3/LiTFSI							
298	0.15	31	0.59	5981	0.26	918	3772
303	0.13	32	0.61	4985	0.26	769	3245
308	0.12	41	0.63	3818	0.25	608	2562
313	0.16	41	0.57	3517	0.27	589	2170
318	0.13	46	0.59	2824	0.28	464	1802
323	0.14	47	0.61	2199	0.25	415	1452
328	0.18	33	0.60	2128	0.22	421	1375
3.2 M G3/LiTFSI							
298	0.29	114	0.71	9425	-	-	6725
303	0.35	75	0.65	6042	-	-	3954
308	0.29	57	0.71	4188	-	-	2990
313	0.28	69	0.72	4812	-	-	3484
318	0.33	54	0.67	4953	-	-	3336
323	0.28	100	0.72	4521	-	-	3283
328	0.25	108	0.75	3539	-	-	2681

Table 4.B.6. Exponential fitting parameters of average rotation times of C102 at various compositions of G3/LiTFSI electrolyte solutions measured at different temperatures (298 - 328 K).

C_{LiTFSI}/M	a_1	τ_1/ps	a_2	τ_2/ps	$< \tau_{rot} >$ /ps
0	1.00	135	-	-	135
0.5	0.70	135	0.30	289	181
1	0.43	98	0.57	413	278
2.1	0.45	108	0.55	3209	1814
2.8	0.48	176	0.52	4032	2181
3.2	0.68	114	0.32	7189	2378

Table 4.B.7. Average rotational times, $<\tau_{rot}>$ for C153 in G3/LiTFSI electrolyte solutions obtained from dynamic anisotropy measurements and predictions from SED relation using stick and slip boundary conditions at different LiTFSI concentrations and temperatures.

C_{LiTFSI}/ M	T/K	η / cP	C153 Rotation		
			Measured $<\tau_{rot}>$/ns	Predicted $<\tau_{rot}>$/ns from SED relation	
				Stick	Slip
0.5	298	3.90	0.82	0.40	0.10
	303	3.49	0.71	0.35	0.08
	308	3.14	0.61	0.31	0.07
	313	2.86	0.57	0.28	0.07
	318	2.62	0.54	0.25	0.06
	323	2.42	0.47	0.23	0.05
	328	2.22	0.39	0.21	0.05
1	298	6.69	0.53	0.68	0.16
	303	6.03	0.46	0.61	0.15
	308	5.33	0.45	0.53	0.13
	313	4.72	0.46	0.46	0.11
	318	4.22	0.39	0.40	0.10
	323	3.79	0.38	0.36	0.09
	328	3.26	0.30	0.30	0.07
2.1	298	34.73	1.47	3.55	0.85
	303	28.18	1.15	2.83	0.68
	308	23.26	1.01	2.30	0.55
	313	19.48	0.94	1.90	0.46
	318	16.50	0.82	1.58	0.38
	323	14.12	0.78	1.33	0.32
	328	10.06	0.57	0.93	0.22
2.8	298	117.5	3.77	12.02	2.88
	303	90.90	3.24	9.14	2.19
	308	71.65	3.15	7.09	1.70
	313	57.47	2.17	5.60	1.34
	318	46.76	1.80	4.48	1.08
	323	38.57	1.45	3.64	0.87
	328	31.46	1.38	2.92	0.70
3.2	298	236.2	6.72	24.16	5.80
	303	179.8	3.95	18.09	4.34
	308	139.6	2.99	13.82	3.32
	313	110.2	3.48	10.73	2.58
	318	88.25	3.34	8.46	2.03
	323	71.72	3.28	6.77	1.62
	328	60.27	2.68	5.60	1.34

Table 4.B.8. Multi-exponential fit parameters of solvation response function S(t), for C153 in G3/LiTFSI electrolyte solutions at temperature range 298-328 K.

T/K	a_1	τ_1/ps	a_2	τ_2/ps	$< \tau_{Sol} >$ /ps
1 M G3/LiTFSI					
298	0.20	90	0.80	9597	7696
303	0.20	84	0.80	8666	6950
308	0.15	95	0.85	7331	6246
313	0.21	95	0.79	7645	6060
318	0.15	91	0.85	7133	6077
323	0.13	85	0.87	6382	5563
328	0.10	89	0.90	5851	5275
2.1 M G3/LiTFSI					
298	0.23	136	0.77	8264	6395
303	0.23	124	0.77	7092	5489
308	0.25	113	0.75	6414	4839
313	0.23	111	0.77	5464	4233
318	0.22	103	0.78	4701	3689
323	0.24	100	0.76	4261	3262
328	0.22	80	0.78	3644	2860
2.8 M G3/LiTFSI					
298	0.25	243	0.75	5368	4087
303	0.23	226	0.77	5020	3917
308	0.23	234	0.77	4507	3524
313	0.26	196	0.74	3593	2710
318	0.25	176	0.75	3224	2462
323	0.26	130	0.74	2518	1897
328	0.25	135	0.75	2344	1792
3.2 M G3/LiTFSI					
298	0.19	264	0.81	2872	2376
303	0.22	282	0.78	2904	2327
308	0.20	256	0.80	2635	2159
313	0.23	229	0.77	2632	2079
318	0.17	200	0.83	2298	1941
323	0.19	277	0.81	2184	1822
328	0.24	370	0.76	2375	1894

Table 4.B.9. Estimated ($\Delta\nu^{t}_{est}$) and observed ($\Delta\nu^{t}_{obs}$) dynamic Stokes shifts and percentage of missing portion of the total dynamic Stokes shift for C153 in G3/LiTFSI electrolyte solutions at temperature range 298 - 328 K.

1 M G3/LiTFSI			
T/K	$\Delta\nu^{t}_{est}/10^{3}$ cm^{-1}	$\Delta\nu^{t}_{obs}/10^{3}$ cm^{-1}	% missed
298	1.717	1.376	20
303	1.346	1.198	11
308	1.268	0.986	22
313	1.255	0.899	28
318	1.236	0.879	29
323	1.266	0.891	30
328	1.243	0.808	35
2.1 M G3/LiTFSI			
298	2.426	1.730	29
303	2.290	1.567	32
308	2.150	1.505	28
313	2.099	1.454	31
318	1.771	1.384	22
323	1.819	1.324	27
328	1.648	1.272	23
2.8 M G3/LiTFSI			
298	1.986	1.494	24
303	1.934	1.441	25
308	1.863	1.382	26
313	1.760	1.315	25
318	1.700	1.262	26
323	1.615	1.134	30
328	1.560	1.202	23
3.2 M G3/LiTFSI			
298	0.889	0.544	39
303	0.795	0.418	47
308	0.799	0.418	48
313	0.821	0.450	45
318	0.849	0.492	42
323	0.862	0.478	45
328	0.858	0.460	46

References

[1] D. Aurbach, Y. Talyosef, B. Markovsky, E. Markevich, E. Zinigrad, L. Asraf, J.S. Gnanaraj, and H.-J. Kim, *Electrochim Acta* **50**(2–3), 247–254 (2004).

[2] V. Etacheri, R. Marom, R. Elazari, G. Salitra, and D. Aurbach, *Energy Environ Sci* **4**(9), 3243 (2011).

[3] H. Moon, T. Mandai, R. Tatara, K. Ueno, A. Yamazaki, K. Yoshida, S. Seki, K. Dokko, and M. Watanabe, *J Phys Chem C* **119**(8), 3957–3970 (2015).

[4] K. Xu, *Chem Rev* **114**(23), 11503–11618 (2014).

[5] Y.-S. Hu, and Y. Lu, *ACS Energy Lett* **5**(11), 3633–3636 (2020).

[6] J. Xu, and C. Wang, *J Electrochem Soc* **169**(3), 030530 (2022).

[7] E.R. Logan, E.M. Tonita, K.L. Gering, J. Li, X. Ma, L.Y. Beaulieu, and J.R. Dahn, *J Electrochem Soc* **165**(2), A21–A30 (2018).

[8] Z. Li, L. Wang, X. Huang, and X. He, *Adv Funct Mater* **34**(48), (2024).

[9] Y. Wang, Z. Wu, F.M. Azad, Y. Zhu, L. Wang, C.J. Hawker, A.K. Whittaker, M. Forsyth, and C. Zhang, *Nat Rev Mater* **9**(2), 119–133 (2023).

[10] D. Kodama, M. Kanakubo, M. Kokubo, S. Hashimoto, H. Nanjo, and M. Kato, *Fluid Phase Equilib* **302**(1–2), 103–108 (2011).

[11] A. Mondal, K. Kumbhakar, and R. Biswas, *J Phys Chem B* **128**(48), 11924–11937 (2024).

[12] S. Parveen, P. Sehrawat, and S.A. Hashmi, *Mater Today Commun* **31**, 103392 (2022).

[13] C.-H. Yim, J. Tam, H. Soboleski, and Y. Abu-Lebdeh, *J Electrochem Soc* **164**(6), A1002–A1011 (2017).

[14] M. Winter, B. Barnett, and K. Xu, *Chem Rev* **118**(23), 11433–11456 (2018).

[15] M. Li, J. Lu, Z. Chen, and K. Amine, *Adv Mat* **30**(33), (2018).

[16] G. Nikiforidis, and M. Anouti, *Battery Supercaps* **4**(11), 1708–1719 (2021).

[17] D. Aurbach, Y. Talyosef, B. Markovsky, E. Markevich, E. Zinigrad, L. Asraf, J.S. Gnanaraj, and H.-J. Kim, *Electrochim Acta* **50**(2–3), 247–254 (2004).

[18] R. Cui, Y. Ma, X. Gao, W. Wang, J. Wang, Z. Xing, and Z. Ju, *Energy Storage Mater* **71**, 103627 (2024).

[19] X. Ma, H. Fu, J. Shen, D. Zhang, J. Zhou, C. Tong, A.M. Rao, J. Zhou, L. Fan, and B. Lu, *Angewandte Chemie International Edition* **62**(49), (2023).

[20] T. Pal, and R. Biswas, *J Phys Chem B* **119**(51), 15683–15695 (2015).

[21] T. Pal, and R. Biswas, *Chem Phys Lett* **517**(4–6), 180–185 (2011).

[22] J. Rajbangshi, and R. Biswas, *J Mol Liq* **341**, 117342 (2021).

[23] S. Banerjee, P.Kr. Ghorai, S. Das, J. Rajbangshi, and R. Biswas, *J Chem Phys* **153**(23), (2020).

[24] J. Rajbangshi, K. Mukherjee, and R. Biswas, *J Phys Chem B* **125**(22), 5920–5936 (2021).

[25] S.-W. Park, S. Kim, and Y. Jung, *Phys Chem Chem Phys* **17**(43), 29281–29292 (2015).

[26] A. Wisitsorasak, and P.G. Wolynes, *J Phys Chem B* **118**(28), 7835–7847 (2014).

[27] H. Sillescu, *J Non Cryst Solids* **243**(2–3), 81–108 (1999).

[28] I. Tah, A. Mutneja, and S. Karmakar, *ACS Omega* **6**(11), 7229–7239 (2021).

[29] L. Wang, N. Xu, W.H. Wang, and P. Guan, *Phys Rev Lett* **120**(12), 125502 (2018).

[30] S. Kumar, S. Sarkar, and B. Bagchi, *J Chem Phys* **160**(22), (2024).

[31] M.L. Horng, J.A. Gardecki, A. Papazyan, and M. Maroncelli, *J Phys Chem* **99**(48), 17311–17337 (1995).

[32] N. Ito, S. Arzhantsev, M. Heitz, and M. Maroncelli, *J Phys Chem B* **108**(18), 5771–5777 (2004).

[33] R. Królicki, W. Jarzęba, M. Mostafavi, and I. Lampre, *J Phys Chem A* **106**(9), 1708–1713 (2002).

[34] H. Jin, G.A. Baker, S. Arzhantsev, J. Dong, and M. Maroncelli, *J Phys Chem B* **111**(25), 7291–7302 (2007).

[35] E. Tarif, J. Mondal, and R. Biswas, *J Phys Chem B* **123**(44), 9378–9387 (2019).

[36] K. Kumbhakar, E. Tarif, K. Mukherjee, and R. Biswas, *J Mol Liq* **290**, 111225 (2019).

[37] J. Mondal, N.C. Maity, and R. Biswas, *J Chem Sci* **135**(3), 84 (2023).

[38] R. Biswas, J.E. Lewis, and M. Maroncelli, *Chem Phys Lett* **310**(5–6), 485–494 (1999).

[39] J.E. Lewis, R. Biswas, A.G. Robinson, and M. Maroncelli, *J Phys Chem B* **105**(16), 3306–3318 (2001).

[40] T. Pradhan, and R. Biswas, *J Phys Chem A* **111**(45), 11514–11523 (2007).

[41] T. Pradhan, P. Ghoshal, and R. Biswas, *J Chem Sci* **120**(2), 275–287 (2008).

[42] Argaman R, and Huppert D, *J Phys Chem A* **102**(31), 6215–6219 (1998).

[43] R. Argaman, and D. Huppert, *J Phys Chem B* **104**(6), 1338–1348 (2000).

[44] H. AL Rasid Gazi, H.K. Kashyap, and R. Biswas, *J Chem Sci* **127**(1), 61–70 (2015).

[45] C.F. Chapman, and M. Maroncelli, *J Phys Chem* **95**(23), 9095–9114 (1991).

[46] X.-X. Zhang, M. Liang, N.P. Ernsting, and M. Maroncelli, *J Phys Chem Lett* **4**(7), 1205–1210 (2013).

[47] A. Samanta, *J Phys Chem B* **110**(28), 13704–13716 (2006).

[48] Z. Hu, and C.J. Margulis, *Proceedings of the National Academy of Sciences* **103**(4), 831–836 (2006).

[49] B. Guchhait, S. Das, S. Daschakraborty, and R. Biswas, *J Chem Phys* **140**(10), (2014).

[50] M. Kondo, X. Li, and M. Maroncelli, *J Phys Chem B* **117**(40), 12224–12233 (2013).

[51] R. Królicki, W. Jarzęba, M. Mostafavi, and I. Lampre, *J Phys Chem A* **106**(9), 1708–1713 (2002).

[52] C.F. Riadigos, R. Iglesias, M.A. Rivas, and T.P. Iglesias, *J Chem Thermodyn* **43**(3), 275–283 (2011).

[53] S. Tang, and H. Zhao, *RSC Adv* **4**(22), 11251 (2014).

[54] A. Pal, and H. Kumar, *J Chem Eng Data* **44**(6), 1330–1334 (1999).

[55] J.R. PARTINGTON, and E.G. COWLEY, *Nature* **135**(3412), 474–474 (1935).

[56] T. Clark, J.S. Murray, P. Lane, and P. Politzer, *J Mol Model* **14**(8), 689–697 (2008).

[57] K. Dobek, J. Karolczak, and J. Kubicki, *Dyes and Pigments* **100**, 222–231 (2014).

[58] X.-X. Zhang, M. Liang, N.P. Ernsting, and M. Maroncelli, *J Phys Chem B* **117**(16), 4291–4304 (2013).

[59] Z.L. Terranova, and S.A. Corcelli, *J Phys Chem B* **117**(49), 15659–15666 (2013).

[60] R.S. Fee, and M. Maroncelli, *Chem Phys* **183**(2–3), 235–247 (1994).

[61] C. Fang, D.M. Halat, N.P. Balsara, and R. Wang, *J Phys Chem B* **127**(8), 1803–1810 (2023).

[62] O. Borodin, L. Suo, M. Gobet, X. Ren, F. Wang, A. Faraone, J. Peng, M. Olguin, M. Schroeder, M.S. Ding, E. Gobrogge, A. von Wald Cresce, S. Munoz, J.A. Dura, S. Greenbaum, C. Wang, and K. Xu, *ACS Nano* **11**(10), 10462–10471 (2017).

[63] S. Indra, and R. Biswas, *J Chem Phys* **142**(20), (2015).

[64] R. Ghosh, and B. Bagchi, *J Phys Chem B* **120**(49), 12568–12583 (2016).

[65] P. Banerjee, and B. Bagchi, *J Chem Phys* **148**(22), (2018).

[66] N. Ohtori, Y. Kondo, and Y. Ishii, *J Mol Liq* **314**, 113764 (2020).

[67] M.G. Mazza, N. Giovambattista, H.E. Stanley, and F.W. Starr, *Phys Rev E* **76**(3), 031203 (2007).

[68] M.-L. Horng, J.A. Gardecki, and M. Maroncelli, *J Phys Chem A* **101**(6), 1030–1047 (1997).

[69] S. Das, R. Biswas, and B. Mukherjee, *J Phys Chem B* **119**(34), 11157–11168 (2015).

[70] B. Guchhait, and R. Biswas, *J Chem Phys* **138**(11), (2013).

[71] D. Laage, and G. Stirnemann, *J Phys Chem B* **123**(15), 3312–3324 (2019).

[72] Y.-L. Wang, B. Li, S. Sarman, F. Mocci, Z.-Y. Lu, J. Yuan, A. Laaksonen, and M.D. Fayer, *Chem Rev* **120**(13), 5798–5877 (2020).

Chapter 5

Investigation of Polymer Dynamics Influencing Ion Transport in Gel Polymer Electrolytes for Li-Ion Cells

5.1 Introduction

The global transition toward renewable energy sources such as solar and wind power has underscored the urgent need for efficient, scalable, and reliable energy storage systems. These intermittent sources demand advanced storage technologies capable of balancing supply and demand, ensuring grid stability, and supporting large-scale deployment. As a result, the development of next-generation energy storage materials, particularly lithium-ion batteries and their solid-state or gel-based alternatives, has become a central focus of materials science and electrochemistry. Among these, gel polymer electrolytes (GPEs) have emerged as promising candidates due to their ability to combine high ionic conductivity with enhanced mechanical and thermal stability, offering safer and more adaptable solutions for renewable energy integration across both consumer and grid-scale applications.[1]

From a fundamental perspective, GPE consists of a polar organic solvent, lithium salt, and a polymeric matrix, forming a unique hybrid structure that combines the high ionic conductivity (in the order of 10^{-3} S cm^{-1}) like typical liquid electrolytes along with the mechanical robustness and processability of solid-state systems.[2,3] However, the presence of multiple interacting components introduces complex ion transport behavior that deviates from classical descriptions, especially as systems transition from liquid-like to gel-like regimes. In such systems, ion motion

is intricately tied to solvent dynamics, polymer segmental mobility, and local structural heterogeneity.[4–7]

Understanding ion transport in GPEs is essential for advancing energy storage technologies. In this study, we investigated a model GPE system composed of propylene carbonate (PC), lithium perchlorate ($LiClO_4$), and polypropylene glycol (PPG425), with systematic variation of PPG concentration and temperature. The ~ 1 M solution of $LiClO_4$ in PC is selected, as it corresponds to the maximum observed ion conductivity. This work aims to elucidate the microscopic structural and dynamical features of the electrolyte, focusing on how polymer incorporation modulates solvation dynamics, polymer relaxation, and ultimately ion transport. Despite their relevance, the intricate coupling between these factors remains inadequately understood, especially in polymer-rich systems where changes in composition lead to substantial alterations in both local solution structure and collective dynamics.

One key advantage of GPEs is their ability to promote the formation of stable and uniform solid electrolyte interphase (SEI) layers on electrode surfaces.[8–10] Unlike liquid electrolytes that often result in unstable SEI due to rapid solvent diffusion and uncontrolled side reactions, GPEs restrict solvent mobility and enable controlled ion transport, leading to compact, passivating interfacial films. Their tunable physicochemical environment including viscosity, polarity, and dielectric properties, arising from complex ion-solvent and ion-polymer interactions, directly influences SEI composition and growth.[11–14] In this context, Raman spectroscopy provides insight into ion coordination and solvation structure, while dielectric relaxation spectroscopy (DRS) reveals dipolar and ionic dynamics, both of which are closely linked to the ion-solvent behavior governing SEI chemistry.[14–17]

From a theoretical standpoint, continuum dielectric models, most notably the Onsager relation, provide a foundational framework for connecting ionic conductivity with dielectric relaxation behavior.[18,19] Rooted in electrostatics and the fluctuation-dissipation theorem, Onsager theory links macroscopic ion transport to microscopic dipolar dynamics by assuming that both processes are

governed by the same underlying frictional mechanisms.[20–22] This approach is particularly effective in idealized, homogeneous, and isotropic systems with single-mode relaxation.[18,23] However, GPE presents a fundamentally different scenario. The presence of polymeric components introduces significant spatial and dynamic heterogeneity, leading to complex relaxation behavior and multiple frictional environments for ions and dipoles. In such systems, assumptions of isotropy and uniformity break down. Yet, applying Onsager theory remains highly instructive; it allows for a systematic comparison between predicted and measured conductivities, thereby serving as a diagnostic tool to reveal deviations arising from polymer-induced effects such as localized segmental dynamics, constrained solvation environments, and non-ideal ion-dipole interactions.

By benchmarking ion transport behavior against Onsager predictions, we gain critical insight into the underlying mechanisms that govern conductivity in GPEs. This comparison highlights the limitations of classical theories in describing soft-matter electrolytes and underscores the need for refined models that can incorporate dynamic heterogeneity and structural complexity. In this context, Onsager theory serves not only as a starting point for interpreting conductivity data but also as a means to identify the fundamental departures that define ion transport in modern, polymer-rich electrolyte systems.[24]

From an experimental perspective, we investigated the interplay between dielectric relaxation behavior and solvation dynamics to gain deeper insight into [Li^+] transport in $PC/LiClo_4$ solutions containing poly(propylene glycol) (PPG). Broadband dielectric relaxation (DR) spectroscopy, spanning a frequency range of $0.2 \leq \nu/GHz \leq 50$, was employed to probe the reorientational relaxation of dipolar species in solution. These include the slow rotational modes of [ClO_4^-] -based complexes and the restricted dynamics of PC molecules coordinating with [Li^+]. Temperature- and concentration-dependent DR measurements provided a detailed dynamical view of how ion-solvent interactions and solution structure evolve with increasing PPG content. This approach enabled us to correlate microscopic dipolar relaxation timescales with macroscopic transport properties, such as viscosity and ionic conductivity, thereby elucidating the dynamic coupling that governs ion mobility in gel-like electrolyte systems.

To complement the DR measurements and gain access to faster solvation processes, we have performed time-dependent fluorescence Stokes shift (TDFSS) experiments using a streak camera setup with an effective temporal resolution of ~ 500 fs. This ultrafast approach enabled the detection of sub-picosecond solvation dynamics governed by the collective polarization mode of the liquid medium, thus bridging the timescales inaccessible by our DR measurements. Together, the DR and TDFSS techniques[25] provide a comprehensive picture of solvent response across a broad temporal window, illuminating the role of polymer concentration in modulating ion solvation environments. This joint approach by combining DR spectroscopy and ultrafast solvation dynamics proves essential for elucidating the complex conductivity behavior in relation to the dynamic properties of the medium across varying PPG content. While dielectric relaxation reveals how slow, cooperative dipolar motions evolve with polymer incorporation, ultrafast solvation dynamics capture the rapid solvent responses tied to local molecular rearrangements. Together, they enable a multiscale understanding of how polymer-induced changes in molecular mobility, viscosity, and solvation environment collectively influence lithium-ion transport. This comprehensive insight is critical for decoding the non-monotonic conductivity trends and identifying the optimal PPG concentration where ion mobility is maximized in gel-like electrolyte systems.

5.2 Experimental Details

5.2.1 Materials and Sample Preparation

Propylene carbonate (PC), lithium perchlorate ($LiClO_4$) salt and polypropylene glycol (PPG425) and trans-2-[4-[(dimethylamino)styryl]benzothiazole (trans-DMASBT) were purchased from Sigma-Aldrich and used without further purification. $LiClO_4$ was vacuum dried for 48 hours prior to experiment. The chemical structures of these materials are shown in **Scheme 5.1**.

The gel electrolyte solutions were prepared by mixing PPG in 1 M $PC/LiClO_4$ solution in weight percentage and then stirring continuously for ~ 6-8 hours to obtain a transparent colorless solution. For UV - vis absorption and fluorescence emission spectroscopic measurements, ~ 2 - 3 mL sample

solution was typically placed in a quartz cuvette preloaded with a small quantity of DMASBT, wherein the concentration of the fluorophore (DMASBT) was maintained at $\leq 10^{-5}$ M. For temperature-controlled measurements sufficient time was allowed for each solution to reach a proper thermal equilibrium before taking the data. For DRS measurements, ~ 4 - 5 mL electrolyte sample was used for experiments in a humidity-controlled environment to avoid moisture absorption.

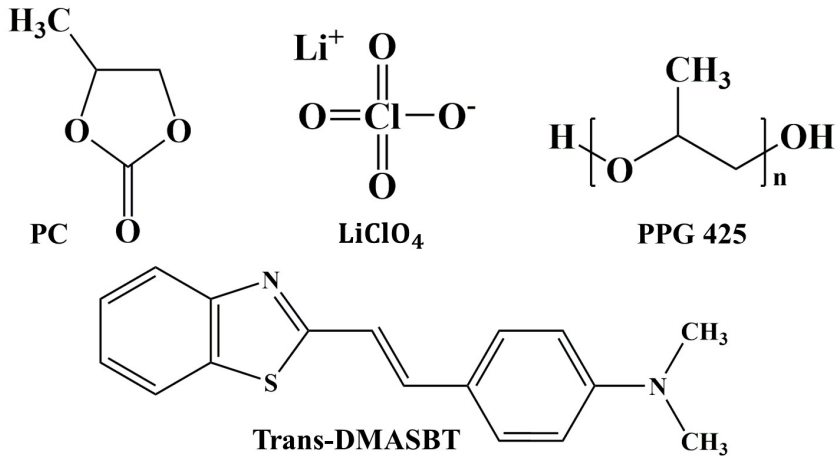

Scheme 5.1. Chemical structures of PC, $LiClO_4$, PPG425 and trans-DMASBT.

5.2.2 Refractive Indices, Densities, Viscosities and Conductivity Measurements

Temperature dependent refractive indices (n), densities (ρ) and viscosity coefficients (η) of all the GPE samples along with neat solvents were collected in an automated temperature-controlled refractometer (RUDOLPH, J357), automated temperature-controlled density-sound velocity analyzer (Anton Paar, model DSA 5000) and automated micro-viscometer (AMVn, Anton Paar), respectively. Measured ρ and η values are provided in **Table 5.B.1**(Appendix 5.B), while n values are given in **Table 5.2**. Conductivity (σ) of the electrolyte solutions were recorded by a Bench-top multi-parameter electrochemical meter (SESHIN BIOTECH, Model: ECM − 610) and the numerical values are summarized in Table **5.B.2** (Appendix 5.B).

5.2.3 Dynamic Light Scattering (DLS) Measurements

DLS measurements were conducted with a Malvern Zetasizer Nano ZS (Malvern Instrument Ltd., Malvern,U. K.) equipped with a 4.0 mW He - Ne laser beam operating at $\lambda = 633$ nm at a scattering angle of 173°. All GPE solutions were filtered through a 0.45 μm syringe filter prior to measurements. Details about DLS measurements have been incorporated in Chapter 2.

5.2.4 Raman Spectroscopy

Raman spectra of GPE solutions were obtained using a micro-Raman spectrometer (LabRam HR Evolution, Horiba France SAS) with a 532 nm laser excitation source at an output power of 11.5 mW. Each spectrum was acquired over a 20 s period, and 20 acquisition data points were collected using 1800 lines/mm grating to generate the Raman spectrum for each sample. Discernible peaks from the raw Raman spectra were subsequently fitted with a Lorentz function. Data collection and analysis protocol of Raman spectrum has been elaborated in Chapter 2.

5.2.5 Steady-State UV-Vis Absorption and Emission Studies

UV-Visible spectrophotometer ($UV - 2600$, Shimadzu) and a fluorimeter (Fluorolog, Jobin-Yvon, Horiba) were used to record steady state absorption and fluorescence emission spectra, respectively. The standard spectral analysis protocol to determine spectral frequencies was outlined in Chapter 2. The error bar for the determined spectral frequencies in these GPE systems was $\pm 120\ cm^{-1}$. Results obtained from steady-state measurements in all the electrolyte samples studied have been presented in **Fig. 5.A.2** and **Table 5.B.4** (Appendix 5.A and Appendix 5.B).

5.2.6 Time-Resolved Fluorescence Spectral Analysis *via* Streak Camera

In this experimental technique, an ultrafast solvent response detection by capturing time-resolved fluorescence spectra has been conducted utilizing a streak camera ($Optoscope\ SC - 10$) coupled with a spectrograph ($HRS - 300SS$, Princeton Instruments). The excitation light was generated by a Ti:Sapphire laser (Mai Tai HP-1040S, Spectra Physics), with a pulse width of 100 fs and a

repetition rate of 80 MHz. Further details of streak camera set-up can be found in literature.[26] The recorded IRF determined using scattering particles in water exhibited a full width at half maximum (FWHM) value of ~ 2.0 ps. To record each 3-D streak image, 2000 acquisitions were permitted while maintaining Micro Channel Plate (MCP) gain at 750 V, and a delay of 33.5% involving a sweep speed of 15 ps/mm. To minimize scattering effects, a bandpass filter centered at 471 nm was employed to collect the fluorescence signal. The magic angle (54.7°) polarization was used to acquire intensity decay profiles at the peak wavelength of the solute's steady-state emission. The details analyses of decoding the decay profiles and determining fluorescence lifetime have been explored in Chapter 2. Further description of the interpretation of the collected 3-D streak images, the analysis of time-resolved emission spectra (TRES), and the construction of the corresponding solvent response function, S(t), have been provided in Chapters 2 and 3.

5.2.7 Dielectric Relaxation Spectroscopy (DRS)

DRS measurements in the frequency range from 200 MHz to 50 GHz at temperatures ranging from 298 K to 323 K were conducted utilizing a PNA − L network analyzer (N5235B) in conjunction with an open-ended coaxial probe kit (N1501A). Experimentally obtained complex DR spectra for $PC/LiClO_4$/PPG electrolyte solutions were simultaneously fitted with multi-Debye relaxation process. Comprehensive information on data collection, analysis protocols, theoretical background and the mathematical formulations used in the fitting process have been presented in Chapter 2.

5.3 Results and Discussion

5.3.1 DLS Analysis: Structural Characteristics of GPE Solutions

The structural characteristics of GPE solutions were investigated using dynamic light scattering (DLS) experiments to determine the hydrodynamic diameter (D_h) of the self-assembled structures formed by PPG molecules. **Fig. 5.1** presents the evolution of D_h as a function of concentration of PPG at room temperature. The results indicate the presence of two distinct size distributions in all electrolyte solutions. A minor population (10 - 20% of the total distribution) with D_h ranging from

~ 1 - 4 nm, observed across the entire concentration range of PPG. This population is typically attributed to individual polymer chains[27–29] and is not a major structural concern. A predominant population (80 - 90% of the total distribution) consisting of larger aggregates with D_h in the range of ~ 2000 - 4000 nm, which represent the primary self-assembled structures in the solutions. At low polymer concentrations (≤ 40 wt%), the PPG molecules predominantly form aggregates of ~ 2000 nm, facilitating Li^+ ion transport. However, at higher polymer concentrations (> 40 wt%), a significant increase in aggregated size is observed, with D_h reaching ~ 5000 nm. This suggests that excessive polymer content leads to the formation of large, highly coordinated structures that restrict Li^+ mobility. Consequently, ion conductivity decreases drastically at high PPG concentrations due to Li^+ being trapped within the aggregated polymer network. Overall, these findings underscore the value of dynamic light scattering (DLS) as a preliminary yet essential tool for probing the structural landscape of GPE solutions. The results reveal that the concentration of PPG plays a pivotal role in governing self-assembly behavior, which subsequently impacts ion transport properties. This structural evolution with concentration suggests a tunable pathway for optimizing electrolyte performance. These insights serve as a foundation for correlating microscopic organization with macroscopic transport phenomena in GPE systems.

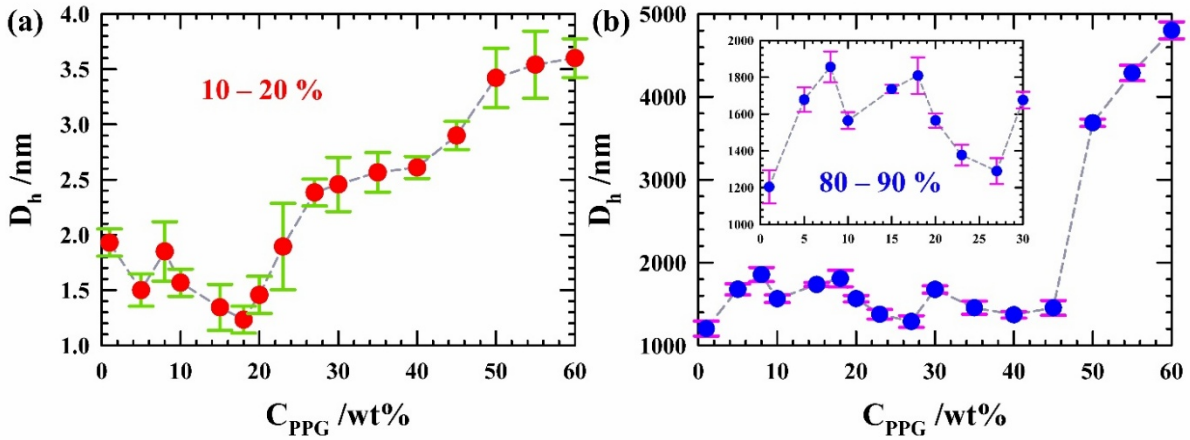

FIG. 5.1. Particle size distributions of $PC/LiClO_4/PPG$ electrolyte solutions as a function of concentration of PPG at 298 K. Color-coding was employed to differentiate between GPE samples with hydrodynamic diameters (D_h) of (a) ≤ 4 nm and (b) ~ 2000 - 5000 nm. Data in the inset are presented in a shorter vertical scale (Y-axis) in order to clearly show the upper and lower bounds of the error associated with each of the D_h values.

5.3.2 Raman Analysis: Exploring Solution Structure and Interactions in GPEs

5.3.2.1 Region 920 – 950 cm^{-1}: ClO_4^- Stretching Modes

The Raman bands in the range of ~ 920 - 950 cm^{-1} for $PC/LiClO_4/PPG$ electrolyte solutions were analyzed using Lorentzian curve fitting, illustrated in **Fig. 5.2** and the corresponding peak positions and spectral widths of all the compositions of electrolyte solutions are summarized in **Table 5.B.3** (Appendix 5.B). This studies could reveal the presence of four distinct complex ionic species, identifiable by their characteristic vibrational frequencies: free ClO_4^- anion at ~ 933 cm^{-1}, solvent-shared ion pairs (i.e., SSIP, $Li^+ - PC - LiClO_4$) at ~ 939 cm^{-1}, contact ion pairs (i.e., CIP, $Li^+ - ClO_4^-$) at ~ 948 cm^{-1}, and multiple ion pairs (i.e., MIP $[Li^+ - ClO_4^-]_n$) at ~ 955 cm^{-1}.[30–34] In $PC/LiClO_4$ electrolyte solution, the Raman spectrum (see **Fig. 5.2**) exhibits a double peak at 932 cm^{-1} and 938 cm^{-1}. This double peak is attributed to the symmetric stretching mode of the ClO_4^-, indicating a significant presence of unassociated ClO_4^- anions surrounded by PC molecules and a lesser number of SSIP.

Upon introduction of PPG, the Raman peak at ~ 938 cm^{-1} associated with SSIP diminishes (see **Fig. 5.2** and **Table 5.B.3**, Appendix 5.B), indicating the disruption of $Li^+ - PC - LiClO_4$ interactions. Concurrently, a red shift of the ClO_4^- vibrational band to ~ 930 cm^{-1} is observed at 10-30 wt% PPG, signifying weakened $Li^+ - ClO_4^-$ interactions and enhanced ion dissociation due to Li^+ coordination by ether oxygen atoms of PPG. This leads to a higher population of free ions and increased ionic conductivity, further supported by enhanced segmental motion from the polymer.

However, at higher PPG contents (40-60 wt%), a blue shift to ~ 932 - 933 cm^{-1} emerges, indicating the absence of typical IP structures yet a decline in conductivity. This behavior is attributed to overcrowding of coordinating PPG chains, reduced Li^+ mobility, and increased viscosity, which collectively hinder effective ion transport despite continued ion dissociation. These findings emphasize the dual role of PPG in modulating ionic conductivity, highlighting the delicate balance between promoting ion dissociation and introducing polymer-induced transport limitations in GPE systems.

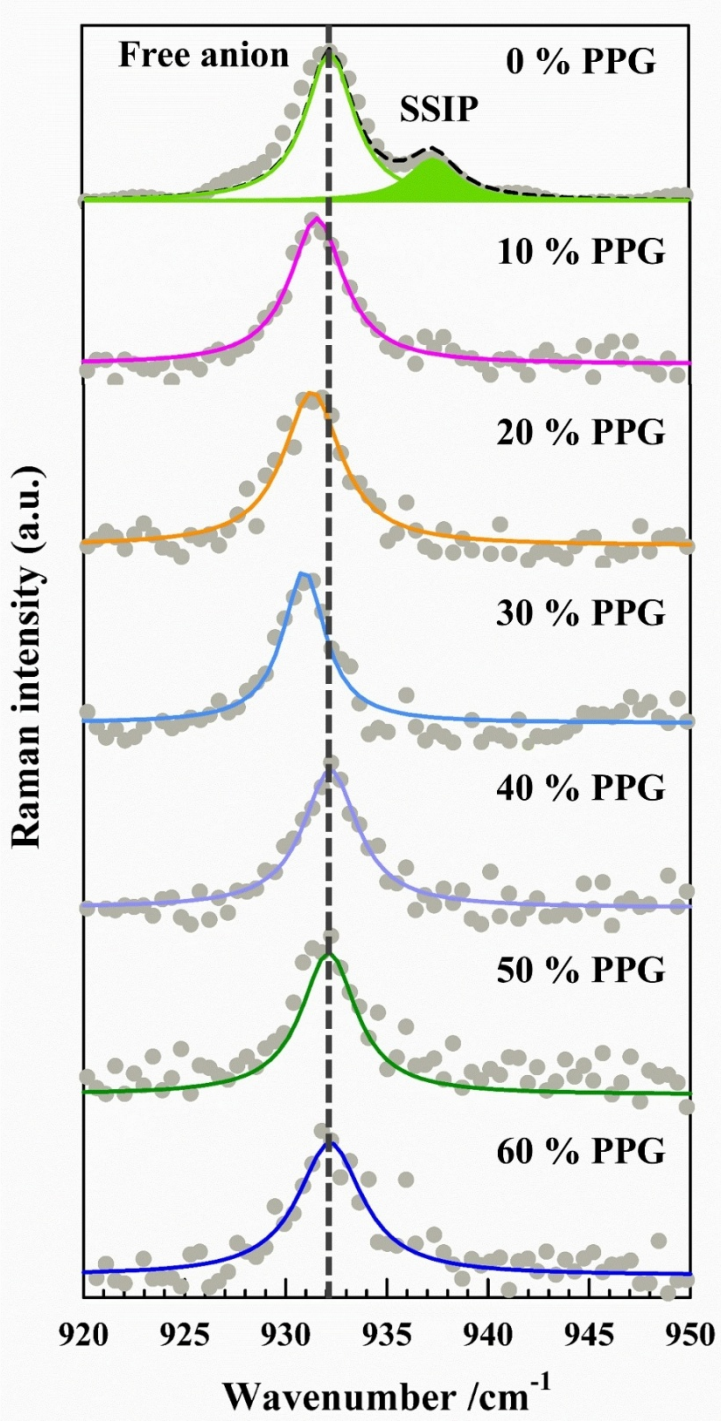

FIG. 5.2. ClO_4^- symmetric stretching modes for $PC/LiClO_4$/PPG electrolyte solutions with different concentrations of PPG. Experimental data points are fitted with Lorentzian function. Solid fitted lines are color-coded according to compositions of GPE.

5.3.2.2. Region 800 – 900 cm^{-1}: Symmetric Vibration Mode of PC Ring

To elucidate the interactions between PC and PPG in PC/$LiClO_4$/PPG ternary electrolyte solutions, we analyzed the Raman spectra around ~ 850 cm^{-1}, as depicted in **Fig. 5.3**. The band at ~ 850 cm^{-1}, corresponding to the symmetrical breathing vibration of the PC ring,[35,36] remains unchanged with the addition of $LiClO_4$ salt and successive additions of PPG. In neat PPG, there are two broad band at ~ 828 cm^{-1} and at ~ 864 cm^{-1}. The 800 - 900 cm^{-1} region in the Raman spectrum of neat PPG is associated with the $-CH_2$ rocking mode, which is highly responsive to conformational changes and internal motions of the polymer backbone.[37,38]

As the concentration of PPG decreases from 100% to 40 wt%, the intensity of the Raman band at ~ 864 cm^{-1} progressively diminishes and undergoes a blue shift, ultimately disappearing in polymer-poor electrolyte compositions. This band is attributed to specific vibrational modes of the PPG backbone, and its suppression suggests a disruption of the original polymer microstructure upon dilution. Simultaneously, the broad peak centered at ~ 828 cm^{-1} in neat PPG exhibits a red shift of ~ 45 cm^{-1} in the presence of PC and $LiClO_4$ as the PPG content decreases. This red shift reflects increasing interactions between PPG and PC molecules, likely involving hydrogen bonding or dipole–dipole interactions, which perturb the vibrational environment of the $-CH_2$ groups.

It is important to note that the above effects are particularly pronounced in highly concentrated GPEs. In low-concentration polymer electrolytes, the two modes at ~ 828 cm^{-1} and ~ 864 cm^{-1} become less prominent or even invisible due to the dominance of the five-membered ring vibrational mode of PC in this spectral region. This observation underscores the intricate balance and interplay between polymer concentration and electrolyte interactions within such complex electrolyte system. These structural modifications imply that the introduction of PC and $LiClO_4$ not only alters the local solvation environment but also induces conformational changes within the PPG chains. Consequently, the observed spectral shifts serve as strong evidence of electrolyte-induced restructuring of the polymer matrix, which could influence both mechanical and transport properties of the GPE.

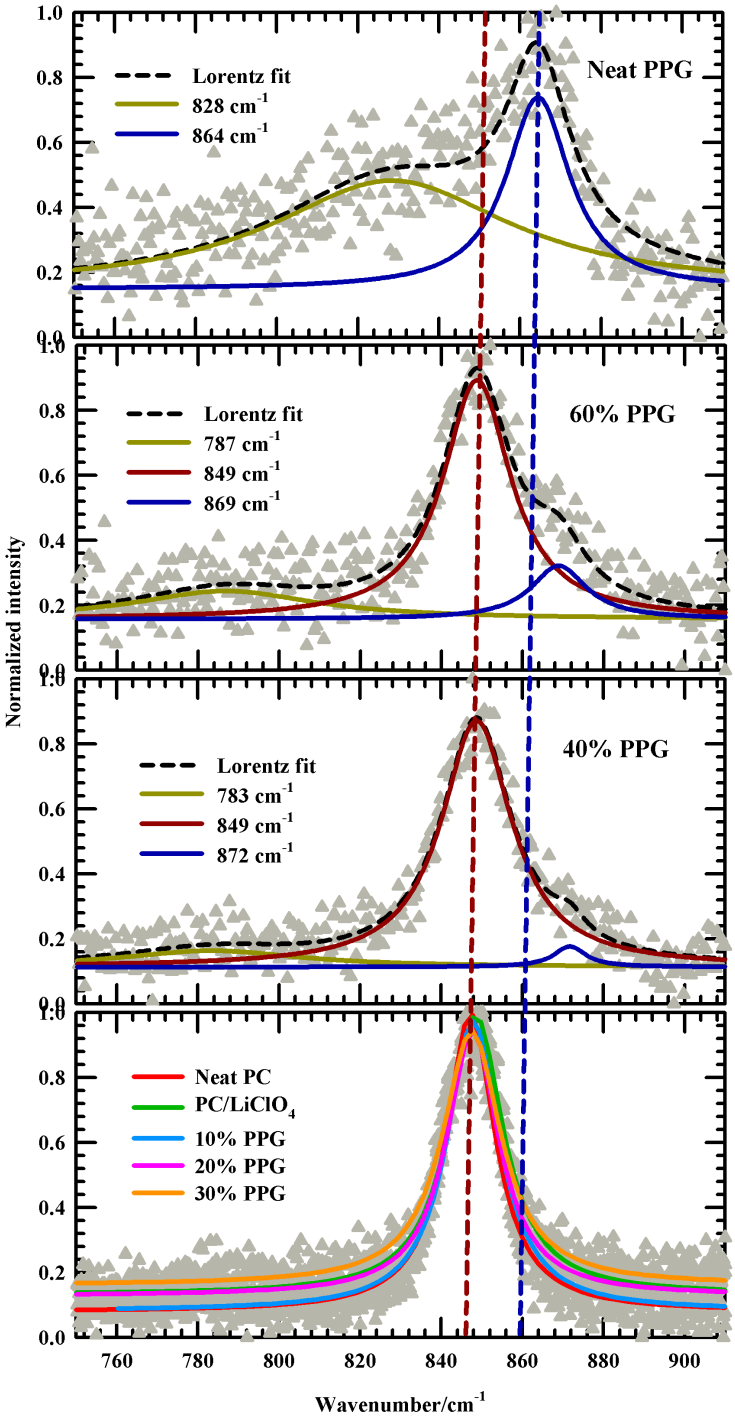

FIG. 5.3. Symmetric stretching band accounting 5-membered ring vibration of PC molecules in electrolyte solutions and compared with $-CH_2$ rocking mode of neat PPG. Straight lines inside the data points denote the Lorentzian band fit and dashed lines over all spectra are indicating peak position of the corresponding deconvoluted spectrum. All different compositions of GPEs are color-coded.

5.3.2.3 Region 1700 – 1850 cm^{-1}: C = O Stretching Modes of PC

Interactions of PC molecules with $LiClO_4$ and PPG is further investigated through examining Raman band of C = O stretching mode of PC in the range 1700 - 1850 cm^{-1}, presented in **Fig. 5.4**. The typical C = O stretching band of neat PC at ~ 1782 cm^{-1} aligns well with previous research findings.[35,39] The observation of a split fundamental C = O band, concomitant with an additional band appearing at ~ 1800 cm^{-1}, is ascribed to the Fermi resonance (FR) phenomenon, indicative of combination of lower frequency vibrational modes.[35,40,41] These two bands are extremely sensitive towards Li^+ ion solvation by coordination with PC through C = O group.

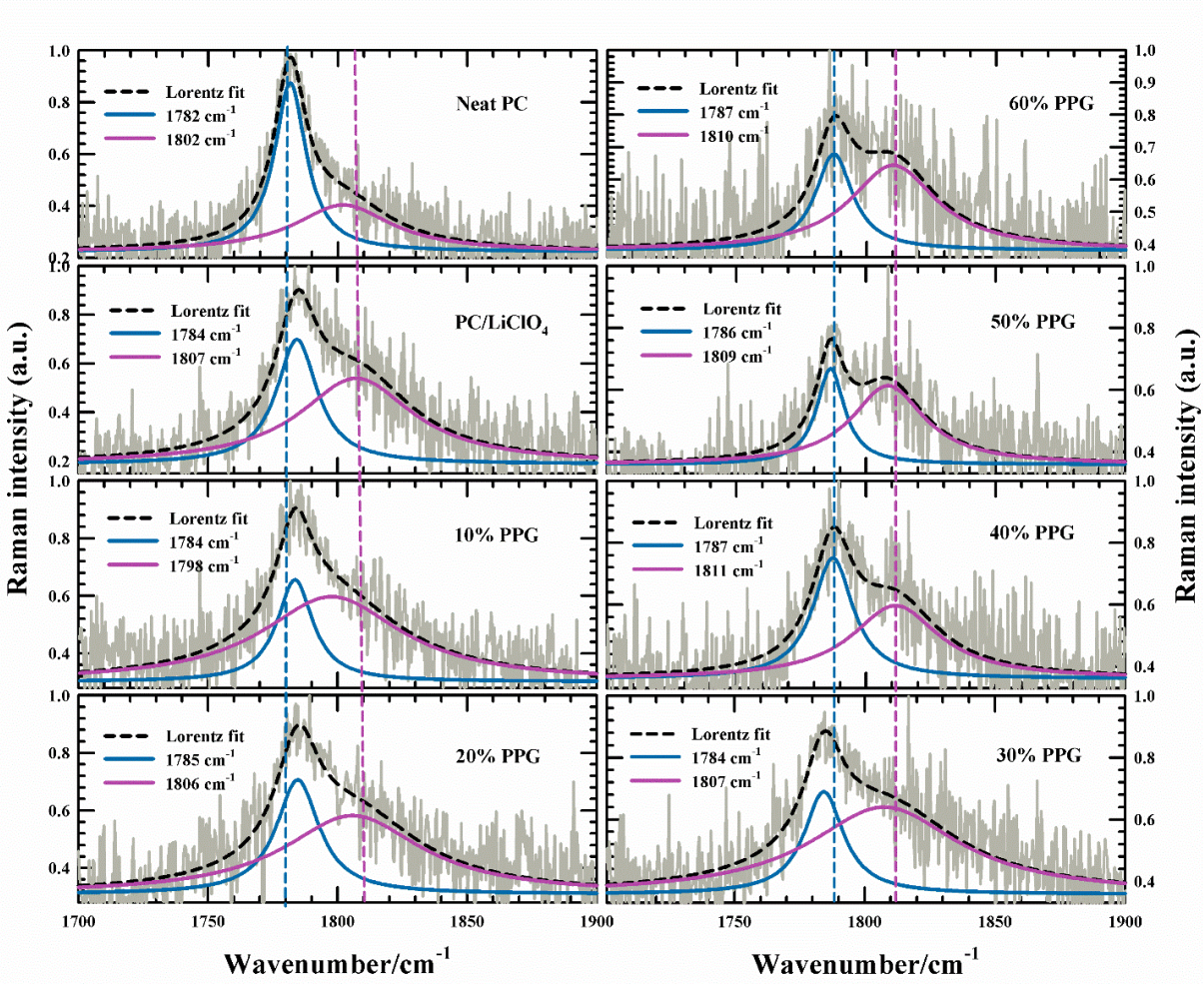

FIG. 5.4. C = O stretching mode of PC in PC/$LiClO_4$/PPG electrolyte solutions at different concentration of PPG. Dashed lines and solid lines are total fit of Lorentzian band shape and their deconvoluted spectra, respectively. All presentations are color-indicated.

A consistent yet marginal reduction in peak intensity, along with a blue shift in the bands at ~ 1782 cm^{-1} and 1800 cm^{-1}, provides strong evidence of a subtle change in Li^+ interaction with the $C=O$ moiety of PC. This suggests a stable coordination between Li^+ and the carbonyl group of PC, with the introduction of PPG exerting minimal influence on the Li^+/PC interaction. PPG interacts with free ClO_4^-, reducing the formation of complex ionic clusters. This leads to better Li^+ solvation, ensuring more availability of free Li^+ for ion conduction. PPG molecules not only increase the viscosity of the GPE system and enhance the mechanical stability of the electrolyte but also polymer network connectivity facilitates Li^+ ion hopping mechanism.

5.3.2.4 Region 2500 - 3200 cm^{-1}: C – H Stretching Modes of PC and PPG

To understand the impact of $LiClO_4$ into conventional symmetric CH_3 stretching mode of both neat PC and PPG, typically observed between 2500 - 3200 cm^{-1},[35,37] the spectra can be deconvoluted into four or five distinct peaks, shown in **Fig. 5.5**. The precise peak positions are dependent upon factors such as the molecular weight of PPG and experimental conditions. As illustrated in **Fig. 5.5**, the deconvolution of neat PC reveals five primary peaks centered at ~ 2711 cm^{-1}, 2881 cm^{-1}, 2936 cm^{-1}, 2992 cm^{-1}, and 3020 cm^{-1}. Notably, the peak at 2881 cm^{-1} (highlighted in green in **Fig. 5.5**) in neat PC undergoes a slight red-shift to 2876 cm^{-1} with an increase in peak area by ~ 40 cm^2 in neat PPG, indicating a strong dipole - dipole or, hydrogen bonding interactions between PC and PPG. Conversely, the prominent peak ~ 2934 cm^{-1} remains unaffected in position or shape upon the addition of $LiClO_4$ to PC/PPG solvent, suggesting minimal interaction of $LiClO_4$ with PPG. Furthermore, the disappearance of the ~ 3000 cm^{-1} sub-peak in PC when PPG content increases to 40 - 100 wt% points to a significant modification in the local chemical environment, likely due to the disruption of specific PC vibrational modes by PPG incorporation. The peak at ~ 2992 cm^{-1} in neat PC red-shifts to ~ 2979 cm^{-1} in neat PPG, with a concomitant decrease in intensity upon increasing polymer content, reinforcing the notion of enhanced PC–PPG interactions. These spectral changes collectively suggest that $LiClO_4$ primarily coordinates with PC, whereas PPG acts as a passive structural modifier that subtly tunes the solvation dynamics without directly engaging with the electrolyte. Such selective interactions have implications for the ion solvation environment, polymer - solvent compatibility, and ultimately the ionic conductivity in the GPE systems.

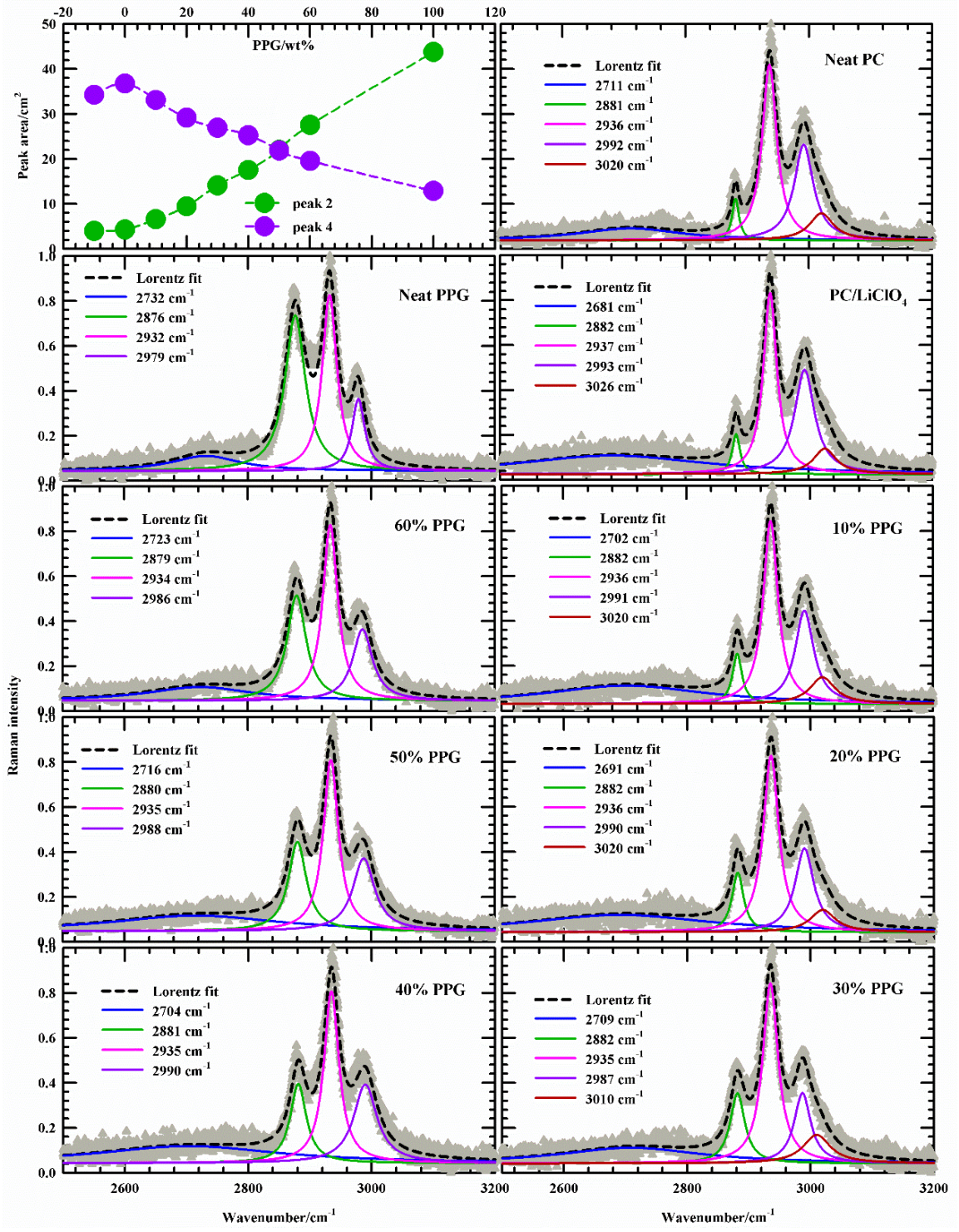

FIG. 5.5. C − H stretching band of PC and PPG in PC/$LiClO_4$/PPG electrolyte solutions at various compositions of PPG at a region 2500 - 3200 cm^{-1}.

5.3.3 Viscosity-Decoupled Ultrafast Solvation Dynamics

To investigate ultrafast solvation timescales in GPE systems, we have employed a streak camera detector-based technique. This method enables the study of solvation dynamics by capturing time-resolved fluorescence emission with high temporal resolution (~ 500 fs). **Fig. 5.A.3** (Appendix 5.A) presents two-dimensional representations of streak camera images, simultaneously resolved in three dimensions: wavelength, time, and intensity. These images correspond to the solvent response of DMASBT in neat PC, neat PPG, and PC/$LiClO_4$/PPG electrolyte solutions at varying PPG concentrations. The corresponding time-resolved emission spectra (TRES) are shown in **Fig. 5.6** and solvation dynamics decays, derived from these measurements, are illustrated in **Fig. 5.7**, with the associated exponential fitting parameters summarized in **Table 5.1**.

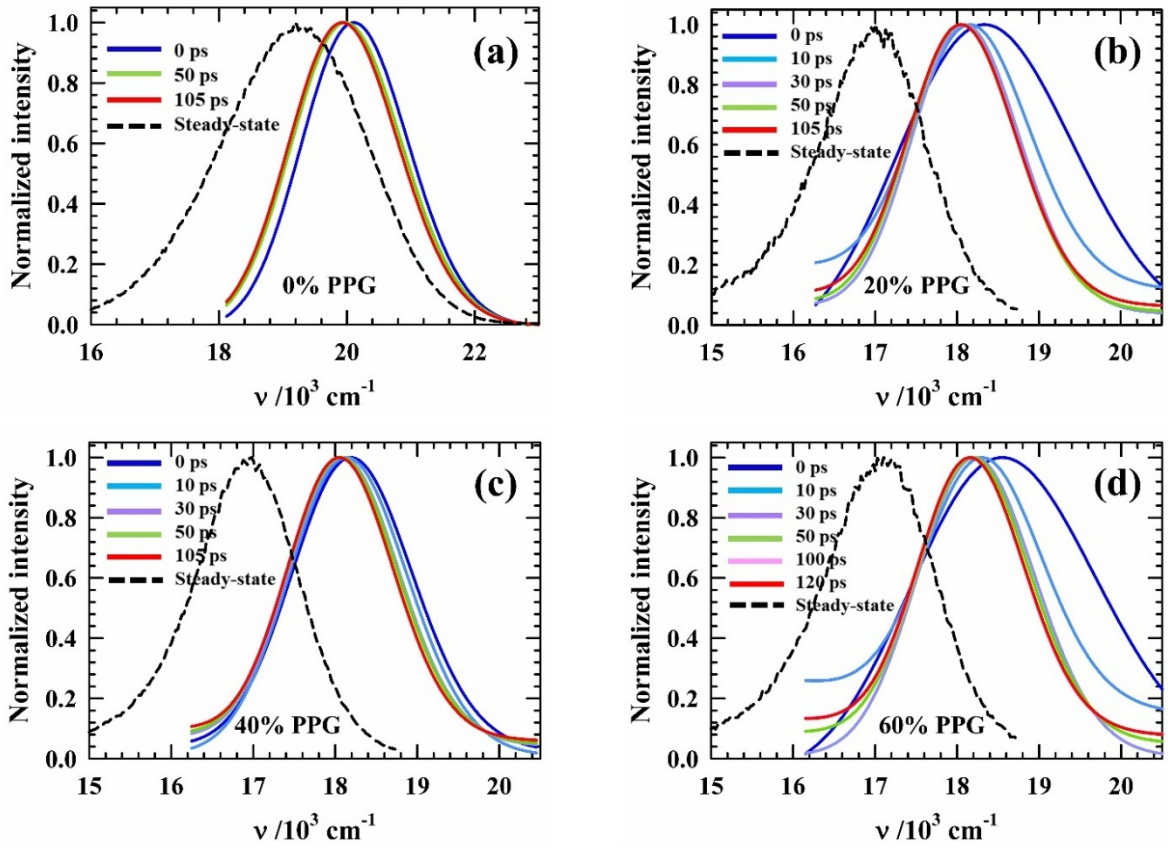

FIG. 5.6 TRES of DMASBT in PC/$LiClO_4$/PPG electrolyte solutions at ~ 298 K for varying PPG concentrations: (a) 0 wt%, (b) 20 wt%, (c) 40 wt%, and (d) 60 wt%. Each plot is color-coded to represent emission wavelength over time.

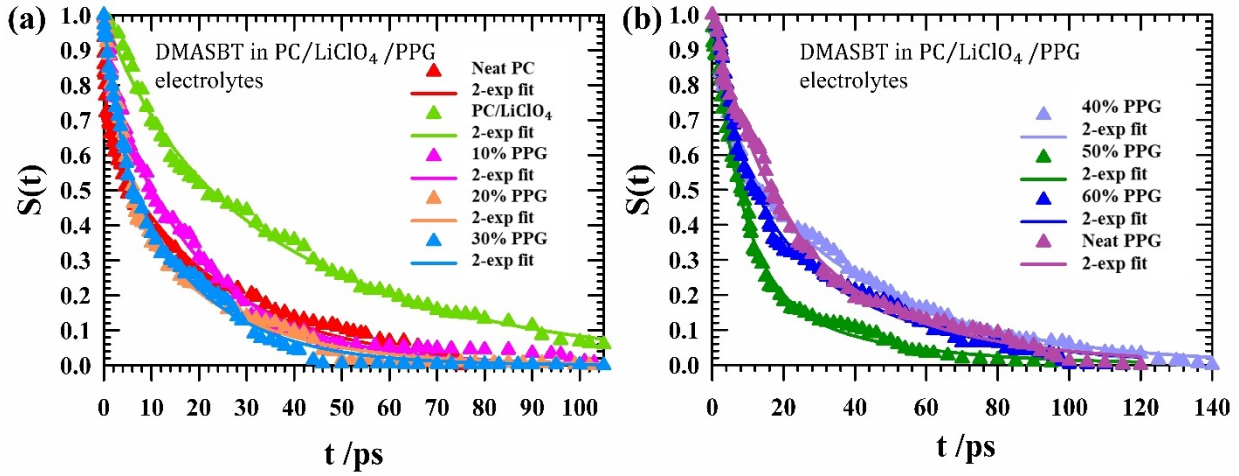

FIG. 5.7. Solvation response functions, S(t) for DMASBT at different compositions [(a) 0-30% PPG and (b) 40-60% PPG] of GPE along with neat solvents at ~298 K. Experimental data are shown by filled triangles and solid lines through the data represent the fits. All compositions are color-coded.

Table 5.1. Decay characteristics of solvent response function, S(t) and observed ($\Delta\tilde{\nu}^{t}_{obs}$) dynamic Stokes for DMASBT at different compositions of $PC/LiClO_4$/PPG electrolyte solutions at ~ 298 K.

System	a_1	τ_1/ps	a_2	τ_2/ps	$<\tau_{sol}>$ /ps	$\tilde{\nu}(0)*10^3$/ cm^{-1}	$\tilde{\nu}(\infty)*10^3$/ cm^{-1}	$\Delta\tilde{\nu}^{t}_{obs}$/ cm^{-1}
Neat PC	0.35	0.45	0.65	23.81	15.63	20.295	20.246	49
$PC/LiClO_4$	0.22	11.14	0.78	44.84	37.43	20.137	19.963	174
$PC/LiClO_4$/10% PPG	0.17	1.82	0.83	19.92	16.84	18.178	17.997	181
$PC/LiClO_4$/20% PPG	0.49	4.47	0.51	21.74	13.28	18.373	18.076	297
$PC/LiClO_4$/30% PPG	0.31	2.81	0.69	17.3	12.81	18.155	17.977	178
$PC/LiClO_4$/40% PPG	0.58	1.5	0.42	42.55	18.74	18.211	18.075	136
$PC/LiClO_4$/50% PPG	0.46	8.58	0.54	37.74	24.33	18.335	18.139	196
$PC/LiClO_4$/60% PPG	0.76	8.21	0.24	35.46	14.75	18.595	18.189	406
Neat PPG	0.31	4.22	0.69	40.65	29.36	20.761	20.540	221

Our results reveal the presence of ultrafast solvation timescales (~1 - 5 ps) in PPG-containing electrolytes, which can be attributed to the rapid rotational motion of dipolar species present in the electrolyte medium. A detailed examination of **Table 5.1** provides insights into the influence of adding electrolyte on solvation dynamics in neat PC. The introduction of $LiClO_4$ into PC significantly increases both the fast (τ_1) and slow (τ_2) solvation time components, resulting in a substantial increase in the average solvation time ($< \tau_{sol} > /ps$) from ~ 16 ps in neat PC to ~38 ps in $PC/LiClO_4$. This prolongation suggests that $LiClO_4$ induces strong ion - dipole interactions between Li^+ and PC molecules, restricting solvent reorganization and consequently slowing down solvation dynamics. These findings align with our Raman spectroscopic data presented earlier.

Next, we focus on the impact of PPG content in the electrolyte medium on solvation dynamics. At low concentrations (10-30 wt%) of PPG, τ_1 and τ_2 generally decrease compared to $PC/LiClO_4$, leading to a reduction in $< \tau_{sol} >$. This indicates that the incorporation of small amounts of PPG enhances segmental mobility, thereby facilitating solvation. At higher PPG concentrations (40-60 wt%), τ_2 increases again, reflecting a hindered solvation process. This is attributed to the increased viscosity of the electrolyte medium, which imposes constraints on solvent mobility and reorganization. Note that the average solvation time in neat PPG ($< \tau_{sol} >$ ~ 30 ps) is longer than that in neat PC but shorter than in $PC/LiClO_4$. This suggests that PPG exerts a moderate influence on solvent restructuring, governed by its polymeric nature and hydrogen bonding interactions. The solvation dynamics in $PC/LiClO_4$/PPG electrolytes are governed by a complex interplay of ion-dipole interactions, viscosity effects, and polymer segmental mobility. While low PPG content enhances solvation by increasing molecular flexibility, higher PPG content and $LiClO_4$ addition contribute to solvation retardation due to increased viscosity and structural constraints. These findings provide valuable insights into the solvation behavior of GPE systems and their dependence on electrolyte composition.

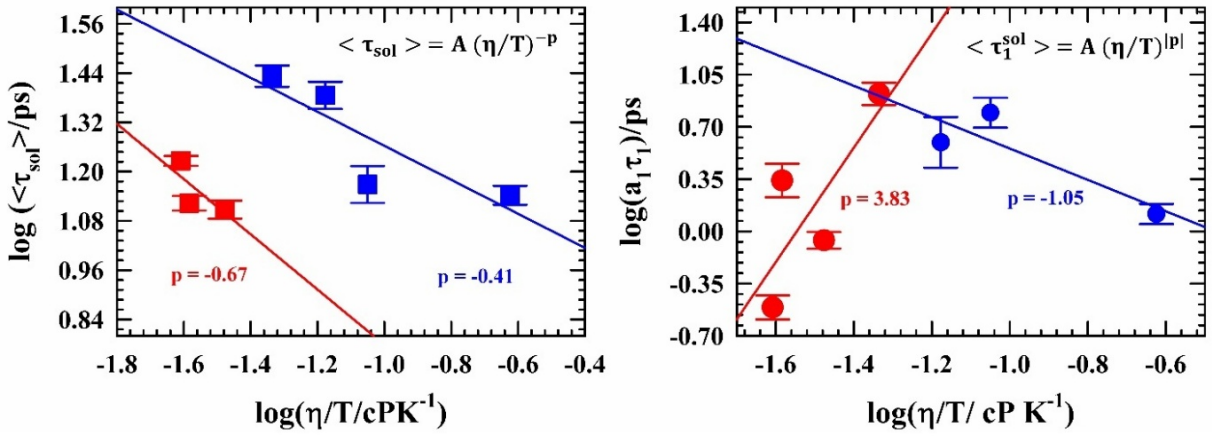

FIG. 5.8. Temperature-scaled viscosity (η/T) dependence of average solvation times ($< \tau_{sol} >$ /ps, left panel) and fast time-component (τ_1^{sol}/ps, left panel) of total solvation dynamics of DMASBT in $PC/LiClO_4$/PPG electrolyte solutions are presented in a log-log fashion. Solid lines through the data points shows the linear fits. Red and blue colored symbols correspond to GPE compositions where C_{PPG} is in the range of 0-30 wt% and 40-60 wt%, respectively.

Fig. 5.8 illustrates the influence of added PPG content on the solvation dynamics of DMASBT in $PC/LiClO_4$/PPG gel polymer electrolytes by examining the viscosity-to-temperature (η/T) scaling of solvation times in a log-log format. In both panels, the red data correspond to samples with higher PPG content, while the blue data represent lower or no PPG content. In the left panel, which shows the average solvation time ($< \tau_{sol} >$) versus log (η/T), the system with higher PPG content exhibits a steeper slope ($p = -0.67$) compared to that with lower PPG content ($p = -0.41$), indicating a stronger coupling of solvation dynamics to the macroscopic viscosity. This suggests that as PPG concentration increases, the local environment becomes more dynamically constrained, likely due to the segmental motions of the polymer chains, and solvation events increasingly reflect bulk viscoelastic behavior. In the right panel, which shows the fast solvation component ($a_1\tau_1$), a stark contrast in p-values is observed: The higher PPG system shows a large positive exponent ($p = 3.83$), while the lower PPG system shows a negative exponent ($p = -1.05$). This inversion of the scaling exponent indicates two distinct aspects of dynamic

heterogeneity depending on PPG concentration. In the polymer-rich system, the fast solvation component becomes dramatically more sluggish with increasing η/T, implying that local environments are highly heterogeneous and strongly immobilized. In contrast, the low- PPG system shows less sensitivity to viscosity, suggesting that fast solvation arises from more uniform, less constrained solvent environments. These differences in p-values highlight that with increasing PPG content, both the average and fast solvation dynamics become more spatially heterogeneous and increasingly governed by the viscoelastic relaxation of the polymeric network.

5.3.4 Dielectric Relaxation Dynamics

5.3.4.1 Origin of DR Timescales and Decoupling of Medium Viscosity and Ion Transport

Representative real (ε') and imaginary components (ε'') of complex dielectric spectra of the current GPE solutions along with spectra for neat solvent (PC) and polymer (PPG) are shown in **Fig. 5.9**. Lines through the ε' and ε'' experimental data points, in **Fig. 5.9**, represent multi-Debye fits and the corresponding fit parameters are summarized in **Table 5.2** and **Table 5.B.5** (Appendix 5.B). In our previous report we have studied dielectric relaxation dynamics for $PC/LiClO_4/PPG425$ electrolyte medium and our present results for neat PC and $PC/LiClO_4$ matches well with that.[42] In neat PC the dynamics is mostly (~ 95%) guided by ~ 40 ps time-component attributed to dipolar reorientation of PC molecules[43] and the fastest time constant, $\tau_3 \sim 4$ ps is related to $C-H$ bond vector relaxation. A new timescale, $\tau_1 \sim 200$ ps appeared with amplitude ~ 30% as $LiClO_4$ was added to PC. But after that adding PPG in electrolyte solution, the amplitudes of two timescales $\tau_1 \sim 200$ ps and $\tau_2 \sim 50-60$ ps came up with 40 - 60 percentage ratio. So, there is always a balancing between these two widely-separated time constants signifying the presence of multiple relaxation processes arising from different molecular motions and interactions within the system. In pure PPG, two distinct relaxation timescales have been observed: a slower component $\tau_1 \sim 260-750$ps and a faster one $\tau_2 \sim 100-45$ ps, with a relative contribution of ~70-30 across the studied temperature range (see **Table 5.2**). The longer τ_1 corresponds to cooperative dipolar relaxation mediated by the hydrogen-bonding network among PPG chains, while the faster τ_2 reflects localized segmental motions, particularly the terminal -OH group of the PPG.[44].

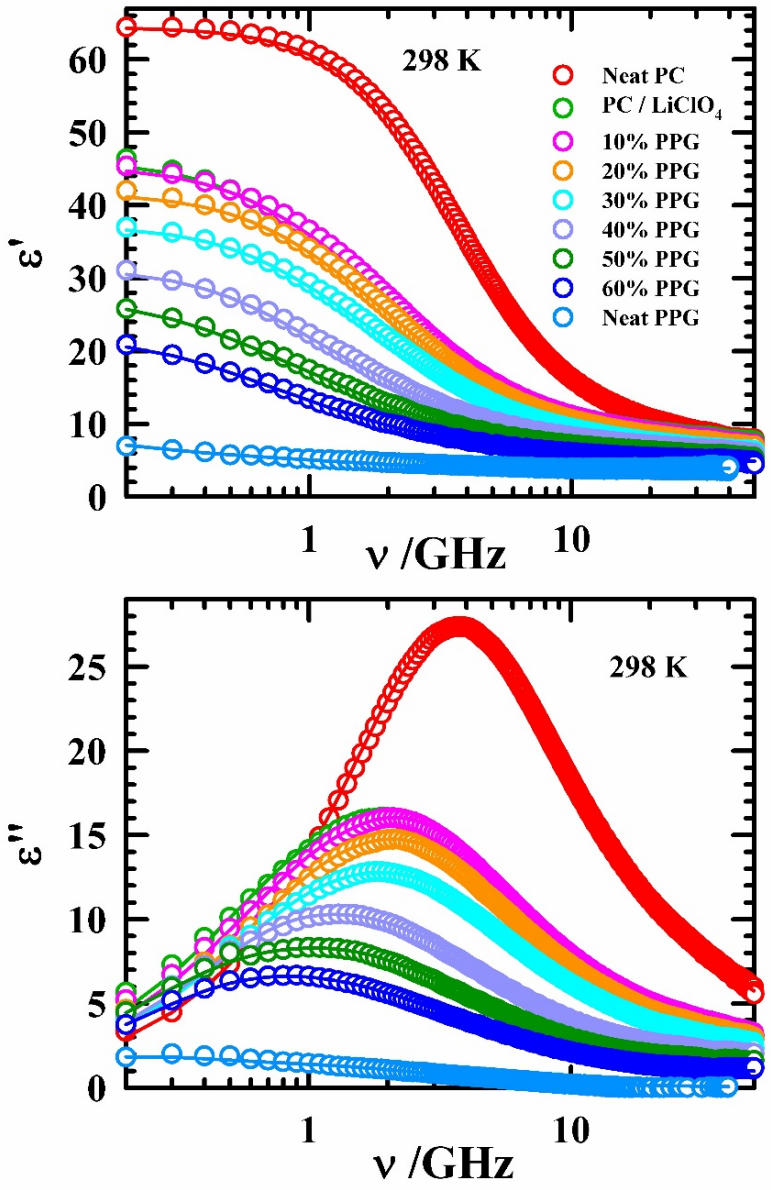

FIG. 5.9. The real (ε') and imaginary (ε'') components of the complex dielectric spectra recorded for neat PC, neat PPG and PC/$LiClO_4$/PPG gel electrolyte solutions at 298 K. Experimental data points are shown as symbols while lines passing through them represent multi-Debye fits. All representations are color-coded.

Table 5.2. Multi-Debye fit parameters of temperature dependent experimentally measured DR spectra for neat PC, neat PPG and PC/$LiClO_4$/PPG electrolyte solutions with various polymer concentrations. The values in the parenthesis represents the percentage of amplitudes.

T/K	ε_s	$\Delta\varepsilon_1$	τ_1 /ps	$\Delta\varepsilon_2$	τ_2 /ps	$\Delta\varepsilon_3$	τ_3 /ps	$\Delta\varepsilon_4$	τ_4 /ps	ε_∞	n^2	$\varepsilon_s - n^2$	$<\tau_{DR}>$ /ps
PC/$LiClO_4$/10% PPG													
298	45.4	12.2 (31)	175	23.5 (60)	58	-	-	3.5 (9)	5	6.2	2.043	4.2	90
303	44.8	12.7 (33)	162	22.7 (58)	55	-	-	3.5 (9)	5	5.9	2.040	3.9	85
308	44.8	12.5 (31)	147	23.8 (60)	49	-	-	3.3 (9)	5	5.2	2.036	3.2	76
313	44.9	10.3 (27)	148	25.6 (65)	46	-	-	3.1 (8)	6	5.9	2.029	3.9	70
318	45.0	9.6 (25)	146	26.1 (68)	42	-	-	2.9 (7)	5	6.4	2.024	4.4	65
323	44.1	8.5 (22)	144	26.7 (70)	40	-	-	3.0 (8)	6	5.9	2.020	3.9	60
PC/$LiClO_4$/20% PPG													
298	41.7	13.6 (38)	146	19.0 (53)	54	-	-	3.1 (9)	5	6.0	2.048	4.0	85
303	41.9	12.4 (35)	147	20.6 (57)	52	-	-	2.8 (8)	6	6.0	2.043	4.0	81
308	41.6	11.3 (32)	145	21.7 (60)	50	-	-	2.8 (8)	6	5.8	2.040	3.8	77
313	41.1	9.9 (27)	148	22.7 (63)	47	-	-	3.4 (10)	5	5.1	2.036	3.1	71
318	41.4	8.1 (23)	155	24.1 (68)	44	-	-	3.1 (9)	6	6.1	2.029	4.1	66
323	40.9	7.3 (21)	150	24.9 (71)	40	-	-	2.8 (8)	6	5.9	2.024	3.9	60
PC/$LiClO_4$/30% PPG													
298	37.2	13.9 (44)	158	15.2 (48)	53	-	-	2.7 (8)	5	5.5	2.059	3.4	95
303	37.4	13.5 (43)	150	15.5 (49)	52	-	-	2.4 (8)	6	5.9	2.051	3.8	91
308	37.1	11.7 (37)	160	17.3 (54)	52	-	-	2.7 (9)	6	5.4	2.045	3.4	88
313	37.6	10.9 (34)	158	18.4 (58)	51	-	-	2.5 (8)	7	5.8	2.042	3.8	84
318	36.3	10.0 (31)	160	19.2 (60)	46	-	-	2.9 (9)	5	4.2	2.039	2.2	78
323	37.5	12.0 (38)	128	17.6 (56)	39	-	-	1.7 (6)	5	6.2	2.034	4.2	71
PC/$LiClO_4$/40% PPG													
298	31.3	14.3 (55)	188	9.5 (36)	58	-	-	2.2 (9)	5	5.3	2.065	3.2	125
303	32.0	13.1 (50)	177	11.2 (43)	56	-	-	2.1 (7)	6	5.6	2.060	3.5	112
308	31.4	12.6 (47)	167	11.8 (44)	51	-	-	2.4 (9)	5	4.7	2.055	2.6	101

313	32.6	10.9 (40)	175	14.2 (52)	53	-	-	2.1 (8)	7	5.6	2.047	3.6	98
318	32.5	9.6 (36)	172	15.1 (56)	50	-	-	2.1 (8)	7	5.6	2.043	3.6	90
323	32.1	8.9 (33)	168	15.6 (58)	47	-	-	2.2 (9)	7	5.3	2.040	3.3	84
PC/$LiClO_4$/50% PPG													
298	27.1	8.9 (40)	330	9.1 (40)	103	2.6 (12)	39	1.7 (8)	4	4.8	2.070	2.7	179
303	27.7	6.3 (28)	307	12.2 (55)	96	2.8 (12)	26	1.1 (5)	5	5.3	2.065	3.2	142
308	28.7	6.8 (28)	352	13.0 (56)	88	2.7 (12)	22	0.9 (4)	4	5.2	2.061	3.1	154
313	28.6	5.5 (24)	342	12.9 (56)	88	3.6 (15)	28	1.2 (5)	6	5.3	2.055	3.2	135
318	28.4	5.3 (23)	316	12.9 (56)	83	3.9 (17)	27	1.1 (4)	6	5.2	2.046	3.2	123
323	28.2	5.0 (23)	313	13.0 (56)	78	4.1 (17)	25	1.1 (4)	5	5.1	2.043	3.1	116
PC/$LiClO_4$/60% PPG													
298	21.8	8.1 (46)	322	6.2 (36)	110	2.1 (12)	33	1.1 (6)	3	4.4	2.063	2.3	192
303	21.7	7.3 (41)	308	6.7 (37)	116	2.8 (15)	34	1.2 (7)	4	3.7	2.061	1.6	174
308	23.1	6.5 (36)	320	8.9 (49)	96	2.1 (12)	24	0.7 (4)	4	4.9	2.059	2.8	164
313	24.2	6.8 (35)	334	9.1 (48)	92	2.7 (14)	24	0.5 (3)	6	5.1	2.057	3.0	166
318	23.7	6.0 (31)	331	9.6 (50)	91	2.8 (15)	25	0.7 (4)	6	4.6	2.056	2.5	154
323	22.4	7.3 (38)	246	7.7 (41)	77	2.6 (14)	24	1.3 (7)	4	3.6	2.050	1.6	130
Neat PPG													
298	8.7	3.2 (67)	793	1.6 (33)	118	-	-	-	-	3.9	2.182	1.7	568
303	8.4	3.2 (65)	620	1.7 (35)	79	-	-	-	-	3.5	2.088	1.4	432
308	7.9	2.8 (62)	424	1.7 (38)	63	-	-	-	-	3.4	2.082	1.3	288
313	7.7	3.0 (70)	370	1.3 (30)	52	-	-	-	-	3.4	2.077	1.3	274
318	8.0	2.8 (62)	356	1.7 (38)	55	-	-	-	-	3.5	2.073	1.4	242
323	8.2	3.0 (64)	272	1.7 (36)	44	-	-	-	-	3.5	2.068	1.4	190

As temperature increases, both τ_1 and τ_2 systematically decrease due to reduced viscosity and enhanced thermal energy, which promote faster segmental dynamics and disrupt intermolecular interactions. This leads to more rapid reorientation of dipoles and faster dielectric relaxation. The breakdown of hydrogen-bond networks at elevated temperatures further contributes to the reduction in τ_1, indicating weakened cooperativity. Simultaneously, the enhanced flexibility of polymer chains accelerates local motions, thereby shortening τ_2 and improving the overall dielectric response of the system.

The variation in static dielectric constant with temperature, as shown in **Fig. 5.A.4** (Appendix 5.A), is relatively modest across all GPE compositions investigated. Temperature-dependent DR spectra for two representative electrolyte formulations are presented in **Fig. 5.10** while **Fig. 5.11** illustrates the corresponding temperature evolution of relaxation amplitudes and timescales for all studied compositions. Notably, both figures demonstrate a pronounced decrease in the effective static dielectric permittivity (ε_s) with increasing PPG concentration at any given temperature. This trend reflects the enhanced rigidity and reduced segmental flexibility of the polymer chains, which restrict dipolar reorientation and thereby suppress the dielectric response of the system.

A close inspection of **Table 5.2** reveals a new time component, τ_3, which contributes an average of 15% in total relaxation dynamics after adding 50% and 60% PPG to the $PC/LiClO_4$ electrolyte. At these high PPG concentrations, the relaxation mechanism of PPG becomes more complex due to structural changes in Li^+ ion solvation. These structural changes, previously discussed in Raman spectroscopic studies, are reflected in the dynamical behavior shown here.

The study showed an intriguing relationship between the average times of dielectric relaxation (DR) and the slower individual components of DR in a gel electrolyte containing PPG. It was observed that average DR times exhibited a strong dependence on fractional power (with p values ranging from 0.3-0.4) (see **Fig. 5.12 (a)**) relative to the reduced viscosity of the medium, suggesting the presence of notable temporal variations within the GPE. Interestingly, the fractional power dependence characterized by p-values calculated from average DR timescales, are aligning

well with the p-values derived from the second slow-component, τ_2, which predominates in the overall dielectric relaxation dynamics as illustrated in **Fig. 5.12 (b)**. The underlying cause of this complex dynamic heterogeneity may be attributed to the significant involvement of both homogeneous and heterogeneous hydrogen bonding between PC and PPG molecules.

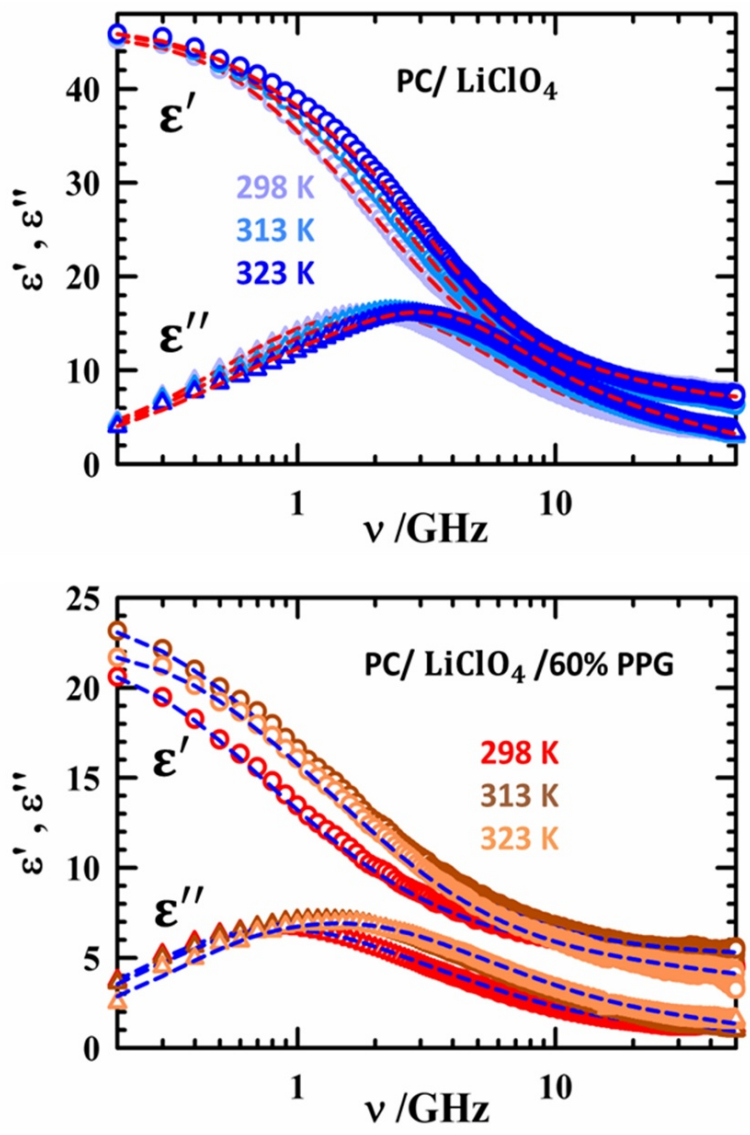

FIG. 5.10. The temperature-dependent real (ε′) and imaginary (ε″) components of the complex dielectric spectra recorded for $PC/LiClO_4$ (upper panel) and for $PC/LiClO_4/60\%PPG$ (lower panel) electrolyte solutions. Experimental data points are shown as symbols while lines passing through them represent multi-Debye fits. All representations are color-coded.

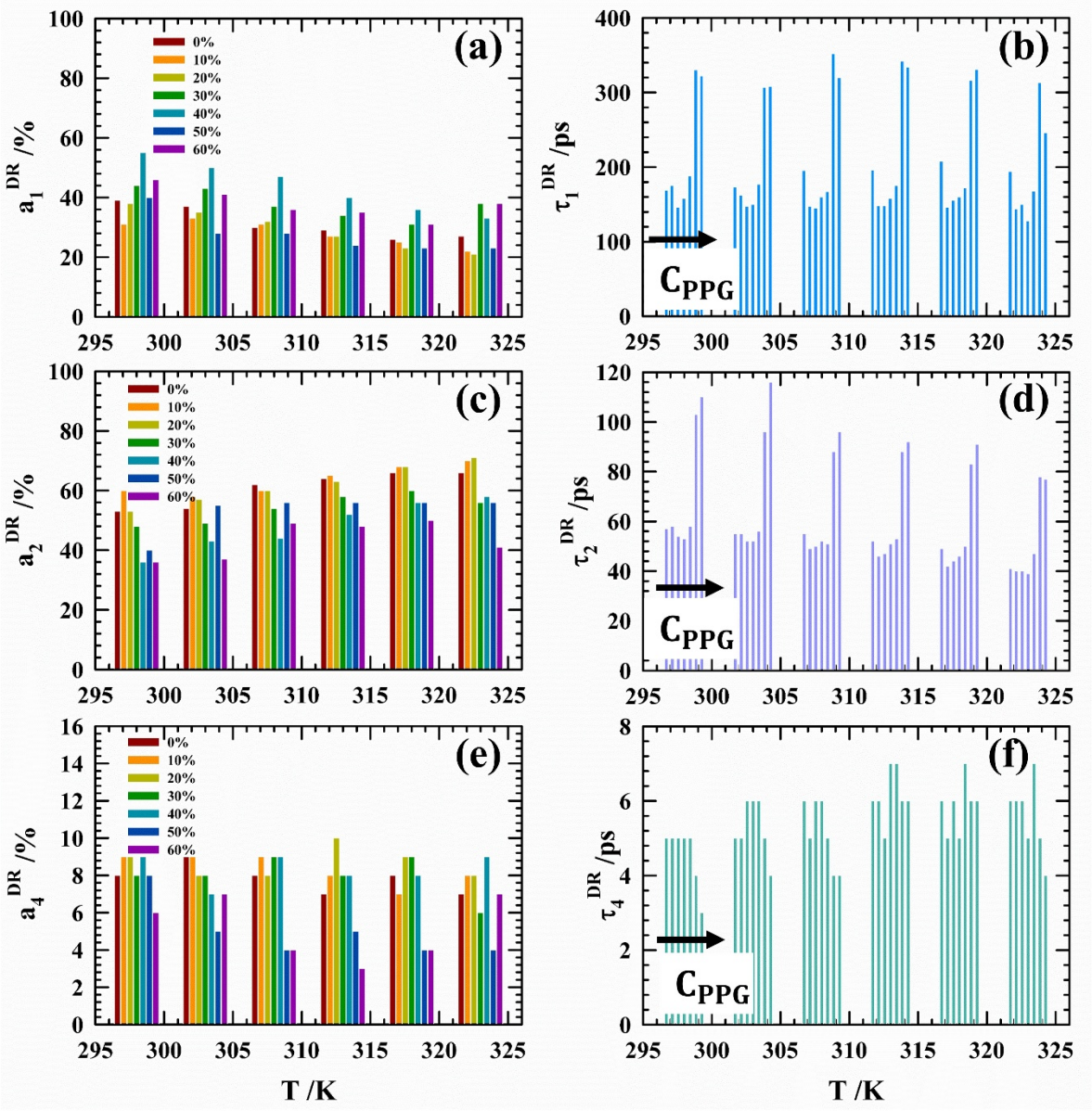

FIG. 5.11. Temperature dependent change in percentage of amplitudes ($a_1^{DR}, a_2^{DR}, a_4^{DR}$, upper panel) and their respective timescales ($\tau_1^{DR}, \tau_2^{DR}, \tau_4^{DR}$, lower panel) of $PC/LiClO_4/PPG$ gel electrolyte. From left to right concentration of PPG is increasing at each respective temperature. Presentation is color-coded.

Next, the DR dynamics and ionic conductivity behavior of $PC/LiClO_4$/PPG gel polymer electrolytes exhibit distinct trends as a function of added PPG, depicted in **Fig. 5.12 (c)**. As shown in this figure, the log-log scaling of the DR time components and ionic conductivity with temperature-reduced viscosity (η/T) reveals progressively decreasing p-values with increasing PPG concentration. For both the average DR times ($< \tau^{DR} >$) and its second component (τ_2^{DR}), as well as ionic conductivities (σ), the p-value systematically declines from ~0.6 at 0% PPG to ~0.3–0.4 at 60% PPG. This reduction in p-values suggests a weakening of the coupling between these DR processes and the macroscopic viscosity. Physically, this implies a transition from a relatively homogeneous, liquid-like medium at low PPG - where dipolar relaxation and ion motion are strongly influenced by the bulk viscosity towards a heterogeneous polymer-rich environment at higher PPG, where these dynamic processes become increasingly localized and decoupled from the global viscous response. Such decoupling indicates the emergence of spatial dynamic heterogeneity, likely due to restricted molecular mobility in PPG-dominated domains where polymer chain dynamics govern local environmental relaxation dynamics.

This interpretation is further supported by Arrhenius analysis in **Fig. 5.13** and the activation energy data summarized in **Table 5.B.6** (Appendix 5.B). The activation energy for viscosity (E_a^{η}) increases sharply with added PPG, from 19.21 kJ mol^{-1} at 0% to a peak of 40.82 kJ mol^{-1} at 20% PPG, suggesting the system becomes more dynamically constrained as polymer content rises. Notably, activation energies associated with DR and ionic conductivity also increase with PPG, indicating that both dipolar reorientation and ion transport require more thermal energy to overcome the increasingly hindered environment. For instance, E_a^{σ} increases from 12.80 kJ mol^{-1} at 0% PPG to over 20 kJ mol^{-1} at 60% PPG, a trend paralleled by E_a^{DR}. This rise reflects the fact that ion hopping and dielectric relaxation mechanisms become more sensitive to segmental motions of the polymer and less influenced by bulk viscosity.

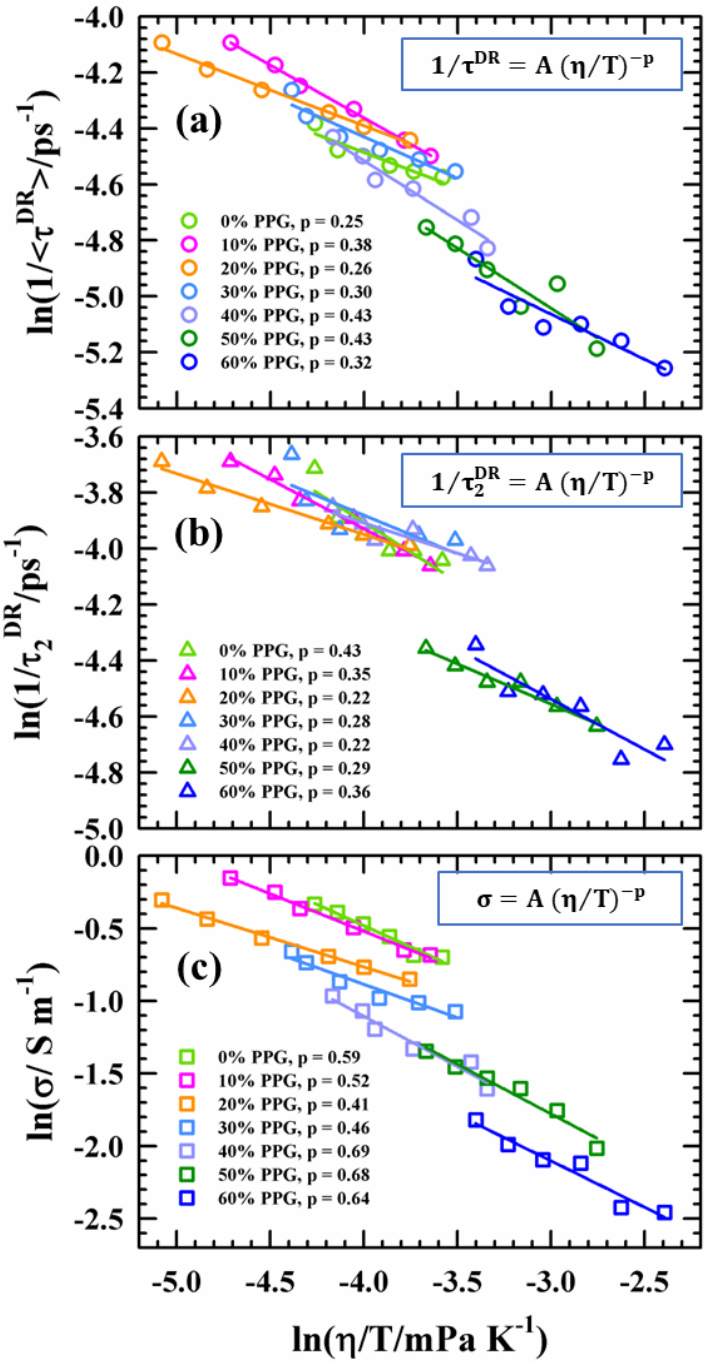

FIG. 5.12. Temperature-reduced viscosity dependence (η/T) of the DR time-component, [(a) τ_{DR}/ (b) τ_2/ps] and (c) ion conductivity (σ) of PC/$LiClO_4$/PPG electrolyte solutions at various concentrations of PPG in double logarithmic fashion. Solid lines passing through the data points represent fits. A global fit through all the data points is shown as black dashed lines. All representations are color-coded.

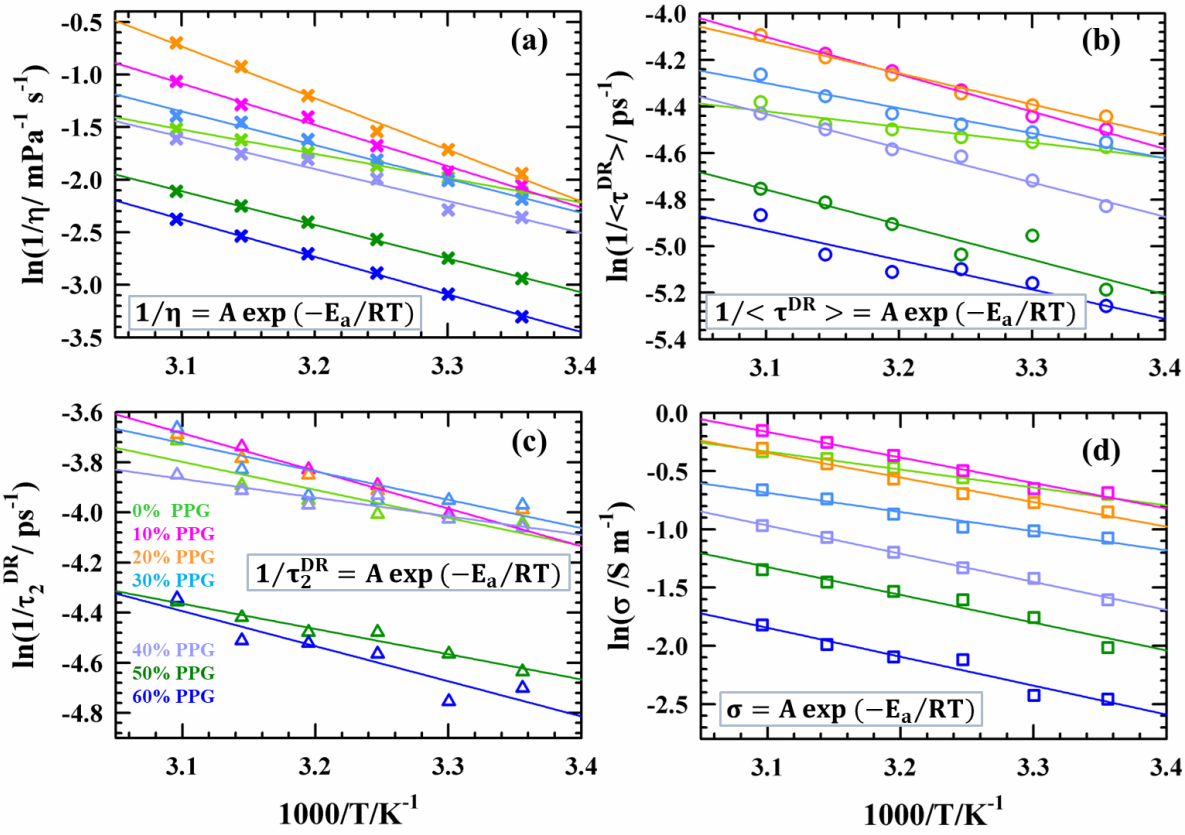

FIG. 5.13. Arrhenius-type temperature dependence of medium viscosity (a), average DR time (b), τ_2^{DR} (c) and ionic conductivity (d) for PC/$LiClO_4$/PPG electrolyte solutions at various concentrations of PPG. Solid lines passing through the data points represent linear fits. All representations are color-coded.

From a physical chemistry standpoint, these results demonstrate two distinct dynamic regimes depending on PPG concentration. At low PPG levels, the electrolyte behaves like a homogeneous viscous liquid where transport and relaxation are tightly viscosity-coupled and governed by continuum-like friction. In contrast, at high PPG concentrations, the system enters a gel-like regime characterized by dynamic heterogeneity: ion motion and dipole reorientation are increasingly dominated by the spatial constraints and time scales of PPG segmental relaxation. This decoupling from viscosity and the increase in activation energies highlight the complex interplay between solution microstructure, polymer dynamics, and ion transport properties in GPEs.

5.3.4.2 Correlating Onsager-Predicted and Experimental Ion Conductivity: Impact of Dynamic Heterogeneity and DR Dynamics

To establish a connection between DR dynamics and ion transport mechanism in GPEs, the Onsager relation for ionic conductivity is employed: $\sigma_{dc} = \chi_D/\tau_D = \frac{\varepsilon_0(\varepsilon_s-\varepsilon_\infty)}{4\pi\tau_D}$, where σ_{dc} is ion conductivity, χ_D is dielectric strength, τ_D is a characteristic DR times that captures dipolar dynamics, ε_s, ε_∞ and ε_0 are static dielectric constant, high-frequency dielectric constant and vacuum permittivity, respectively.[45,46] This relation provides a conceptual bridge between the microscopic polarization dynamics of dipoles and macroscopic ion transport, assuming that charge movement and dipole relaxation are correlated through similar frictional or viscous forces.[47–49] The Onsager model is grounded in continuum dielectric theory and makes several simplifying assumptions.[50,51] It assumes the response of the system to an external field is linear and isotropic and the theory treats the system as a continuous, uniform dielectric, neglecting microscopic spatial heterogeneities. The model assumes that a single dominant dipolar relaxation time which controls both dielectric and conductive behavior, which may not hold in complex chemical systems. It ignores IP formation and ion clustering which could significantly reduce free ion mobility. In polymer-rich systems ion motion often coupled with slow segmental polymer dynamics which is beyond the original scope of Onsager theory. Keeping these assumptions, deviations from Onsager-predicted conductivity are expected in heterogeneous, polymer-containing, or non-ideal electrolytic systems.

In **Fig. 5.14**, the Onsager conductivity is estimated using the average DR times, $< \tau^{DR} >$. This $< \tau^{DR} >$ includes contributions from both fast (e.g., dipolar reorientation of PC) and slow (e.g., segmental motion of PPG) processes. The result is a consistent underestimation of conductivity across all PPG concentrations when compared to experimentally measured values (σ^{exp}). The underprediction is particularly pronounced at low PPG content, where solvent-like behavior dominates. To refine the prediction, **Fig. 5.15** shows Onsager conductivities recalculated using τ_1^{DR}, the slowest dielectric component typically associated with cooperative segmental relaxation and H-bonded dynamics of PPG. This approach produces much lower predicted conductivities, and importantly, the discrepancy between predicted and experimental conductivities decreases

systematically with increasing PPG content. At high PPG concentrations (≥40%), τ_1^{DR}-based predictions align more closely with experiment, suggesting that ion transport becomes increasingly coupled to slow, localized polymer segmental dynamics.

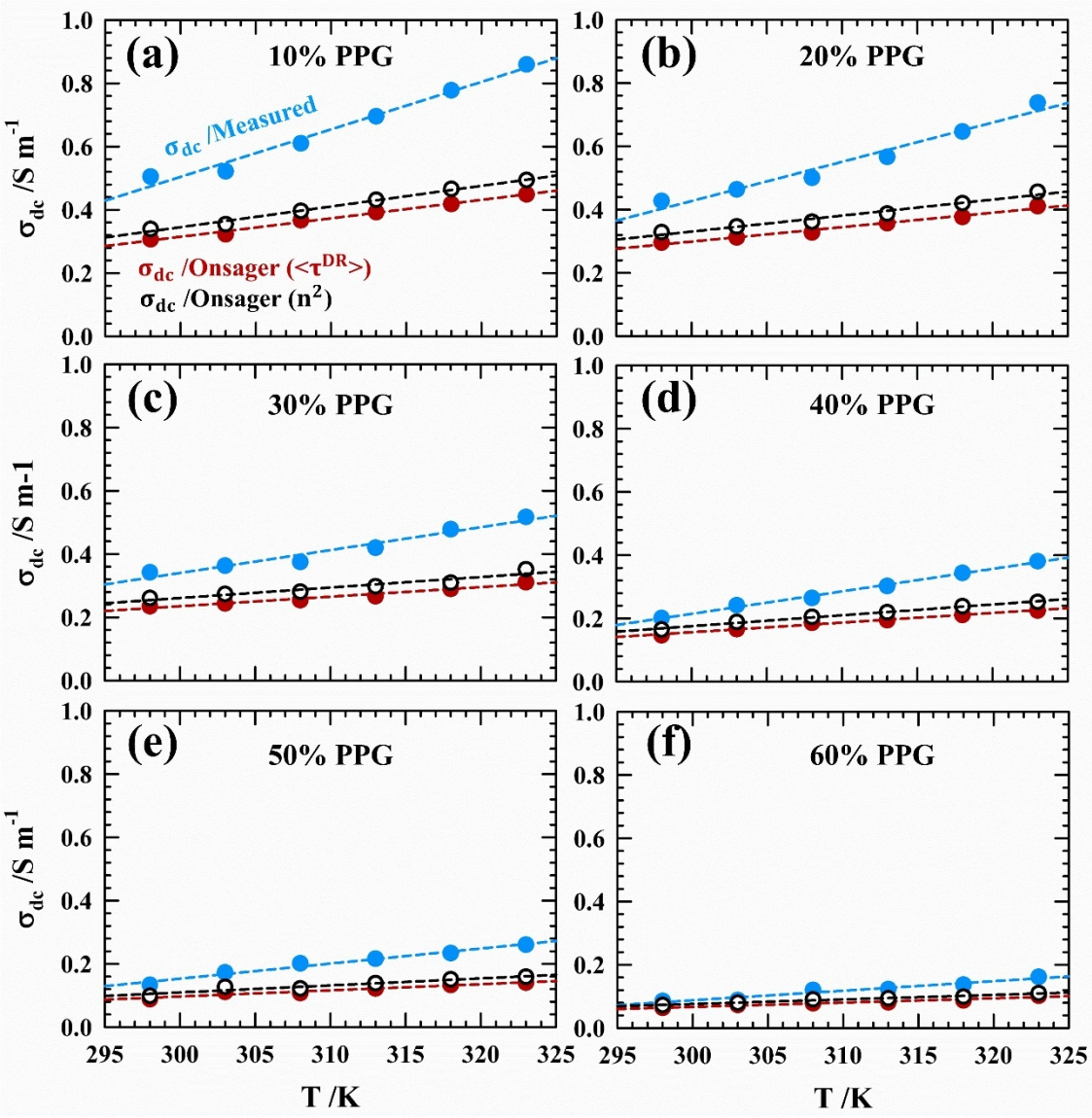

FIG. 5.14. Comparison of Onsager predicted and experimentally measured conductivities across temperatures from 298 to 323 K in PC/$LiClO_4$/PPG electrolyte solutions. Blue circles represent experimentally measured conductivities (σ^{exp}/S m^{-1}). Red circles denote the Onsager-predicted conductivities calculated using the average DR time ($< \tau^{DR} >$) and static dielectric permittivity (ε_s). Black symbols indicate Onsager-predicted conductivities where the high-frequency dielectric constant (ε_s) is approximated using the square of the refractive index (n^2).

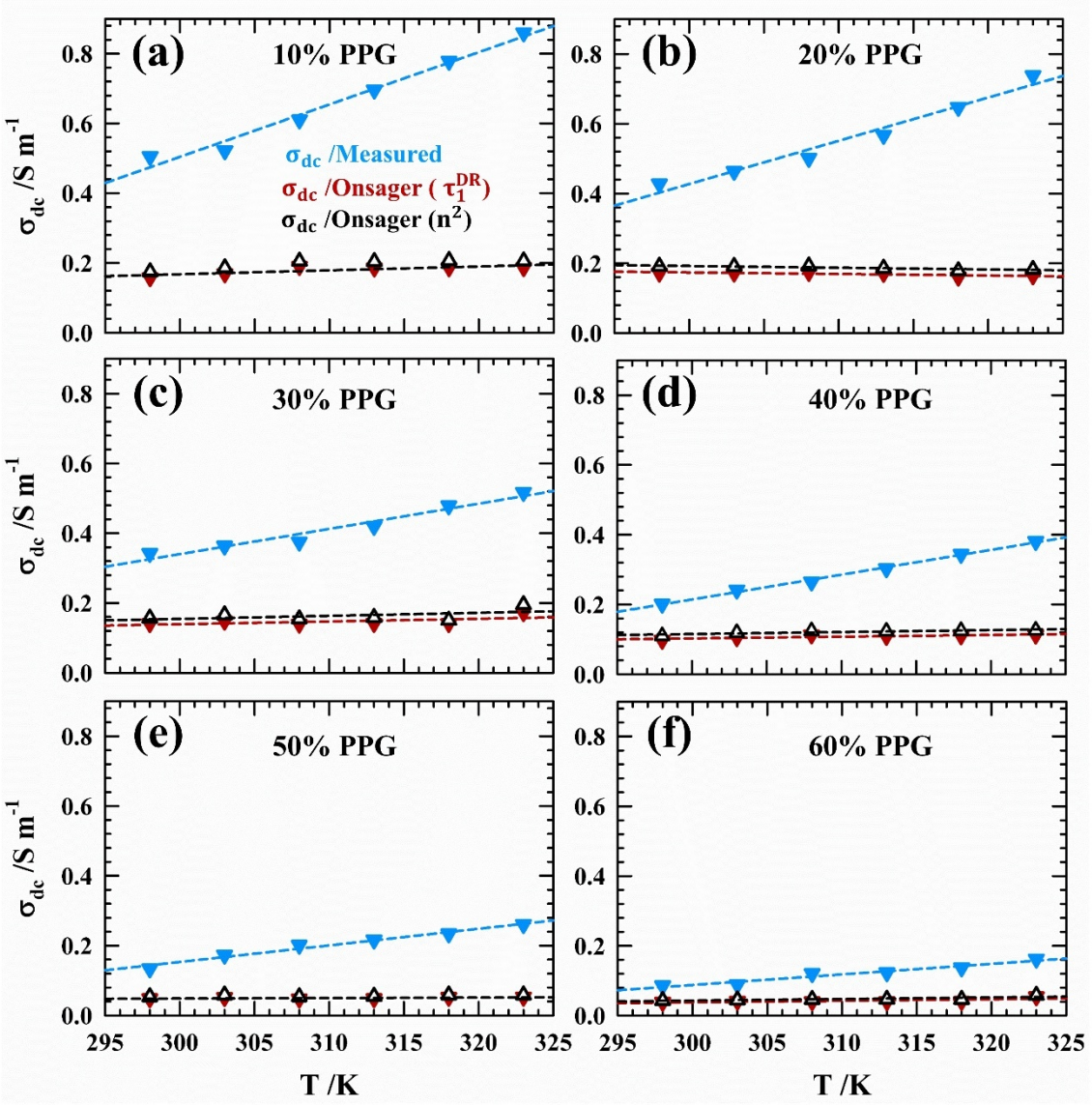

FIG. 5.15. Comparison of Onsager predicted and experimentally measured conductivities across temperatures from 298 to 323 K in PC/$LiClO_4$/PPG electrolyte solutions. Blue triangles represent experimentally measured conductivities (σ^{exp}/S m^{-1}). Red triangles denote the Onsager-predicted conductivities calculated using the longest DR time-component (τ_1^{DR}) and static dielectric permittivity (ε_s). Black symbols indicate Onsager-predicted conductivities where the high-frequency dielectric constant (ε_s) is approximated using the square of the refractive index (n^2).

The observed deviation between Onsager predictions and experimental results at low PPG content arises from a mismatch in relevant timescales: ion motion remains governed by faster solvent dynamics, while Onsager theory assumes a single frictional timescale applies. As PPG content increases, structural and dynamic heterogeneity emerge as evidenced from dielectric relaxation spectra, viscosity scaling behavior, and Raman studies showing shifts in Li^+ solvation from PC to PPG-dominated coordination environments. This transition from a homogeneous, viscous liquid-like regime to a gel-like, dynamically heterogeneous medium implies that charge transport is increasingly restricted to spatially localized domains. These domains are characterized by the slow relaxation of PPG chains, which impose constraints on Li^+ ion hopping and reorientation of ion-dipoles. Therefore, using τ_1^{DR} in the Onsager framework becomes more physically meaningful in this regime, capturing the dominant frictional interactions that govern ion mobility. Moreover, the improved agreement between τ_1^{DR}-based predictions and experimental conductivity at high PPG concentrations (≥40%) further validates the hypothesis that ion transport in GPEs is not guided by medium viscosity, but rather controlled by slow polymer relaxation and dynamically heterogeneous segmental mobility, phenomena beyond the original Onsager formulation. Thus, paradoxically, although PPG -rich systems are more structurally complex and dynamically heterogeneous, their transport properties become more consistent with Onsager theory - not because the theory fully applies, but because the dominant ion transport mechanism aligns with its assumptions. This provides further evidence of PPG-mediated dynamic heterogeneity in the electrolyte solutions and underscores the limitations of classical continuum theories. It highlights the necessity for incorporating dynamic heterogeneity-aware models to more accurately describe ion transport in gel-like soft condensed systems.

5.4 Summary

This study elucidates the intricate interplay between microscopic structure, dynamic relaxation processes, and macroscopic ion transport in $PC/LiClO_4$/PPG gel polymer electrolytes (GPEs). By systematically combining DLS, Raman spectroscopy, dielectric relaxation spectroscopy (DRS), and ultrafast fluorescence measurements, a unified framework has been developed to describe how polymer incorporation modulates electrolyte behavior across different length and timescales.

- DLS experiments reveal that PPG incorporation drives self-assembly into nanostructured domains (~2000–5000 nm), whose size increases markedly at high PPG concentrations (>40 wt%). This structural evolution transitions the system from a homogeneous liquid-like regime to a heterogeneous, gel-like environment, where Li^+ ion motion becomes increasingly confined by polymer networks. This structural confinement underpins much of the observed dynamical behavior.

- Raman spectroscopy confirms that PPG plays a dual role in regulating Li^+ ion speciation and solvent (PC) coordination. At low concentrations of PPG ($\leq 30\%$), PC governs solvation with significant ion pairing, whereas high PPG content suppresses ion pairing (e.g., SSIP signatures diminish) and shifts coordination preferences. This shift enhances the availability of free ClO_4^- anions and stabilizes Li^+– carbonyl interactions without significantly perturbing PC–Li^+ coordination, suggesting that PPG mediates ion dynamics indirectly through altering the solvation shell and facilitating mechanical network formation.

- Ultrafast streak camera analysis highlights how solvation dynamics are finely tuned by the balance between solvent freedom and polymer-induced viscosity. The solvation dynamics across $PC/LiClO_4/PPG$ electrolyte systems reveal a non-monotonic trend with increasing PPG content. Neat PC shows fast solvation, which slows significantly upon addition of $LiClO_4$ due to strong ion-dipole interactions. Introducing low-to-moderate PPG (10 - 30%) partially disrupts ion pairing, enhancing mobility and leading to faster solvation. At higher PPG concentrations ($\geq 40\%$), solvation dynamics exhibit a moderate slowdown, primarily due to increased viscosity and the restricted mobility of polymer segments within the growing network structure. This is accompanied by a greater contribution from slower relaxation components, indicating the onset of pronounced dynamic heterogeneity. In this regime, solvation is no longer dominated by bulk solvent behavior but becomes increasingly influenced by localized segmental dynamics of PPG, reflecting the transition from a liquid-like to a more structured, gel-like environment.

- DRS measurements further support this heterogeneous dynamical landscape. Neat PC shows dominant ~ 40 ps dipolar relaxation and a fast ~ 4 ps C– H bond vector relaxation. Upon adding $LiClO_4$, a new slower time-component (~ 200 ps) emerges, reflecting strong ion-dipole interactions, aligned with the results of our solvent relaxation dynamics. The emergence and evolution of slow dielectric relaxation modes (~ 200 - 350 ps and ~ 50 - 60 ps) with increasing PPG content reflect growing cooperative motion of polymer segments and modified ion-dipole interactions. At high PPG loadings (C_{PPG} ~ 50% and 60%), a third DR time-component (τ_3^{DR} ~ 30 ps) emerges, contributing ~15% to the overall response. This additional timescale reflects increased spatial and temporal heterogeneity arising from restricted polymer chain mobility and formation of an interconnected polymer network. These findings are consistent with DLS measurements, which reveal the presence of large aggregates (D_h~5000 nm) at these concentrations, further supporting the presence of structural complexity and dynamic heterogeneity in the system.

- Notably, the correlation between structure, dynamics, and transport converges within the framework of Onsager conductivity analysis. While classical Onsager theory assumes a uniform frictional environment and single relaxation timescale, valid mainly for simple component liquids, it becomes increasingly applicable at higher PPG concentrations (> 40%), where ion motion couples to the slow segmental relaxations of the polymer matrix. This apparent convergence in a dynamically heterogeneous system arises as frictional interactions become more localized and temporally extended, aligning with continuum assumptions. The transition from a liquid-like to gel-like regime thus marks a shift from viscosity-dominated to polymer-constrained ion transport. These findings underscore that structural and dynamic heterogeneity are not limitations but critical parameters that govern conductivity, necessitating refined models incorporating local solvation, spatial confinement, and complex relaxation behavior to accurately describe ion transport in GPEs.

Appendix 5.A

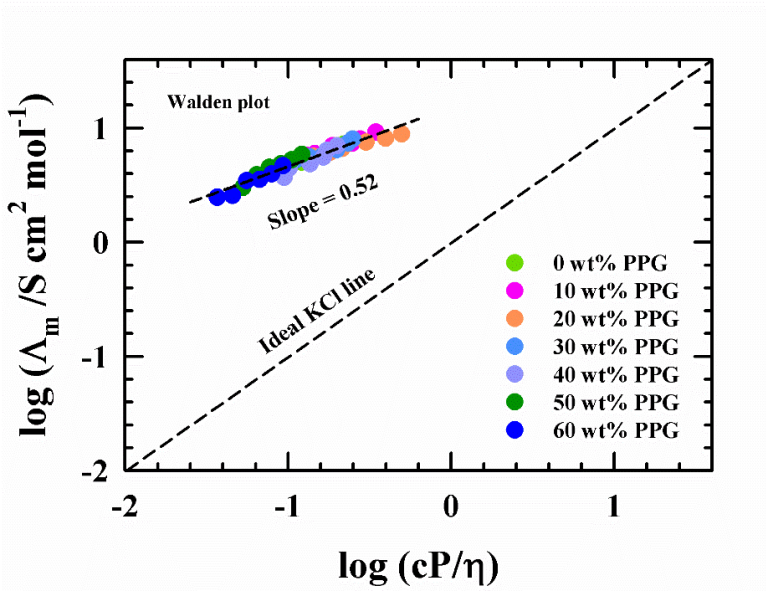

FIG. 5.A.1. Walden plot representing correlation between viscosity (η/ cP) and molar conductivity (Λ_m/ S cm^2 mol^{-1}) in $PC/LiClO_4$/PPG electrolyte solutions.

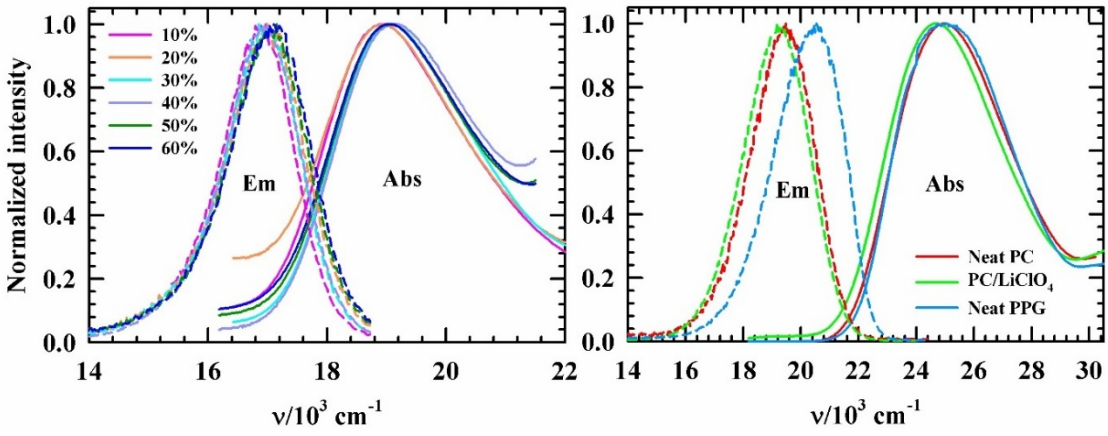

FIG. 5.A.2. The left panel displays the normalized UV-vis absorption (solid lines) and emission (dashed lines) spectra of DMASBT in $PC/LiClO_4$/PPG electrolyte solutions at varying PPG concentrations. The right panel presents the spectra for neat PC, PPG and $PC/LiClO_4$ solutions at ~298 K. All GPE compositions are color-coded for clarity.

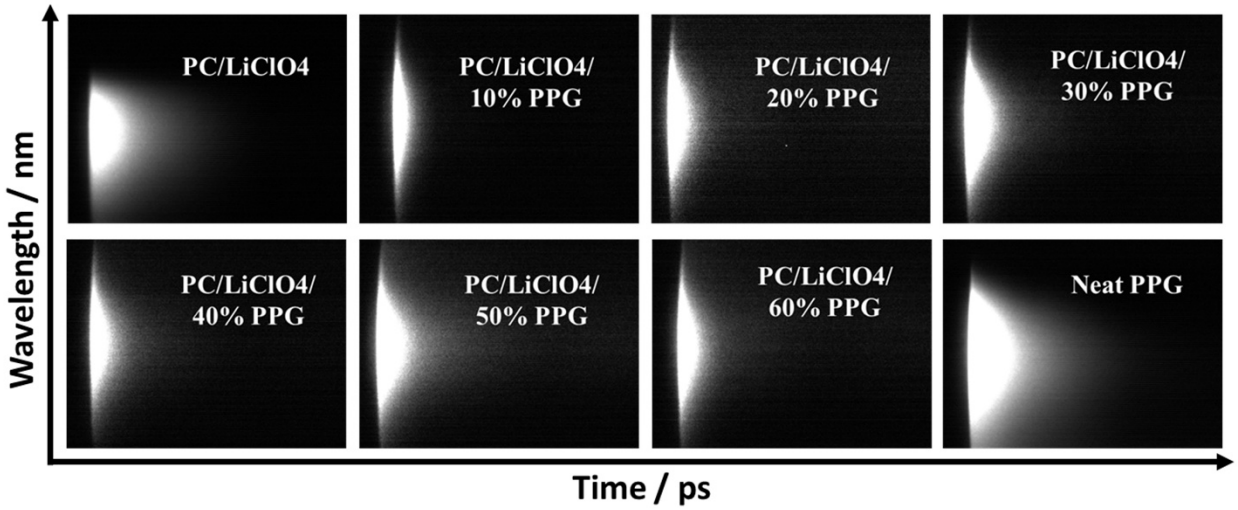

FIG. 5.A.3. 2-D streak camera images of DMASBT in $PC/LiClO_4$/PPG electrolyte solutions at ~298 K capture inherently 3-D data: X-axis shows time evolution of fluorescence intensity, and Y-axis corresponds to emission wavelength. Thus, vertical slices reflect wavelength-dependent emission at a fixed time, while horizontal slices denote time-dependent intensity at a fixed wavelength.

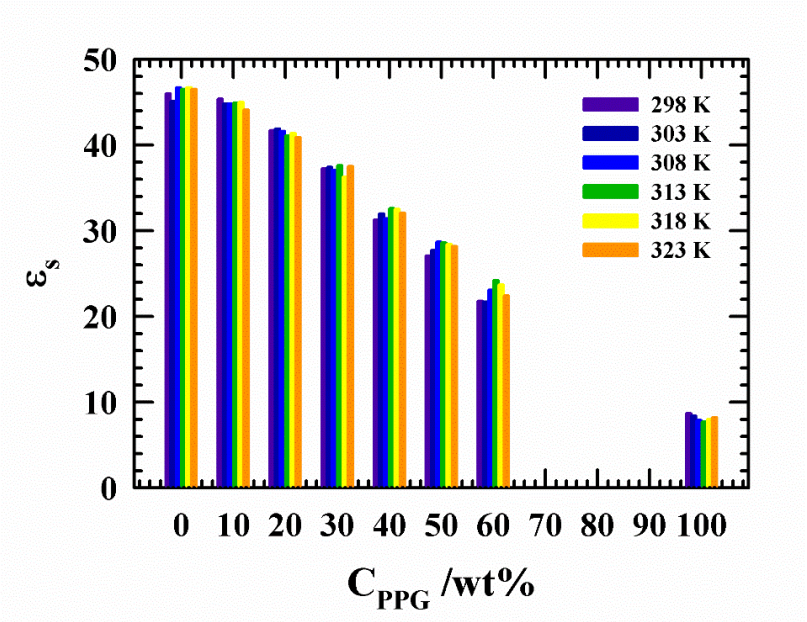

FIG. 5.A.4. Temperature dependent static dielectric constant (ε_s) in $PC/LiClO_4$/PPG electrolyte solutions at various concentrations of PPG. All presentations are color-coded.

Appendix 5.B

Table 5.B.1. Temperature dependent measured densities (ρ) and viscosities (η) in $PC/LiClO_4/PPG$ electrolyte solutions with varying PPG concentrations from 0 to 60 wt%.

C_{PPG}/ wt%	$PC/LiClO_4/PPG$					
	Density (ρ/ g cm^{-3})					
	298 K	303 K	308 K	313 K	318 K	323 K
0	1.258	1.253	1.248	1.243	1.238	1.233
10	1.227	1.221	1.217	1.212	1.206	1.202
20	1.199	1.195	1.190	1.184	1.178	1.175
30	1.174	1.170	1.165	1.161	1.154	1.150
40	1.146	1.141	1.137	1.132	1.128	1.123
50	1.123	1.118	1.114	1.109	1.106	1.101
60	1.097	1.092	1.089	1.084	1.080	1.076
C_{PPG}/ wt%	Viscosity (η/ cP)					
	298 K	303 K	308 K	313 K	318 K	323 K
0	8.30	7.24	6.47	5.71	5.06	4.55
10	7.79	6.88	5.34	4.07	3.62	2.90
20	6.98	5.55	4.67	3.32	2.52	2.01
30	8.89	7.44	6.13	5.04	4.28	4.02
40	10.56	9.84	7.33	6.08	5.78	5.01
50	18.94	15.59	13.04	11.07	9.49	8.25
60	27.21	21.94	17.96	14.94	12.60	10.76

Table 5.B.2. Measured conductivities (σ/μ S cm^{-1}) and refractive indices (n) in $PC/LiClO_4/PPG$ electrolyte solutions.

C_{PPG}/ wt%	T/ K	σ (μ S cm^{-1})	Λ_m (S cm^2 mol^{-1})	n
0	298	4981	5.0120	1.4229
	303	5036	5.0674	1.4215
	308	5734	5.7697	1.4203
	313	6254	6.2930	1.4201
	318	6774	6.8162	1.4196
	323	7178	7.2227	1.4181
10	298	5051	5.7817	1.4293
	303	5220	5.9751	1.4284
	308	6102	6.9847	1.4270
	313	6956	7.9623	1.4244
	318	7780	8.9055	1.4225
	323	8596	9.8395	1.4213
20	298	4275	5.6415	1.4311
	303	4638	6.1205	1.4294
	308	5008	6.6088	1.4284
	313	5671	7.4837	1.4270
	318	6470	8.5381	1.4245
	323	7382	9.7416	1.4226
30	298	3421	5.2644	1.4349
	303	3634	5.5921	1.4322
	308	3751	5.7722	1.4301
	313	4199	6.4616	1.4290
	318	4784	7.3618	1.4279
	323	5173	7.9604	1.4262
40	298	2009	3.6985	1.4370
	303	2415	4.4459	1.4354
	308	2644	4.8675	1.4336
	313	3025	5.5689	1.4306
	318	3439	6.3310	1.4293
	323	3806	7.0066	1.4282
50	298	1335	3.0073	1.4389
	303	1729	3.8948	1.4370
	308	2012	4.5323	1.4355
	313	2161	4.8680	1.4336
	318	2339	5.2690	1.4305
	323	2605	5.8682	1.4292
60	298	857	2.4744	1.4363
	303	885	2.5553	1.4357
	308	1202	3.4706	1.4349
	313	1230	3.5514	1.4343
	318	1369	3.9528	1.4337
	323	1620	4.6775	1.4318

Table 5.B.3. Raman band characteristics of the ClO_4^- stretching mode for all the compositions of $PC/LiClO_4$/PPG gel electrolyte solutions.

C_{PPG}/ wt%	ClO_4^- stretching/ cm^{-1}	FWHM/ cm^{-1}	Peak assignment
0	932	3.20	Free ClO_4^-
	938	3.20	SSIP
10	932	3.22	Free ClO_4^-
20	931	3.53	Free ClO_4^-
30	931	2.54	Free ClO_4^-
40	932	3.38	Free ClO_4^-
50	932	3.29	Free ClO_4^-
60	932	3.87	Free ClO_4^-

Table 5.B.4. UV-Vis absorption and emission frequencies[a] ($\tilde{\nu}_{abs/em}$) and FWHM[b] ($\Gamma_{abs/em}$) of DMASBT in $PC/LiClO_4$/PPG electrolyte solutions at ~298K.

System	$\tilde{\nu}_{abs}/10^3 cm^{-1}$	$\tilde{\nu}_{em}/10^3 cm^{-1}$	$\Gamma_{abs}/10^3 cm^{-1}$	$\Gamma_{em}/10^3 cm^{-1}$
Neat PC	25.06	19.33	4.79	2.65
$PC/LiClO_4$	25.57	19.15	4.80	2.72
$PC/LiClO_4$/10% PPG	20.12	16.84	3.09	1.44
$PC/LiClO_4$/20% PPG	19.85	16.91	3.19	1.59
$PC/LiClO_4$/30% PPG	19.99	16.86	2.99	1.50
$PC/LiClO_4$/40% PPG	19.43	16.87	2.77	1.48
$PC/LiClO_4$/50% PPG	19.32	16.98	2.84	1.57
$PC/LiClO_4$/60% PPG	19.28	17.01	2.86	1.62
Neat PPG	25.40	20.25	4.77	2.89

[a]Uncertainty in measured spectral frequencies: ~ 120 cm^{-1}

[b]FWHM represents full width half maxima of the spectra.

Table 5.B.5: Multi-Debye fit parameters of measured DR spectra for neat PC and PC/$LiClO_4$ electrolyte solutions. The values in the parenthesis represents the percentage of amplitudes.

T/K	ε_s	$\Delta\varepsilon_1$	τ_1 /ps	$\Delta\varepsilon_2$	τ_2 /ps	$\Delta\varepsilon_3$	τ_3 /ps	ε_∞	n^2	$\varepsilon_s - n^2$	$<\tau_{DR}>$/ ps
Neat PC											
298	64.4	-	-	54.3 (93)	44	4.0 (7)	5	6.2	2.023	4.2	41
303	64.4	-	-	55.2 (95)	41	3.1 (5)	5	6.1	2.021	4.1	39
308	64.1	-	-	55.6 (95)	39	2.8 (5)	4	5.7	2.001	3.7	37
313	63.8	-	-	56.2 (96)	37	2.2 (4)	4	5.5	1.998	3.5	36
318	62.9	-	-	55.6 (97)	34	1.9 (3)	4	5.4	1.996	3.4	33
323	62.1	-	-	54.7 (97)	32	1.8 (3)	3	5.6	1.992	3.6	31
PC/$LiClO_4$											
298	46.0	15.5 (39)	169	20.9 (53)	57	3.1 (8)	5	6.5	2.025	4.5	97
303	45.1	14.9 (37)	173	21.4 (54)	55	3.5 (9)	5	5.2	2.021	3.2	95
308	46.7	12.0 (30)	195	24.8 (62)	55	3.1 (8)	6	6.7	2.017	4.7	93
313	46.5	11.6 (29)	196	26.0 (64)	52	2.9 (7)	6	6.0	2.016	4.0	90
318	46.7	10.6 (26)	208	26.7 (66)	49	3.0 (8)	6	6.4	2.015	4.4	88
323	46.6	10.2 (25)	203	26.9 (67)	47	3.02 (8)	6	6.4	2.011	4.4	84

Table 5.B.6. Estimated activation energies calculated from viscosity, ionic conductivity and DR rate for PC/$LiClO_4$/PPG gel electrolyte solutions.

C_{PPG}/wt%	E_a^{η} /kJ mol^{-1}	$E_a^{\frac{1}{<\tau^{DR}>}}$/kJ mol^{-1}	$E_a^{\frac{1}{\tau_2^{DR}}}$/kJ mol^{-1}	E_a^{σ}/kJ mol^{-1}
0	19.21	5.57	9.31	12.80
10	32.67	13.30	12.47	18.21
20	40.82	11.14	9.39	17.54
30	26.69	8.98	9.39	13.72
40	25.27	12.22	6.15	20.12
50	26.60	12.47	8.40	19.87
60	29.68	10.48	11.64	20.62

References

[1] M. Zhu, J. Wu, Y. Wang, M. Song, L. Long, S.H. Siyal, X. Yang, and G. Sui, *Journal of Energy Chemistry* **37**, 126–142 (2019).

[2] G. Li, Z. Li, P. Zhang, H. Zhang, and Y. Wu, *Pure and Applied Chemistry* **80**(11), 2553–2563 (2008).

[3] K. Aruchamy, S. Ramasundaram, S. Divya, M. Chandran, K. Yun, and T.H. Oh, *Gels* **9**(7), 585 (2023).

[4] A. Chandra, and B. Bagchi, *J Chem Phys* **110**(20), 10024–10034 (1999).

[5] T. Dam, S.S. Jena, and A. Ghosh, *J Appl Phys* **126**(10), (2019).

[6] R. Bhandary, and M. Schönhoff, *Electrochim Acta* **174**, 753–761 (2015).

[7] C. Svanberg, R. Bergman, L. Börjesson, and P. Jacobsson, *Electrochim Acta* **46**(10–11), 1447–1451 (2001).

[8] X. Yu, Z. Jiang, R. Yuan, and H. Song, *Nanomaterials* **13**(11), 1789 (2023).

[9] J. Pan, P. Zhao, N. Wang, F. Huang, and S. Dou, *Energy Environ Sci* **15**(7), 2753–2775 (2022).

[10] Z. Wen, Z. Zhao, T. Zhang, Y. Wang, J. Zhang, Z. Sun, L. Li, Y. Li, F. Wu, and R. Chen, *J Mater Chem A Mater* **10**(41), 21905–21911 (2022).

[11] S. Yuan, K. Ding, X. Zeng, D. Bin, Y. Zhang, P. Dong, and Y. Wang, *Adv Mat* **35**(13), (2023).

[12] Y.-H. Lin, L.-T. Wu, Y.-T. Zhan, J.-C. Jiang, Y.-L. Lee, J.-S. Jan, and H. Teng, *Energy Storage Mater* **61**, 102868 (2023).

[13] S. Wang, L. Zhang, Z. Hu, B. Zhang, N. Li, Y. Tong, D. Cao, X. Zheng, W. Lai, Z. Jin, F. Wu, and Q. Wang, *Adv Mat* **37**(11), (2025).

[14] M. Ma, R. Huang, M. Ling, Y. Hu, and H. Pan, *Interdisciplinary Materials* **2**(6), 833–854 (2023).

[15] J. Scheers, L. Niedzicki, G.Z. Żukowska, P. Johansson, W. Wieczorek, and P. Jacobsson, *Phy Chem Chem Phy* **13**(23), 11136 (2011).

[16] P. Jayathilaka, M.A.K.L. Dissanayake, I. Albinsson, and B.-E. Mellander, *Solid State Ion* **156**(1–2), 179–195 (2003).

[17] D. Wei, and G.N. Patey, *J Chem Phys* **94**(10), 6795–6806 (1991).

[18] J. Hubbard, and L. Onsager, *J Chem Phys* **67**(11), 4850–4857 (1977).

[19] J.B. Hubbard, *J Chem Phys* **68**(4), 1649–1664 (1978).

[20] R. Kubo, *Reports on Progress in Physics* **29**(1), 306 (1966).

[21] O. Darrigol, *The European Physical Journal H* **48**(1), 10 (2023).

[22] B. Bagchi, and A. Chandra, (1991), pp. 1–126.

[23] L. Onsager, and R.M. Fuoss, *J Phys Chem* **36**(11), 2689–2778 (1932).

[24] B.D. Paulsen, S. Fabiano, and J. Rivnay, *Annu Rev Mater Res* **51**(1), 73–99 (2021).

[25] A. Mondal, K. Kumbhakar, and R. Biswas, *J Phys Chem B* **128**(48), 11924–11937 (2024).

[26] J. Mondal, N.C. Maity, and R. Biswas, *J Chem Sci* **135**(3), 84 (2023).

[27] K. Kumbhakar, B. Saha, P. De, and R. Biswas, *J Phys Chem B* **123**(51), 11042–11054 (2019).

[28] C.-C. Cheng, F.-C. Chang, H.-C. Yen, D.-J. Lee, C.-W. Chiu, and Z. Xin, *ACS Macro Lett* **4**(10), 1184–1188 (2015).

[29] F. Ye, W. Sun, Y. Zhang, C. Wu, X. Zhang, J. Yu, Y. Rong, M. Zhang, and D.T. Chiu, *Langmuir* **31**(1), 499–505 (2015).

[30] N.D. Cvjetićanin, and S. Šašić, *Journal of Raman Spectroscopy* **31**(10), 871–876 (2000).

[31] M. Chabanel, and K. Touaj, J. Chem. Soc., *Faraday Trans.* **92**(21), 4207–4213 (1996).

[32] D. Battisti, G.A. Nazri, B. Klassen, and R. Aroca, *J Phys Chem* **97**(22), 5826–5830 (1993).

[33] J.M. Alía, H.G.M. Edwards, and J. Moore, J. Chem. Soc., *Faraday Trans.* **92**(7), 1187–1196 (1996).

[34] Y.-S. Kim, and S.-K. Jeong, *Journal of Spectroscopy* **2015**, 1–5 (2015).

[35] G.J. Janz, J. Ambrose, J.W. Coutts, and J.R. Downey, *Spectrochim Acta A* **35**(2), 175–179 (1979).

[36] B. Klassen, R. Aroca, M. Nazri, and G.A. Nazri, *J Phys Chem B* **102**(24), 4795–4801 (1998).

[37] S. Schantz, L.M. Torell, and J.R. Stevens, *J Appl Phys* **64**(4), 2038–2043 (1988).

[38] B.L. Papke, M.A. Ratner, and D.F. Shriver, *J Electrochem Soc* **129**(7), 1434–1438 (1982).

[39] T.F. Sun, J.B. Chan, S.L. Wallen, and J. Jonas, *J Chem Phys* **94**(11), 7486–7493 (1991).

[40] B. Fortunato, P. Mirone, and G. Fini, *Spectrochim Acta A* **27**(9), 1917–1927 (1971).

[41] M.G. Giorgini, K. Futamatagawa, H. Torii, M. Musso, and S. Cerini, *J Phys Chem Lett* **6**(16), 3296–3302 (2015).

[42] K. Mukherjee, K. Kumbhakar, and R. Biswas, *J Mol Liq* **360**, 119491 (2022).

[43] J. Barthel, K. Bachhuber, R. Buchner, J.B. Gill, and M. Kleebauer, *Chem Phys Lett* **167**(1–2), 62–66 (1990).

[44] S. Matsuoka, and A. Hale, *J Appl Polym Sci* **64**(1), 77–93 (1997).

[45] L. Onsager, *Transactions of the Faraday Society* **23**, 341 (1927).

[46] J. Hubbard, and L. Onsager, *J Chem Phys* **67**(11), 4850–4857 (1977).

[47] B. Bagchi, *Annu Rev Phys Chem* **40**(1), 115–141 (1989).

[48] B. Bagchi, and B. Jana, *Chem Soc Rev* **39**(6), 1936 (2010).

[49] P. Banerjee, and B. Bagchi, *J Chem Phys* **150**(19), (2019).

[50] D.Fennell. Evans, T. Tominaga, J.B. Hubbard, and P.G. Wolynes, *J Phys Chem* **83**(20), 2669–2677 (1979).

[51] R. Blossey, and R. Podgornik, *Europhys Lett* **139**(2), 27002 (2022).

Chapter 6

Tracking Sol - Gel Phase Transition in Hydrophobically Modified Poly-(acrylic acid) Based Copolymers

6.1 Introduction

Smart polymeric materials have garnered considerable interest for their potential in creating versatile and promising solutions for both industrial and pharmaceutical applications, enabling innovative medicines and miniature electronic devices.[1–4] In an aqueous medium, many smart polymers are known to exhibit various phase transitions like sol-gel, hydrophobic-hydrophilic transition, etc. generating well-defined architectures. Owing to the versatile morphology like micelles, reverse-micelles, vesicles, hydrogels, smart polymers have been widely applied as delivery vehicles, reaction microspheres, for sensor development, surface creation and alteration, and membrane modifications.[5,6] Self-assembly of polymers in aqueous medium can form supramolecular physical hydrogel *via* three-dimensional network involving non-covalent interaction, such as, hydrogen bonding, ionic interactions, van der Waals forces, metal-ligand coordination, electrostatic interaction, hydrophobic interactions, etc.[7–13] These supramolecular polymeric hydrogels, which combine the responsiveness of noncovalent linkages along with the mechanical stability of polymers, are gaining popularity because of their high tensile strength,[8] multi-responsive behavior towards stimuli,[14,15] and superior processability.[14] Earlier studies reveal that physical hydrogels with high tensile strength and adjustable sol-gel transition should be perfect candidates for various applications, such as, printing and dyeing[16], wastewater treatment,[16] tissue engineering,[17] and controlled drug release.[17–19] Properties of hydrogels can be modulated by tuning the composition of copolymers. Unfortunately, most physical hydrogels are weak and at that point, the supramolecular chemistry should be a viable strategy for developing strong physical

gels with the regulated sol-gel transition.[7,20–22] In an aqueous medium, the long alkyl chains form hydrophobic associations, which serve as the physical crosslinking junctions of gels, leading to better mechanical strength.[19,23,24]

The molecular-level understanding of the sol-gel transition mechanism in supramolecular polymer gels with complex intermolecular non-covalent bonding is critical for their application and further development. The heterogeneous nature of the polymer-water interface presents a significant challenge in exploring the interactions and dynamics within these complex supramolecular gel systems. In literature, researchers have employed various experimental techniques, including small angle X-ray scattering experiments,[25] X-ray diffraction (XRD) studies,[26] nuclear magnetic resonance (^1H-NMR),[27,28] atomic force microscopy (AFM),[26,28] and infra-red (IR) spectroscopy[27,29] to investigate temperature-induced change in the structure, morphology, rheological analysis and critical micelle concentration of smart copolymer solutions during their sol-gel phase transition. Despite the progress made in understanding smart polymeric gels, there remains a significant gap regarding interactions, dynamics, and the sol-gel transition-driven changes in water dynamics in aqueous media. Unlike previous reports, the first major distinction of our work is that the copolymers studied here are not stimuli-responsive polymers. Secondly, we track the sol-gel phase transition by following the relaxation dynamics, which was not done earlier. Further studies are needed to elucidate the subtle interplay among the polymer chain motions, solute dynamics, and the relaxation of the host water molecules during the sol-gel transition.

Here we introduce an interesting idea to probe the sol-gel transition in complex liquid systems. Attaching a fluorescent probe (here, coumarin 343, C343) chemically to the polymer backbone offers several scientific advantages that enhance its ability to probe specific properties and dynamics of polymer systems, including the polymer-water interface and sol-gel phase transitions. Chemically bound fluorophore resides directly on the polymer backbone, ensuring its proximity to the polymer-water interface. This enables it to more accurately report on the microenvironment, including hydrogen bonding, polarity and hydration dynamics. The attached probe (C343) is specifically exposed to the regions where polymer and water interactions dominate, reducing interference from bulk water dynamics. In this way, the chemically bound C343 can serve as a

direct sensor of changes in structural distribution in polymer network, the polymer chain mobility and segmental interactions during the sol-gel phase transition.[30–33] Unlike externally added probes, chemically tethered C343 does not diffuse away from the polymer matrix, providing stable and consistent reporting on local dynamics over time.

We have synthesized a series of hydrophobically modified poly(acrylic acid)-based copolymers *via* reversible addition-fragmentation chain transfer (RAFT)[34–38] polymerization. These copolymers consist of a hydrophobically modified unit (**M2**, **Scheme 6.1**) and acrylic acid (**M1**, **Scheme 6.1**). Subsequently, MHz-GHz dielectric relaxation (DR) experiments, steady-state UV-visible absorption and fluorescence emission measurements, and time-resolved fluorescence (TRF) spectroscopic experiments were performed in order to explore the sol-gel transition mediated interaction and dynamics in aqueous solutions of hydrophobically modified copolymers (**P0**, **P4**, **P6)** and their C343-attached analogous copolymers (**P4'**, **P6'**). C343 was chemically attached to the polymeric backbone in **P4'**, **P6'** using a C343-tagged monomer (**M3**, see **Scheme 6.1**) to explore the sol-gel mediated interaction and dynamics at the polymer-water interface.

In the present work, we are focusing to address the following key scientific questions: How do hydrophobic modifications in copolymers influence the intermolecular interactions and relaxation dynamics within the sol-gel transition phase? Specifically, how do these modifications alter the microenvironment and structural evolution at a given pH and polymer concentration in aqueous media? What are the differences in interaction and relaxation dynamics when C343 is externally introduced versus chemically attached to the copolymer backbone? Does the mode of probe integration significantly impact its ability to report on the surrounding polymer-water interface? To what extent does the presence of chemically bound C343 affect the intrinsic dynamics of the sol-gel phase transition? By exploring these questions, the work seeks to unravel the interplay between polymer structural modifications, probe dynamics, and the phase transition behavior of copolymer systems, offering deeper insights into their physicochemical and functional properties.

6.2 Experimental Details

6.2.1 Materials

Acryloyl chloride (Sigma-Aldrich), *N*-18-alkylamine (Sigma-Aldrich), 2-aminoethyl methacrylate hydrochloride (Sigma-Aldrich), coumarin 343 (C343, Sigma-Aldrich), triethylamine (Et_3N, Merck), 4-(dimethylamino)pyridine (DMAP, 99%, Sigma-Aldrich), dicyclohexylcarbodiimide (DCC, 99%, Sigma-Aldrich), 1-(3-dimethylaminopropyl)-3-ethylcarbodiimide hydrochloride (EDC.HCl, Spectrochem), sodium chloride (NaCl, Merck), anhydrous *N,N′*-dimethylformamide (DMF, 99.9%, Sigma-Aldrich), HPLC water (Sigma-Aldrich), NaOH pellets (Merck) and HCl (Merck) were used as received. Acrylic acid (**M1**) procured from Merck was passed through a basic alumina column prior to polymerization. 2,2′-Azobis(2-methylpropionitrile) (AIBN, 98%, Sigma-Aldrich) was purified by crystallization in methanol twice before being used as an initiator during polymerization. The 4-cyano-(dodecylsulfanylthiocarbonyl)sulfanylpentanoic acid (CDP) was synthesized according to the procedure reported previously.[39] For the ^1H NMR study, $CDCl_3$ (99.8% D) and methanol-d_4 (99.8% D) was purchased from Cambridge Isotope Laboratories, Inc., USA. Solvents such as hexanes (mixture of isomers), ethyl acetate (EA), dichloromethane (DCM), chloroform, etc. were purified by standard distillation procedures. The details of synthesis and characterization of copolymers are not recorded in this chapter.*

*This part has been performed in collaboration with Prof. Priyadarsi De from IISER Kolkata, India. It has been already published in J. Chem. Phys. 162, 164903 (2025).

6.2.2 Sample Preparation

The synthesis strategy of copolymers produced *via* RAFT polymerization is depicted in **Scheme 6.1**. Next, to prepare 0.5 wt% aqueous copolymer solution, 5 mg of each copolymer was initially dissolved in a small amount (~ 200 µL) of dil. HCl and then 1 mL of HPLC water was added. The mixture was stirred continuously with a magnetic stirrer for about 30 - 40 min. The initial pH of the solution was recorded. After that NaOH solution was added to adjust the pH to 5. For all the measurements reported here, ~ 4 - 5 mL of the sample solutions were taken and studied for 30

days. We have considered all copolymers concentration fixed at 0.5 wt% and solution pH to 5. DLS and DRS measurements were taken at different time intervals. For optical spectroscopic measurements, ~ 2.0 - 3.0 mL aqueous solution of each copolymer was taken into a quartz cuvette of 1 cm optical path length and the concentration of externally added C343 was maintained at $\leq 10^{-5}$ M.[40] Such trace amount of C343 is unlikely to have considerable interactions between C343 and the polymer matrix and instead functions as a local reporter to monitor environmental interactions and dynamics All the experiments were carried out in a humidity-controlled environment, and the temperature was kept constant at ~ 298 ± 1 K.

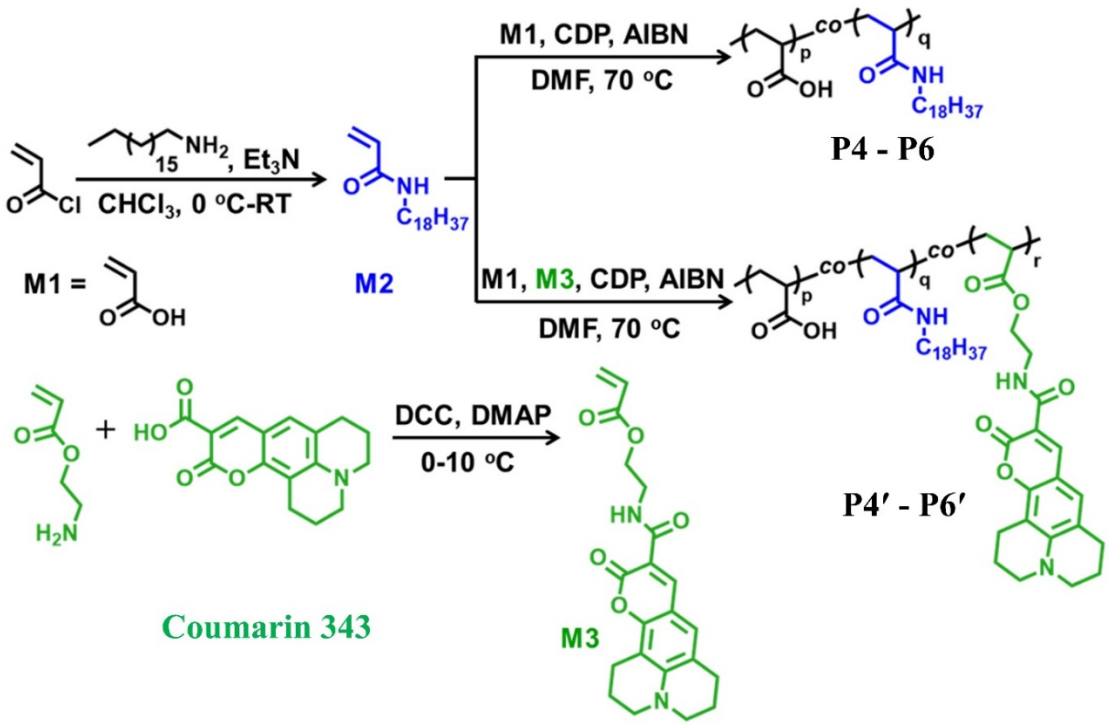

Scheme 6.1. Synthetic route for the synthesis of hydrophobically modified poly(acrylic acid) (**P4, P6**) and C343 tagged hydrophobically modified poly(acrylic acid) (**P4′, P6′**).

We acknowledge that interactions between C343 and the polymer matrix can influence the fluorescence properties, leading to artifacts in the investigations of local environment and dynamics. The interaction between the anionic C343 in solutions at pH = 5 and the hydrogen atom attached to nitrogen atom bonded to the hydrophobic moiety can lead to a dynamics that may be somewhat different from the local dynamics surrounding the fluorescent probe molecule. However, the present study focusses on the relative change of dynamics with time and therefore a specific interaction between the probe molecule and the amide hydrogen does not influence the conclusion regarding the onset of sol-gel transition during the incubation period.

Previous studies have shown that C343 primarily reports on the polarity and viscosity of its environment through solvatochromic and fluorescence lifetime changes, rather than forming strong interactions with the polymer matrix.[41–45] However, to confirm this, we conducted control experiments where we measured spectral properties of C343 in neat water also. These results indicate that any spectral shifts observed during the sol-gel transition are consistent with changes in the local microenvironment rather than probe-polymer interactions.

6.2.3 Instrumentation and Methods

6.2.3.1 pH Measurements

A Bench-top multi-parameter electrochemical meter (SESHIN BIOTECH, Model: ECM − 610) was used to perform pH measurements of copolymer samples at 298±1 K. Accuracy associated with pH data is ± 0.3.

6.2.3.2 Differential Scanning Calorimetry (DSC)

DSC (TA Instruments Q2000) technique was employed on all the aqueous polymer samples in the temperature range 113 - 353 K and heat flow was maintained at 5 K/min. In order to prevent evaporation during the measurements, the solutions were hermetically sealed in an aluminum pan (40 µL, TA Tzero) under nitrogen atmosphere. DSC thermograms of aqueous copolymer solutions have been provided in **Fig. 6.A.12** (Appendix 6.A).

6.2.3.3 Dynamic Light Scattering (DLS) Experiments

DLS measurements were carried out using a Zetasizer Nano ZS instrument (Malvern Instruments Ltd., UK) fitted with a laser beam of He-Ne, functioning at 633 nm wavelength, and the scattering angle is 173°. The values of hydrodynamic diameter (D_h) and corresponding polydispersity index (PDI) were calculated from the correlation function using the Zetasizer software (Malvern Instruments Ltd., UK).

6.2.3.4 Steady-State and TRF Spectroscopic Measurements

UV -visible spectrophotometer (PerkinElmer LAMBDA 35 and UV − 2600, Shimadzu) and a fluorimeter (Fluorolog, Jobin-Yvon, Horiba) were employed to record steady-state absorption and fluorescence emission spectra, respectively. Details about steady-state UV-vis absorption and emission spectra have been discussed in Chapter 2.

In this study, a Peltier temperature controller was used to fix the temperature of the samples (accuracy ±1 K). All spectra were acquired using a 1 nm slit width for both excitation and emission. Standard spectral analysis protocols were employed to extract peak positions and FWHM.[46–50] TRF measurements were conducted by employing TCSPC set-up to determine fluorescence lifetimes and rotational anisotropy for all the copolymer solutions at ~ 298 K. Here, the geometric correction factor (G) was found to be 1.6 ± 0.2.

6.2.3.5 Dielectric Relaxation (DR) Measurements

The experimentally obtained complex DR spectra of aqueous copolymer solutions were best described using a 2-Debye model. Various models, including multi-Debye, Cole - Davidson, and Cole - Cole functions, have been tested for fitting, with the 2-Debye function providing the most accurate representation. The fit quality was determined by inspecting both the “goodness-of-fit” parameter (χ^2) and the associated residuals. Further methodological details have been provided in Chapter 2.

6.3 Results and Discussion

6.3.1 DLS Measurements of Copolymer Solutions: Sol - Gel Phase Transition

The structural characteristics of the copolymer solutions have been investigated through dynamic light scattering (DLS) experiments, with a focus on determining the hydrodynamic diameter (D_h) of self-assembled structures formed by copolymers. DLS measurements were systematically performed for all copolymer solutions in appropriately sealed condition at concentration 0.5 wt% and pH 5 over an extended incubation period of up to 50 days. The corresponding DLS profiles are provided in **Fig. 6.A.1** (Appendix 6.A). Data in this figure indicate a saturation in the D_h value after approximately 30 days of incubation. This suggests that the sol-gel phase transition in these aqueous copolymer solutions is completed within the first 30 days of incubation. The onset time for the sol-gel transition is, however, shorter than the incubation period (30 days), and may be estimated from the intersection of two slopes produced by the incubation period dependent D_h values.

The small variations in D_h values observed beyond 30 days further support that the aggregation due to transition is complete (or nearly complete) within 30 days. This is shown in **Fig. 6.1**, which depicts the evolution of D_h during the incubation period, highlighting the progression of the aggregation process over time. The size distribution profiles of aggregates formed in each copolymer sample are presented in **Fig. 6.A.2** (Appendix 6.A), and representative numerical values of D_h and the polydispersity index (PDI) are summarized in **Table 6.B.1** (Appendix 6.B). The value of PDI quantifies how consistent the size of aggregates of polymer chains in the solution. In our study, the calculated PDI values, ranging from ~ 0.1 - 0.3, indicate a monodispersed size distribution, suggesting a highly uniform aggregation process.[51,52] This relatively low polydispersity further implies that the copolymer solutions form stable and well-defined self-assembled structures, which is essential for maintaining reproducible phase behavior and ensuring consistency in further experimental results.

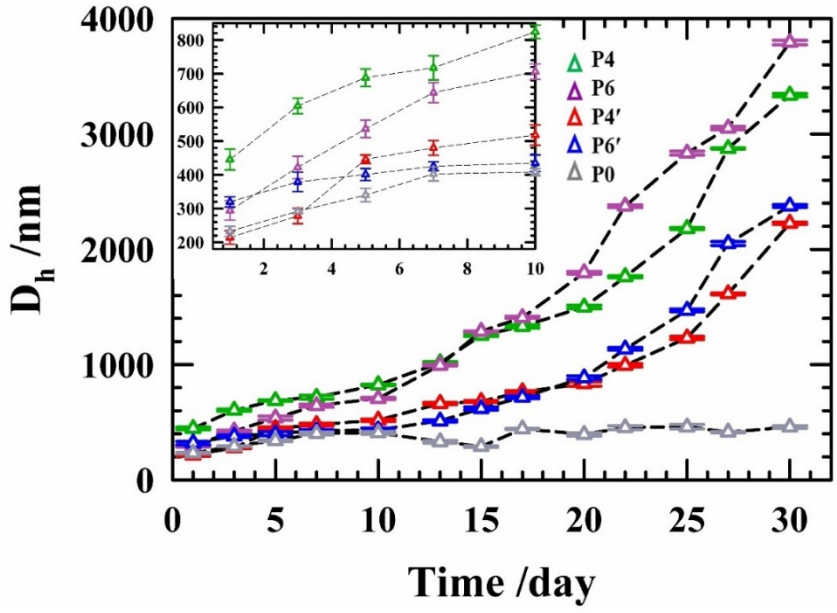

FIG. 6.1. Time-dependent DLS profile of aqueous solutions of **P0**, **P4**, **P6** and their C343 tagged (chemically bound) copolymers (**P4′** and **P6′**) over an incubation period of 30 days. Data in the inset are presented in a shorter vertical scale in order to clearly show the upper and lower bounds of the error associated with each of the D_h values.

In case of **P0** without hydrophobic moiety, D_h is found to be in the range of ~ 200 - 450 nm throughout the incubation period. However, copolymers with hydrophobic modifications, **P4** and **P6**, showed an increase in the D_h over time to ~ 4000 nm. Now, C343 tagged (chemically bound) polymers **P4′** and **P6′** also formed large aggregated structures with D_h ~ 3000 nm. The absence of sol-gel phase transition in **P0** highlights the crucial role of hydrophobic moieties in the self-assembly and gelation process of copolymers. **P0**, lacking hydrophobic modifications, maintains a relatively stable particle size range of ~ 200 - 450 nm throughout the incubation period. This stability suggests that **P0** does not undergo significant aggregation or structural changes during the incubation period. In contrast, the copolymers with hydrophobic modifications, namely **P4**, **P6**, **P4′**, and **P6′**, exhibit a dramatic increase in aggregate size over time, reaching dimensions of ~ 3000 - 4000 nm. This substantial growth in size indicates the formation of larger aggregates or

networks, which is characteristic of sol-gel phase transition. The hydrophobic moieties in these modified copolymers likely promote intermolecular interactions, driving the self-assembly process and leading to the formation of a gel-like structure. This phenomenon may be described by the fact that in **P0** only electrostatic interactions are present but on hydrophobic modification (in case of **P4, P6, P4′** and **P6′**), the long alkyl chains (**M2**) form hydrophobic pockets, act as physical crosslinker, leading to a close arrangement of the carboxyl groups for better interactions. Thus, larger aggregates act as junction points between different copolymer chains connecting through various intermolecular interactions, such as hydrophobic interactions and hydrogen bonding. From day 1 to day 30 of incubation period, the degree of aggregation increases (in **P4, P6, P4′** and **P6′**), the copolymer network becomes more interconnected and eventually reaching a critical point where the system transitions from a liquid-like state to a gel-like state.

The specific mechanisms underlying the size change of polymer aggregates during gel transition are complex and depend on various factors, including polymer concentration, temperature, pH, and solvent conditions.[53–56] Hydrophobic interactions between non-polar segments of the copolymer chains can drive the formation of larger aggregates, while hydrogen bonding can contribute to the stability and growth of these structures. Additionally, the balance between attractive and repulsive forces among polymer chains, as well as the flexibility and conformation of the polymers, can influence the size and shape of the aggregates.[57,58] Further experimental and simulation studies of these microscopic mechanisms could enhance control and optimization of gel formation.

Next, we explored the onset point of the sol-gel transition for each of the copolymer solutions by studying gradual changes in the aggregate size distributions throughout the incubation period (30 days). Note that the sol-gel phase transition point is estimated from the intersection of the two slopes obtained from the plot of average D_h values with respect to time (in days), shown in **Fig. 6.2**.

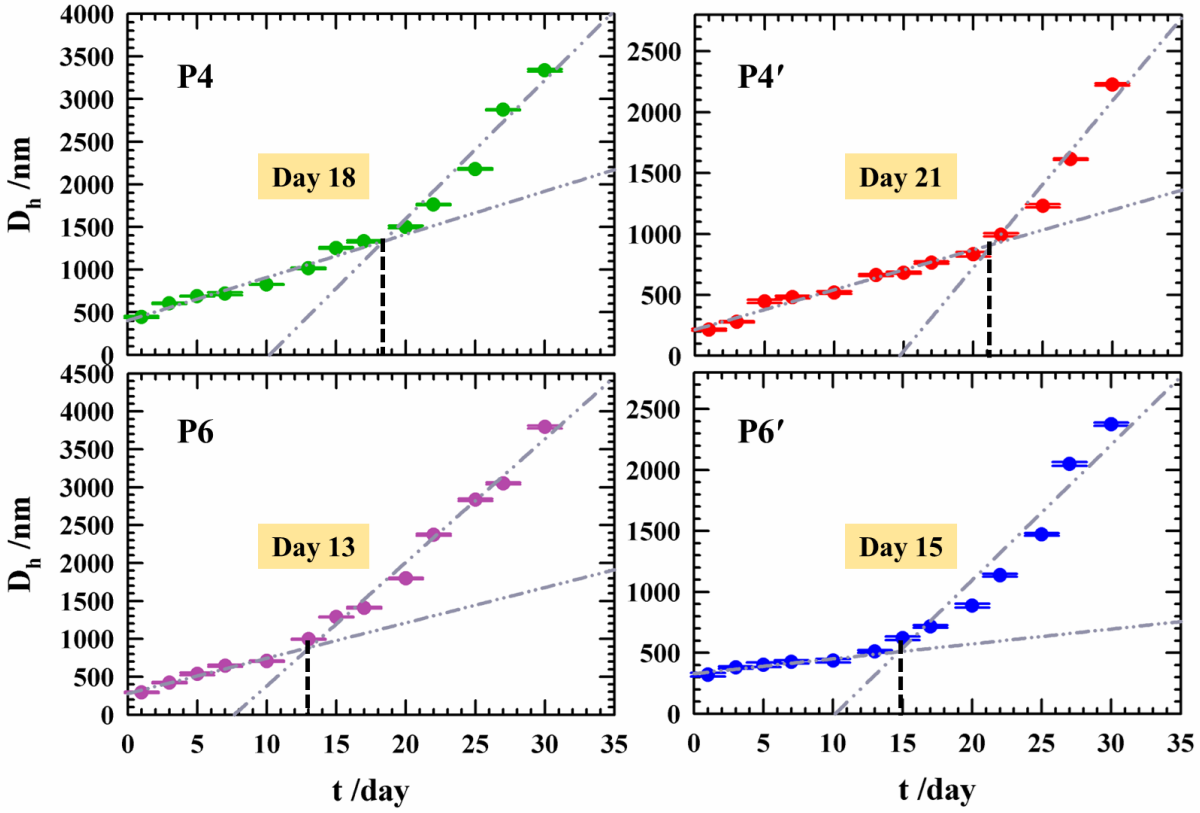

FIG. 6.2. Particle size distributions of aqueous copolymer solutions of **P4** (upper left panel), **P4′** (upper right panel), **P6** (lower left panel) and **P6′** (lower right panel) from day 1 to day 30. The intersecting point in each plot indicated by black dashed line represents the onset of sol-gel phase transition. All the copolymers are color-coded. Horizontal lines in each data points represent the error bar in D_h.

For **P4** and **P6**, the intersection point is around day 18 and day 13, respectively, whereas for **P4′** and **P6′** the intersection point is around day 21 and day 15, respectively. This suggests that with increasing hydrophobic unit (**M2**) in copolymer facilitates the gel formation which (the onset time) undergoes a minor change upon chemical binding of the fluorescent probe C343. Results obtained from DLS studies imply a kinetic process is continuing involving the copolymer and water molecules. It is evident that water molecules play a pivotal role in reshaping the structural and dynamical changes in the solution, heralding the emergence of precursory signals for a prospective sol-gel transition without any external stimuli over a time span of 30 days. Now to investigate the

solute-medium interactions in this phase transition we have performed steady-state and time-resolved fluorescence spectroscopic measurements of aqueous **P4′** and **P6′** solutions and also in **P4** and **P6** solutions with addition of fluorescent probe C343 externally.

6.3.2 Steady State UV-visible Absorption and Fluorescence Emission Studies

The representative steady-state UV-visible absorption and fluorescence emission spectra of C343 in aqueous copolymer solutions are provided in **Fig. 6.A.3** (comparing hydrophobicity in copolymer network, Appendix 6.A) and **Fig. 6.3** (comparing 'bound'/ 'unbound' probe). The corresponding peak frequencies are shown in **Table 6.1**. Note that as we move from **P0** to **P6** with an increase in hydrophobic moiety in PAA copolymers, the absorption peak undergoes a significant redshift of ~ 400-700 cm^{-1}. The reason for such an observation can be linked to the larger size of the aggregated structures. The curvature of the interfacial aqueous environment becomes larger with hydrophobic modification, allowing more number of water molecules at the interface producing higher polar environment. On the other hand, the emission spectra of C343 in aqueous **P0**, **P4** and **P6** are quite similar to that in neat water. This can be understood in terms of increased interactions between the interfacial water molecules and excited C343 possessing larger dipole moment (compared to that in the ground electronic state).

Now, we discuss about the local environment of aqueous copolymer solutions (**P4′** and **P6′**) as reported by the chemically bound C343, presented in **Fig. 6.3**. The location of the probe is now restricted within the polymer-chain of these copolymers. The chemically attached C343 in **P4′** and **P6′** solutions clearly register a considerable blue-shift in both absorption and emission spectra with respect to **P4** and **P6** solutions and the extent of blue shift increases from **P4′** to **P6′** solution. So, with increasing hydrophobicity in the copolymers, the C343 in chemically 'bound' condition reports gradually decreased local medium polarity, unlike in the cases for **P4** and **P6** solutions. This suggests that the copolymers form structural aggregates, where bound and unbound C343 can probe two distinct locations of varying polarities in the aqueous copolymer solutions. This provides an insight into the structural modification of these copolymers while undergoing the sol-gel transition.

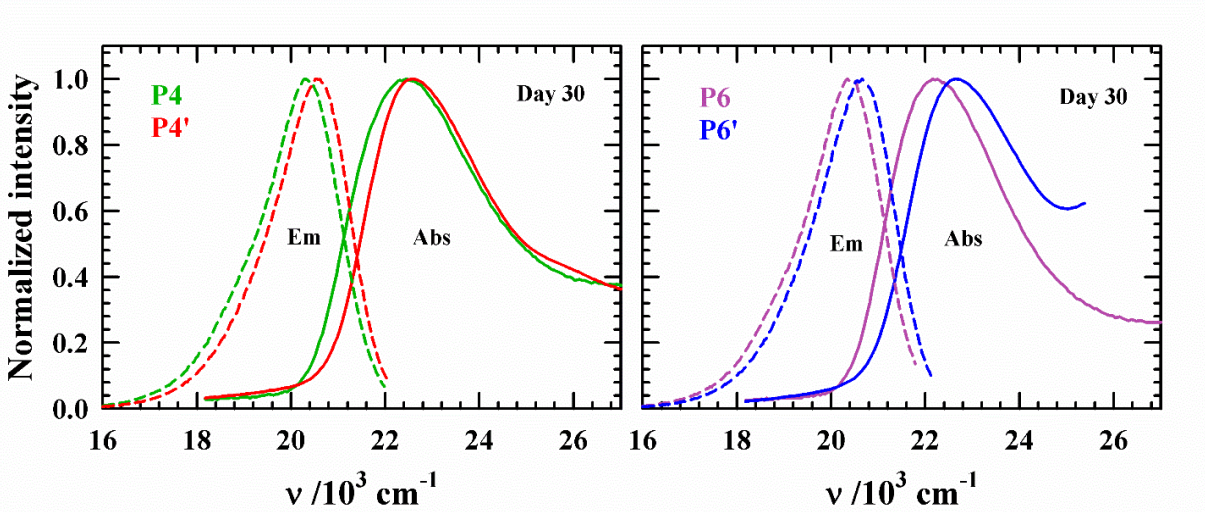

FIG. 6.3. Representative steady-state UV-vis absorption (solid lines) and fluorescence emission spectra (dashed lines) of C343 in aqueous solutions of **P4**, **P4′** (left panel) and**, P6**, **P6'** (right panel) at day 30. Presentations are color-coded.

Table 6.1. Steady-state absorption and emission peak frequencies of C343 in aqueous **P0 - P6'** solutions on four different incubation days.

Co-polymer	Absorption				Emission			
	Peak frequency[a,b] (10^3 cm^{-1})				Peak frequency[a,b] (10^3 cm^{-1})			
	Day 1	Day 10	Day 20	Day 30	Day 1	Day 10	Day 20	Day 30
P0	23.02	23.16	23.25	23.38	20.02	20.03	20.02	20.03
P4	22.80	22.87	22.90	22.93	20.15	20.14	20.12	20.12
P4'	23.07	23.12	23.15	23.28	20.29	20.30	20.32	20.36
P6	22.66	22.68	22.71	22.71	20.19	20.17	20.17	20.18
P6'	23.44	23.48	23.54	23.61	20.38	20.40	20.42	20.44
Neat Water	22.80				19.92			

[a]Peak frequency is estimated by averaging the average peak frequency and first moment frequency.

[b]Uncertainty ±100 cm^{-1}

Next, time-dependent (day 1 to day 30) steady-state measurements (see **Fig. 6.A.4**, Appendix 6.A) reflects a mild blue-shift (~ 200 cm^{-1}) in the absorption spectra of C343 in **P4′** and **P6′** solution but in case of **P4** and **P6**, it is unchanged. The mild blue shift in absorption spectra of chemically attached C343 in aqueous **P4′** and **P6′** solutions is a manifestation of sol-gel transition induced "less-exposure" of the probe to the aqueous interface. This less-exposure occurs due to the restricted location of the chemically bound C343 inside the aggregated structure. The externally added probe molecules (C343), however, do not experience such restrictions and thus are free to locate at the interface guided solely by the interactions with interfacial environment.

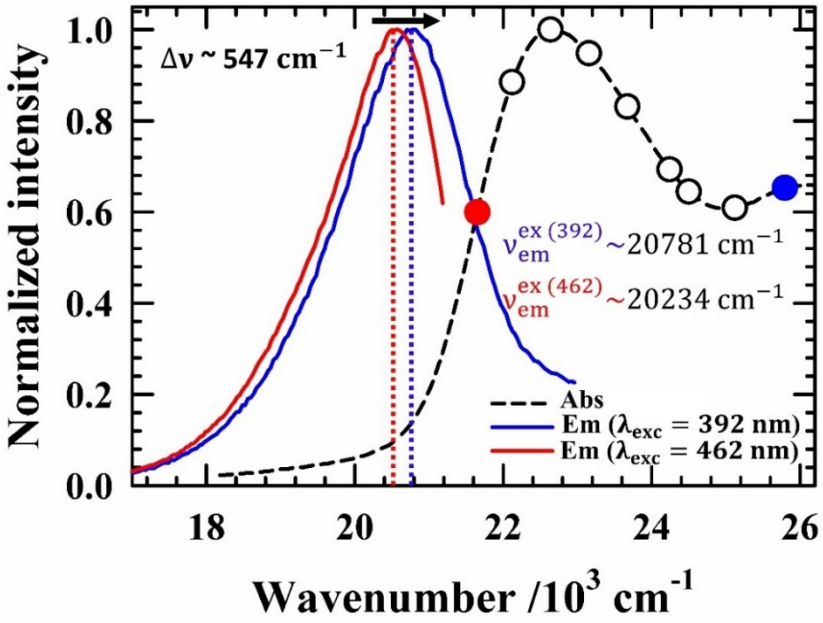

FIG. 6.4. A representative steady-state absorption and emission spectra of C343 in aqueous solution of **P6'** at day 30. Black symbols are indicating the excitation points at which emission spectra are collected for estimating λ_{exc} driven total emission shift. The values of the emission peak frequencies (ν_{em}) were calculated by averaging peak frequencies and first spectral moments of the respective spectrum. All presentations are color-coded.

Next, to explore microscopic spatial inhomogeneity in aqueous copolymer solutions, C343 was excited at various wavelengths (λ_{exc}) across their respective absorption spectrum (see **Fig. 6.4**).[59,60] If the solvation shell surrounding the fluorophore, C343, doesn't relax faster than the average fluorescence lifetime of C343, then the emission spectra will shift gradually with λ_{exc}.[60–62] The greater is the λ_{exc} dependent emission shift, the more heterogeneous is the immediate environment. **Fig. 6.5** shows the λ_{exc} dependent shift of fluorescence emission frequencies and corresponding spectral widths (FWHM, Γ_{em}) of C343 in aqueous copolymer solutions (see also **Fig. 6.A.5** and **Fig. 6.A.6**). Note all these polymer solutions have registered a mild to considerable amount of emission frequency shift of C343 with λ_{exc} which indicates the presence of spatial heterogeneity of the local environment of the fluorescent probe.

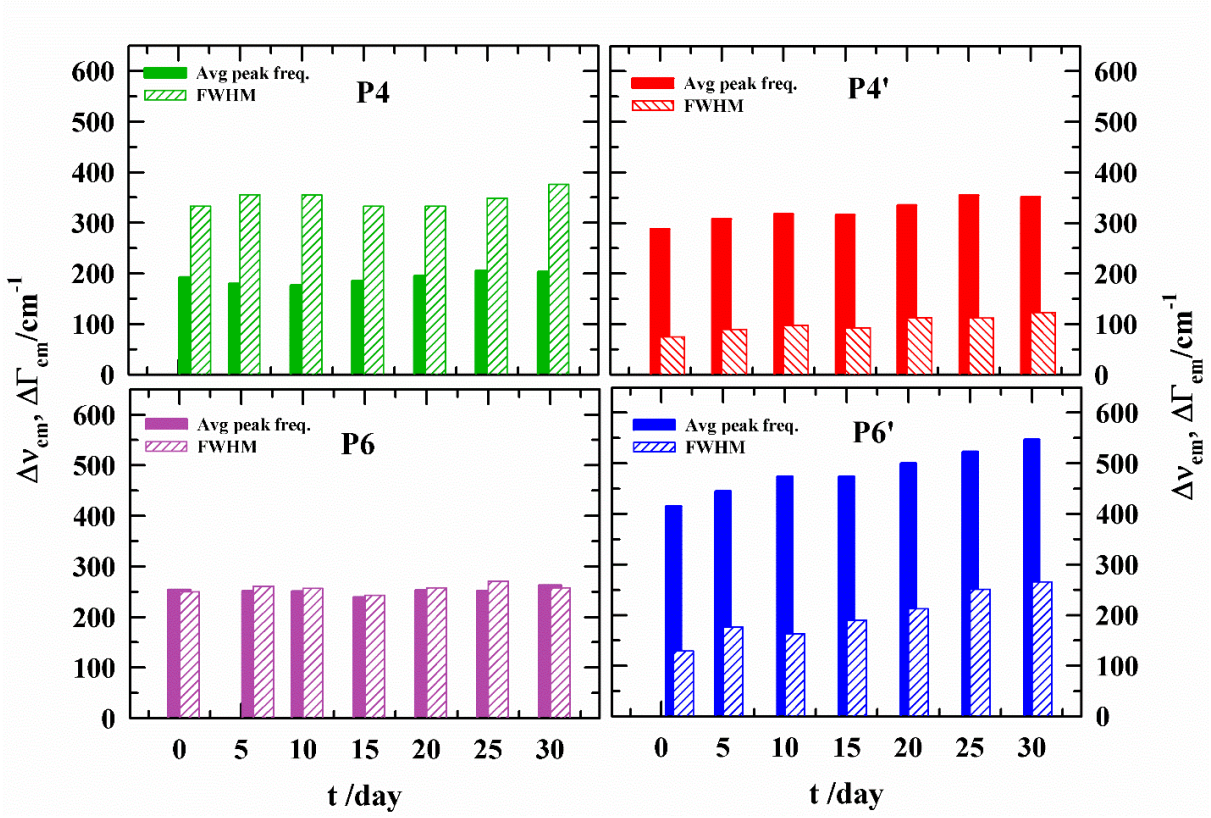

FIG. 6.5. λ_{exc} dependent total emission frequency shift and spectral width (FWHM) shift of C343 in aqueous solutions of **P4, P4', P6** and **P6'** at different time interval after sample preparation. Here, $\Delta X_{em}(x = \nu, \Gamma)\,(\lambda_{exc}) = X_{em}\,(\lambda_{exc}^{blue\ end}) - X_{em}(\lambda_{exc}^{red\ end})$ where the respective blue and red end in each polymer solutions are as follows: 395 nm and 465 nm for **P4**, 393 nm and 463 nm for **P4'**, 399 nm and 469 nm for **P6** and 392 nm and 462 nm in case of **P6'**.

Apparently, from **Fig. 6.5**, we can say that **P4′** and **P6′** solutions are more heterogeneous than **P4** and **P6** throughout the incubation period of 30 days. The magnitude of λ_{exc} induced total emission frequency shift in **P4** and **P6** solutions remains nearly unchanged over this incubation time. For **P4′** and **P6′** solutions, in contrast, λ_{exc} dependent total emission frequency shift exhibits an increase with incubation time (day). This manifests the structural change that accompany while undergoing the sol-gel transition. It appears that chemically bound fluorophores are better positioned to experience and report such transition than the externally added fluorophores. The changes in spectral widths (see **Fig. 6.5**) provide further support to the view that C343 in **P4'** and **P6'** solutions is exposed to the local environment differently than that in the solutions of **P4** and **P6**.

6.3.3 Time-Resolved Fluorescence Anisotropy Decay Measurements

Representative r(t) decays of C343 in aqueous copolymer solutions along with their multi-exponential fits are shown in **Fig. 6.6** and the corresponding day-dependent r(t) decay characteristics of each copolymer solution along with residuals are provided in **Fig. 6.A.7** and **Fig. 6.A.8** (Appendix 6.A). The r(t) decay fit parameters are summarized in **Table 6.2**. The single and biexponential anisotropy decays in **P0** solution are characterized by a dominant (~ 80 - 90%) fast relaxation (~ 70 - 100 ps) component and a relatively slower sub-nanosecond component. This behavior of relaxation is quite typical in polymer-water systems[60,61] and represents the bimodal nature of the friction profile exerted by the local environments on the rotating solutes in these polymer solutions.

A detailed examination of **Table 6.2** reveals that the long-time component (τ_3^{rot}) of few nanoseconds range is completely absent in **P0** solutions. This absence can be attributed to the lack of long hydrophobic chains (**M2** units) in the polymer network, consistent with our DLS results. In **P0** solutions, the fluorescent probe C343 molecules reside at the loosely bound polymer-water interface, leading to rapid rotational anisotropy decay, which is ~ 4 - 5 times faster than in hydrophobically modified copolymer (**P4**, **P6**) solutions from day 1 of incubation. By day 30, due to scarcity of polymer aggregation or coiling, and the lack of sol-gel transition in **P0**, the $< \tau^{rot} >$

remains nearly unchanged. In contrast, in **P4** and **P6** solutions, as hydrophobic associations strengthen and gelation progresses, $< \tau^{rot} >$ slows down significantly, becoming approximately 7 - 9 times longer than **P0**.

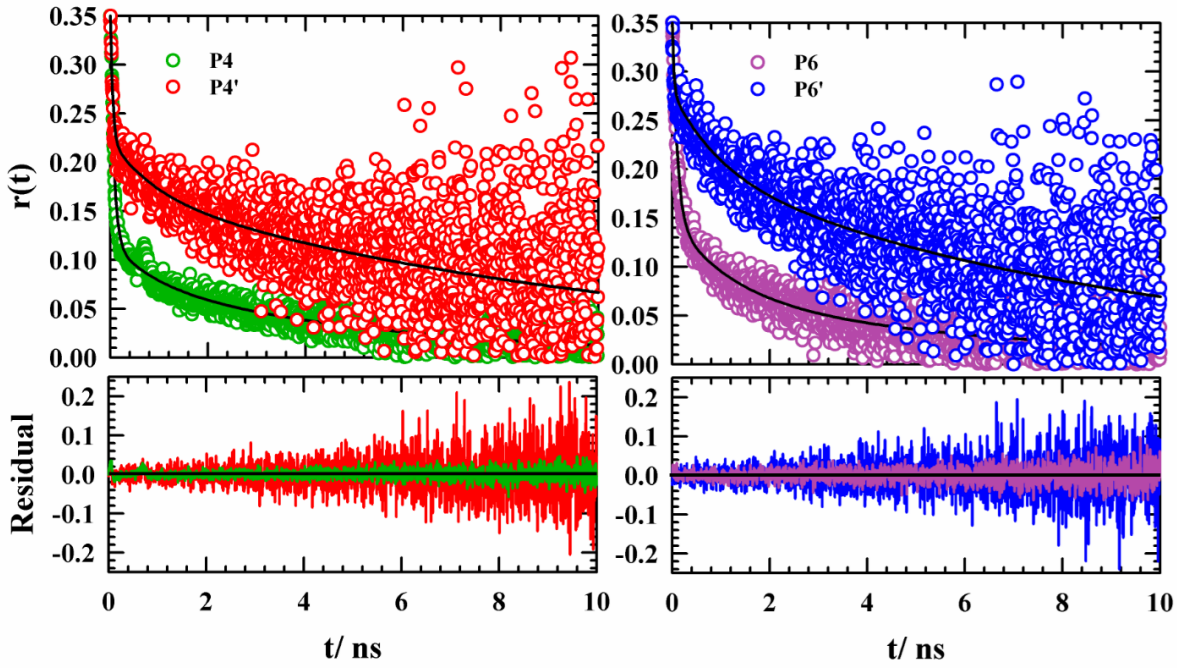

FIG. 6.6. Representative time-dependent rotational anisotropy decays, r(t) of C343 in aqueous solutions of **P4**, **P4'** (left panel) and **P6**, **P6'** (right panel). The corresponding residuals are shown in lower panels. In the upper panel, experimental data points are presented as symbols and lines through them depict multiexponential fits. Specific identities of polymers are color-coded.

Tri-exponential r(t) decays (see **Table 6.2**) are obtained in aqueous solutions of **P4**, **P6**, **P4'** & **P6'** where again a bound-probe driven solute-relaxation in polymer-water solution has been observed. The slowest rotational time $\langle \tau_3^{rot} \rangle$ of C343 in **P4** and **P6** solutions is approximately ~ 3-5 ns which slows down to ~10-12 ns in **P4'** and **P6'** solutions, although the bulk viscosity of all the aqueous polymeric solution is comparable to that of neat water. This implies that the rotation of the chemically bound C343 is because of the aggregation. This slower rotational dynamics of C343 in complex aqueous environment is again supported by our fluorescence lifetime measurements

(see **Fig. 6.A.9** and **Table 6.B.2**) where average excited state lifetime is getting shorter due to successive incorporation of **M2** unit leading to the enhancement of the non-radiative decay rate.

Furthermore, **Table 6.2** reveals a notable impact of hydrophobic units in the copolymers on the average rotational times ($\langle\tau_r\rangle$) of C343. Moving from **P4** to **P6**, aggregation propensity of polymer chains increases due to increased hydrophobic interactions. This increased propensity of aggregation can trap C343 molecules in the environments created by the loosely organized polymer chains in the initial period of incubation. The anisotropy decays of these 'trapped' C343 molecules can lead to slow down of the $\langle\tau_r\rangle$. This is not conflicting to our steady state absorption spectral shift data because of the following. The steady state spectral frequency is dominated by those probe molecules distributed in the more polar region of the interface, while the rotational relaxation rate is governed by those located inside the regions created by the loosely organized polymer chains. For C343-tagged copolymers (**P4'** to **P6'**), blue-shifted absorption and emission spectra appeared as hydrophobicity enhanced. Intriguingly, despite this blue shift, faster rotational dynamics are noted in **P6'**. This unusual observation can be explained as follows: the increase in hydrophobicity from **P4'** to **P6'** leads to an increase of the size of the aggregated structure, as evidenced by DLS data. This larger size is, although inside is less polar because of increased expulsion of water molecules, probably not as tightly packed as in the case of **P4'**, allowing C343 to rotate slightly more freely in **P6'** solutions. Consequently, despite the blue-shifted emission spectra from **P4'** to **P6'**, the rotational dynamics of C343 become faster, and the associated timescales diminish.

The impact of rotational dynamics of C343 during the sol-gel transition is depicted in **Fig. 6.7** and **Fig. 6.8**. Notably, the overall increase in average rotational times of C343 in copolymer solutions exhibits a nonlinear trend up to day 30, as shown in **Fig. 6.A.10**. Specifically, the variation in the slope of $\langle\tau^{rot}\rangle$ over time suggests an onset of the sol-gel transition, which can be attributed to changes in microscopic friction associated with supramolecular interactions through hydrophobic units (**M2**). In the case of **P4** and **P4′** solutions, the onset of the sol-gel transition is observed approximately on day 10, while for **P6** and **P6′** solutions, this transition occurs around day 20, as exhibited by the rotational anisotropy data.

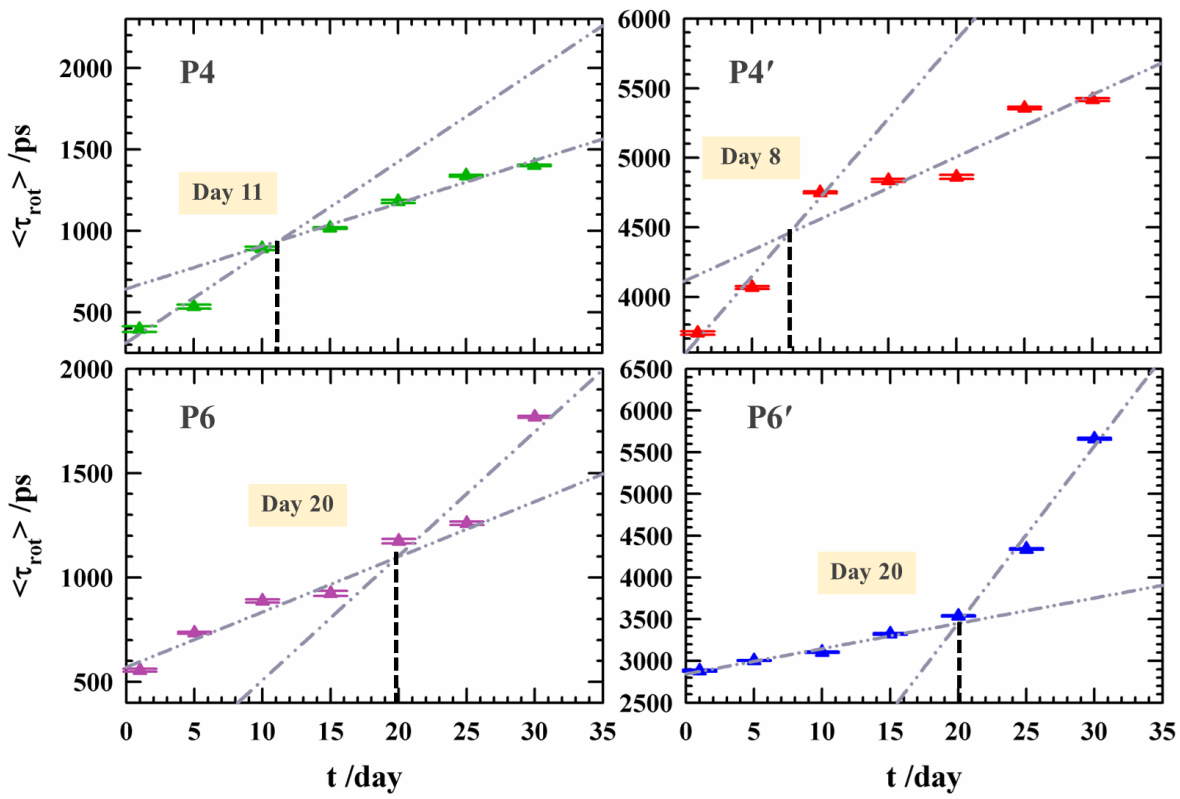

FIG. 6.7. Average rotation times $< \tau_{rot} >$ of C343 of aqueous copolymer solutions of **P4** (upper left panel), **P4′** (upper right panel), **P6** (lower left panel) and **P6′** (lower right panel) from day 1 to day 30. The intersecting point in each plot indicated by black dashed line represents the starting of phase-transition in solutions. All the presentations are color-coded.

To further elucidate the influence of individual rotational times, a detailed analysis was performed, focusing on the amplitudes and time constants for all copolymers. It was found that the parameter $a_3\tau_3^{rot}$ exhibited the strongest correlation with time progression toward the sol-gel transition (see **Fig. 6.8**). This result suggests that the slowest rotational time component plays a critical role in governing the average frictional response of C343, thereby providing key insights into the phase-transition behavior of aqueous copolymer solutions.

Table 6.2. Rotational anisotropy r(t) decay fit parameters of C343 in aqueous solutions of copolymers.[c]

Copolymer	Day	a_1	τ_1/ ps	a_2	τ_2/ ps	a_3	τ_3/ ps	$< \tau_{rot} >$/ ps
P0	1	1	102	-	-	-	-	102
	5	1	99	-	-	-	-	99
	10	1	106	-	-	-	-	106
	15	0.91	83	0.09	477	-	-	117
	20	0.88	79	0.12	392	-	-	117
	25	0.86	79	0.14	608	-	-	151
	30	0.81	69	0.19	676	-	-	184
P4	1	0.49	75	0.08	182	0.43	2358	396
	5	0.43	67	0.17	301	0.40	3253	535
	10	0.63	52	0.09	461	0.28	2994	891
	15	0.64	58	0.09	478	0.27	3469	1017
	20	0.64	57	0.09	576	0.27	4045	1180
	25	0.64	74	0.12	789	0.24	4983	1338
	30	0.66	67	0.11	664	0.23	5444	1402
P6	1	0.55	71	0.08	151	0.37	1361	555
	5	0.66	69	0.15	587	0.19	3160	734
	10	0.59	66	0.18	533	0.23	3269	887
	15	0.63	65	0.17	656	0.20	3860	924
	20	0.66	75	0.18	894	0.16	6024	1174
	25	0.55	60	0.24	735	0.21	5000	1259
	30	0.58	104	0.23	1255	0.19	7474	1769
P4′	1	0.55	46	0.11	992	0.34	10604	3740
	5	0.51	43	0.18	1314	0.31	12285	4067
	10	0.47	48	0.09	630	0.44	10616	4750
	15	0.33	44	0.16	598	0.51	9268	4837
	20	0.38	47	0.15	865	0.47	10030	4862
	25	0.38	36	0.14	820	0.48	10893	5357
	30	0.36	49	0.15	914	0.49	10741	5418
P6′	1	0.39	45	0.33	1282	0.28	8718	2882
	5	0.36	36	0.28	997	0.36	7536	3005
	10	0.40	45	0.40	1591	0.20	12255	3105
	15	0.35	41	0.29	1012	0.36	8375	3323
	20	0.37	43	0.33	1281	0.30	10331	3538
	25	0.35	48	0.38	1633	0.27	13717	4341
	30	0.20	30	0.22	967	0.58	9381	5660

[c]Individual time constants are better than within ±5% of the reported value.

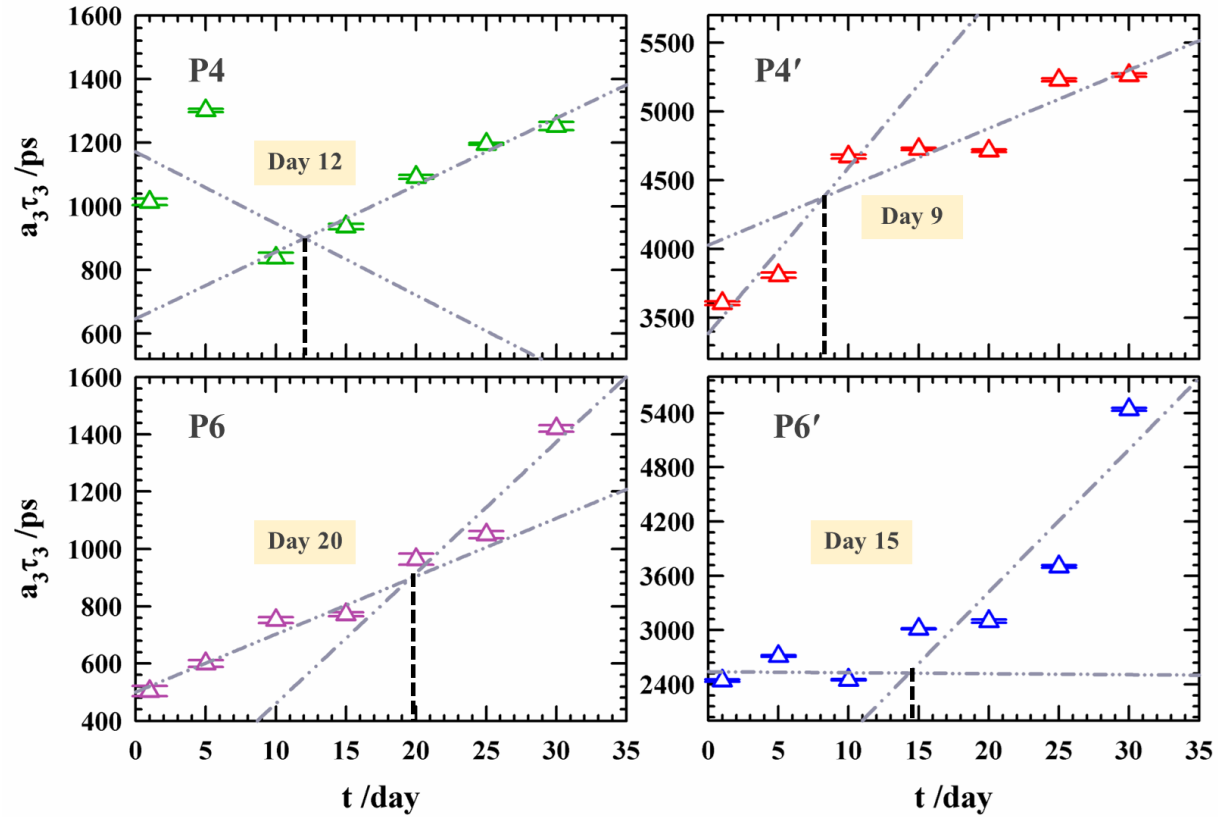

FIG. 6.8. Average slowest ($< \tau_3^{rot} >$/ps) rotation times of C343 with their amplitudes in aqueous copolymer solutions of **P4** (upper left panel), **P4′** (upper right panel), **P6** (lower left panel) and **P6′** (lower right panel) from day 1 to day 30. The intersecting point in each plot indicated by black dashed line represents the starting of phase-transition. All the presentations are color-coded.

6.3.4 Dielectric Relaxation Spectroscopy

6.3.4.1 Possible Origin of DR Timescales Associated with Polymer-Water Solution Structure

The real (ε') and imaginary (ε'') components of the complex dielectric spectra of aqueous copolymer solutions (**P0**, **P4**, **P6**, **P4'** and **P6'**) are presented in **Fig. 6.9**. Clearly, the experimental spectra are adequately described by the 2-Debye fits when compared against other models (see **Fig. 6.A.11 (a)**, Appendix 6.A). **Table 6.3** summarizes the corresponding DR fit parameters.

Table 6.3. Parameters obtained from simultaneous 2-Debye fits to real (ε′) and imaginary (ε″) components of the measured DR data for the aqueous solutions of all the co-polymers.[d]

Co-polymer	Day	ε_0	$\Delta\varepsilon_1$	τ_1^{DR}/ps	$\Delta\varepsilon_2$	τ_2^{DR}/ps	ε_∞	$<\tau_{DR}>$/ps
P0	1	79.82	1.64 (2)	313	73.15 (98)	9	5.03	16
	5	79.90	1.70 (2)	362	73.07 (98)	9	5.13	17
	10	80.01	1.91 (3)	434	72.61 (97)	9	5.49	20
	15	79.97	2.04 (3)	501	72.49 (97)	8	5.44	21
	20	80.17	2.33 (3)	493	73.21 (97)	8	4.63	23
	25	79.48	1.98 (3)	521	72.13 (97)	8	5.37	22
	30	80.14	2.06 (3)	521	72.11 (97)	9	5.97	23
P4	1	80.05	2.36 (3)	478	72.19 (97)	8	5.50	23
	5	80.41	2.70 (4)	569	72.53 (96)	8	5.18	28
	10	80.25	2.68 (4)	637	72.13 (96)	8	5.44	31
	15	81.10	3.14 (4)	730	72.36 (96)	9	5.60	39
	20	81.84	3.92 (5)	810	72.44 (95)	8	5.48	49
	25	82.32	4.46 (6)	1078	72.66 (94)	8	5.20	70
	30	84.11	6.51 (8)	1430	72.69 (92)	8	4.91	125
P6	1	80.13	2.51 (3)	519	72.30 (97)	8	5.32	25
	5	80.24	2.75 (4)	585	71.90 (96)	8	5.59	29
	10	80.33	3.03 (4)	661	72.30 (96)	8	5.00	34
	15	81.23	3.48 (5)	677	72.47 (95)	8	5.28	39
	20	81.21	3.30 (4)	745	72.38 (96)	9	5.53	41
	25	83.10	5.16 (7)	1257	72.62 (93)	8	5.32	91
	30	85.76	8.40 (11)	1923	71.14 (89)	8	6.21	210
P4′	1	78.93	1.18 (2)	578	72.53 (98)	8	5.48	15
	5	79.07	1.31 (2)	619	72.83 (98)	8	4.93	19
	10	80.18	2.32 (3)	810	74.17 (97)	8	3.69	32
	15	80.49	2.51 (3)	1030	73.36 (97)	8	4.62	42
	20	81.08	3.43 (4)	1328	72.83 (96)	8	4.82	67
	25	82.58	4.91 (6)	1808	72.50 (94)	8	5.17	122
	30	83.87	6.13 (8)	2160	72.39 (92)	8	5.35	176
P6′	1	78.56	0.80 (1)	519	72.75 (99)	8	5.01	14
	5	78.46	0.72 (1)	661	72.33 (99)	8	5.41	14
	10	80.99	3.09 (4)	1290	73.99 (96)	8	3.91	59
	15	80.47	2.5 (3)	1498	72.73 (97)	8	5.24	58
	20	81.35	3.64 (5)	1712	72.81 (95)	8	4.90	89
	25	87.32	9.3 (11)	3420	72.75 (89)	8	5.27	395
	30	92.04	14.25 (16)	4311	72.72 (84)	8	5.07	713

[d]The values in the parentheses represent the percentage of corresponding amplitudes.

Data in this table strongly suggest presence of two well-separated relaxation timescales. The dominating relaxation component of these two with a time constant of ~ 8 ps resembles to that for bulk water.[63–67] The other time constant, depending on incubation period, can be divided into two groups: one is in the ~ 300 - 500 ps range and the other in the half-a-nanosecond to several nanoseconds. Since this slow timescale (τ_1^{DR}) becomes longer with incubation period for all the copolymers (**P4**, **P6, P4'** and **P6'**) considered except for **P0,** this timescale is probably connected to the aggregation process. In the case of **P0**, previous observations indicated a faster rotational anisotropy decay of C343 compared to **P4** and **P6** copolymer solutions, suggesting reduced local friction exerted on the fluorophore. Similarly, dielectric relaxation measurements of **P0** demonstrated that the long-time component (τ_1^{DR} ~ 300 - 500 ps) remained essentially unchanged throughout the 30-days incubation period. This observation implies that the aqueous solutions of **P0** do not undergo the sol-gel phase transition.

The next question then naturally arises as to what could be responsible for such a slow timescale (τ_1^{DR}). It may be recalled that DR measurements of aqueous solutions of lipids, proteins, and nucleic acids, as well as micelles, and reverse micelles have already reported a DR timescale of ~ 100 ps and attributed to the relaxation of 'quasi-bound' water molecules.[60,68,69] This means that the ~ 300 - 700 ps timescale found in the present measurements may not be connected to such 'quasi-bound' water; rather, it may have origin in the rotation of the side chains of these polymer molecules that contain polar groups such as $-COOH$ and $-CONH$. This proposition derives support from the observation that this sub-nanosecond timescale grows with incubation time into a couple of nanoseconds. Notice that for aqueous solutions of copolymers with chemically bound C343 (dipolar probe), this timescale further slows down to ~ 4 ns. This provides further support to restricted rotation of the sidechain of these hydrophobically modified polymer, although cannot exclude the possibility of the presence of non-freezable 'tightly bound' water. Our DSC measurements (**Fig. 6.A.12**, Appendix 6.A), however, do not show any sub-zero endothermic dip[70] within the temperature regime 260 - 320 K. These observations, therefore, strongly indicate that the slower of the two DR timescales arise from the polymer sidechain motion which becomes slower with incubation period as aggregation progresses.

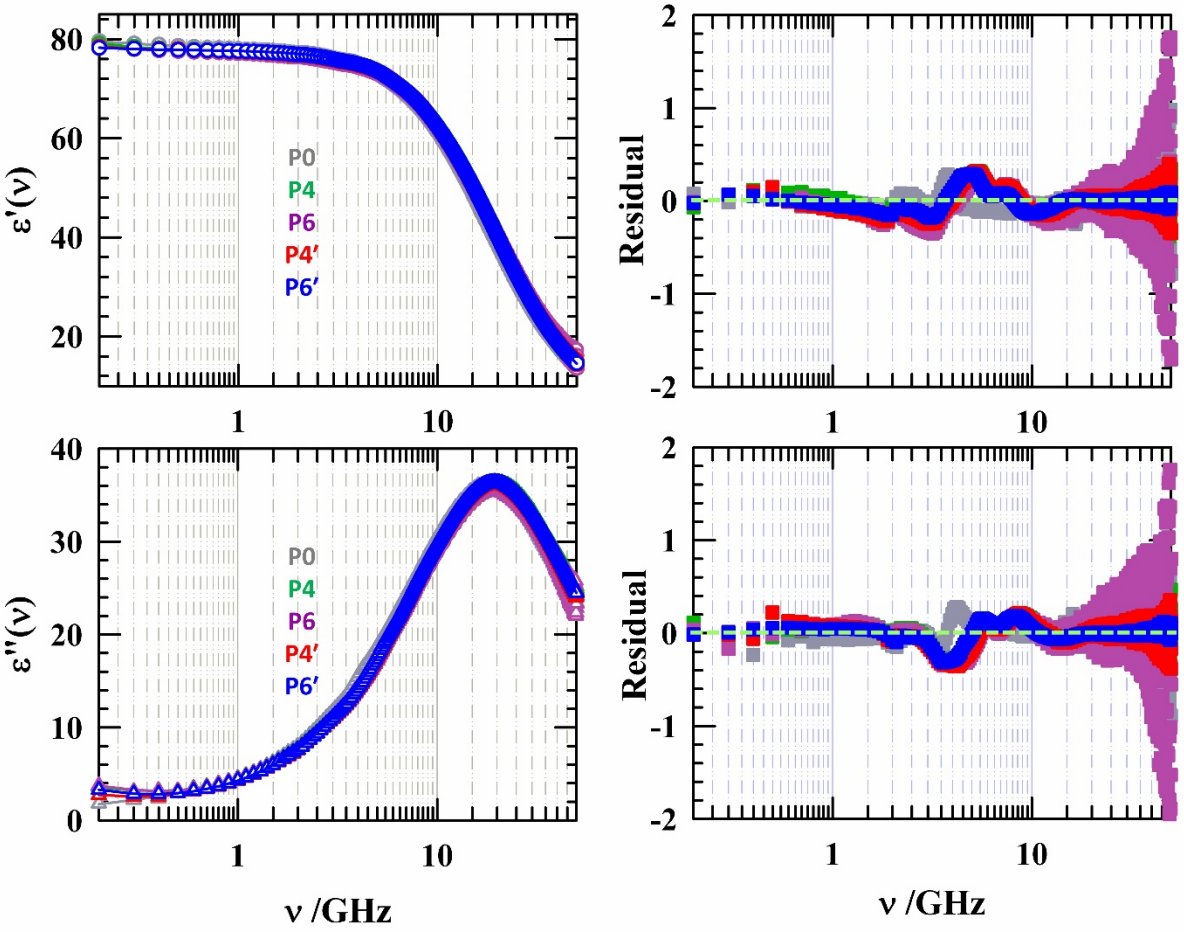

FIG. 6.9. Representative real (ε′) and imaginary (ε″) components of complex dielectric spectra for aqueous copolymer solutions of **P0**, **P4**, **P6, P4'** and **P6'** at day 30. Symbols denote the experimental data and solid lines passing through them denote the multi-Debye fits. Color-coding is used to represent different copolymers. Here, residuals are shown in the inset of each panel.

6.3.4.2 DR Dynamics: Signature of Sol - Gel Phase Transition

From the perspective of sol-gel transition, a compelling correlation in dielectric relaxation (DR) dynamics related to the phase transition has been found over a 30-day period, shown in Figure 10. The overall rise in both the average dielectric relaxation times ($\langle\tau^{DR}\rangle$) and the slowest time-component (τ_1^{DR}) is represented in **Fig. 6.A.11 (b)** (Appendix 6.A) for all studied copolymers.

A detailed analysis of **Table 6.3** reveals that the amplitude and magnitude of τ_1^{DR} in **P4'** and **P6'** experience a remarkable increase, around two to threefold (τ_1 ~ 2-5 ns), after day ~ 10 and day ~ 20, respectively, unlike the progression observed in **P4** and **P6** up to 30 days. The τ_1^{DR} in **P4'** and **P6'** suggest a more hindered environment for sol-gel transition, likely due to the chemical attachment of C343 to the copolymer chain, which restricts its reorientation and exhibits further slower relaxation times. Notably, the magnitude of τ_1^{DR} experiences substantial growth, and the overall relaxation time, $\langle\tau^{DR}\rangle$, subsequently increases as one moves from **P4** to **P6**, or, from **P4'** to **P6'**.

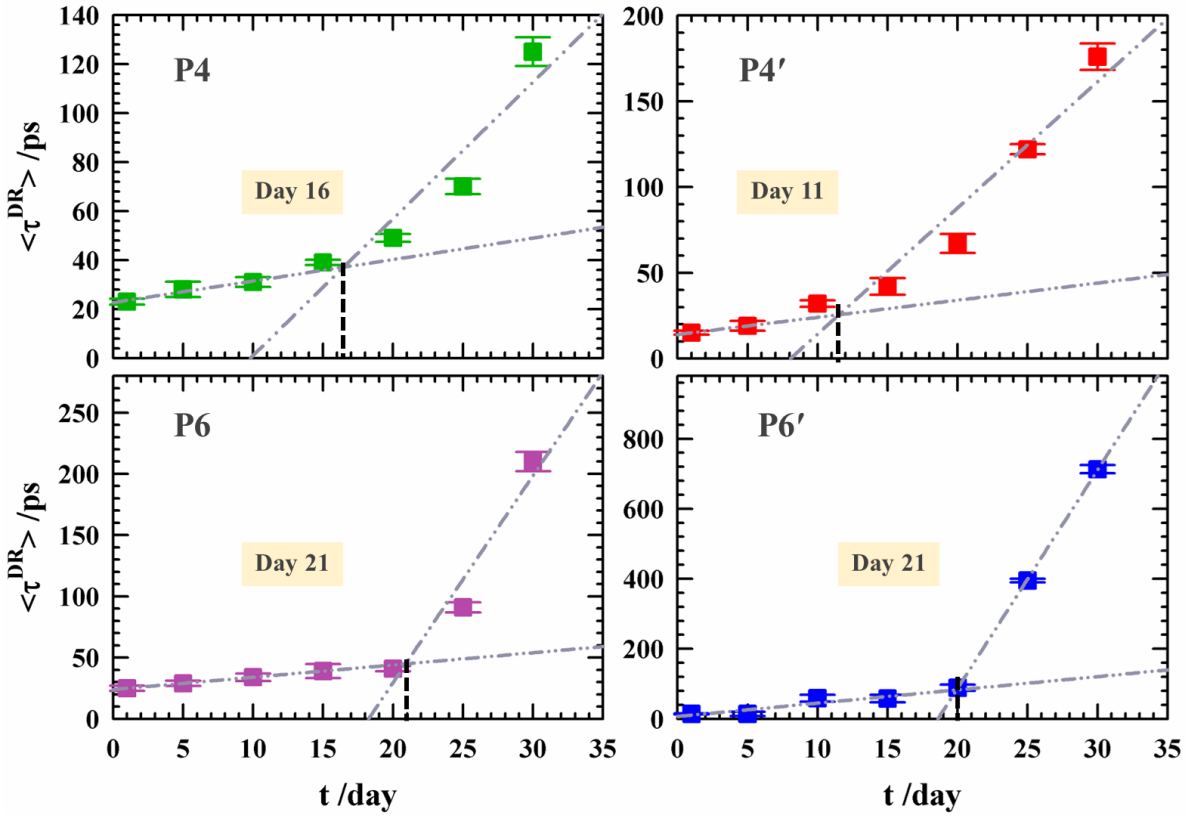

FIG. 6.10. Change in average DR times ($< \tau^{DR} >$/ps) of aqueous copolymer solutions of **P4** (upper left panel), **P4′** (upper right panel), **P6** (lower left panel) and **P6′** (lower right panel) from day 1 to day 30. The intersecting point in each plot indicated by black dashed line represents the onset of phase-transition in solutions. All the presentations are color-coded.

The onset of sol-gel transition for these copolymers, as shown in **Fig. 6.10** and **Fig. 6.11**, can be estimated from DR dynamics, with phase transition occurring ~ day 10 - 15 for **P4** and **P4'** and ~ day 20 for **P6** and **P6'**. Consistent with our rotational anisotropy decay results, the transition point, marked by the slowest component (τ_1^{DR}) in the DR timescales, aligns closely with the estimation from the average DR times ($\langle\tau^{DR}\rangle$) for all copolymers. This indicates that the sol-gel phase transition is reflected emphatically by the slowest relaxation dynamics.

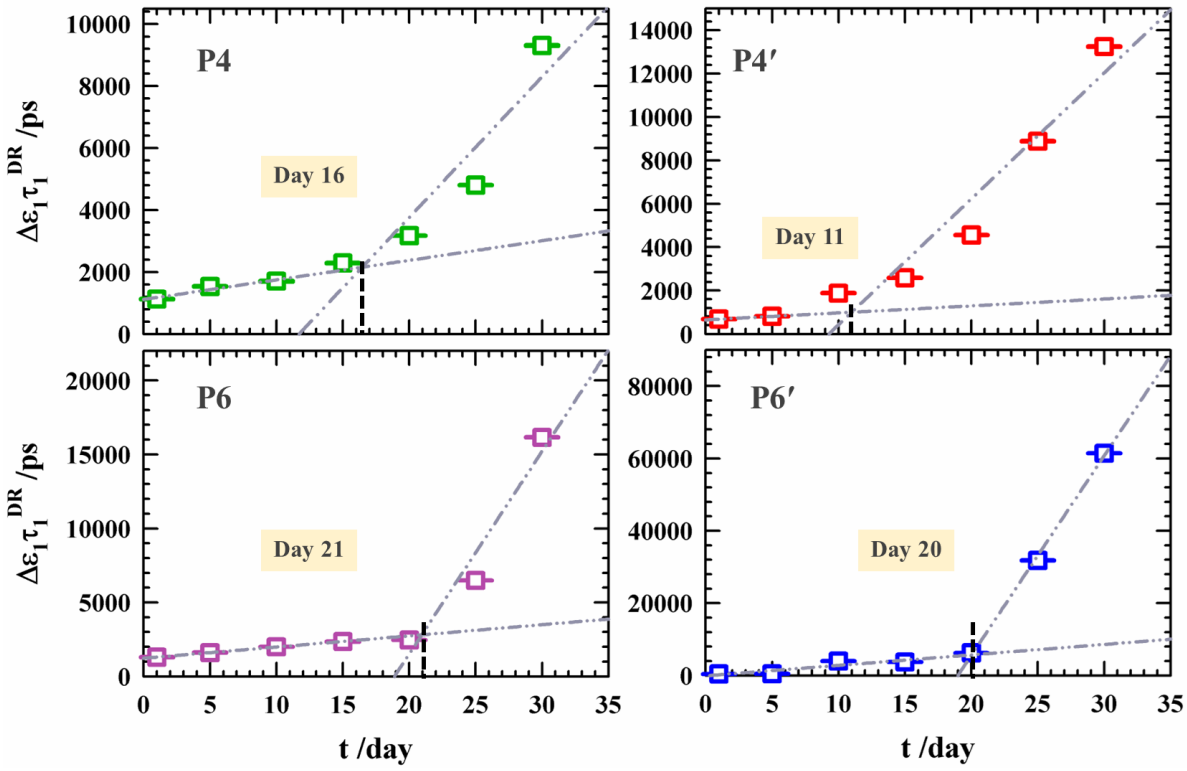

FIG. 6.11. Change in average slowest (τ_1^{DR}/ps) DR times with their dispersion amplitudes ($\Delta\varepsilon_1$) of aqueous copolymer solutions of **P4** (upper left panel), **P4′** (upper right panel), **P6** (lower left panel) and **P6′** (lower right panel) from day 1 to day 30. The intersecting point in each plot indicated by black dashed line represents the onset of phase-transition in solutions. All the presentations are color-coded.

Considering molecular-level understanding of interactions and dynamics, we observe that hydrophobic units in aqueous copolymer solutions play an important role in guiding the relaxation behavior during the sol - gel transition process. Over the incubation period of 30 days, as hydrophobic interaction drives the aggregation process of theses polymer molecules in aqueous solutions, the mobilities of the polymer chains become progressively restricted. This, in turn, increases the rigidity of the aggregated structures, leading to slower relaxation times of polymer chains, and probe molecules located near those interfaces. Additionally, the hydrophobicity driven aggregation leads to formation of domains of differing sizes (confirmed by DLS measurements) that may possess varying relaxation timescales. This leads to dynamic heterogeneity and a broader distribution of relaxation rates that continuously evolve throughout the sol-gel transition from day 1 to day 30. Furthermore, hydrophobic units impact the local structure of water molecules by forming hydration shells around hydrophobic domains. These hydration effects modulate intermolecular interactions and further influence the gelation process in **P4**, **P6**, **P4'** and **P6'** solutions.

6.4 Summary

In summary, we observed significant indications to the onset of sol-gel transition in the hydrophobically modified poly(acrylic acid) (PAA) copolymers through experiments involving steady-state UV-vis absorption, fluorescence emission spectroscopy, and MHz-GHz DR spectroscopy over an investigation period of 30 days. The PAA-based copolymers exhibited a well-defined sol-gel structural shift, evident in the DLS particle size distribution as time of incubation progressed. The steady-state UV-visible absorption, fluorescence emission, and rotational anisotropy studies highlighted distinctive features in the local environment for externally added C343 in **P4** and **P6** solutions versus chemically attached C343 in **P4'** and **P6'** solutions. The chemically bound C343 in **P4'** and **P6'** copolymers reveals an enhanced medium spatial heterogeneity and is more effective at detecting micro sol-gel transition-induced structural changes within the polymer-water interfacial region.

The onset time of the sol-gel transition in these copolymer solutions has been primarily estimated from a structural perspective using dynamic light scattering (DLS) studies. From a dynamical viewpoint, the phase transition is found to be closely correlated to the dielectric relaxation dynamics of these polymer solutions and anisotropy dynamics of an externally added or chemically bound fluorescent dipolar probe molecule. Notably, the sol-gel transition in these copolymer systems is reflected clearly by the slowest of relaxation timescales measured via different techniques employed in this study. While the estimated onset time from the inflection point may vary experimental techniques differ, a consistent indication of structural and dynamical changes is observed before and after the phase transition. The intricate nature of structural and dynamical fluctuations during the sol-gel transition in these designed copolymers suggests the need for further measurements to generate a more comprehensive understanding.

Appendix 6.A

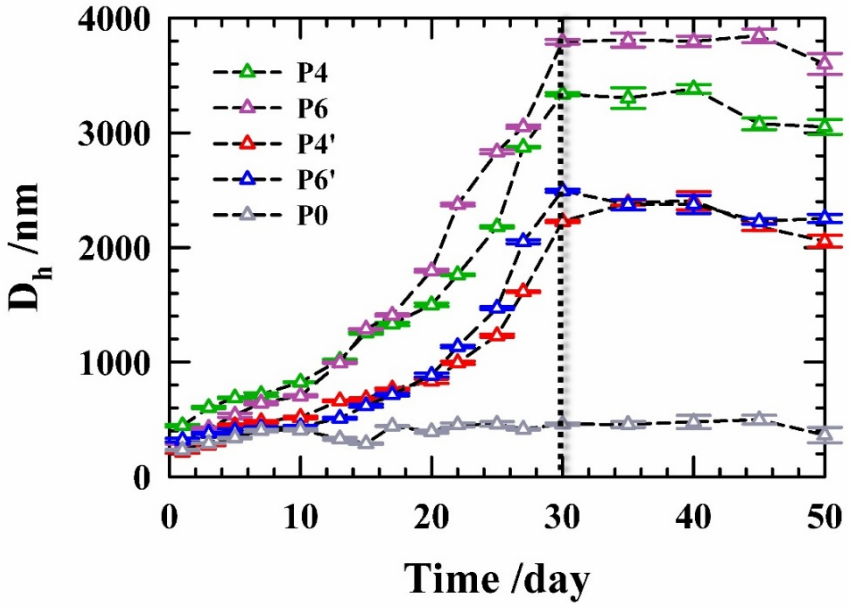

FIG. 6.A.1. Time-dependent DLS profile of aqueous solutions of **P0**, **P4**, **P6** and their C343 tagged (chemically bound) copolymers (**P4′** and **P6′**) over an incubation period of 50 days. Horizontal lines in each data points represent the error bar in D_h. Saturation of D_h values are clearly shown after 30 days of incubation by black dashed vertical line.

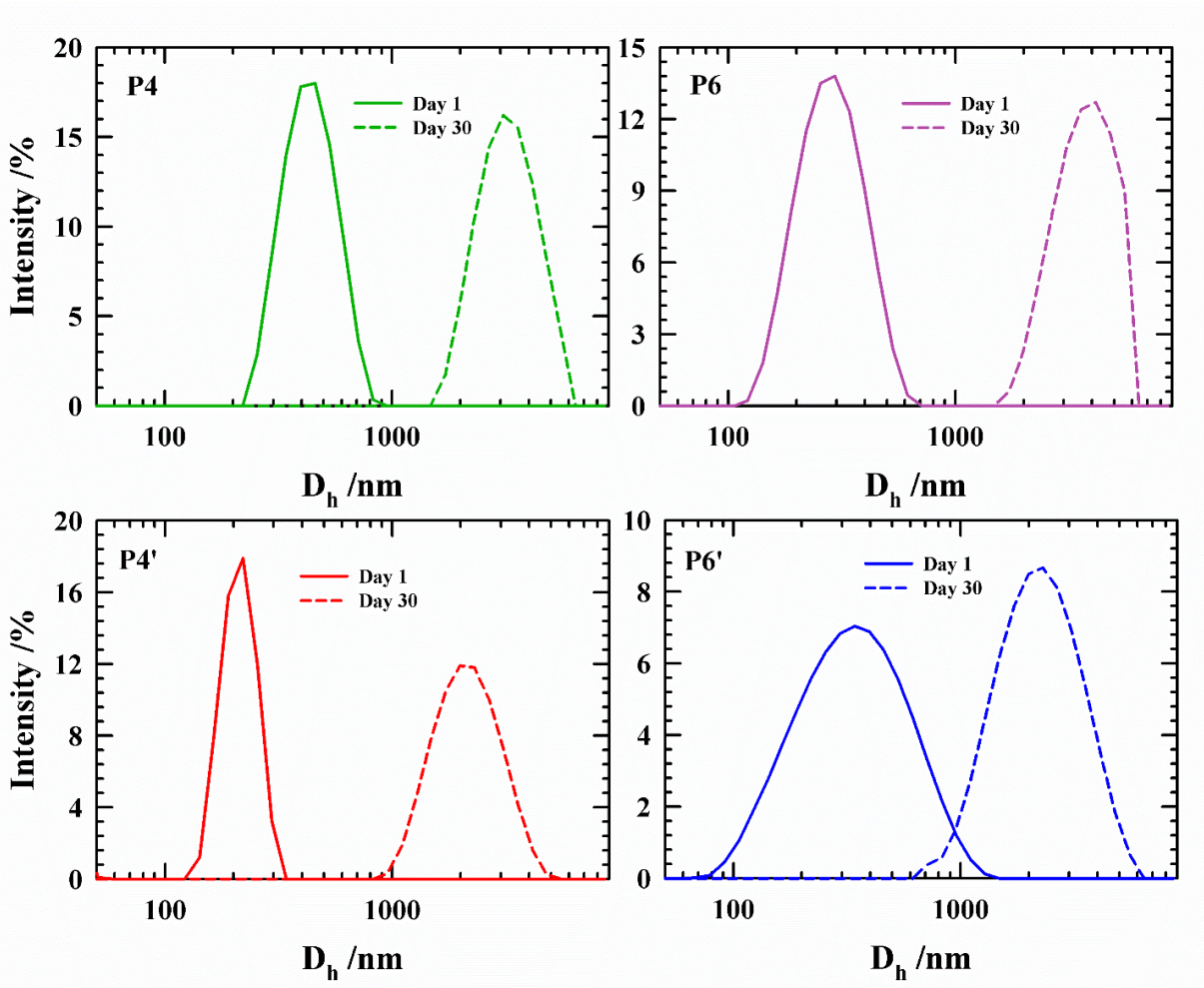

FIG. 6.A.2. Particle size distributions of aqueous copolymer solutions of **P4** (upper left panel), **P6** (upper right panel), **P4′** (lower left panel) and **P6′** (lower right panel) at day 1 and after 30 days of incubation.

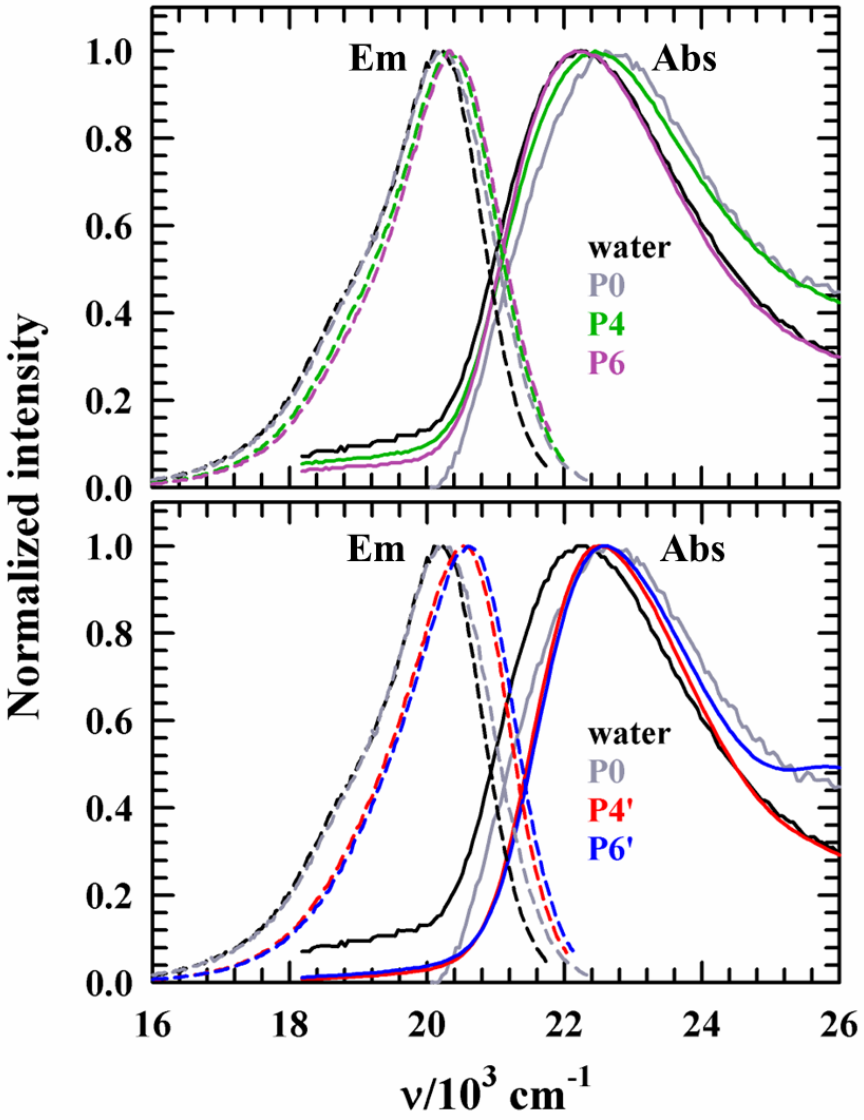

FIG. 6.A.3. UV-visible absorption (solid lines) and steady-state fluorescence emission spectra (dashed lines) of C343 in aqueous solutions **P0**, **P4**, **P6** (upper panel) and **P4′, P6'** (lower panel). The absorption and emission spectra of C343 in neat HPLC water at pH 5 are shown as black line in each panel. All presentations are color-coded.

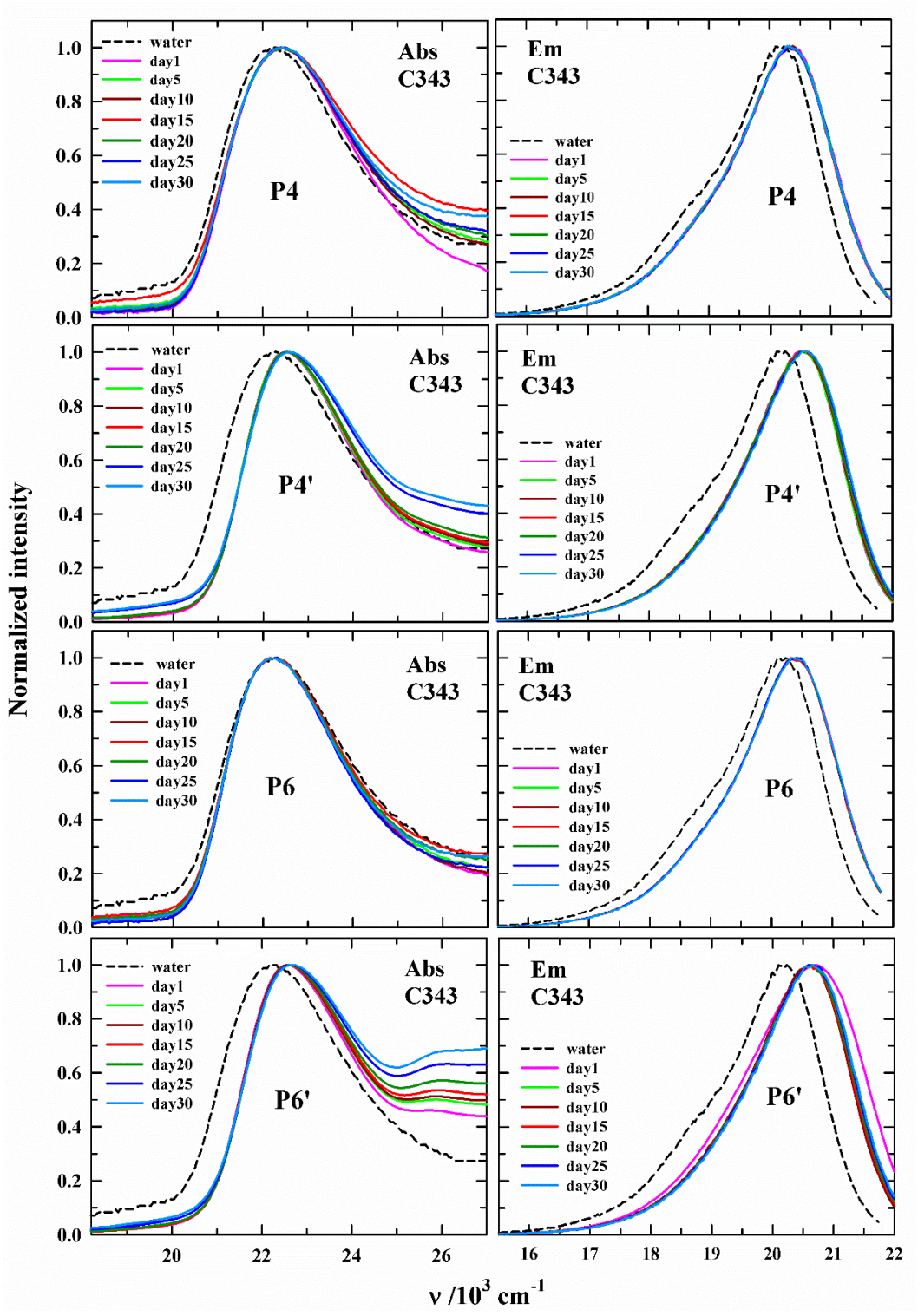

FIG. 6.A.4. Time-dependent steady-state UV-vis absorption and fluorescence emission spectra of C343 in aqueous solutions of copolymers (**P4**, **P6**, **P4′**, **P6'**). Spectra taken at different days are color-indicated. Black dashed lines are representing the absorption and emission spectra of C343 in HPLC water at pH 5.

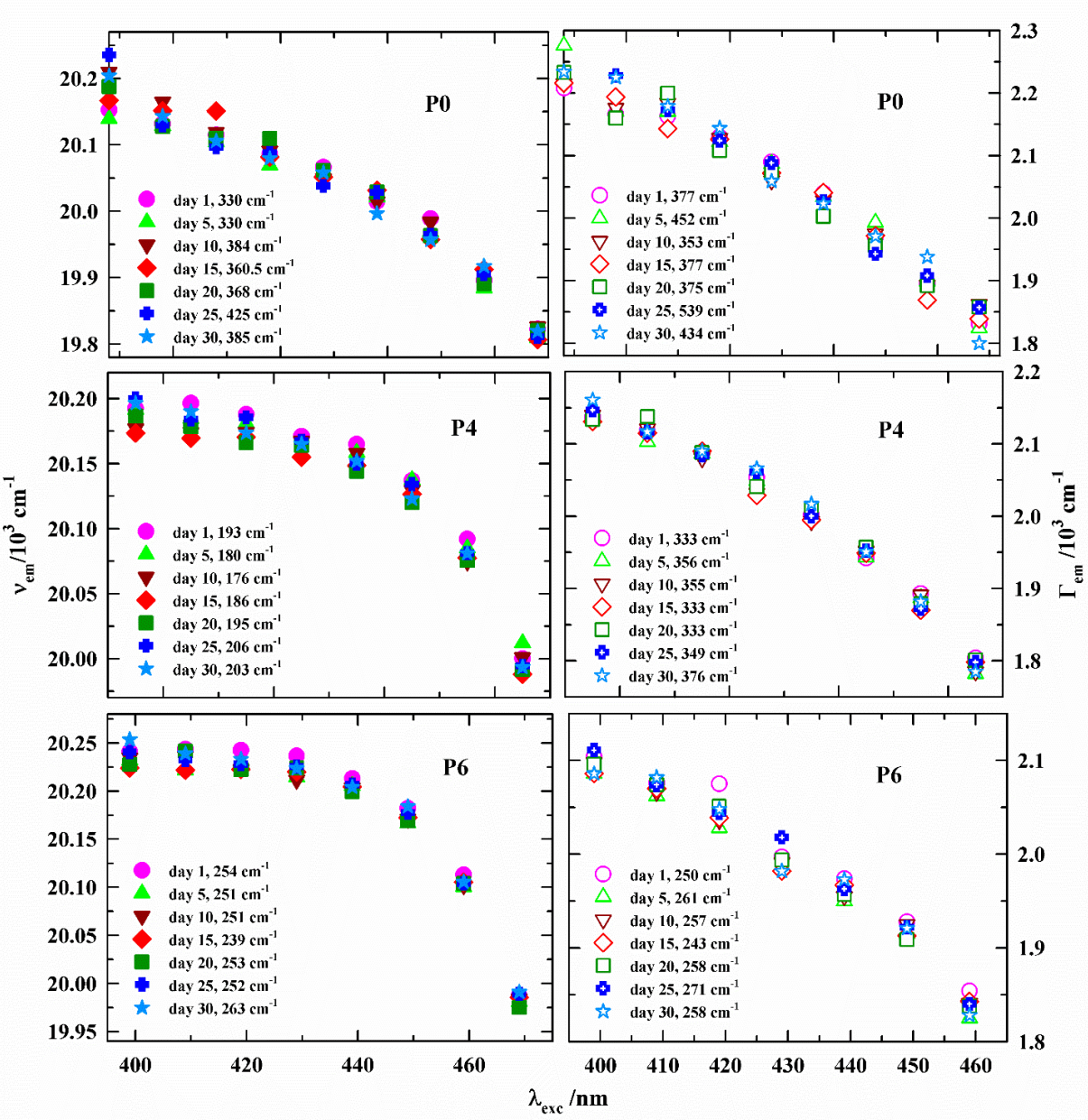

FIG. 6.A.5. Excitation wavelength dependence (λ_{exc}) of steady-state emission peak frequencies (ν_{em}) (left panel) and spectral widths (FWHM, Γ_{em}) (right panel) of C343 in aqueous solutions of **P0**, **P4** and **P6** at different time after preparation of samples. All presentations are color-coded.

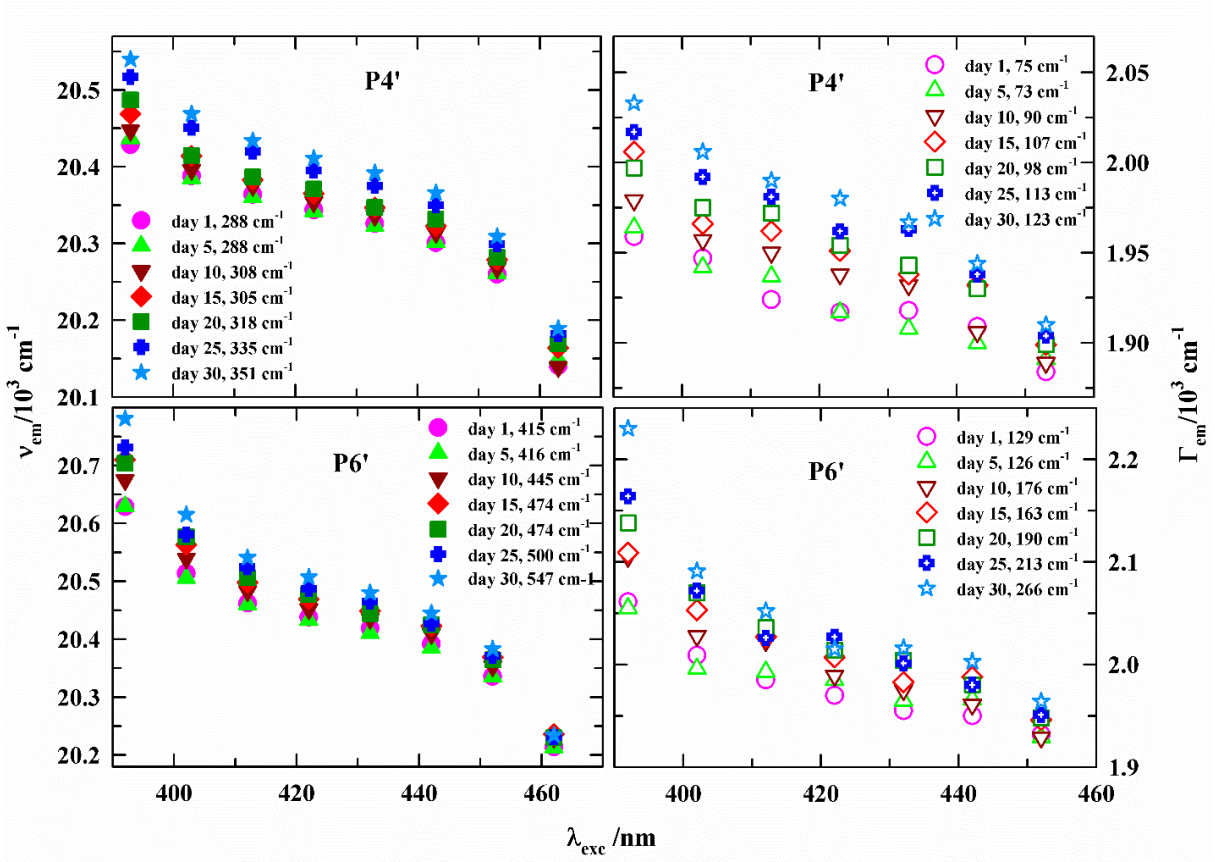

FIG. 6.A.6. Excitation wavelength dependence (λ_{exc}) of steady-state average emission peak frequencies (ν_{em}) (left panel) and spectral widths (FWHM, Γ_{em}) (right panel) of C343 in aqueous solutions of **P4'** and **P6'** at different time after preparation of samples. All presentations are color-coded.

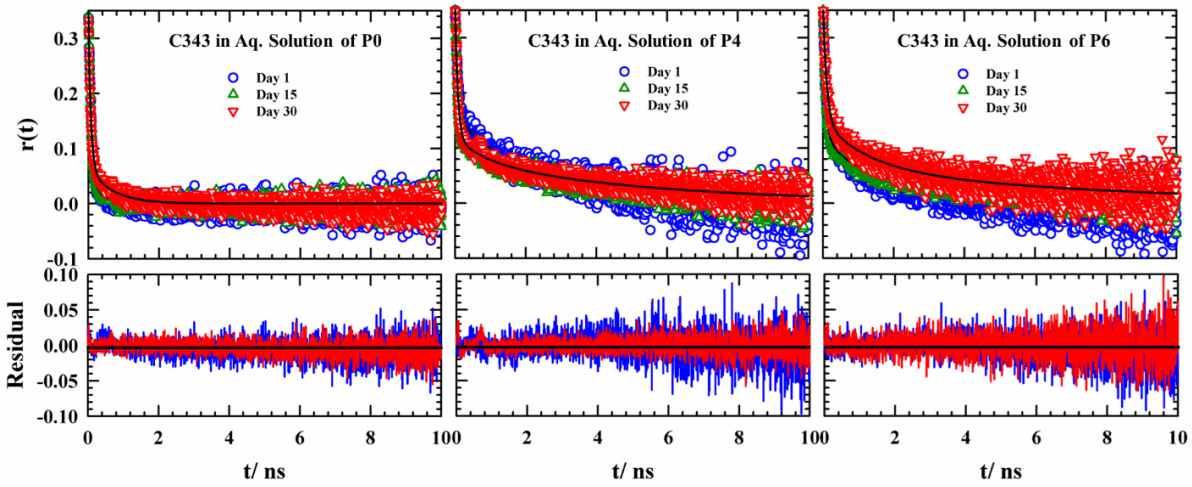

FIG. 6.A.7. Representative time-dependent rotational anisotropy decays, r(t), (upper panel) and the corresponding residuals (lower panel) of C343 in aqueous copolymer solutions of **P0, P4 & P6**. In the upper panel, experimental data points are presented as symbols and lines through them depict multiexponential fits. Specific identities of copolymers are shown in the inset.

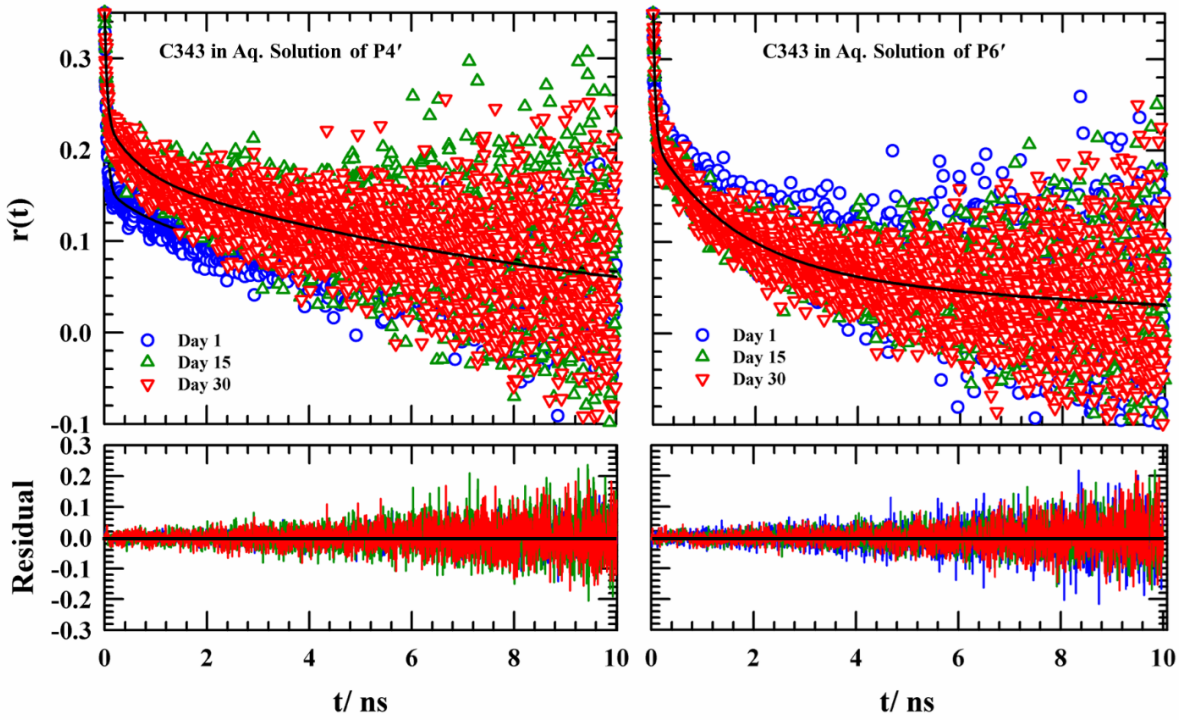

FIG. 6.A.8. Representative time-dependent rotational anisotropy decays, r(t) (upper panel) and the corresponding residuals (lower panel) of C343 in aqueous polymer solutions of **P4'** & **P6'**. In the upper panel, experimental data points are presented as symbols and lines through them depict multiexponential fits. Specific identities of polymers are shown in the inset.

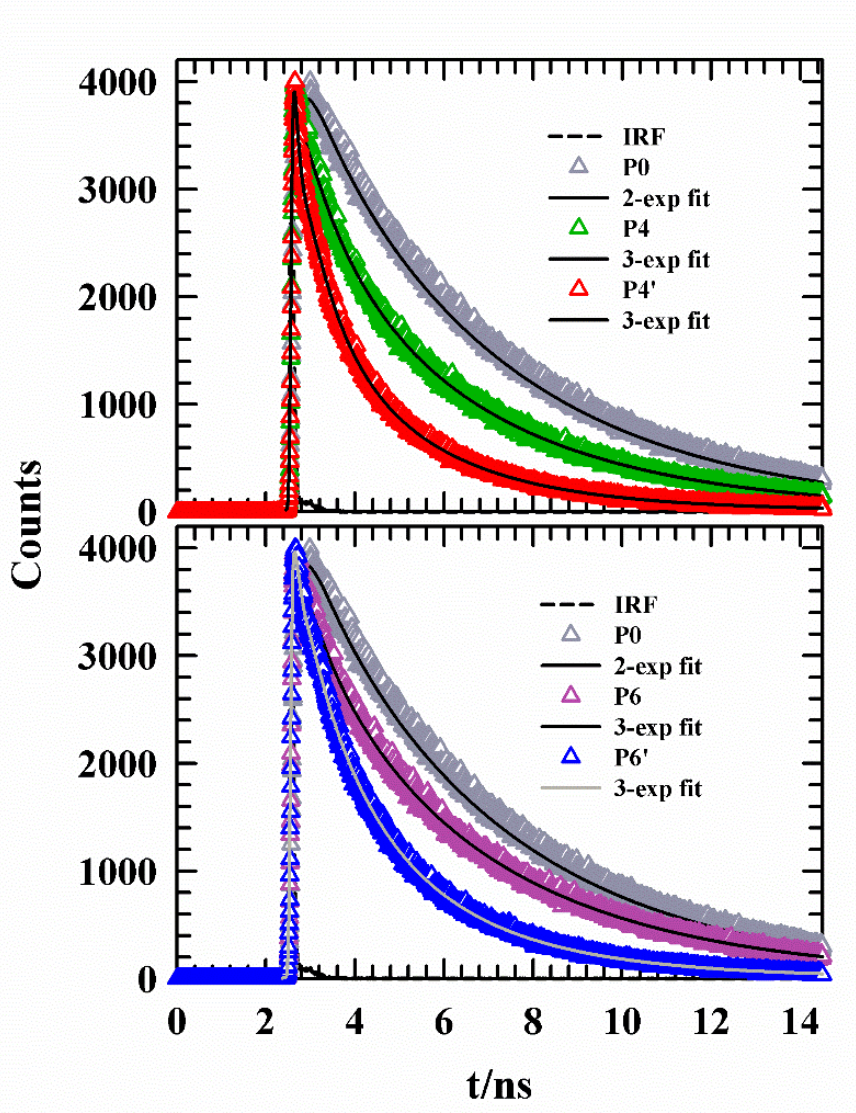

FIG. 6.A.9. Fluorescence lifetime emission decays of C343 in aqueous solutions of **P0**, **P4**, **P6** and their C343-tagged copolymers collected at day 30. All copolymers are color-indicated. Solid lines through the data points represent the corresponding multi exponential fit.

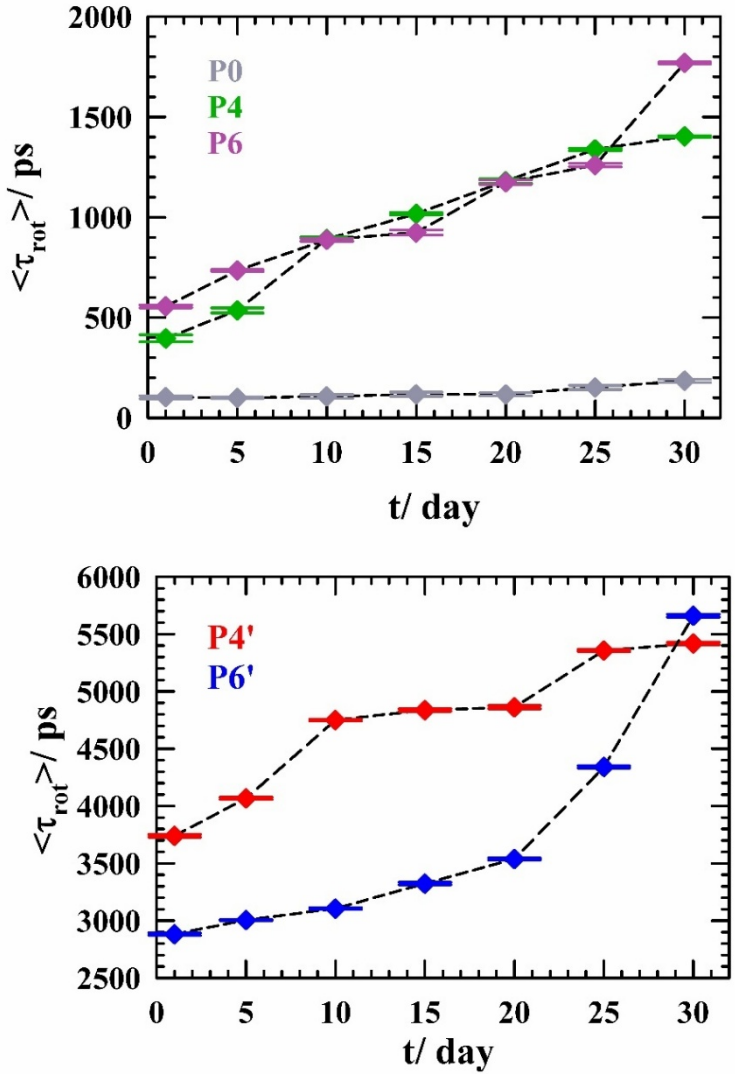

FIG. 6.A.10. Change in average rotational diffusion times of C343 with day of incubation in aqueous copolymer solutions of **P0**, **P4**, **P6** (left panel) and **P4′**, **P6′** (right panel). Black dashed lines are for eye-guidance.

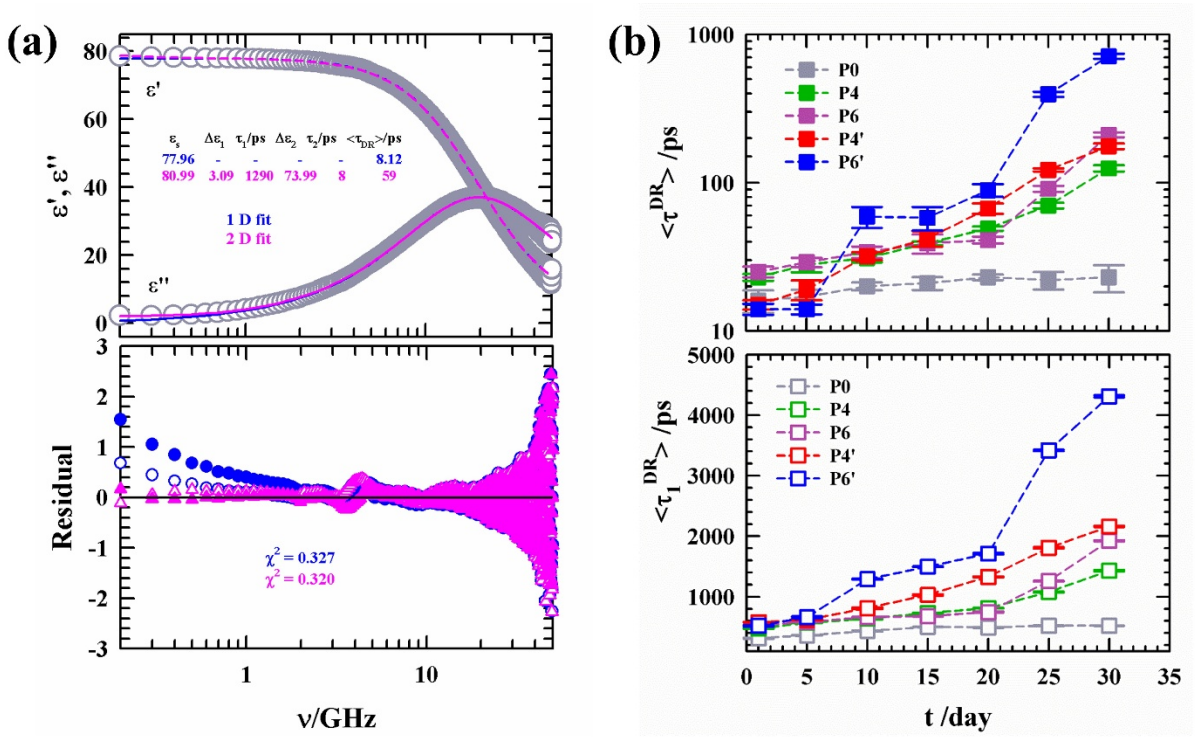

FIG. 6.A.11. (a) Representative comparison between 1-Debye (blue) and 2-Debye (pink) fits (upper panel) along with their residual (lower panel) for aqueous solution of **P6'** at day 30. Circles (unfilled for real part, filled for imaginary part of DR spectra) and triangles (unfilled for real part, filled for imaginary part of DR spectra) in lower panel represent residuals of 1-Debye and 2-Debye fits, respectively. Presentations are color coded.

(b) Change in average DR times (upper panel) and slowest timescales (lower panel) of DR dynamics with respect to incubation time for aqueous copolymer solutions of **P0**, **P4**, **P6**, **P4′**, **P6′**. The dashed lines are for eye-guidance. All the copolymers are color-coded.

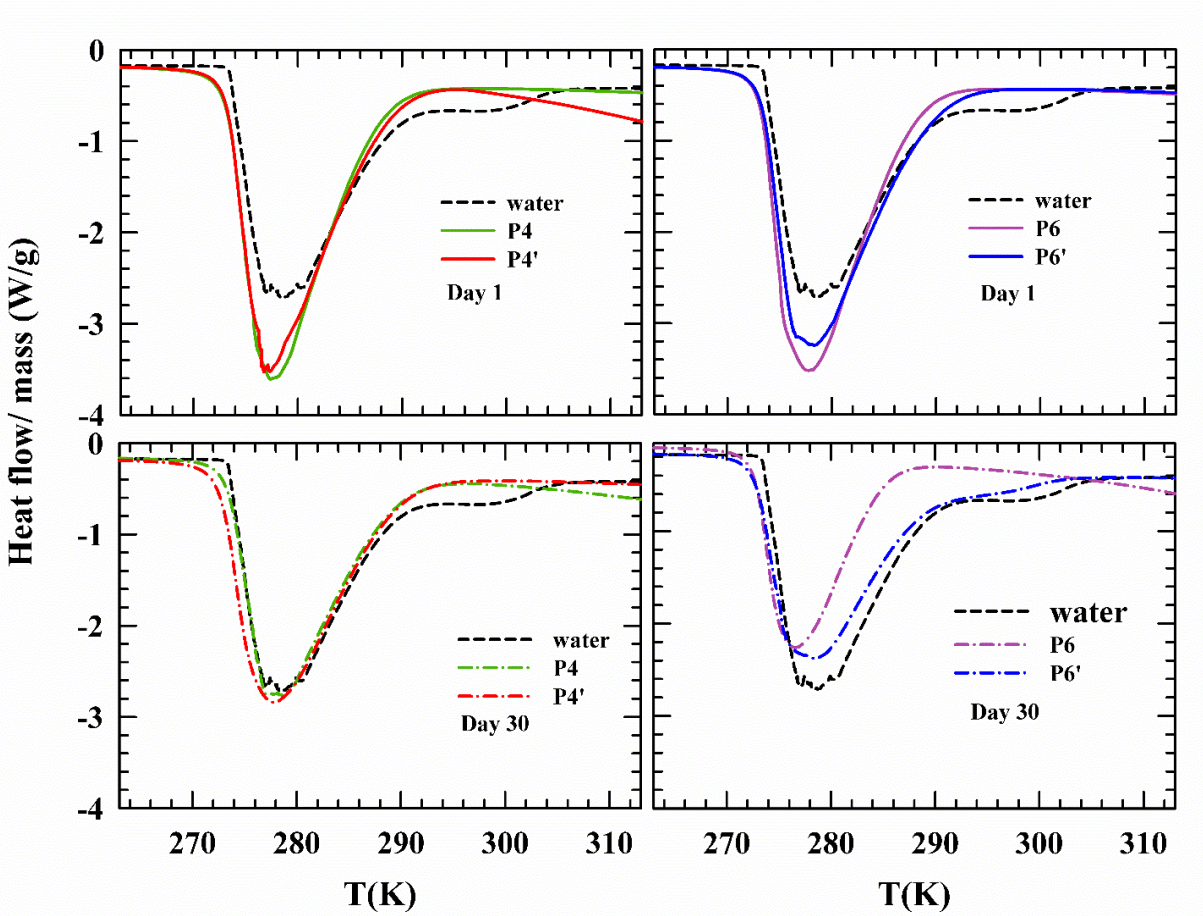

FIG. 6.A.12. DSC thermogram for aqueous copolymer solutions of **P4**, **P6, P4'** and **P6'**. Solid and dash-dot lines represent the DSC data collected on incubation period of day 1 (upper panel) and day 30 (lower panel), respectively. Black dashed lines in each plot display the DSC curve for neat HPLC water. All the copolymers are color-coded.

Appendix 6.B

Table 6.B.1. Particle size (hydrodynamic diameter, D_h) obtained by DLS analysis based on intensity of aqueous copolymer solutions measured on incubation period of 30 days.

Co-polymer	Time of incubation/ day	D_h/ nm*	PDI**
P0	1	232.5 ± 5.09	0.01
	10	407.9 ± 10.77	0.11
	20	394.2 ± 13.79	0.11
	30	459.4 ± 10.57	0.04
P4	1	445.5 ± 10.68	0.07
	10	824.1 ± 4.45	0.05
	20	1499 ± 15.57	0.05
	30	3335 ± 14.99	0.04
P6	1	294.3 ± 8.57	0.10
	10	706.1 ± 13.78	0.10
	20	1797 ± 10.89	0.08
	30	3793 ± 19.90	0.07
P4′	1	214.1 ± 9.09	0.03
	10	517.9 ± 11.01	0.14
	20	833.2 ± 18.91	0.05
	30	2373 ± 9.11	0.22
P6′	1	319.9 ± 15.27	0.12
	10	434.8 ± 14.79	0.26
	20	885.9 ± 16.01	0.07
	30	2375 ± 13.10	0.17

*Mean of ten replications ± standard deviation

**PDI = Polydispersity index

Table 6.B.2. Time-dependent average fluorescence lifetimes ($\langle\tau_{life}\rangle$) of C343 in aqueous solutions of hydrophobically modified PAA copolymers (0.5 wt%) at 298 K.[e]

Co-polymer	Day	a_1	τ_1/ns	a_2	τ_2/ns	a_3	τ_3/ns	$<\tau_{life}>$ /ns
P0	1	0.13	0.55	0.87	4.22	-	-	3.72
	30	0.10	0.85	0.90	4.31	-	-	3.97
P4	1	0.26	0.16	0.22	1.10	0.52	4.07	2.40
	30	0.28	0.12	0.25	0.95	0.47	3.84	2.08
P6	1	0.20	0.25	0.17	1.24	0.63	4.27	2.94
	30	0.25	0.26	0.18	1.49	0.58	4.30	2.81
P4'	1	0.40	0.16	0.32	0.98	0.28	2.29	1.22
	30	0.36	0.10	0.31	0.73	0.33	2.53	1.10
P6'	1	0.27	0.10	0.30	0.78	0.43	2.55	1.38
	30	0.25	0.21	0.35	1.21	0.40	2.81	1.60
Water	-	-	-	-	-	1.00	4.28	4.28

[e]Individual amplitudes and time constants can be reproduced within ±5% of the reported values.

References

[1] Z. Tang, C. He, H. Tian, J. Ding, B.S. Hsiao, B. Chu, and X. Chen, *Prog Polym Sci* **60**, 86–128 (2016).

[2] Y. Que, Y. Liu, W. Tan, C. Feng, P. Shi, Y. Li, and H. Xiaoyu, *ACS Macro Lett* **5**(2), 168–173 (2016).

[3] A.N. Singh, R.D. Thakre, J.C. More, P.K. Sharma, and Y.K. Agrawal, *Polym Plast Technol Eng* **54**(10), 1077–1095 (2015).

[4] A. El Jundi, S.J. Buwalda, Y. Bakkour, X. Garric, and B. Nottelet, *Adv Colloid Interface Sci* **283**, 102213 (2020).

[5] P. Sar, S. Ghosh, Y.D. Gordievskaya, K.G. Goswami, E.Yu. Kramarenko, and P. De, *Macromolecules* **52**(21), 8346–8358 (2019).

[6] A. Dey, U. Haldar, T. Rajasekhar, P. Ghosh, R. Faust, and P. De, *J Mater Chem B* **10**(45), 9446–9456 (2022).

[7] E.A. Appel, J. del Barrio, X.J. Loh, and O.A. Scherman, *Chem Soc Rev* **41**(18), 6195 (2012).

[8] X. Dai, Y. Zhang, L. Gao, T. Bai, W. Wang, Y. Cui, and W. Liu, *Adv Mat* **27**(23), 3566–3571 (2015).

[9] H. Chen, X. Ma, S. Wu, and H. Tian, *Angewandte Chemie* **53**(51), 14149–14152 (2014).

[10] L. Voorhaar, and R. Hoogenboom, *Chem Soc Rev* **45**(14), 4013–4031 (2016).

[11] M. Bustamante-Torres, D. Romero-Fierro, B. Arcentales-Vera, K. Palomino, H. Magaña, and E. Bucio, *Gels* **7**(4), 182 (2021).

[12] T.L. Sun, T. Kurokawa, S. Kuroda, A. Bin Ihsan, T. Akasaki, K. Sato, Md.A. Haque, T. Nakajima, and J.P. Gong, *Nat Mater* **12**(10), 932–937 (2013).

[13] F. Brandl, F. Sommer, and A. Goepferich, *Biomaterials* **28**(2), 134–146 (2007).

[14] X. Yan, F. Wang, B. Zheng, and F. Huang, *Chem Soc Rev* **41**(18), 6042 (2012).

[15] X. Ma, and H. Tian, *Acc Chem Res* **47**(7), 1971–1981 (2014).

[16] Z. Chang, Y. Chen, S. Tang, J. Yang, Y. Chen, S. Chen, P. Li, and Z. Yang, *Carbohydr Polym* **229**, 115431 (2020).

[17] H.J. Chung, and T.G. Park, *Nano Today* **4**(5), 429–437 (2009).

[18] P. Li, C. Zhang, R. Li, L. Qu, X. Dai, Y. Sui, and J. Hou, *ACS Appl Bio Mater* **2**(1), 527–532 (2019).

[19] Y. Geng, X.Y. Lin, P. Pan, G. Shan, Y. Bao, Y. Song, Z.L. Wu, and Q. Zheng, *Polymer* (Guildf) **100**, 60–68 (2016).

[20] L. Yang, X. Tan, Z. Wang, and X. Zhang, *Chem Rev* **115**(15), 7196–7239 (2015).

[21] Q. Zhang, D.-H. Qu, X. Ma, and H. Tian, *Chem Comm* **49**(84), 9800 (2013).

[22] S. Dong, Y. Luo, X. Yan, B. Zheng, X. Ding, Y. Yu, Z. Ma, Q. Zhao, and F. Huang, *Angewandte Chemie* **50**(8), 1905–1909 (2011).

[23] Y. Gao, L. Duan, S. Guan, G. Gao, Y. Cheng, X. Ren, and Y. Wang, *RSC Adv* **7**(71), 44673–44679 (2017).

[24] X. Liu, X. He, B. Yang, L. Lai, N. Chen, J. Hu, and Q. Lu, *Adv Funct Mater* **31**(3), (2021).

[25] M.J. Hwang, M.K. Joo, B.G. Choi, M.H. Park, I.W. Hamley, and B. Jeong, *Macromol Rapid Commun* **31**(23), 2064–2069 (2010).

[26] M.S. Kim, H. Hyun, K.S. Seo, Y.H. Cho, J. Won Lee, C. Rae Lee, G. Khang, and H.B. Lee, *J Polym Sci A Polym Chem* **44**(18), 5413–5423 (2006).

[27] J. Spěváček, and J. Dybal, *Macromol Symp* **303**(1), 17–25 (2011).

[28] C.W. Park, S.J. Lee, D. Kim, D.S. Lee, and S.C. Kim, *J Polym Sci A Polym Chem* **46**(6), 1954–1963 (2008).

[29] H. De Paz, A. Chemtob, C. Croutxé-Barghorn, D. Le Nouen, and S. Rigolet, *J Phys Chem B* **116**(17), 5260–5268 (2012).

[30] H. Mao, C. Wang, X. Chang, H. Cao, G. Shan, Y. Bao, and P. Pan, *Mater Chem Front* **2**(2), 313–322 (2018).

[31] Z. Wu, Y. Xiong, C. Li, H. Cheng, Y. Li, and W. Chen, *Macromolecules* **56**(17), 7113–7124 (2023).

[32] T. Miura, H. Okumoto, and H. Ichijo, *Phys Rev E* **54**(6), 6596–6602 (1996).

[33] Y.-M. Chung, K.L. Simmons, A. Gutowska, and B. Jeong, *Biomacromolecules* **3**(3), 511–516 (2002).

[34] M.F. Llauro, J. Loiseau, F. Boisson, F. Delolme, C. Ladavière, and J. Claverie, *J Polym Sci A Polym Chem* **42**(21), 5439–5462 (2004).

[35] D.J. Keddie, *Chem. Soc. Rev.* **43**(2), 496–505 (2014).

[36] G. Moad, Y.K. Chong, A. Postma, E. Rizzardo, and S.H. Thang, *Polymer* (Guildf) **46**(19), 8458–8468 (2005).

[37] M.R. Hill, R.N. Carmean, and B.S. Sumerlin, *Macromolecules* **48**(16), 5459–5469 (2015).

[38] A. York, S. Kirkland, and C. Mccormick, *Adv Drug Deliv Rev* **60**(9), 1018–1036 (2008).

[39] S. Kumar, R. Acharya, U. Chatterji, and P. De, *J. Mater. Chem. B* **1**(7), 946–957 (2013).

[40] M.L. Horng, J.A. Gardecki, A. Papazyan, and M. Maroncelli, *J Phys Chem* **99**(48), 17311–17337 (1995).

[41] R. Jimenez, G.R. Fleming, P. V. Kumar, and M. Maroncelli, *Nature* **369**(6480), 471–473 (1994).

[42] D. Pant, and H.H. Girault, *Phys Chem Chem Phys* **7**(19), 3457 (2005).

[43] E.M. Corbeil, and N.E. Levinger, *Langmuir* **19**(18), 7264–7270 (2003).

[44] K.H. Drexhage, G.R. Erikson, G.H. Hawks, and G.A. Reynolds, *Opt Commun* **15**(3), 399–403 (1975).

[45] N.M. Correa, and N.E. Levinger, *J Phys Chem B* **110**(26), 13050–13061 (2006).

[46] R. Biswas, J.E. Lewis, and M. Maroncelli, *Electronic Spectral Shifts, Reorganization Energies, and Local Density Augmentation of Coumarin 153 in Supercritical Solvents* (1999).

[47] J.E. Lewis, R. Biswas, A.G. Robinson, and M. Maroncelli, *J Phys Chem B* **105**(16), 3306–3318 (2001).

[48] B. Guchhait, and R. Biswas, *J Chem Phys* **138**(11), (2013).

[49] H.A.R. Gazi, B. Guchhait, S. Daschakraborty, and R. Biswas, *Chem Phys Lett* **501**(4–6), 358–363 (2011).

[50] T. Pradhan, P. Ghoshal, and R. Biswas, *J Chem Sc* **120**(2), 275–287 (2008).

[51] R. Priyadarshi, S. Roy, and J.-W. Rhim, *J Nanostructure Chem* **12**(3), 389–399 (2022).

[52] R. Karimirad, M. Behnamian, and S. Dezhsetan, *Food Hydrocoll* **100**, 105387 (2020).

[53] M. Taylor, P. Tomlins, and T. Sahota, *Gels* **3**(1), 4 (2017).

[54] A.R. Khokhlov, S.G. Starodubtzev, and V. V. Vasilevskaya, (1993), pp. 123–171.

[55] C. Tsitsilianis, *Soft Matter* **6**(11), 2372 (2010).

[56] S. Dai, P. Ravi, and K.C. Tam, *Soft Matter* **4**(3), 435 (2008).

[57] W. Jiao, H. Yang, Z. Wu, J. Liu, and W. Zhang, *Expert Opin Drug Deliv* **17**(7), 947–961 (2020).

[58] J. Zierenberg, M. Marenz, and W. Janke, *Polymers* (Basel) **8**(9), 333 (2016).

[59] K. Kumbhakar, E. Tarif, K. Mukherjee, and R. Biswas, *J Mol Liq* **290**, 111225 (2019).

[60] K. Kumbhakar, A. Dey, A. Mondal, P. De, and R. Biswas, *J Phys Chem B* **125**(22), 6023–6035 (2021).

[61] K. Kumbhakar, B. Saha, P. De, and R. Biswas, *J Phys Chem B* **123**(51), 11042–11054 (2019).

[62] B. Guchhait, S. Das, S. Daschakraborty, and R. Biswas, *J Chem Phys* **140**(10), (2014).

[63] R. Buchner, J. Barthel, and J. Stauber, *The Dielectric Relaxation of Water between 08C and 358C* (1999).

[64] N. Nandi, and B. Bagchi, *J Phys Chem B* **101**(50), 10954–10961 (1997).

[65] J. Swenson, and J. Teixeira, *J Chem Phys* **132**(1), 014508 (2010).

[66] F. Mallamace, C. Corsaro, P. Baglioni, E. Fratini, and S.-H. Chen, *J Phys: Cond Mat* **24**(6), 064103 (2012).

[67] Y. Ono, and T. Shikata, *J Phys Chem B* **110**(19), 9426–9433 (2006).

[68] E. Tarif, B. Saha, K. Mukherjee, P. De, and R. Biswas, *J Phys Chem B* **123**(27), 5892–5901 (2019).

[69] H.S. Tan, I.R. Piletic, and M.D. Fayer, *J Chem Phys* **122**(17), (2005).

[70] K. Mukherjee, A. Barman, and R. Biswas, *J Chem Phys* **151**(18), (2019).

Chapter 7

Understanding pH-Tuned Aggregation Dynamics of Tryptophan: Implications for Amyloid Fibrillation

7.1 Introduction

Amyloid diseases constitute a broad class of progressive neurodegenerative disorders, including Alzheimer's disease, Parkinson's disease, and prion diseases, that are primarily characterized by the pathological misfolding and aggregation of amyloidogenic proteins.[1–4] A hallmark of these conditions is the conversion of soluble, functionally benign protein monomers into highly ordered, β-sheet-rich fibrillar aggregates.[5] Despite the sequence and structural diversity among amyloid-forming proteins, their aggregation processes often share striking similarities in kinetics, morphology, and cytotoxicity, suggesting a potentially conserved molecular mechanism underlying diverse amyloid diseases.[6–9]

In recent years, non-proteinaceous and small biomolecular systems have also been recognized for their ability to form amyloid-like aggregates under favorable conditions. Tryptophan (Trp), an essential aromatic amino acid, is a key intrinsic fluorophore in proteins due to its strong fluorescence properties. Beyond its role in protein biochemistry, Trp itself has been shown to undergo self-assembly into amyloid-like fibrils under specific physicochemical conditions. The formation of these fibrillar aggregates has been implicated in pathological conditions such as hypertryptophanemia and Hartnup disorder, which are associated with neurological dysfunctions.[10,11] Analogous to classical amyloidogenic proteins, Trp is non-toxic in its monomeric form but exhibits potential cytotoxicity upon fibril formation. To mitigate fibril-

associated cytotoxicity, various strategies have been explored, among which the use of small-molecule inhibitors have garnered significant attention.[12–17] These exogenous agents often interfere with aggregation pathways, thereby impeding fibril growth. However, despite their efficacy in *in vitro* systems, translating these approaches to *in vivo* contexts remains a formidable challenge due to issues of bioavailability, specificity, and off-target effects.[18]

Given these limitations, there is a growing need to delineate the fundamental molecular mechanisms that govern Trp fibrillation. A deeper understanding of the physicochemical factors, such as pH, charge states, and hydrogen bonding, that modulate aggregation propensity may offer novel, inhibitor-free strategies for controlling fibril formation. This study aims to investigate these aspects by examining the role of ionizable groups, pH-dependent structural transitions, and environmental conditions on the self-assembly behavior of Trp.

The mechanism underlying fibril formation of Trp remains relatively underexplored in the literature, despite increasing recognition of its importance. Among the various non-covalent interactions driving fibrillation, hydrogen bonding has emerged as a critical determinant in stabilizing β-sheet-rich aggregated structures commonly observed in amyloid-like fibrils.[19–22] The ability of a molecule like Trp to engage in hydrogen bonding is intimately linked to the protonation states of its ionizable functional groups, which are, in turn, governed by the pH of the surrounding environment. Trp possesses two key ionizable groups: a carboxylic acid ($-COOH$) and a primary amine ($-NH_2$). The respective pKa values are approximately 2.38 for the $-COOH$ and 9.39 for the $-NH_3^+$ functionalities.[23] According to the Henderson - Hasselbalch principle,[24] when the pH of the medium exceeds the pKa of a functional group, that group tends to lose a proton (i.e., becomes deprotonated). Thus, at pH values below 2.38, both groups remain protonated, making Trp cationic and more hydrophilic. At neutral pH (~ 7.4), the carboxyl group is deprotonated while the amine remains protonated, giving Trp a zwitterionic character. At alkaline pH (~11), both groups are deprotonated, resulting in an overall anionic structure. Such alterations in charge states and hydrogen-bonding potential critically influence the self-assembly behavior of Trp, modulating its tendency to undergo aggregation and form fibrillar structures. It has been reported that

environmental pH can modulate not only the rate of fibril formation but also the thermodynamic stability, morphological characteristics, and the nature of inter- and intra-molecular interactions within aggregates.[25,26] Therefore, our experimental strategy is grounded in a systematic pH-dependent study of Trp fibrillation kinetics, correlating the protonation states determined by its intrinsic pK_a values with the extent of fibril formation. This approach allows us to dissect the fundamental structural and environmental parameters that facilitate or hinder the aggregation process, offering mechanistic insights into the physicochemical principles of Trp fibrillation.

In this study, we investigated Trp aggregation behavior across three distinct pH conditions to elucidate the influence of ionizable groups and molecular charge on fibrillation. At pH 2, all ionizable groups remain protonated, rendering Trp cationic. At physiological pH 7.4, only the carboxylic acid group of Trp is deprotonated, resulting in a zwitterionic or overall neutral structure. At alkaline pH 11, both the carboxyl and primary ammonium groups are deprotonated, making Trp anionic. By combining spectroscopic techniques, specifically, the intrinsic fluorescence[27,28] of Trp and the photophysical properties of the amyloid-specific dye Thioflavin-T (Th-T),[29–33] we were able to dissect how these charge states and ionizable groups influence the aggregation process. Furthermore, the morphological characteristics of Trp aggregates under different pH conditions have been explored using field emission scanning electron microscope (FESEM). Overall, this work aims to identify the structural prerequisites essential for Trp fibrillary propagation, providing insights that may guide strategies to slow down or, inhibit Trp fibrillation.

7.2 Experimental Methods

7.2.1 Materials

L-Tryptophan (Trp), Thioflavin T (Th-T), sodium chloride, potassium chloride, disodium hydrogen phosphate, potassium dihydrogen phosphate, hydrochloric acid, and sodium hydroxide were purchased from Sigma-Aldrich (purity of all the chemicals is ≥99%). Milli-Q water was used for the preparation of Phosphate Buffered Saline (PBS). All the measurements have been

performed at room temperature (T/K ~ 300 ± 1). The chemical structures of Tryptophan and Thioflavin-T are shown in **Scheme 7.1**.

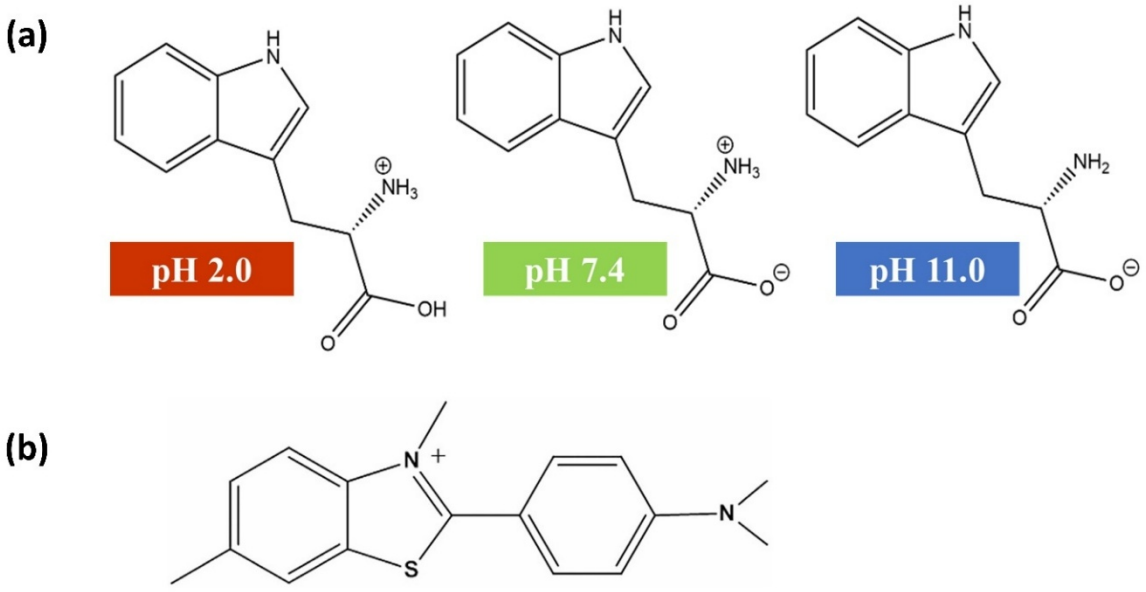

Scheme 7.1. Chemical structures of (a) Trp at respective pH of the medium and (b) Thioflavin-T.

7.2.2 Sample Preparation

PBS buffer was prepared using a conventional protocol to maintain a physiological pH of 7.4 and ionic strength. To obtain the desired pH conditions (pH 2.0, 7.4, and 11.0), the pH of buffer was carefully adjusted by the dropwise addition of hydrochloric acid (HCl) and sodium hydroxide (NaOH) solutions, using a calibrated bench-top multiparameter electrochemical meter (SESHIN BIOTECH, Model: ECM − 610).

Trp (~ 40 mg) was dissolved in 10 mL of the respective buffer under continuous stirring at ~ 363 K, followed by a controlled cooling process to room temperature (~ 300 K) using a LABMAN LMMS − 5LC ceramic hot plate magnetic stirrer. The resulting solutions were then incubated at ~ 300 K to allow for subsequent measurements. A fresh stock solution of Th-T was

prepared and added to the Trp solutions in such a way that the final concentration of Th-T was maintained at ~ 20 μM.

7.2.3 Spectroscopic Techniques

Several spectroscopic measurements were carried out to investigate the structural and dynamic properties of aqueous Trp solutions. Steady-state fluorescence emission spectra were collected using a fluorimeter (Fluorolog, Jobin-Yvon, Horiba). Both excitation and emission slits were kept at 2 nm. For samples containing Th-T, fluorescence measurements have been performed using an excitation wavelength of 409 nm. The intrinsic fluorescence of Trp was probed using an excitation wavelength of 280 nm. Time-resolved fluorescence measurements were conducted to determine fluorescence lifetimes and solvation dynamics, utilizing a Streak Camera system (Optoscope SC − 10) coupled with a spectrograph (HRS − 300SS, Princeton Instruments).

Raman spectroscopic analysis was carried out using a micro-Raman spectrometer (LabRam HR Evolution, Horiba France SAS) equipped with a 532 nm laser excitation source. Prominent vibrational features observed in the raw spectra were subsequently fitted using Lorentzian function to extract relevant spectral parameters.

Dielectric relaxation spectroscopy (DRS) measurements were performed in the frequency range of 200 MHz to 50 GHz and temperature range of 298 - 323 K, employing a PNA − L network analyzer (N5235B) integrated with an open-ended coaxial probe kit (N1501A). The complex dielectric spectra obtained for Trp solutions were fitted using a 2-Debye relaxation process to extract relaxation parameters. Further methodological details regarding the Streak Camera, Raman spectroscopy, and DRS measurements, including data acquisition and analysis protocols, are provided in Chapter 2.

7.2.4 Field Emission Scanning Electron Microscope (FESEM)

FESEM was employed to investigate the morphological characteristics of Trp aggregates formed in buffer solutions of varying pH. Three representative samples have been prepared from Trp solutions incubated for 11 days in PBS buffer media at pH 2, 7.4, and 11, respectively. For FESEM analysis, a 10 µL aliquot of each sample was drop-cast onto a clean silicon wafer, followed by drying at room temperature. The dried samples were then sputter-coated with a thin layer of gold alloy to ensure surface conductivity. Imaging was performed using a QUANTA FEG 250 microscope operated at an accelerating voltage of 20 kV, equipped with a backscattered electron detector and run in high-vacuum mode.

7.3 Results and Discussion

7.3.1 Steady-State and Time-Resolved Spectral Analysis of Trp Aggregation

The kinetics of Trp fibrillation under varying pH conditions were investigated by employing steady-state fluorescence spectroscopy using Th-T as a fibril-sensitive probe. **Fig. 7.1** (upper panel) displays the time-dependent fluorescence emission spectra of Th-T in the presence of 20 µM Trp across different pH environments, while **Fig. 7.A.1 (a)** (Appendix 7.A) quantitatively presents the changes in fluorescence intensity (ΔF) over 14 days of incubation.

As shown in **Fig. 7.A.1 (a)**, the rate and extent of fibril formation are strongly influenced by the pH of the solution. At acidic pH (~ 2), the red curve reveals an initial increase in Th-T fluorescence intensity during the first four days, suggesting some degree of Trp aggregation. However, from day 5 onwards, the intensity decreases, indicating a possible disassembly or structural rearrangement of the aggregates which could lead to an inhibition of further fibrillation process. At neutral pH (~ 7.4), the blue curve shows a steady, monotonic increase in fluorescence intensity, plateauing around day 11, suggesting a slower but sustained aggregation process leading to fibril saturation. In contrast, the green curve at pH 11 depicts an initial lag phase followed by a pronounced exponential increase in fluorescence intensity, with no apparent saturation even at day

14. This trend signifies that a highly basic environment significantly enhances Trp aggregation kinetics, promoting extensive fibril formation over time.

To further corroborate these findings, time-resolved fluorescence measurements of Th-T in 20 mM Trp were performed using a streak camera setup. **Fig. 7.A.1 (b)** (Appendix 7.A) presents the fluorescence decay profiles across pH values of 2, 7.4, and 11. The decay parameters are summarized in **Table 7.B.1** (Appendix 7.B). The average fluorescence lifetime of Th-T (~ 0.9 ps) remains essentially unchanged across all pH conditions in buffer alone. However, in Trp - containing solutions, the average fluorescence lifetime increases progressively with rising pH, indicating that Th-T experiences a more constrained, hydrophobic environment due to enhanced fibrillation at higher pH levels.

To complement the Th-T-based aggregation measurements, intrinsic fluorescence of Trp was also assessed by exciting at 280 nm. The comparison of fluorescence spectra on day 1 versus day 11 of incubation at pH 2, 7.4, and 11 is shown in the lower panel of **Fig. 7.1**. At pH 2, a minimal red shift (~ 5 nm) was observed over 11 days, indicating negligible structural or environmental changes around Trp. At pH 7.4 and 11, however, significant red shifts of ~ 36 nm and ~ 39 nm, respectively, were detected. These shifts suggest progressive self-aggregation of Trp, forming increasingly hydrophobic or larger-sized structures with time. It has been assigned for tyrosine system that red shift of emission maximum indicates the increase of the size of the aggregation.[34] Furthermore, the full width at half maximum (FWHM) values of the emission spectra (see **Table 7.B.2**, Appendix 7.B) support this trend. No substantial change in spectral width was found at pH 2 or 7.4 between day 1 and day 11, implying relatively uniform and restricted conformational states. In contrast, a notable broadening of the emission spectrum at pH 11 by day 11 indicates a heterogeneous and dynamic fibril environment, characteristic of mature aggregates.

Collectively, the steady-state and time-resolved fluorescence results underscore the strong pH dependence of Trp aggregation and subsequent fibrillation. Under acidic conditions, fibril formation is significantly suppressed, whereas at neutral pH, aggregation proceeds gradually over

time. In contrast, alkaline conditions markedly accelerate fibrillation, likely driven by increased deprotonation of COO^- group and enhanced intermolecular hydrogen bonding between Trp molecules, which together promote the stabilization and growth of Trp aggregates.

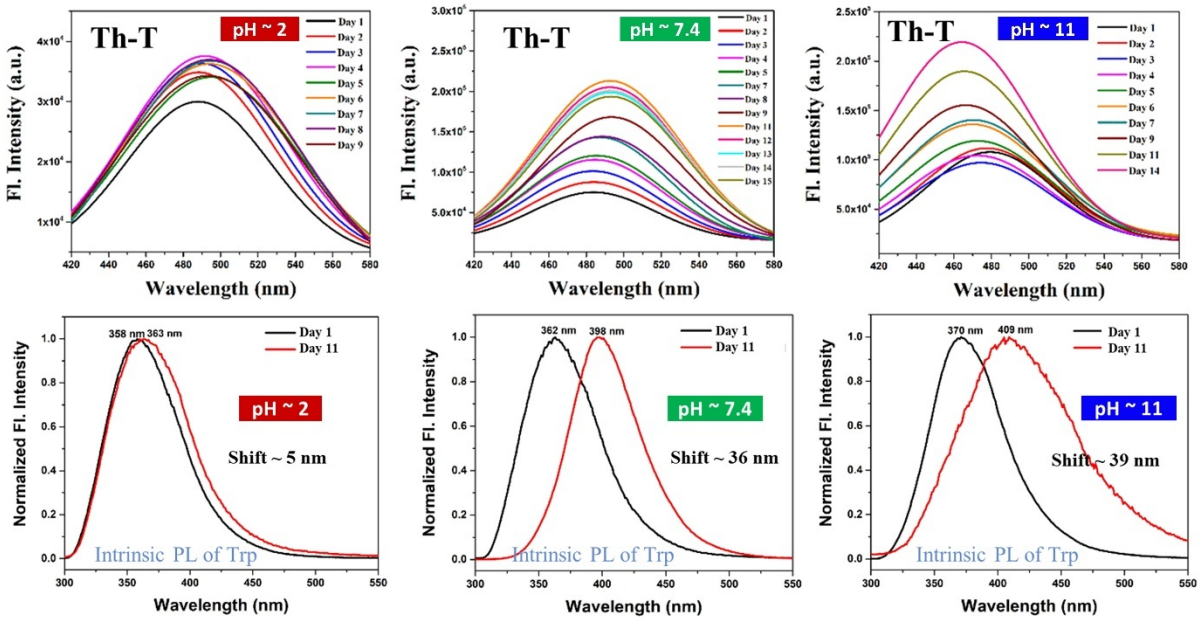

FIG. 7.1. The steady state fluorescence spectra of 20 µM Th-T dissolved in 20 mM Trp solution (upper panel) and the intrinsic fluorescence of Trp (lower panel) recorded in PBS buffer at different pH over the incubation period. All the spectra are color-coded according to incubation time.

7.3.2 Raman Spectroscopic Analysis

The Raman spectral analysis provides valuable insights into the molecular-level transformations associated with the aggregation behavior of Trp under varying pH conditions and incubation times. **Fig. 7.2** highlights the spectral features corresponding to the asymmetric bending mode of the protonated amine group (NH_3^+), centered ~ 2330 cm^{-1}. On day 1, a distinct and sharp peak is consistently observed across all tested pH levels (2, 7.4, and 11), indicative of a relatively homogeneous chemical environment and minimal intermolecular interaction. However, by day 11,

this peak evolves into a well-resolved doublet with components at ~ 2328 and 2329 cm^{-1}. The emergence of this spectral splitting suggests the development of multiple microenvironments, likely arising from enhanced intermolecular interactions and hydrogen bonding as Trp molecules begin to self-assemble into fibrillar structures. This effect is especially pronounced at alkaline pH, supporting the premise that the deprotonation of the carboxyl group facilitates closer molecular packing and aggregation.

Fig. 7.3 further explores the broader vibrational region encompassing N – H symmetric and asymmetric stretching (3200 - 3500 cm^{-1}) as well as O – H stretching (~ 3600 cm^{-1}).[35–37] The left panel of this figure shows a progressive blue shift in the cm^{-1} bands from pH 2 to pH 11, with deconvoluted peak shifts of ~ 32 cm^{-1} and ~ 19 cm^{-1}, respectively. This shift reflects the reduction in hydrogen bonding interactions at higher pH, where the NH_3^+ group transitions to a neutral NH_2 state. At pH 2, extensive hydrogen bonding with water molecules is favored, while at pH 11, the reduced polarity and lower availability of protonated groups limit such interactions, instead promoting intermolecular association and fibril formation. After 11 days of incubation, these effects become more evident. The right panel of **Fig. 7.3** reveals the emergence of a new Raman band near ~ 3600 cm^{-1}, corresponding to free O – H stretching modes. The presence of this band indicates an increasing population of non-hydrogen-bonded water molecules, consistent with Trp molecules increasingly interacting with each other rather than with the solvent, implying another hallmark of fibrillation.

While the Raman spectral evolution does not conclusively identify a single pH condition as most favorable for fibril formation, the results clearly demonstrate that significant changes in molecular interactions and local environments occur over time. These changes reflect a shift from water-mediated solvation toward Trp – Trp associations, especially under conditions that reduce hydrogen bonding with water. Overall, the findings underscore the critical role of both pH and incubation time in modulating the hydrogen bonding network and promoting fibrillation. To further probe the dynamic behavior of water underlying this process, solvent relaxation dynamics and dielectric relaxation dynamics have been studied, as discussed in the following sections.

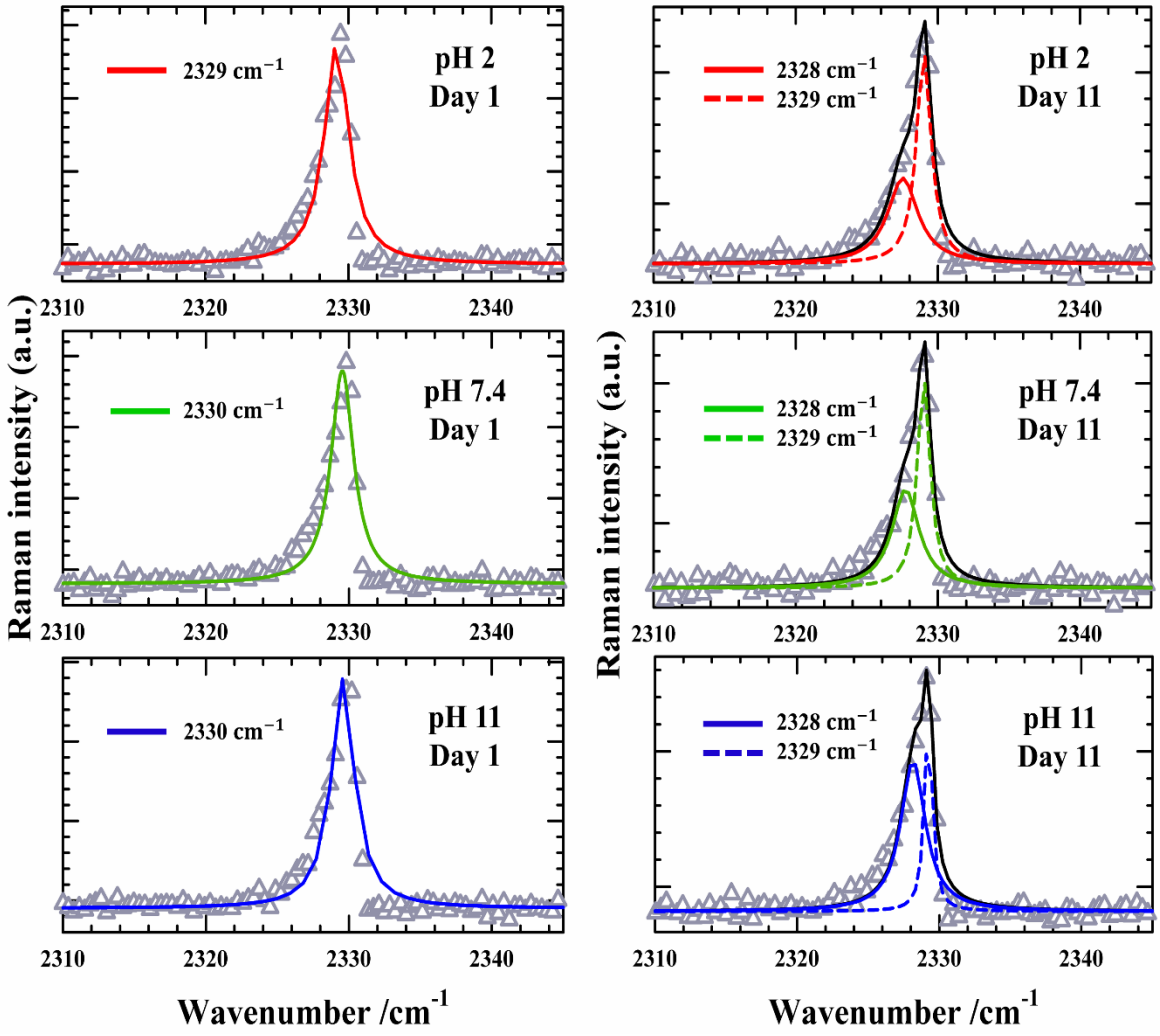

FIG. 7.2. Lorentzian-fitted Raman spectral data and corresponding deconvolutions for 20 mM Trp solutions at three different pH levels, collected on day 1 (left panel) and day 11 (right panel) of incubation. In the right panel, solid black lines indicate the cumulative fits, while dashed and colored solid lines represent the individual deconvoluted spectral bands. All plots are color-coded.

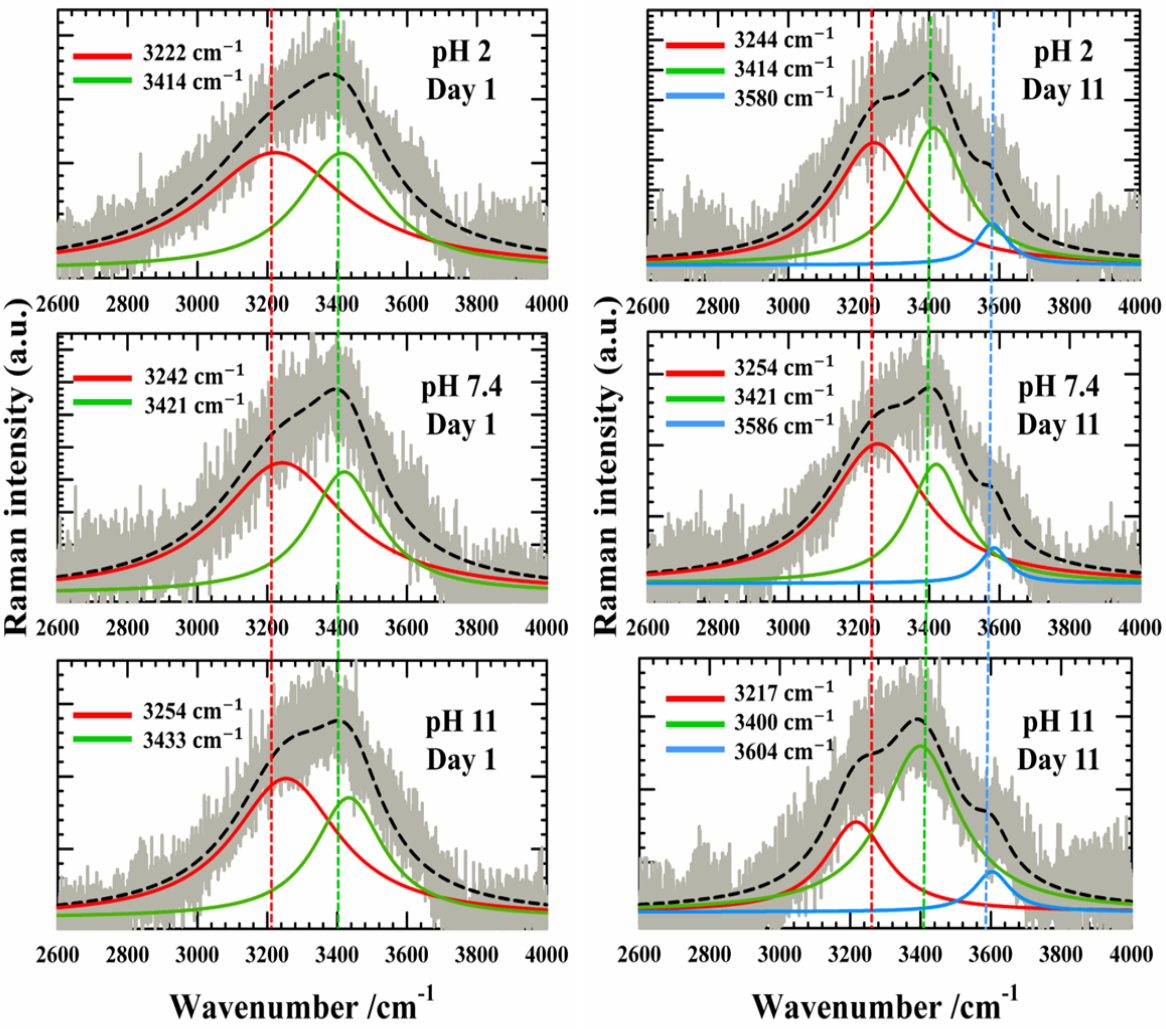

FIG. 7.3. N – H and O – H stretching mode of Trp and water, respectively, recorded from 20 mM Trp solutions at three different pH levels on day 1 (left panel) and day 11 (right panel) of incubation. Dashed black lines represent the cumulative fits, while solid-colored lines correspond to the deconvoluted spectral components. All presentations are color-indicated.

7.3.3 Solvation Dynamics Analysis

Fig. 7.4 illustrates representative three-dimensional streak images obtained from the streak camera detection setup, along with the time-dependent evolution of the steady-state emission spectra of Th-T in 20 μM Trp solutions. Each time-resolved emission spectrum (TRES) extracted from the streak images has been fitted using a log-normal function and displayed in normalized intensity and frequency format. From these TRES, the peak emission frequencies have been used to construct the solvent response function, S(t), depicted in the lower panel of **Fig. 7.4**. The corresponding shifts in emission peak frequencies (see **Fig. 7.A.1 (c)**) and spectral widths (FWHM) have been further shown in **Fig. 7.A.1 (d)** (Appendix 7.A). Analysis of the solvent relaxation dynamics, as summarized in **Table 7.1**, reveals distinct pH-dependent behaviors. At acidic pH (~ 2), the decay of S(t) is best described by a biexponential function, indicating relatively fast solvent reorganization. At physiological pH (~ 7.4), both the fast and slow temporal components exhibit significantly increased, implying slower solvent relaxation. This retardation in dynamics is indicative of the early stages of fibril formation, which alters the microenvironment and restricts solvent motion. Notably, at alkaline pH (~ 11), a new, prominent long-time decay component (~ 111 ps) emerges, suggesting substantial alteration in the local solvent dynamics due to extensive fibril formation.

These observations underscore the critical role of pH in modulating the collective solvent relaxation behavior in Trp solutions containing Th-T. At higher pH, enhanced fibril formation likely arises from increased Trp– Trp hydrogen-bonded interactions, which immobilize solvent molecules in the vicinity and lead to an overall slowing down of solvent dynamics. The solvation response in the presence of Th-T is predominantly governed by a slower component (a_2 ~ 60%) with characteristic timescales ranging from ~ 50 - 100 ps. This prolonged relaxation aligns well with the presence of a more viscous, fibril-rich microenvironment at elevated pH of the medium. Furthermore, these findings highlight the sensitivity of Th-T as a molecular probe for monitoring changes in local hydrogen-bonding environments during Trp aggregation. The increased micro-viscosity associated with fibril formation not only enhances fluorescence lifetimes but also prolongs solvation time constants, reinforcing the use of solvation dynamics as a reliable indicator of aggregation and microstructural reorganization in such systems.

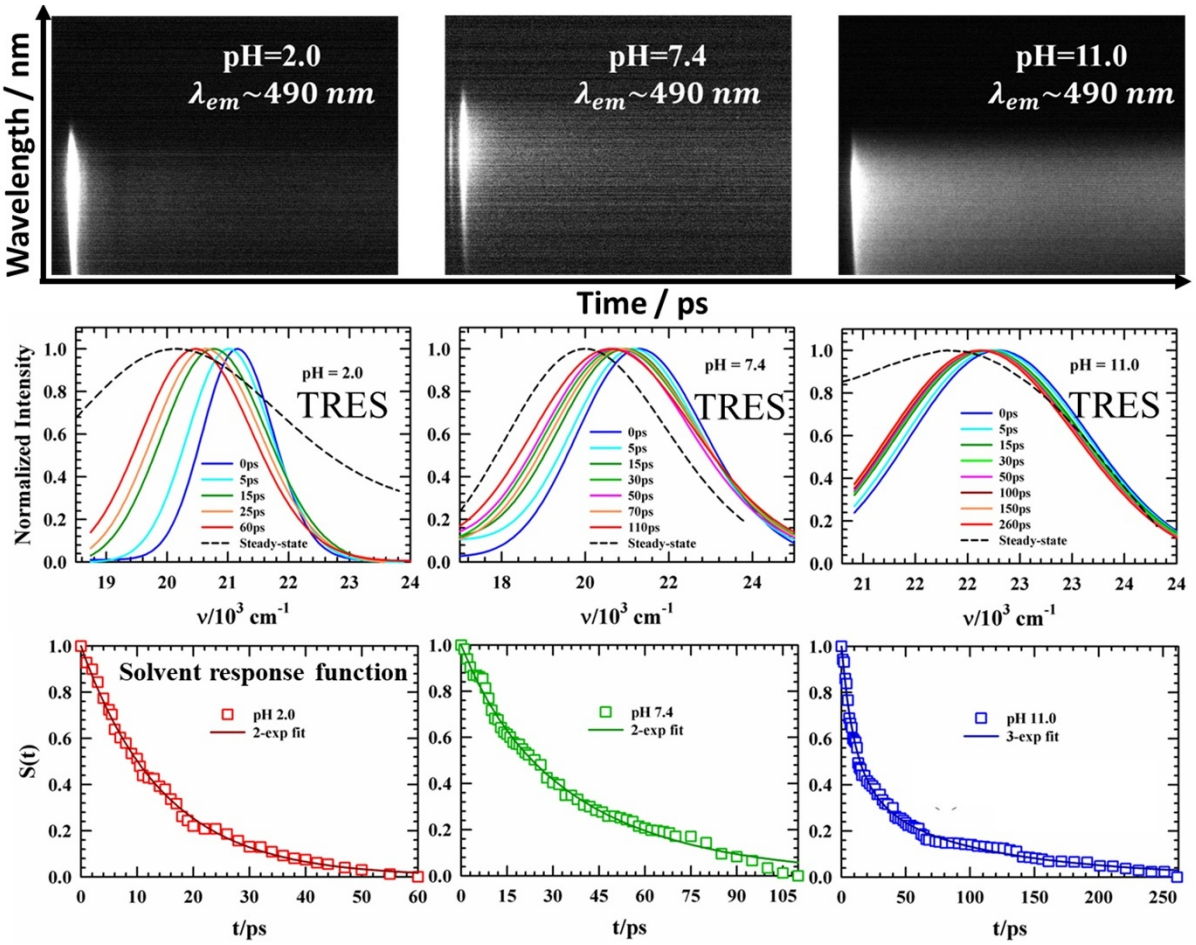

FIG. 7.4. Three-dimensional streak images (upper panel), constructed TRES (middle panel) and solvent relaxation decay profiles (lower panel) of Th-T dissolved in 20 mM Trp solution at three different pH of the medium on day 11 of incubation. All the presentations are color-coded.

Table 7.1. Fit parameters for the S(t) decays for Th-T in 20 mM Trp solution at three different pH of the medium at ~ 300 K.

pH	a_1	τ_1/ps	a_2	τ_2/ps	a_3	τ_3/ps	$\langle\tau_S\rangle$/ps	$\Delta\nu^t_{obs}/cm^{-1}$
2.0	0.98	14.39	0.02	32.15	-	-	14.74	657
7.4	0.18	13.14	0.82	41.49	-	-	36.39	672.6
11.0	0.40	8.20	0.28	23.92	0.32	111.11	45.53	171.3

7.3.4 Dielectric Relaxation Dynamics

Representative real (ε') and imaginary components (ε'') of complex dielectric spectra collected in Trp solutions with varying pH levels at day 1 and day 11 of incubation period are presented in **Fig. 7.5**. Solid lines through the ε' and ε'' experimental data points, in **Fig. 7.5**, displayed multi-Debye fits and the corresponding fit parameters are summarized in **Table 7.2**.

The DRS data presented in **Table 7.2** reveal important insights into the pH-dependent fibrillation behavior of Trp over time. The relaxation spectra have been analyzed using a multi-Debye model, which resolves two distinct relaxation components: a slow relaxation process ($\tau_1 \sim 50$ ps) with a small amplitude (~ 2 - 3%) and a faster component ($\tau_2 \sim 8$ ps, associated with 'bulk' water dynamics[38]) with a dominant amplitude (~ 97 - 98%). The slower relaxation time (τ_1), typically associated with interfacial water or, 'slow' water molecules, shows a marked increase with rising pH and incubation time. On day 1, τ_1 is lowest at pH 2 (~ 41 ps) and increases to ~ 57 ps at pH 11, respectively. By day 11, τ_1 further increases across all pH levels, reaching ~ 49 ps at pH 2 and peaking at ~ 65 ps at pH 11, indicating a progressive restriction in dipolar mobility likely caused by growing fibrillar networks.

This trend in τ_1 signifies that higher pH environments and longer incubation times promote greater molecular ordering and self-assembly of Trp. Notably, the dielectric strength ($\Delta\varepsilon$) and the average relaxation time $\langle\tau_{DR}\rangle$ remain largely unchanged, suggesting that while the number of relaxing dipoles remains constant, their dynamics are increasingly hindered as fibrillation proceeds. Overall, these findings align well with the known role of ionization states of Trp functional groups: deprotonated carboxylate groups at higher pH promote aggregated fibril structures, while protonated amino and carboxylic groups at low pH inhibit it. The DRS results thus offer strong evidence that Trp fibril formation is significantly influenced by both the pH of the medium and the duration of incubation, with neutral to basic conditions favoring more extensive fibrillation.

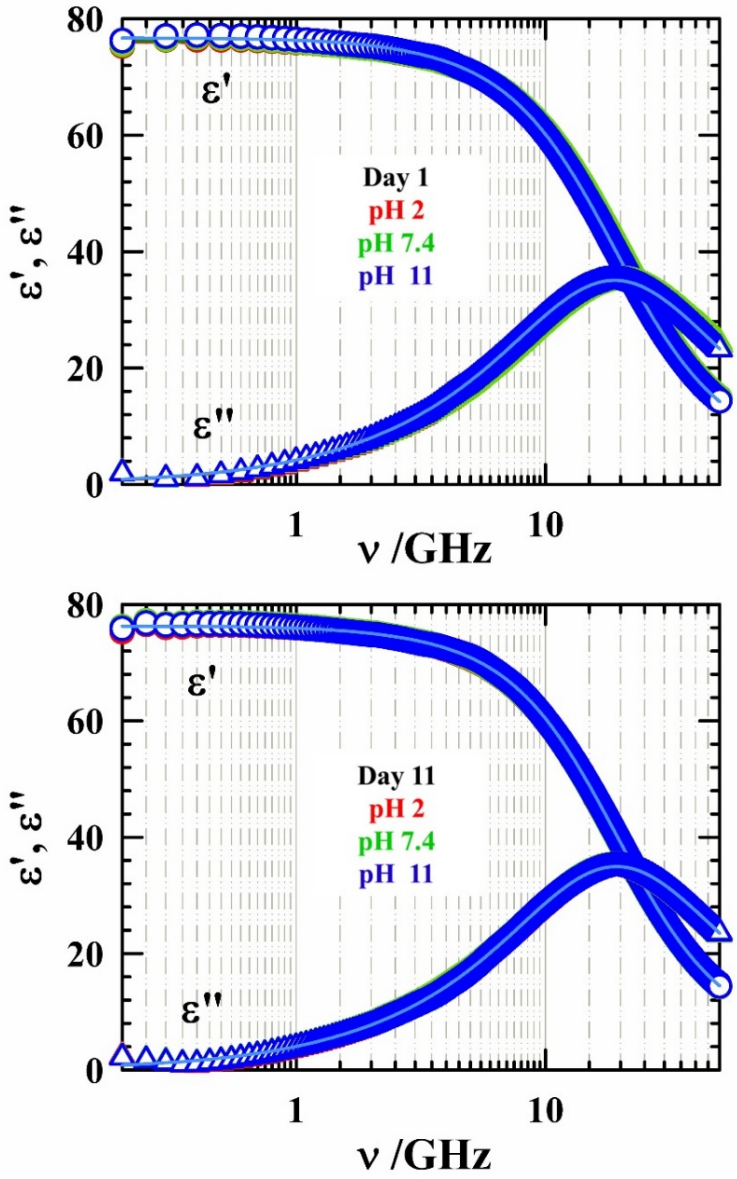

FIG. 7.5. The real (ε′) and imaginary (ε′′) components of the complex dielectric spectra recorded in 20 mM Trp solutions at three different pH levels, collected at day 1 (upper panel) and day 11 (lower panel) of incubation. Experimental data points are shown as symbols while solid lines passing through them represent multi-Debye fits. All representations are color-coded.

Table 7.2. Multi-Debye fit parameters of experimentally measured DR spectra for 20 mM Trp solutions at three different pH levels on day 1 and day 11 of incubation. The values in the parenthesis represents the percentage of amplitudes.

pH	ε_S	$\Delta\varepsilon_1$	τ_1/ps	$\Delta\varepsilon_2$	τ_2/ps	ε_∞	$<\tau_{DR}>$/ps
Day 1							
2	76	1.54 (2%)	41	69.42 (98%)	8	5.0	9
7.4	77	1.79 (3%)	63	69.43 (97%)	8	5.4	9
11	77	1.70 (2%)	57	69.62 (98%)	8	5.4	9
Day 11							
2	76	1.48 (2%)	49	69.28 (98%)	8	5.4	9
7.4	76	1.50 (2%)	66	69.83 (98%)	8	5.0	9
11	76	1.33 (2%)	65	69.56 (98%)	8	5.4	9

7.3.5 Morphology of Tryptophan Aggregates: FESEM Study

To investigate the morphological characteristics of Trp fibril assemblies under different pH conditions, FESEM was employed. Representative micrographs of Trp assemblies at three distinct pH levels throughout the incubation periods have been presented in **Fig. 6.6**. The images reveal striking differences in fibril morphology across the pH range, highlighting the pH-sensitive nature of the self-assembly process. At lower pH (~ 2), the fibrils appear relatively sparse and less branched, whereas at higher pH (~ 11) levels, the assemblies exhibit a notable increase in both fibril density and branching. This trend suggests that alkaline environments promote more extensive and interconnected fibrillar networks. The enhanced fibril formation under basic conditions is likely attributed to the deprotonation of functional groups within Trp molecules.[39]

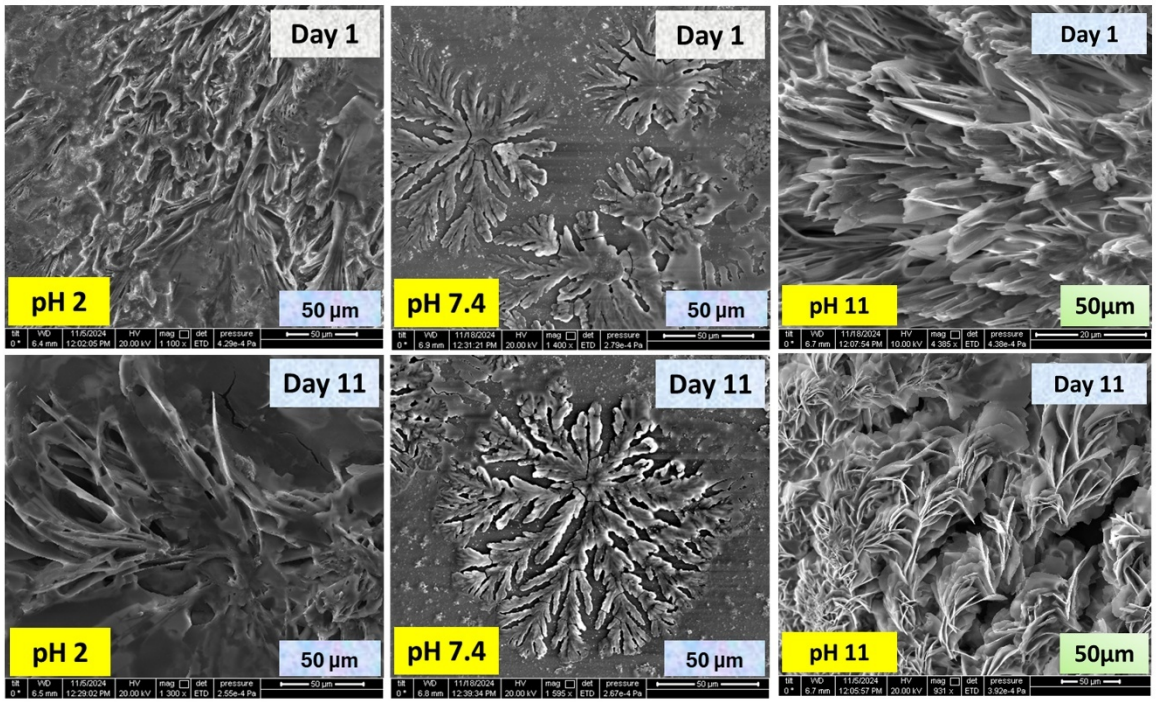

FIG. 7.6. FESEM micrographs of the fibrillary assembly of 20 mM Trp solutions in PBS buffer at different pH on day 11 of incubation.

From a chemical perspective, the fibrillation behavior of Trp can be rationalized by considering the ionization states of its functional groups. The carboxylic acid group, with a lower pKa, becomes deprotonated at elevated pH, while the primary amine group remains protonated at lower pH. The presence of deprotonated carboxylate anions appears to facilitate intermolecular interactions conducive to fibril growth. In contrast, the protonated ammonium form of the amine group may introduce electrostatic repulsion or, steric hindrance, thereby inhibiting fibril assembly under acidic conditions. These findings lead to an important mechanistic insight: the carboxylate functionality plays a key role in initiating or, stabilizing fibril formation. Therefore, under physiological pH, selective modification or, blocking of the carboxylic acid group might serve as a strategic approach to modulate or, slow down the fibrillation process. This hypothesis opens new avenues for therapeutic interventions aimed at controlling unwanted peptide or, amino acid aggregation.

7.4 Summary

In summary, this study provides comprehensive insights into the pH-dependent fibrillation behavior of Tryptophan (Trp), leveraging both steady-state and time-resolved fluorescence spectroscopy, alongside morphological and vibrational analyses. Our findings demonstrate that the charge state of Trp, modulated by the ionization of its carboxylic and amine groups, critically governs its aggregation propensity. Acidic conditions hinder fibril formation due to electrostatic repulsion between positively charged species, while basic conditions favor self-assembly through enhanced hydrogen bonding and decreased electrostatic barriers. The use of amyloid-specific dye Th-T allowed sensitive detection of aggregation kinetics, further supported by intrinsic fluorescence shifts and spectral broadening. The emergence of long solvation times and increased fluorescence lifetimes at higher pH (~ 11) levels strongly correlates with the formation of ordered, hydrogen-bonded fibrillar aggregates. These results not only unravel the molecular basis of Trp fibrillation but also offer mechanistic insight relevant to amyloid research, potentially aiding in the development of fibrillation control strategies without relying on external inhibitors. Ultimately, the pH-tunable nature of Trp fibrillation underscores the broader implication of electrostatic and hydrogen bonding interactions in amyloidogenic pathways.

The findings of this study hold significant implications for biomedical research, particularly in understanding the molecular mechanisms underlying amyloid-related disorders. By elucidating how pH modulates the self-assembly and fibrillation behavior of tryptophan, a key aromatic amino acid often involved in protein misfolding, this work contributes valuable insight into the physicochemical conditions that promote or hinder amyloid formation. Such knowledge can aid in designing pH-based strategies to control or mitigate pathological aggregation processes, offering a non-invasive alternative to chemical inhibitors. Moreover, the methodology and principles outlined here can be extended to study other aggregation-prone biomolecules, potentially supporting the development of diagnostic tools or therapeutic interventions for neurodegenerative diseases such as Alzheimer's and Parkinson's.

Appendix 7.A

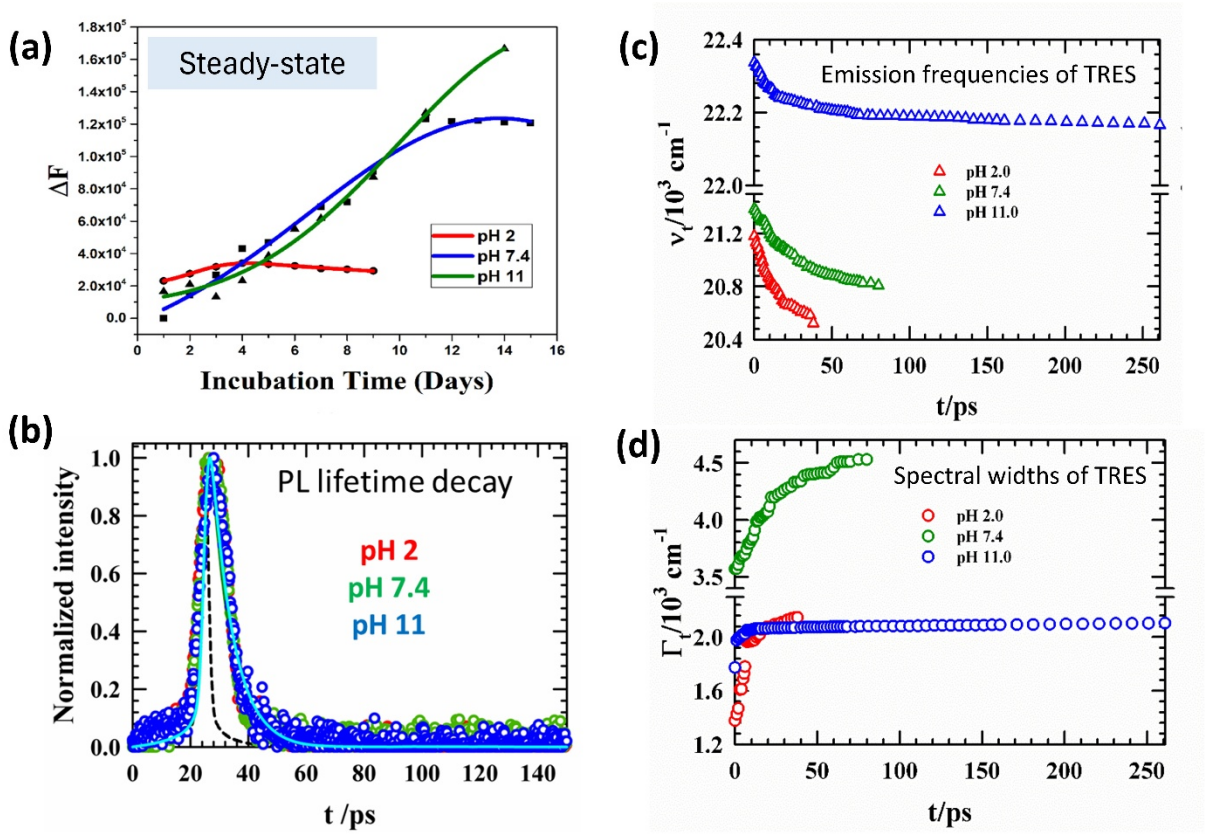

FIG. 7.A.1. (a) Variation in steady-state fluorescence peak intensity and (b) fluorescence lifetime emission decays of Th-T dissolved in 20 mM Trp solutions prepared in PBS buffer at different pH over the incubation period. In panel (b), the black dashed line represents the instrument response function (IRF), while the solid lines through the data points indicate the fits. Emission frequencies (c) and spectral widths (d) of each TRES of Th-T dissolved in Trp solutions at various pH under study. Each pH of the medium in each panel is color-coded.

Appendix 7.B

Table 7.B.1. Fit parameters for the fluorescence lifetime decay of Th-T in 20 mM Trp solution at three different pH of the medium at ~ 300 K.

pH	λ_{exc}/nm	a_1	τ_1/ps	a_2	τ_2/ps	a_3	τ_3/ps	$<\tau_{life}>$/ps
2	490	0.99	0.9	-	-	0.01	50	1.39
7.4	490	0.87	0.9	0.09	17.27	0.04	40	3.94
11	490	0.85	0.9	0.05	11.17	0.10	57.52	7.08

Table 7.B.2. The full width half maximum (FWHM) of the intrinsic fluorescence emission spectra of Trp solutions at pH 2, 7.4 and 11 at day 1 and day 11 of incubation.

System	Spectral width (FWHM /nm)	
	Day 1	Day 11
Trp /pH 2	68.56	74.38
Trp /pH 7.4	69.06	63.61
Trp /pH 11	67.06	103.91

References

[1] A.H.S. Martinelli, F.C. Lopes, E.B.O. John, C.R. Carlini, and R. Ligabue-Braun, *Int J Mol Sci* **20**(6), 1322 (2019).

[2] S. Basha, D.C. Mukunda, J. Rodrigues, M. Gail D'Souza, G. Gangadharan, A.R. Pai, and K.K. Mahato, *Ageing Res Rev* **90**, 102017 (2023).

[3] P. Sweeney, H. Park, M. Baumann, J. Dunlop, J. Frydman, R. Kopito, A. McCampbell, G. Leblanc, A. Venkateswaran, A. Nurmi, and R. Hodgson, *Transl Neurodegener* **6**(1), 6 (2017).

[4] Y.E. Choonara, V. Pillay, L.C. Du Toit, G. Modi, D. Naidoo, V.M.K. Ndesendo, and S.R. Sibambo, *Int J Mol Sci* **10**(6), 2510–2557 (2009).

[5] A. Francioso, P. Punzi, A. Boffi, C. Lori, S. Martire, C. Giordano, M. D'Erme, and L. Mosca, *Bioorg Med Chem* **23**(8), 1671–1683 (2015).

[6] Z.L. Almeida, and R.M.M. Brito, *Molecules* **25**(5), 1195 (2020).

[7] T. Sinnige, *Chem Sci* **13**(24), 7080–7097 (2022).

[8] M. Zhang, J. Zhao, and J. Zheng, *Soft Matter* **10**(38), 7425–7451 (2014).

[9] P.C. Ke, R. Zhou, L.C. Serpell, R. Riek, T.P.J. Knowles, H.A. Lashuel, E. Gazit, I.W. Hamley, T.P. Davis, M. Fändrich, D.E. Otzen, M.R. Chapman, C.M. Dobson, D.S. Eisenberg, and R. Mezzenga, *Chem Soc Rev* **49**(15), 5473–5509 (2020).

[10] P. Ferreira, I. Shin, I. Sosova, K. Dornevil, S. Jain, D. Dewey, F. Liu, and A. Liu, *Mol Genet Metab* **120**(4), 317–324 (2017).

[11] P.F. Borrie, and C.A. Lewis, *Proc R Soc Med* **55**(3), 231–232 (1962).

[12] G. Soldi, G. Plakoutsi, N. Taddei, and F. Chiti, *J Med Chem* **49**(20), 6057–6064 (2006).

[13] H.-Z. Mou, C.-L. Zhao, J. Song, L. Xing, H.-Y. Chen, and J.-J. Xu, *ACS Omega* **8**(28), 24999–25008 (2023).

[14] M.E. DeSantis, E.H. Leung, E.A. Sweeny, M.E. Jackrel, M. Cushman-Nick, A. Neuhaus-Follini, S. Vashist, M.A. Sochor, M.N. Knight, and J. Shorter, *Cell* **151**(4), 778–793 (2012).

[15] D. Zaguri, T. Kreiser, S. Shaham-Niv, and E. Gazit, *Molecules* **23**(6), 1273 (2018).

[16] M.K. Siddiqi, N. Majid, P. Alam, S. Malik, A. Alam, S. Rajan, M.R. Ajmal, and R.H. Khan, Int *J Biol Macromol* **143**, 102–111 (2020).

[17] A.L. Pey, M. Ying, N. Cremades, A. Velazquez-Campoy, T. Scherer, B. Thöny, J. Sancho, and A. Martinez, *Journal of Clinical Investigation* **118**(8), 2858–2867 (2008).

[18] K. Debnath, A.K. Sarkar, N.R. Jana, and N.R. Jana, *Acc Mater Res* **3**(1), 54–66 (2022).

[19] K. Tsemekhman, L. Goldschmidt, D. Eisenberg, and D. Baker, *Protein Science* **16**(4), 761–764 (2007).

[20] N. Aggarwal, D. Eliaz, H. Cohen, I. Rosenhek-Goldian, S.R. Cohen, A. Kozell, T.O. Mason, and U. Shimanovich, *Commun Chem* **4**(1), 62 (2021).

[21] D. Willbold, B. Strodel, G.F. Schröder, W. Hoyer, and H. Heise, *Chem Rev* **121**(13), 8285–8307 (2021).

[22] S. Chimon, M.A. Shaibat, C.R. Jones, D.C. Calero, B. Aizezi, and Y. Ishii, *Nat Struct Mol Biol* **14**(12), 1157–1164 (2007).

[23] B.S. Vig, K.M. Huttunen, K. Laine, and J. Rautio, *Adv Drug Deliv Rev* **65**(10), 1370–1385 (2013).

[24] J. Parascandola, *Medizinhist J* **6**, 297–309 (1971).

[25] E. Žerovnik, M. Škarabot, K. Škerget, S. Giannini, E. Žerovnik, M. Škarabot, K. Škerget, S. Giannini, V. Stoka, S. Jenko-Kokalj, and R.A. Staniforth, *Amyloid* **14**(3), 237–247 (2007).

[26] Y. Tian, and J.H. Viles, *Angewandte Chemie* **134**(48), (2022).

[27] H. Yang, X. Xiao, X. Zhao, and Y. Wu, edited by Y. Lv, J. Le, H. Chen, J. Wang, and J. Shao, (2017), p. 102554M.

[28] A. Ghisaidoobe, and S. Chung, *Int J Mol Sci* **15**(12), 22518–22538 (2014).

[29] H. Naiki, K. Higuchi, M. Hosokawa, and T. Takeda, *Anal Biochem* **177**(2), 244–249 (1989).

[30] H. Levine, *Protein Science* **2**(3), 404–410 (1993).

[31] H. LeVine, (1999), pp. 274–284.

[32] Y. Yoshiike, D.-H. Chui, T. Akagi, N. Tanaka, and A. Takashima, *Journal of Biological Chemistry* **278**(26), 23648–23655 (2003).

[33] V.I. Stsiapura, A.A. Maskevich, V.A. Kuzmitsky, K.K. Turoverov, and I.M. Kuznetsova, *J Phys Chem A* **111**(22), 4829–4835 (2007).

[34] A. Singh, S. Khatun, and A. Nath Gupta, *ChemPhysChem* **21**(23), 2585–2598 (2020).

[35] C. Chuang, and Y. Chen, *Journal of Raman Spectroscopy* **40**(2), 150–156 (2009).

[36] Q. Sun, *Vib Spectrosc* **51**(2), 213–217 (2009).

[37] F. Rull, *Pure and Applied Chemistry* **74**(10), 1859–1870 (2002).

[38] U. Kaatze, *Subsurface Sensing Technologies and Applications* **1**(4), 377–391 (2000).

[39] V. Singh, R.K. Rai, A. Arora, N. Sinha, and A.K. Thakur, *Sci Rep* **4**(1), 3875 (2014).

Chapter 8

Conclusion and Future Directions

8.1 Concluding Remarks

This doctoral research has centered on unraveling the interactions and dynamics within complex liquid systems using a variety of advanced spectroscopic techniques. The systems investigated, ranging from neat solvents to binary/ternary mixtures of liquid electrolytes, gel polymer electrolytes, aqueous copolymer solutions, and biologically relevant media that are inherently heterogeneous, both structurally and dynamically. Given the intrinsic complexity and spatio-temporal heterogeneity in these systems, the focus has been on elucidating qualitative yet molecular-level insights into various physicochemical phenomena in the solution phase. Our study on ion - solvent interactions and solvation dynamics in electrolyte solutions highlights how ion pairing and ultrafast medium responses influence ionic transport, offering insights relevant to battery electrolyte performance. Furthermore, in polymer and biomolecular systems, we have explored phase transitions and conformational changes to understand mechanisms underlying gelation and protein aggregation, with implications for materials and biomedical applications. Overall, this thesis contributes valuable insights into the microscopic dynamics, structural heterogeneity, and functional behavior of multicomponent soft matter systems, with implications for electrolyte design, biopolymer engineering, and disease-related protein aggregation.

As specific conclusions have been provided at the end of each chapter in this thesis, a separate general conclusion is omitted. Instead, this section outlines a few intriguing and relevant problems that warrant further investigation in the near future.

8.2 Future Scope of Study

8.2.1 Influence of Chain Polarity on Polymer Dynamics and Ion Transport in Gel Polymer Electrolytes for Li-Ion Batteries

Building on our current study involving a ternary gel polymer electrolyte ($PC/LiClO_4/PPG$), where we have systematically analyzed salt, solvent and salt - polymer interactions, a compelling future direction would be to investigate the influence of polymer polarity on the dynamics and ion transport behavior in gel polymer electrolytes (GPEs). The polarity, dielectric constant, and segmental mobility of the polymer matrix, governed by the chemical nature of its monomeric units, are expected to play a pivotal role in mediating ion dynamics. Polymers such as poly(ethylene oxide) (PEO), poly(propylene oxide) (PPO), poly(acrylonitrile) (PAN), poly(methyl methacrylate) (PMMA), poly(vinyl chloride) (PVC), poly(vinylidene fluoride) (PVdF), represent a diverse set of hosts with varying polarities and glass transition behaviors.[1] A systematic investigation correlating polymer polarity with segmental dynamics and ionic conductivity would provide fundamental insights into the mechanisms driving ion transport in GPEs. Dielectric relaxation spectroscopy, coupled with molecular dynamics simulations, could enable a molecular-level understanding of how the polymer environment governs medium relaxation processes and conductivity pathways. Such a study would not only advance the design principles of high-performance polymer electrolytes but also uncover fundamental correlations between polymer characteristics and ion transport behavior, which are critical for next-generation electrochemical energy storage systems.

8.2.2 Role of Ionic Liquid in Modulating Solution Structure and Dynamics in Environment Compatible Aqueous Zinc-Metal Battery Electrolytes

In the light of rising energy demands and environmental concerns, non-polluting metal batteries, particularly those with higher energy densities, longer cycle lives, and improved safety, are the focus of intensive research. Zinc metal batteries (ZMBs), while promising, still suffer from intrinsic challenges such as dendrite growth and SEI layer instability.[2] Ionic liquids (ILs), known as “greener

solvents," (e.g. EmimFSI, $Pry_{14}FSI$, BMITFSI, $TMAmHSO_4$) offer high electrochemical stability, broad electrochemical windows, and excellent solubility for a range of salts, making them attractive additives to aqueous zinc electrolytes.[3] Incorporating ILs may mitigate interfacial issues and enhance electrochemical performance.[4] However, the molecular-level interactions between ILs and zinc salts (e.g. $ZnSO_4$, $Zn(TFSI)_2$) remain poorly understood, representing a critical area for future investigation to unlock their full potential in zinc-based energy storage systems. Future studies could employ broadband dielectric spectroscopy and Raman analysis to resolve the frequency and time scales of ion and solvent motion, providing insight into coupling between ionic conductivity and structural relaxation in presence of IL.

8.2.3 Bio-Inspired Electrolytes: Unveiling Amino Acid Dynamics for Advanced Metal Battery Performance

In our broader research framework, we have independently investigated electrolyte dynamics and the self-aggregation behavior of tryptophan in aqueous media. Recent studies have highlighted the potential of amino acids as multifunctional additives to improve the performance of lithium, sodium, and zinc metal batteries.[5–7] Amino acids, as the fundamental building blocks of proteins, offer tunable chemical functionalities and amphiphilic properties that can influence solvation structure, interfacial stability, and ion transport. Unlike conventional synthetic polymers, amino acids and protein-based systems possess inherent structural diversity and dynamic flexibility, which are advantageous for tailoring electrolyte environments. For instance, L-glutamic acid, L-leucine, and L-arginine exhibit distinct polarities and side-chain functionalities, enabling interactions with both cations and solvents that can modulate ion mobility and suppress parasitic reactions such as dendrite formation or, SEI degradation. A focused investigation into the molecular-level dynamics of selected amino acids in battery electrolyte environments, through dielectric relaxation spectroscopy, NMR, Raman and MD simulations, could provide critical insights into their role in enhancing interfacial resilience, ion transport mechanisms, and overall battery performance. This line of research could pave the way for a biologically inspired strategy in electrolyte design, leveraging the unique physicochemical properties of amino acids to engineer next-generation metal batteries.

8.2.4 Probing Confined Water Dynamics in Hydrogel Electrolytes

Understanding the altered dynamics of water confined within aqueous gel electrolytes presents a compelling area of study from a physical chemistry perspective.[8] Unlike bulk water, confined water exhibits restricted mobility and unique relaxation behavior that directly influence ion transport and thermal stability and mechanical stability. A focused study using techniques like dielectric spectroscopy, small-angle neutron scattering, and fluorescence spectroscopic measurements can reveal how hydration dynamics couple with the electrolyte solvent and ionic environment. Investigating such interactions is key to uncovering dynamic heterogeneities and relaxation processes that govern electrolyte functionality under varying thermal and mechanical conditions. This direction offers a scientifically rich pathway toward designing gel electrolytes with tunable transport properties and enhanced performance across broad operating temperatures.

References

[1] A. Manuel Stephan, *European Polymer Journal* **42**(1), 21–42 (2006).

[2] T. Zhang, Y. Tang, S. Guo, X. Cao, A. Pan, G. Fang, J. Zhou, and S. Liang, *Energy Environ. Sci.* **13**(12), 4625–4665 (2020).

[3] M.I. Ahmad, D. Bahtiyar, H.W. Khan, M.U.H. Shah, L. Kiran, M.K. Aydinol, M. Yusuf, H. Kamyab, and S. Rezania, *Journal of Energy Storage* **72**, 108765 (2023).

[4] M. Zhong, Y. Wang, Y. Xie, S. Yuan, K. Ding, E.J. Begin, Y. Zhang, J.L. Bao, and Y. Wang, *Adv. Funct. Mat.* **34**(33), (2024).

[5] G. Ni, Z. Pan, G. Zou, F. Cao, L. Qin, P. Cui, and C. Zhou, *J. Mater. Chem. A* **12**(11), 6610–6622 (2024).

[6] J. Zhong, L. Ren, C. Ying, Y. Guo, J. Liu, and W.-H. Zhong, *Journal of Energy Storage* **109**, 115251 (2025).

[7] J. Wang, H. Liang, L. Zhou, X. Yu, J. Li, Z. Yang, and X. Liu, *Chemical Engineering Science* **309**, 121493 (2025).

[8] D. Ji, and J. Kim, *Nano-Micro Lett.* **16**(1), (2024).

Addendum I

Ion Conductivity and Dielectric Relaxation Behavior in Dual-Ion Hybrid Water-in-Salt Electrolytes (HWiSE)

Ad.1.1 Introduction

Hybrid water-in-salt electrolytes (HWiSEs) represent a compelling class of next-generation electrolytes for high-voltage aqueous energy storage, combining intrinsic safety, low cost, and broadened electrochemical stability.[1–3] Unlike conventional electrolytes, which typically operate at dilute concentrations (~ 2 $\mathrm{mol.\,kg^{-1}}$), HWiSEs fall under the broader category of "solvent-in-salt" systems, characterized by a salt-to-solvent weight or volume ratio exceeding unity. This shift in composition fundamentally transforms the solvation structure and ion-solvent interactions. The introduction of a polar organic cosolvent, such as acetonitrile (ACN), into these concentrated aqueous environments gives rise to acetonitrile/water-in-salt electrolytes (AWiSEs), which further suppress water activity, expand the electrochemical stability window, and facilitate more efficient ion transport.[4] The incorporation of dual salts, LiTFSI and $\mathrm{Zn(OTf)_2}$, introduces a mixed cationic system that supports simultaneous lithium and zinc ion transport, making AWiSEs highly attractive for hybrid dual-ion battery technologies.[5–8] To fully exploit the potential of such complex electrolyte matrices, a detailed understanding of their molecular-level relaxation processes is essential. DRS and Raman measurements together offer powerful, complementary insights into the microscopic dynamics of dipolar reorientation, solvation shell restructuring, and the extent of ion pairing or, aggregation, providing a fundamental basis for the rational design of high-performance multi-ion aqueous electrolytes.

Ad.1.2 Experimental Sections

Ad.1.2.1 Materials

Acetonitrile (CH_3CN, ≥99.9%), deionized water, bis(trifluoromethane)sulfonimide lithium salt (LiTFSI, ≥99%) and zinc trifluoromethanesulfonate ($Zn(OTf)_2$, ≥98%) were purchased from Sigma-Aldrich and used without further purification. LiTFSI and $Zn(OTf)_2$ were vacuum dried prior to experiment. The chemical structures of the materials are shown in **Scheme Ad.1.1**.

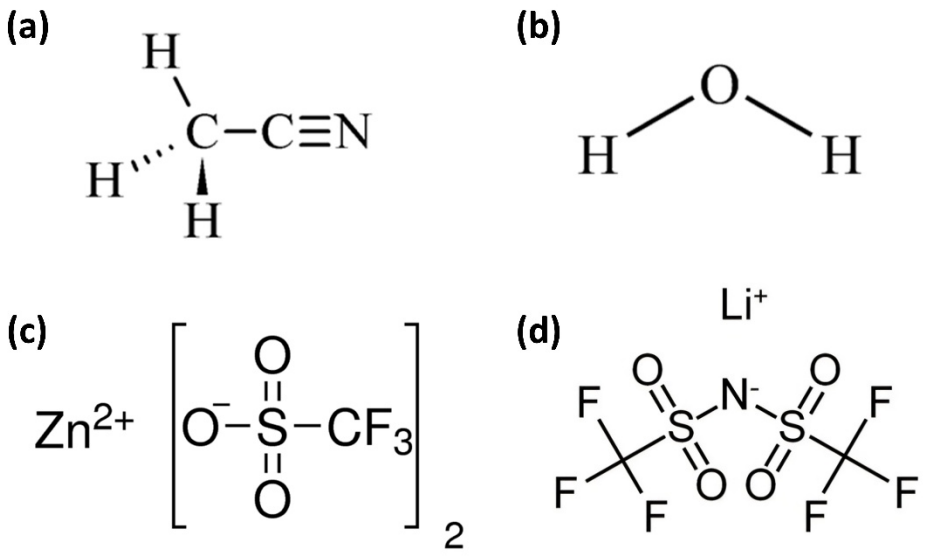

Scheme Ad.1.1. Chemical structure of (a) acetonitrile, (b) water, (c) $Zn(OTf)_2$, and (d) LiTFSI.

Ad.1.2.2 Electrolyte Preparation

Requisite amounts of LiTFSI and $Zn(OTf)_2$ were dissolved in deionized water to prepare the aqueous electrolyte solutions forming WiSE [21 m LiTFSI + 3 m $Zn(OTf)_2$] and the mixture heated at ~ 330 K under continuous stirring (here, "m" is molality, standing for mol of salt per kg of solvent). For example, to prepare 4 gm WiSE, LiTFSI (0.01035 mol, 2.97 gm) was mixed with

$Zn(OTf)_2$ (0.00148 mol, 0.5372 gm) at 300 K and then water was added accordingly (0.02738 mol, 0.4928 gm). The transparent solutions of WiSE thus prepared were allowed to cool down gradually to room temperature. Next, WiSE solution was diluted by stoichiometric amount of ACN. **Table Ad. 1.1** represents the ratio of added chemical components to prepare the final hybrid AWiSE solutions. In this table, the notation $H_2O/ACN\ /1$ indicates 21 m LiTFSI and 3 m $Zn(OTf)_2$ are dissolved in ACN/water mixture with a 10/90 wt% ratio and other entries follow the same convention. Sample preparation, preservation and subsequent experiments were performed in a tightly humidity-controlled environment to prevent moisture contamination.

Table Ad. 1.1 Chemical compositions of WiSE and AWiSE solutions studied in this work.

Total amount of solution: 4 gm				
Electrolyte	LiTFSI /gm	$Zn(OTf)_2$ /gm	H_2O /gm	ACN /gm
WiSE	2.97	0.5372	0.4928	0
$H_2O/ACN\ /1$	2.97	0.5372	0.4434	0.0494
$H_2O/ACN\ /2$	2.97	0.5372	0.3941	0.0987
$H_2O/ACN\ /3$	2.97	0.5372	0.3448	0.1480
$H_2O/ACN\ /4$	2.97	0.5372	0.2956	0.1972
$H_2O/ACN\ /5$	2.97	0.5372	0.2464	0.2464

Ad.1.2.3 Ion Conductivity, Refractive Index, Raman and DR Measurements

Ion conductivity (σ) of all the electrolyte samples have been measured by a bench-top multi-parameter electrochemical meter (SESHIN BIOTECH, Model: $ECM-610$). Refractive indices (n) of the samples have been recorded by using an automated temperature-controlled refractometer ($RUDOLPH, J357$). Experimentally measured values of σ and n are provided in **Table Ad. 1.2**.

Raman spectra of our studied electrolyte solutions were collected by employing a micro-Raman spectrometer (LabRAM HR Evolution, Horiba France SAS) using a 532 nm laser excitation source. DR measurements in the frequency range from 200 MHz to 50 GHz were covered at ~ 300 K by using the $PNA-L$ network analyzer ($N5235B$) integrated with an open-ended coaxial probe kit ($N1501A$).

Table Ad. 1.2 Ion conductivity and refractive index measured in WiSE and AWiSE solutions at ~ 300 K.

Electrolyte	Ion conductivity (σ /mS cm^{-1})	Refractive index (n)
WiSE	3.092	1.38156
H_2O/ACN /1	2.462	1.38147
H_2O/ACN /2	1.553	1.38216
H_2O/ACN /2.5	1.429	1.38218
H_2O/ACN /3	1.202	1.38232
H_2O/ACN /4	0.638	1.38338
H_2O/ACN /4.5	0.488	1.38351
H_2O/ACN /5	0.365	1.38397

Ad.1.3 Experimental Results

Ad.1.3.1 Raman Characterization

We have analyzed the LiTFSI breathing mode (700 - 800 cm^{-1}) via the $S-N-S$ vibrational band to probe the coordination environment of $TFSI^-$ anions, and the $S-O_3$ stretching mode[9] (1000 - 1050 cm^{-1}) of $Zn(OTf)_2$ to assess OTf^- coordination. Baseline-corrected Raman spectra have been fitted with Lorentz functions and deconvoluted to identify the presence of multiple ionic species, as shown in **Fig. Ad. 1.1**. Previous studies have established that the $S-N-S$ bending region reflects $TFSI^-$ coordination, with peaks at ~ 743 cm^{-1} and 750 cm^{-1} corresponding to CIP and AGGIP, respectively, while the $S-O_3$ stretch (~1037 - 1050 cm^{-1}) indicates CIP/AGGIP structures of OTf^-, with no free anions, typical in WiSE. In our study, Raman spectra of LiTFSI in AWiSE solutions show a persistent presence of both CIPs and AGGIPs across all acetonitrile compositions, indicating that the ion association mode of $TFSI^-$ remains largely unchanged. In contrast, for $Zn(OTf)_2$, increasing acetonitrile content leads to a noticeable blue shift in the $S-O_3$ stretching band. This spectral evolution signifies a transition from a CIP + AGGIP mixture toward a structure dominated by AGGIPs, reflecting enhanced ion association and more extensive cation–anion clustering at higher ACN content.

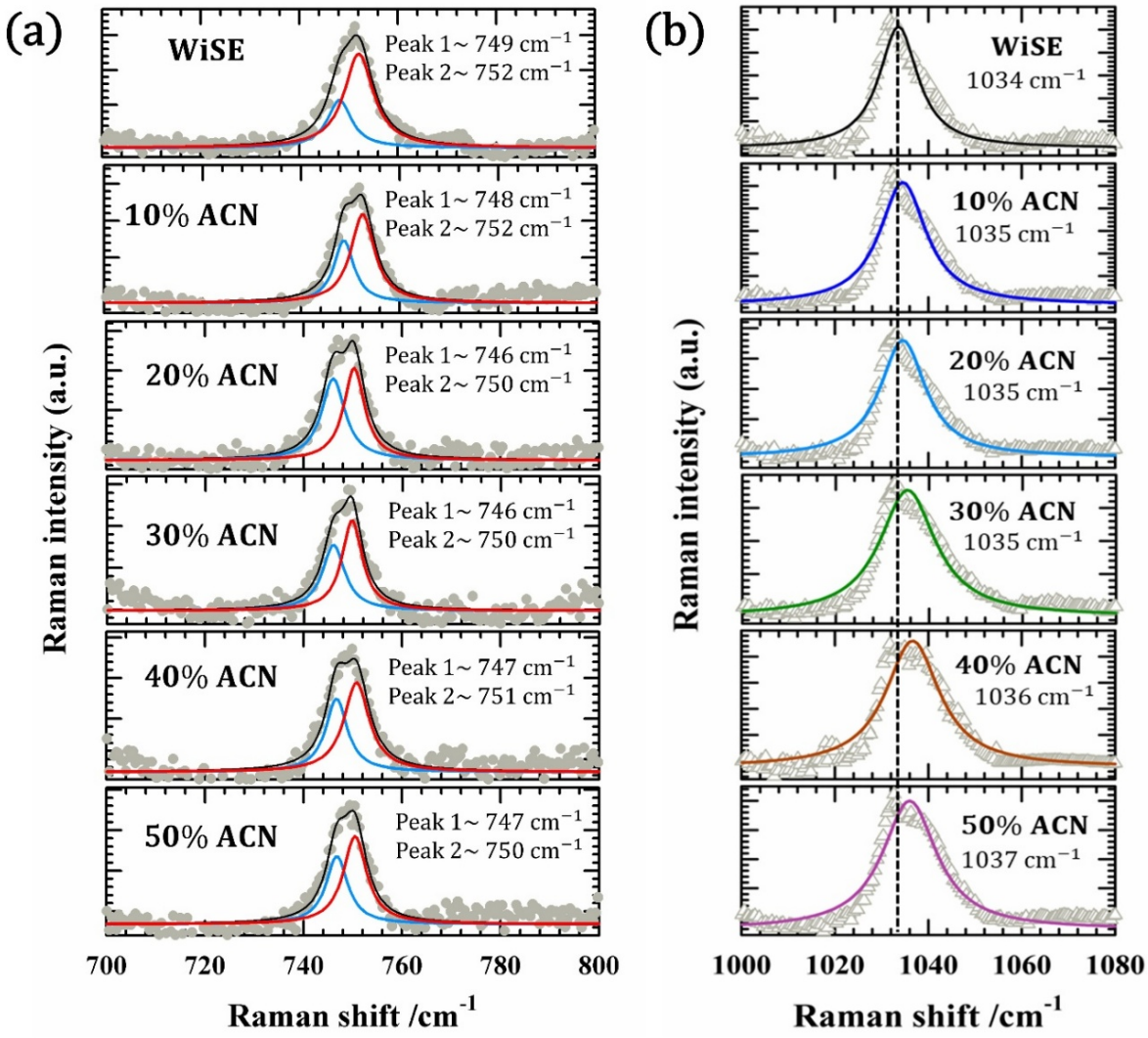

FIG. Ad. 1.1. (a) S–N–S bending mode of LiTFSI **(b)** $S-O_3$ stretching mode of $Zn(OTf)_2$. Raman spectral data fitted using Lorentzian functions, along with their deconvolutions at varying ACN concentrations. The deconvoluted spectral components are color-coded for clarity and the peak frequencies are shown in each graph.

Ad.1.3.2 Examination of Relaxation Dynamics

Fig. Ad. 1.2 displays the real (ε') and imaginary (ε'') components of the complex dielectric spectra for WiSE and AWiSE solutions, comprising 21 m LiTFSI and 3 m $Zn(OTf)_2$ in water/ACN mixture, measured at various ACN concentrations at 300 K. The middle and lower panels of **Fig. Ad.1.2** present the imaginary (ε'') parts of the DR spectra involving the raw conductivity-influenced data and the conductivity-corrected spectra, along with the corresponding multi-Debye model fits, respectively. The parameters extracted from the multi-Debye fits to the conductivity-corrected DR spectra are summarized in **Table Ad.1.3**.

In pure WiSE (21 m LiTFSI and 3 m $Zn(OTf)_2$ in water), DR spectra reveal three distinct relaxation timescales, reflecting the complex microscopic dynamics of the system. The longest relaxation time ($\tau_1 \sim 275$ ps) corresponds to a slow, collective relaxation mode, likely arising from strongly bound water-ion clusters associated with long-range correlated ionic motions within the highly concentrated electrolyte matrix. The intermediate timescale ($\tau_2 \sim 46$ ps) is attributed to the reorientation of loosely bound water molecules or, weakly solvated ions that retain partial rotational freedom. The fastest relaxation process ($\tau_3 \sim 5$ ps) is associated with the rapid motion of dipolar species, though it does not represent the dynamics of free water molecules, which typically exhibit relaxation times on the order of 8 - 10 ps. Instead, this ultrafast component is likely due to localized dipolar fluctuations in constrained or, transient environments.

As the ACN content increases from 10 to 50 wt%, the DR behavior evolves significantly. The longest relaxation time τ_1 increases from 307 ps to 406 ps, indicating a progressive slowing down of collective dynamics. This change is consistent with the disruption of the water-ion hydrogen bonding network and a reduction in free water molecules, both of which hinder large-scale dipolar reorganization. The fastest relaxation component τ_3 remains nearly constant ~ 5 ps for lower ACN contents but becomes undetectable at higher ACN concentrations (≥40 wt%), implying a diminished population of rapidly rotating dipolar species. This behavior indicates that the increasing ACN content not only dilutes the aqueous domain but also stabilizes specific solvation structures that constrain molecular dynamics and suppress ultrafast dielectric responses.

In addition to the changes in relaxation timescales, the static dielectric constant (ε_s) decreases systematically with increasing ACN concentration. This trend arises from two primary effects: the dilution of the high-permittivity water phase ($\varepsilon_s \sim 78$) by the lower-permittivity ACN ($\varepsilon_s \sim 36$), and the reduction in the population of free or loosely bound water molecules, which contribute significantly to the dielectric response through their strong dipolar relaxation. As a result, the overall polarizability of the mixture decreases, and dipolar reorientation becomes increasingly restricted. Taken together, these observations highlight the progressive transition from a highly dynamic, water-rich environment in WiSE to a more heterogeneous and rigid solvation structure in ACN-rich AWiSE solutions, providing valuable insight into the microscopic solvation dynamics, hydrogen-bonding disruption, and dynamic heterogeneity of these complex electrolyte systems.

Table Ad. 1.3. Multi-Debye fit parameters for experimental DR spectra for WiSE and AWiSE solutions. The values in parenthesis denote the corresponding amplitudes in percentage.

Electrolyte	ε_s	$\Delta\varepsilon_1$	τ_1 /ps	$\Delta\varepsilon_2$	τ_2 /ps	$\Delta\varepsilon_3$	τ_3 /ps	ε_∞	n^2	$\varepsilon_\infty - n^2$	$<\tau_{DR}>$ /ps
WiSE	14.9	5.4 (58)	275	2.8 (30)	46	1.1 (12)	6	5.6	1.909	3.691	174
H_2O/ACN /1	14.5	5.3 (60)	307	2.7 (31)	49	0.8 (9)	7	5.8	1.908	3.892	201
H_2O/ACN /2	13.2	4.6 (61)	357	2.3 (31)	53	0.6 (8)	8	5.6	1.910	3.69	236
H_2O/ACN /3	12.1	4.2 (64)	345	2.0 (30)	48	0.4 (6)	5	5.5	1.911	3.589	234
H_2O/ACN /4	9.4	2.8 (68)	296	1.3 (32)	38	-	-	5.3	1.914	3.386	214
H_2O/ACN /5	8.3	2.0 (62)	406	1.25 (38)	55	-	-	5.1	1.915	3.185	271

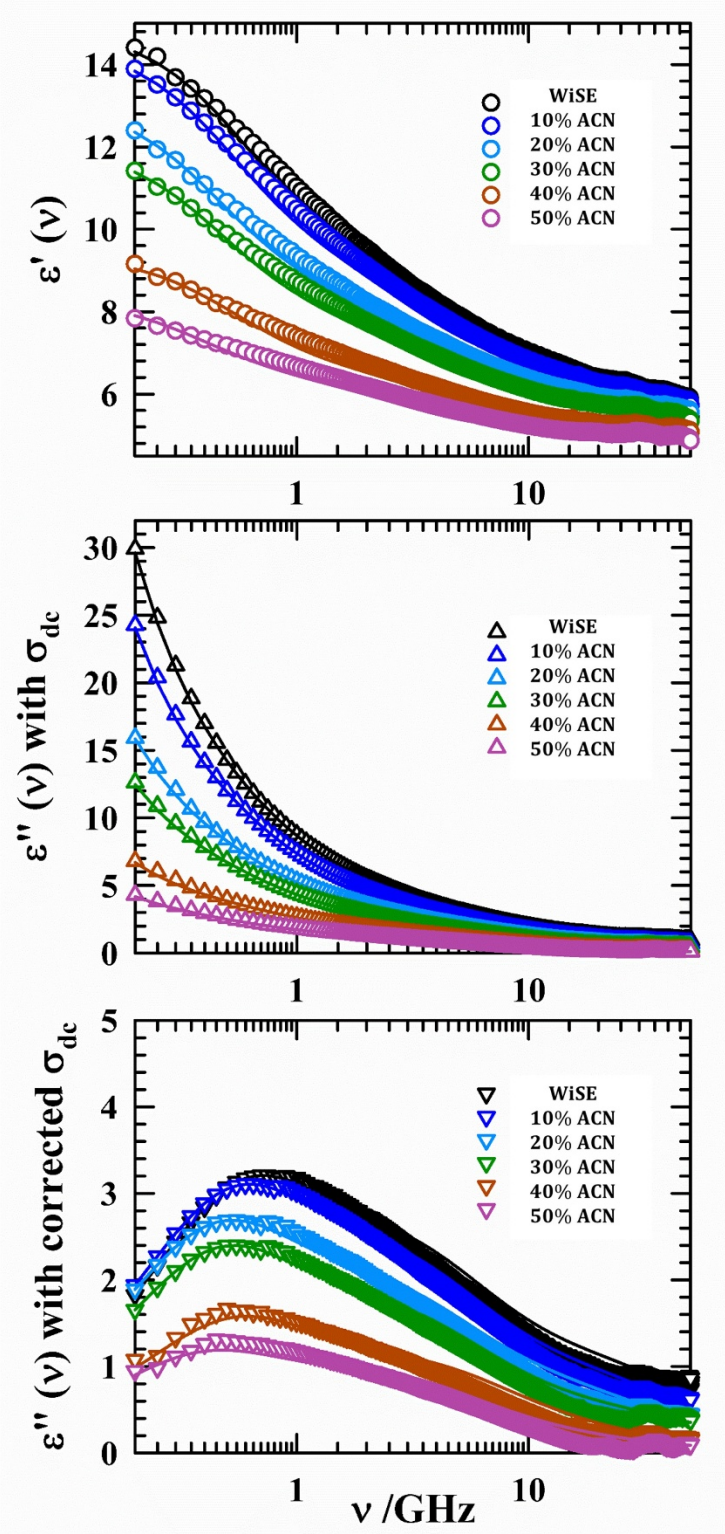

FIG. Ad. 1.2. Frequency dependent real (ε′, upper panel) and imaginary (ε′′) components (middle- with σ_{dc} and lower panel- with corrected σ_{dc}) of the complex DR spectra recorded for WiSE and AWiSE solutions at all the compositions.

References

[1] P. Inoue, E. Fileti, and T. Malaspina, *J. Phys. Chem. B* **124**(27), 5685–5695 (2020).

[2] P. Kulkarni, D. Ghosh, and R.G. Balakrishna, *Sustainable Energy Fuels* **5**(6), 1619–1654 (2021).

[3] M. Zhang, S. Makino, D. Mochizuki, and W. Sugimoto, *Journal of Power Sources* **396**, 498–505 (2018).

[4] J. Chen, J. Vatamanu, L. Xing, O. Borodin, H. Chen, X. Guan, X. Liu, K. Xu, and W. Li, *Advanced Energy Materials* **10**(3), 1902654 (2020).

[5] A. Clarisza, H.K. Bezabh, S.-K. Jiang, C.-J. Huang, B.W. Olbasa, S.-H. Wu, W.-N. Su, and B.J. Hwang, *ACS Appl. Mater. Interfaces* **14**(32), 36644–36655 (2022).

[6] J. Li, S. Qin, M. Xu, W. Wang, J. Zou, Y. Zhang, H. Dou, and Z. Chen, *Adv Funct Mat* **34**(37), 2402186 (2024).

[7] Z. Khan, D. Kumar, and X. Crispin, *Adv Mat* **35**(36), 2300369 (2023).

[8] D.E. Ciurduc, C.D.L. Cruz, N. Patil, A. Mavrandonakis, and R. Marcilla, *Energy Storage Materials* **53**, 532–543 (2022).

[9] Y. Dong, L. Miao, G. Ma, S. Di, Y. Wang, L. Wang, J. Xu, and N. Zhang, *Chem. Sci.* **12**(16), 5843–5852 (2021).